Norwegian University of Life Sciences

Master's Thesis 2019 30 ECTS
Faculty of Science and Technology

Comparative analysis of the effect of soiling on solar electricity production in utility-scale solar parks

Øystein Øvrum
Renewable Energy

Acknowledgements

Before you lies the dissertation which concludes my Master's degree in Renewable Energy at Norwegian University of Life Sciences (NMBU). I was engaged in researching and writing the thesis from February to August 2019.

The thesis was written in close cooperation with Institute of Energy Technology (IFE) and two large-scale solar PV industry companies. The work has been a true adventure from the start until the end: I had the pleasure of doing field work in Rwanda, Jordan and Egypt, following which I have been allowed working with highly professional scientists on the frontline in the research on soiling with access to top laboratories. Finally, a large portion of the final writing was done with my better half in beautiful surrounding in Dilijan, Armenia.

I would like to express my deeply felt gratitude for this opportunity to my splendid main supervisors Prof. Erik S. Marstein at IFE and Prof. Jorge M. Marchetti at NMBU for meaningful discussions and valuable inputs, which have challenged and encouraged me throughout the entire period. Additionally, I am extremely grateful to Simona Palencsar and Serkan Kelesoglu for their assistance and extraordinary guidance with regards to different laboratory devices. And to my dear colleagues at IFE: I would like to thank you for your wonderful cooperation, feedbacks and time together.

Finally, I would like to address a sincere note of gratefulness to my closest family for your sacrifices and retained belief in me. It has been a long run, but it is finally over. And at last, but not least my girlfriend, Gohar, who has stood by me like a supporting column in times of bewilderment and enabled me to complete this work.

I hope you will enjoy reading.

Øystein Øvrum
NMBU, Ås August 9, 2019

Abstract

Dust accumulation on solar panels is a significant decreasing factor for the electricity production from utility scale solar power parks. In this master's thesis, a literature study and an experimental research is conducted to broaden the knowledge of dust characteristics and its optical impacts. The studied literature is structured according to a concept of dust life cycle, which comprises five steps: Generation, transport, deposition, adhesion and removal. For all of the dust life cycle phases, the most important natural and anthropogenic factors are presented. This is followed by a discussion of the possible impacts of soiling on the electricity production. The main concern is related to loss of irradiance reaching the panel, which reduces the current of the solar cell. A secondary, indirect effect of soiling is related to reduction in voltage, due to an enhanced cell temperature.

The experimental study has shown that for open, barren regions, the dust deposited on the solar panels is strongly correlated with the topsoil in the vicinity of the park. The dust collected from a vegetated area in the middle of the blooming season revealed dissimilar visual and chemical composition between module dust and topsoil.

Furthermore, the transmission loss of sunlight through a dust layer indicated a dependency on three dust parameters. Firstly, the most crucial determinant proved to be particle size distribution, followed by albedo which has a distinct, yet secondary role. Additionally, weak indications have pointed towards an increased transmission loss at high iron oxide content in the dust, but more data is required to confirm this result.

The results from the transmission measurements revealed an α-coefficient for panel dust from arid areas in the range between 0.0203 m^2/g and 0.0309 m^2/g. This gave a difference of almost 5% in attenuation of the sunlight between the "worst" and the "best" dust types at a typical soiling layer of 5 g/m^2. Assuming an equal climate, the solar power plant contaminated with the worst dust type would experience either a higher deficit in the electricity production or increased frequency of cleaning the modules. In either case, it will inevitably result in a increased loss in total revenue.

The concluded interrelationship between transmission of sunlight and particle size distribution, albedo and iron oxide content has culminated in a proposed standard procedure for collection and analyzing dust at a potential location prior to establishment of a utility scale power plant. Sufficient dust collection from a panel with low dust density can be achieved with a squeegee and water spray gun. The dust sample can in a next step be measured in situ with a FBRM device to detect the particle size distribution. The albedo can be found by imaging with ImageJ and an XRD device could assess the iron oxide content of the dust samples. These parameters can be fed into a proposed model for assessing the transmission of sunlight as a function of the density of dust. The model can be developed on the basis of data from this thesis and future research. Alongside a thorough assessment of the natural and anthropogenic factors influencing the dust life cycle, transmission estimations can provide decision makers with valuable information before deciding on a future solar power plant project.

Sammendrag

Akkumulasjon av støv på solceller er en vesentlig reduserende faktor for elektrisitetsproduksjonen ved storskala solkraftanlegg. Denne masteroppgaven inneholder en litteraturstudie og eksperimentell forskning for å utvide kunnskapen om støvets karakteristikk og påvirkningen på belysningen av solceller. Litteraturstudiet er strukturert rundt et konsept om støvets livssyklus, som består av fem faser: Generasjon, transport, deposisjon, heftelse og fjerning. For alle fasene i støvets livssyklus presenteres også de viktigste naturlige og antropogene påvirkningsfaktorene. Hovedtapet av støvakkumulasjon er som en følge av lavere innstråling av sollys på solcellene, som reduserer produsert strøm. I tillegg utgjør støv en indirekte reduserende effekt på spenningen ved å potensielt påføre økt celletemperatur.

Den eksperimentelle delen av studiet har vist i et åpent, goldt landskap er det en klar sammenheng mellom panelstøvet og støv på overflaten av bakken rundt anlegget. Støv som ble samlet inn midt i blomstringssesongen fra en solpark i et område med mye vegetasjon avslørte visuelle og kjemiske forskjeller mellom støvet på bakken og på panelet.

Transmisjonstapet av sollys gjennom et støvlag avdekket en korrelasjon til tre parametere. Den mest fremtredende ble påvist å være størrelsen på partiklene. Dernest spiller støvets albedo en sekundær rolle i transmisjonen av solinnstrålingen. Svake indikasjoner tydet også på at jernoksider i støvet kan akselerere transmisjonstapet, men mer data kreves for å verifisere dette.

Resultatene fra transmisjonsmålingene indikerte en α-koeffisient for panelstøv fra ørkenområder på mellom 0.0203 m^2/g og 0.0309 m^2/g. Dette gav nærmere 5% forskjell i transmisjonstap av sollys mellom den "verste" og den "beste" støvtypen ved et støvlag på 5 g/m^2. Antatt like klimatiske forhold vil et solkraftanlegg kontaminert med den verste støvtypen enten oppleve et høyere tap i elektrisitetsproduksjonen eller økt freksvens av vasking av modulene. Uansett hvilken handling man velger er det uunngåelig å lide økt tap av inntekt.

Den konkluderte relasjonen mellom transmisjon av sollys og partikkelstørrelsen, albedo og jernoksidinnhold har kulminert i en foreslått standard prosedyre for innsamling og analyse av støv

ved en potensiell kraftstasjon før etablering av hele solcelleanlegget. Tilstrekkelig støv kan innhentes fra et panel med lav støvtetthet ved hjelp av nal og sprayflaske med vann. Støvet kan i neste omgang bli målt for størrelsesdistribusjon med en FBRM måler. Bildebehandling for å finne albedo kan gjøres med ImageJ og en XRD maskin kan anslå innholdet av jernoksid i støvprøvene. Disse parameterne kan så mates inn i en foreslått modell for evaluering av transmisjonen av sollys som funksjon av støvtetthet. Modellen kan utvikles på bakgrunn av dataene fra denne studien og fremtidig forskning. Ved siden av en helhetlig vurdering av naturlige og antropogene påvirkninger av støvets livssyklus kan transmisjonsestimater gi beslutningstagere verdifull informasjon allerede før en bestemmelse om etablering av et solkraftanlegg foreligger.

Nomenclature

E	Energy	J
c	Speed of light	2.998 x 10^{8} m/s
λ	Wavelength	m
k_B	Boltzmann constant	1.381 x 10^{-23} J/K
h	Planck constant	6.626 x 10^{-34} J·s
T	Temperature	K
L	Spectral irradiation	W/(m²·µm)
H	Power density	W/m²
σ	Stefan-Boltzmann constant	5.670 x 10^{-8} W/(m²·K⁴)
E_{Ph}	Photon energy	J
f	Frequency	Hz
AM	Air mass ratio	-
θ_z	Solar zenith angle	°
θ	Angle of incidence	°
β	Tilt angle	°
γ	Module orientation	°
γ_s	Solar azimuth angle	°
ρ_g	Ground reflectance	-
I_{DN}	Direct normal radiation	W/m²
I_d	Diffuse radiation	W/m²
I_T	Total radiation on tilted surface	W/m²
T	Transmission	-
A	Absorption	-
R	Reflection	-
n_i	Real part of the refractive index of medium i	-
θ_t	Angle of refracted light	°
$\propto$	Absorption coefficient	-

x	Layer thickness	m
I_R	Rayleigh scattered light intensity	W/m²
θ_s	Scattering angle	°
r	Radius	m
EQE	External quantum efficiency	-
q	Elementary charge	1.602 x 10^{-19} C
I_{Ph}	Photogenerated current	A
Ψ	Spectral photon flux	amount/s
S	Soiling loss factor	-
V_{OC}	Open source voltage	V
I_{SC}	Short circuit current	A
J_{Ph}	Photogenerated current density	A/m²
J_0	Saturation current density	A/m²
I	Current	A
V	Potential/Voltage	V
R_s	Series resistance	Ω
R_p	Shunt resistance	Ω
P	Power	W
FF	Fill factor	-
P_{Max}	Maximal achievable power	W
V_{MPP}	Voltage at maximal power point	V
I_{MPP}	Current at maximal power point	A
η	Efficiency	-
P_{in}	Incoming power from the solar radiation	W
$\varepsilon_{I_{SC}}$	Temperature correction factor for short circuit current	%
$\widetilde{I_{SC}}$	Temperature corrected short circuit current	A
T_{cell}	Cell temperature	K
T_{STC}	Temperature at standard test conditions	298 K
$\widetilde{V_{OC}}$	Temperature corrected open circuit voltage	V
$\varepsilon_{V_{Oc}}$	Temperature correction factor for open circuit voltage	-
κ_{Dust}	Brightness index of dust	-
κ_{WP}	Brightness index of white paper	-
ϱ	Albedo	-
ϱ_{WP}	Albedo of white paper	-
ω	Circularity	%
ρ	Density	g/m²

Δm	Difference in mass	g
m_{con}	Mass of dust-contaminated glass plate	g
m_{clean}	Mass of clean glass plate	g
A	Area	m^2
PSD	Single value for particle size distribution	mm
α	Slope coefficient	m^2/g

List of tables

List of figures

Contents

1 Introduction

1.1 Solar PV energy in a global perspective

The population of the world is continuously growing, leading to an increased worldwide demand for energy. When combined with a greater concern and awareness of global climate change, renewable energy sources are obliged to obtain the position as the main energy supply source if the world is to be sustained as prolific as today [1-3]. The dual challenge for a need of more energy and reduced greenhouse gas emissions is driving the shift from fossil energy, such as coal, oil and gas to renewable, abundant energy sources like solar, wind, biomass and hydropower [3]. The transfer to renewables is mainly driven by a lower levelized cost of energy, the potential of a natural, abundant and emission-free usage and a growing concern of the environmental consequences of fossil energy utilization [4]. During the last decade solar energy became one of the main renewable suppliers of energy because of reduced cost on components and installation [5, 6]. Solar energy can be divided into solar collectors, that utilize the incoming heat from the sun and photovoltaic (PV) solar cells, which convert solar radiation directly to electricity [7]. Due to the free access to sunlight, low installation and maintenance costs and no emissions of greenhouse gases or noise during electricity production, PV technology is a promising alternative for high-quality energy[1] production [8]. As of 2017, the worldwide PV power production supplied the electricity power sector with 460 TWh, having a total of 398 GW_p installed capacity [9]. Just above 60% of the total capacity is assigned to utility-scale power plants [9]. The installed peak power from PV solar cells has been exponentially rising during the last decade [7]. In 2017 and 2018 a total of 97 GW_p and over 100 GW_p was added to the global PV capacity respectively [10, 11]. According to the report ”World Energy Outlook 2018” from IEA installed PV capacity will exceed that of wind before 2025, expanding by almost 580 GW_p by 2023 under the main case scenario in a market report analysis [2, 11].

1 High-quality energy refers to energy with a high level of exergy.

1.2 Motivation for improving the awareness of soiling effects

A downside of electricity production from sunlight is the comparatively poor efficiency of a solar cell. Already in 1961, Shockley and Quiesser found that the upper efficiency limit for a single junction semiconductor with band gap at 1.1 eV is 30% at standard test conditions [12]. Normally, the efficiency of a single material solar PV cell lies around 15-25% [5, 13], which is, in comparison to e.g. hydropower (90-95%) [14], very low. In spite of that, PV still grows tremendously fast, due to its cheap, renewable and abundant energy source.

Even if PV energy is appraised to gain an even stronger foothold in the power sector in the close future and the production costs have already tremendously decreased of solar cells in the past decades, many mechanisms still require extensive research for an optimized electricity production system [13, 15, 16]. By reducing the loss of sunlight due to dust accumulation on the PV-panels (called "soiling" [2]), it is possible to substantially improve the production from a solar power plant [15]. This complex determinant can stand for up to 30% annual reduction in electricity production by reflection and absorption of the solar radiation [17]. Having the worlds driest climate and countless clear sunny days, Middle East and North Africa are also reported to have the highest rate of dust accumulation in the world [16]. Despite risk of extensive soiling, establishments of large scale solar parks continue worldwide [18]. Both in order to improve resource assessments prior to PV park construction, as well as to be able to evaluate the relevant costs for cleaning, a better estimate of dust impact prior to installation is desirable.

1.3 Scope of the thesis

To expand the knowledge about soiling and its impacts on the electricity production of utility scale solar parks, the thesis will be divided in two parts. First an extensive literature study on soiling will be presented, followed by a laboratory research including field work. Figure 1.1 depicts the context of the thesis in a holistic overview on soiling. The green and blue boundaries represent the scope of this study.

The literature review (figure 1.1, blue square) aims to explain the term dust, give an overview of the natural and anthropogenic factors that affects the dust life cycle and present the most crucial impacts on solar electricity production. In the experimental part of the thesis (figure 1.1, green square), collected panel and topsoil samples from four different locations will be subjected to dust characterization analyses and transmission measurements. The attention is aimed at better understanding the relationship between dust particle parameters and transmission losses, as well as comparing the decrease in transmission loss at various densities of soiling over the relevant

[2] In the PV industry, the term "soiling" refers to the optical effects of the soiling layer (e.g. light transmission loss).

solar light spectrum. The transmission loss can further be converted to electrical power production loss, which will have a direct impact on the economical revenue from the solar power park. From such an economical investigation, an optimal cleaning cycle of the panels can be found. A thorough investigation of the electrical and economic impacts is, however, beyond the scope of the thesis.

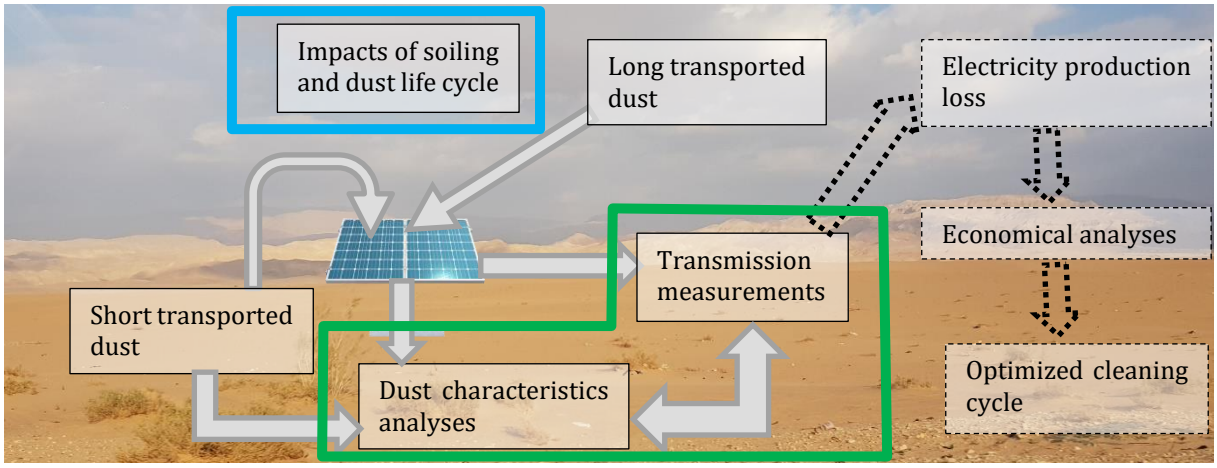

Figure 1.1: The scope of the study in a holistic overview on soiling. The green polygon represents the field and laboratory analyses, while the blue square frames the boundaries of the literature review.

1.4 Goals and objectives

It has previously been reported that dust from the Saharan desert can be detected on PV panels in Portugal [19]. The first goal of this thesis is to compare the dust characteristics of the topsoil in close proximity of the solar panels and soiling on the PV panels. This will provide valuable insight on the source of the dust and influence of long transported particles. If a strong correlation between topsoil and panel dust is detected, measurements of the topsoil would be sufficient for determining possible soiling loss in dependency of accumulated dust density on the PV panels. Combined with knowledge on local climate, transmission loss curves due to soiling could aid decision makers in estimating lost revenue from power production ex ante installation and operation of a solar power plant.

The second goal of this thesis is to develop an overview of the decrease in transmission by miscellaneous types of soiling. Some papers [20-23] have outlined differences between ash, gypsum, cement, salt, soil, sand, limestone, clay, white sand and red soil. In this study, transmission of sunlight through soiling from four locations will be evaluated alongside to an artificial dust sample of cement. Both average transmission over a broad wavelength band and spectrally resolved transmission loss will be discussed. A comparison of the attenuation of sunlight by the different dust types gives a direct feedback to the industry, which of the four sites studied is the “worst” and the

"best" in terms of soiling induced transmission loss. This could be valuable for estimation of future projects for solar power production.

It has been reported that the average grain size has an impact on the transmission of sunlight through a dust layer [21, 22], yet little information is known about the influence other dust characteristics. The third aim is therefore to detect the influence of different attributes of dust on the transmission of sunlight, including particle size, visual appearance, particle shape and chemical composition of the dust. Due to the many environmental and anthropogenic factors that influence the dust life cycle, it is beyond human scientific capacities to achieve a global function for reduction in transmission dependent on dust exposure time, like many authors have tried for larger regions [24-30]. The third objective will attempt to shed light on the most important dust particle parameters involved in sunlight attenuation. These parameters can in a next step be utilized in building a transmission model.

Today there exists no standard procedure for dust collection and laboratory investigation of the soiling. A uniform methodology is required if a transmission overview of miscellaneous dust types is to be extended by other scientists and institutions. The fourth and final aim of this pioneer study is consequently to develop a simple, but accurate protocol that allows other scientists to conduct the exact same experiment on other dust types.

1.5 Thesis structure

The thesis is structured as follows: The present chapter, *chapter 1* has given a brief introduction into the great potential of solar PV energy, and the motivation, scope and goals for this work. *Chapter 2* gives a short summary of the key physics of solar cell operation to enable a novice reader to sufficiently understand the impact soiling may inflict on the power production. *Chapter 3* presents a literature review on the work that has been done in the field of soiling. In this section the dust life cycle is presented and the different factors that influence this life cycle. Also, the impact of dust on the PV electricity production is reviewed. *Chapter 4* describes the detailed methodology of the sample collection and laboratory analysis. *Chapter 5* presents and discusses the results from the studied samples, answering to the four goals of the thesis. In addition, this section evaluates the error sources during the study and suggests potential solutions and improvements for future work. *Chapter 6* concludes the key findings of the thesis.

2 Solar electricity prerequisites

This chapter briefly presents the energy conversion from solar radiation to usable electricity production from a photovoltaic (PV) panel and an overview of the factors that negatively affect the electricity production from the solar panels. The chapter is mainly based on the physics presented in [7, 8].

2.1 Solar radiation

Solar cells utilize the enormous amount of energy that comes from the sun in form of electromagnetic radiation. In the following paragraph the generation of solar radiation and its way to the solar cell is described. In detail, the subchapter highlights the influence of the atmosphere on the radiation from the sun.

2.1.1 Energy from the sun

Continously, protons in the center of the sun participate in nuclear fusion reactions where the mass of the products is lighter than that of the reactants. About four million tons of mass are lost every second [7], which is transferred into energy through the famous Einstein equation:

$$1)\ E = mc^2 \qquad [J]$$

This gives a total power production of approximately $3.8 \cdot 10^{26}$ W, but most is absorbed by the sun itself. The energy released from the surface of the sun mainly consists of electromagnetic radiation[3]. The temperature of the surface is approximately 5778 K and the emitted power is about $6.3 \cdot 10^7$ W/m^2. When the distance to the sun increases, the energy density is reduced. The total irradiance that reaches the Earth's atmosphere at the mean Earth-sun distance is 1361 W/m^2 and is called the solar constant. Figure 2.1 illustrates the abovementioned situation.

[3] Neutrinos can leave the solar core without interacting with matter. They carry 2% of the energy from the sun.

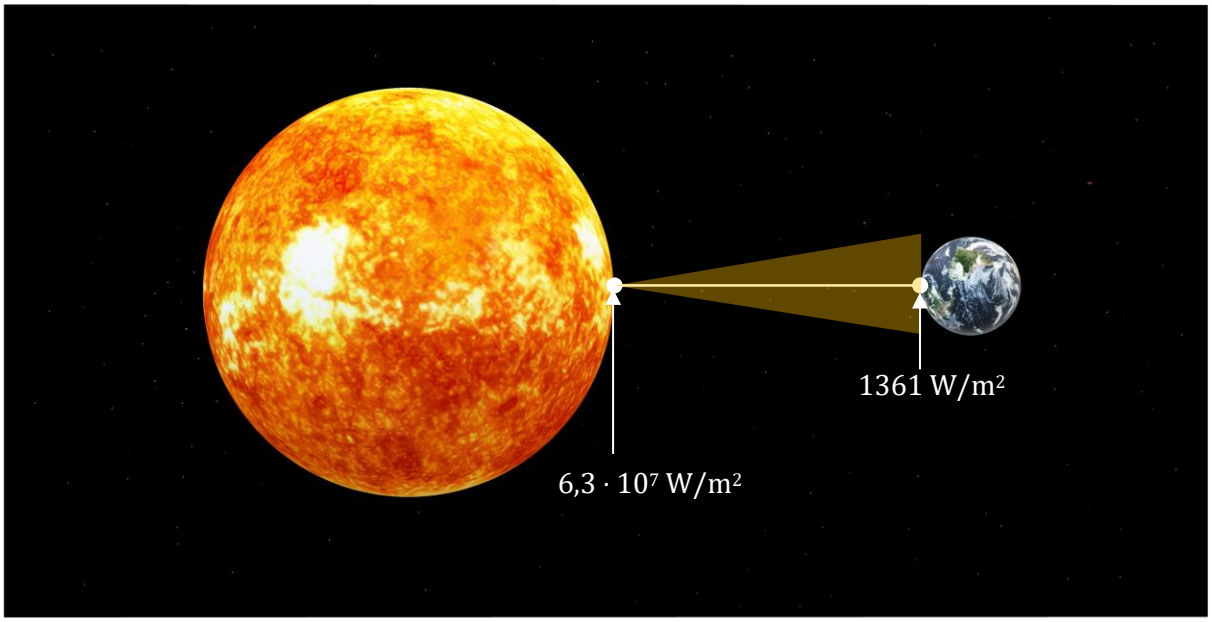

Figure 2.1: The solar power from the sun decreases considerably before it reaches the Earth. Outside the Earth's atmosphere at a mean distance between the sun and the Earth is the power 1361 W/m² (solar constant).

2.1.2 Definition of radiation

Electromagnetic radiation is transfer of energy in form of electromagnetic waves that propagate with the speed of light [31]. The sun emits most of its energy as electromagnetic waves in three parts of the light spectrum: Ultraviolet (UV), visible (VIS) and Infrared (IR) ranging from ca 250 nm to ca 2500 nm (figure 2.2 below). The sun can be modelled as a black body, which means that it absorbs all incident light and emits radiation uniquely dependent on its temperature [8]. The emitted spectral irradiation per area and wavelength (L) from the sun can be described with Planck's radiation law:

$$2)\ L(\lambda, T) = \frac{2\pi hc}{\lambda^5\left(exp\left(\frac{hc}{k_B \lambda T}\right)-1\right)} \qquad [W/(m^2 \cdot \mu m)]$$

where h is the planck constant (h = 6,626 × 10^{-34} Js), λ is the wavelength of light, T is the temperature of the sun at the surface, k_B is the Boltzmann's constant (k_B = 1.3806488 × 10^{-23} J/K) and c the speed of light (c = 2.998 × 10^8 m/s). When integrating over the entire spectrum, the total emitted power density (H) from the sun can be described with the Stefan-Boltzmann law (equation 3):

$$3)\ H = \sigma T^4, \qquad [W/m^2]$$

where σ is the Stefan-Boltzmann constant (σ = 5.670 × 10^{-8} W/(m²·K⁴)).

Characteristic for all electromagnetic radiation is the wave-particle duality, which was developed by Planck and Einstein. This duality indicates that, dependent on the situation, a photon may appear as a wave and a particle. It was shown that light comes in energy quanta, labelled photons, that are tied to the excitation or release of electrons from an atom [31]. The relationship between photon energy (E_{Ph}) and the frequency of light (f) is defined in equation 4.

$$4)\ E_{Ph} = hf, \qquad [J]$$

The frequency of light can easily be converted to wavelength (λ) through equation 5 by introducing the speed of light (c):

$$5)\ f = \frac{c}{\lambda} \qquad [Hz]$$

These two equations imply that photons with a short wavelength contain more energy than photons with longer wavelengths. More specifically, it means that UV radiation is more energetic than radiation in the VIS and NIR spectrum.

2.1.3 Air Mass ratio (AM) and attenuation of solar radiation by the atmosphere

The radiation intensity is variable at different wavelengths, as demonstrated with the green line in figure 2.2. This line represents the radiation from an ideal black body at 6000 K. The red line indicates the solar insolation just outside the Earth's atmosphere (AM0).

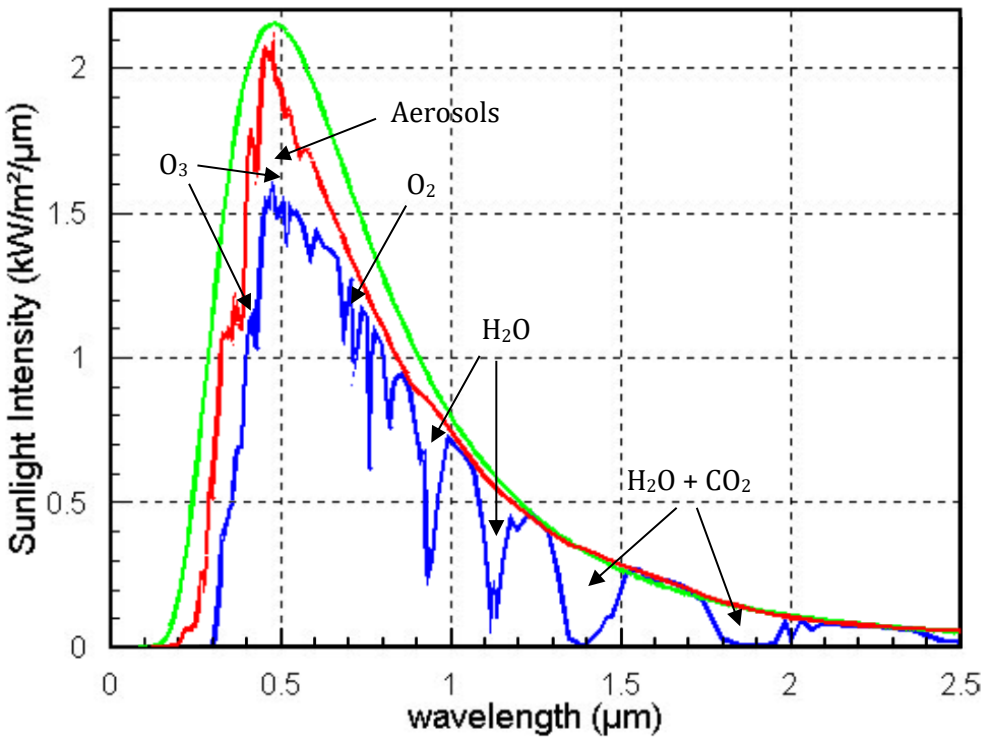

Figure 2.2: The radiation spectrum for an ideal black body with a temperature of 6000 K (green), solar radiation outside of the Earth's atmosphere (red), and solar radiation at the Earth's surface (blue). The most important molecular compounds that attenuates the sunlight are also shown. Reprinted with permission of Bowden, S. [8].

When the solar radiation enters the atmosphere, the intensity reduces due to absorption and scattering of the sunlight by particles, aerosols and gas molecules in the air. This is visualized with a blue line that represents the spectral solar radiation at the Earth's surface. The photon energy can be taken up by particles or gas molecules in two different ways. Either an electron can absorb energy to excite to a higher energetic atomic or molecular shell or the energy can be transformed into vibration or rotation [32]. The former mostly occurs for gasous substances when exposed to higher energetic light, like UV light or in the blue part of the visual spectrum [32]. Due to the abundance of O_2 and N_2 in the atmosphere, light with wavelength below 300 nm is completely absorbed, because at this wavelength the photons have enough energy to excite the electrons from these gases. The uptake of IR light is due to absorption by H_20 and CO_2 molecules, and hence the solar radiation is very low or negligible in this region.

Some of the most important molecular compounds for absorption in the range between 250 nm and 2500 nm are noted in figure 2.2. The severity of the attenuation of the sunlight intensity relies on the distance the light travels within the atmosphere before it reaches the ground: A long pathway increases the possibility for absorption or reflection of the solar radiation. In other words, when the sun is at its highest in the sky (at zenith), the distance to Earth is the lowest and therefore the highest intensity of radiation hits the ground. In comparison, in the morning and the afternoon, the solar radiation travels longer through the atmosphere and thus attenuates more before reaching the surface of the Earth.

The air-mass ratio (AM) is defined as the ratio of the distance between the actual path the light has to travel and the minimum possible length (at zenith). It can be calculated using equation 6, where θ_z is the angle between the position of the sun from the zenith.

$$6)\ AM = \frac{1}{\cos\theta_z} \qquad [-]$$

As a standard test condition (STC) in the PV industry, it is normal to use AM1.5, which corresponds to a solar zenith angle (θ_z) of ca 48°, along with a solar irradiance at 1000 W/m^2 and temperature of 25°C.

2.1.4 Relevant angles for solar PV systems

The sun's and the PV panel's positions are decisive parameters for the power production of the solar cells. Figure 2.3 introduces the angles necessary for the determination of the position of the sun relative to the PV panel: Solar zenith angle (θ_z), solar altitude angle (α_s), solar azimuth angle (γ_s), module tilt angle (β) and module orientation angle (γ).

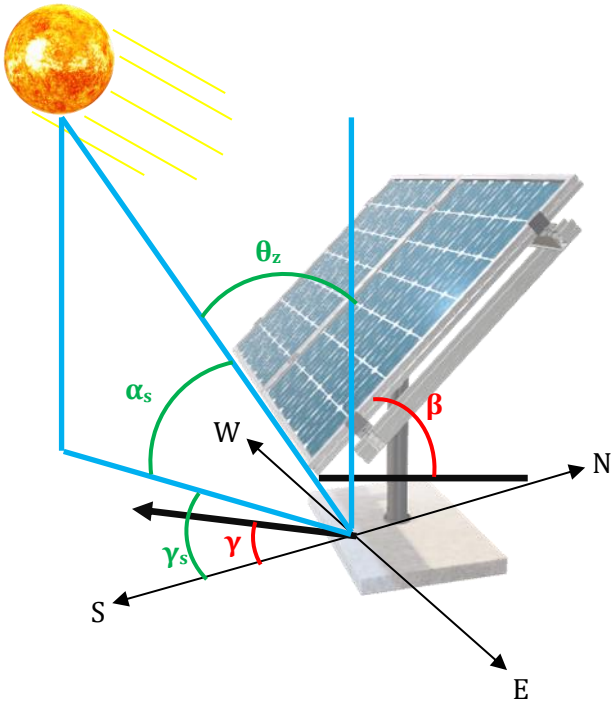

Figure 2.3: The green angles determine the position of the sun: θ_z = solar zenith angle, α_s = solar altitude angle, γ_s = solar azimuth angle. The red angles in the figure describes the position of the module: β = tilt angle, γ = module orientation.

The position of the sun and the module are often described relative to eachother with the angle of incidence (θ). This angle is defined as the angle of incoming sunlight relative to the normal from the panel's surface. Figure 2.4 demonstrates this situation in 2D, and equation 7 mathematically describes the dependency of the sun's and the module's orientation. All the angles in the computation of θ are described in figure 2.3.

$$7)\ \theta = cos^{-1}(cos\,\theta_z \cdot cos\,\beta + sin\,\theta_z \cdot sin\,\beta\, cos(\gamma_s - \gamma)) \qquad [°]$$

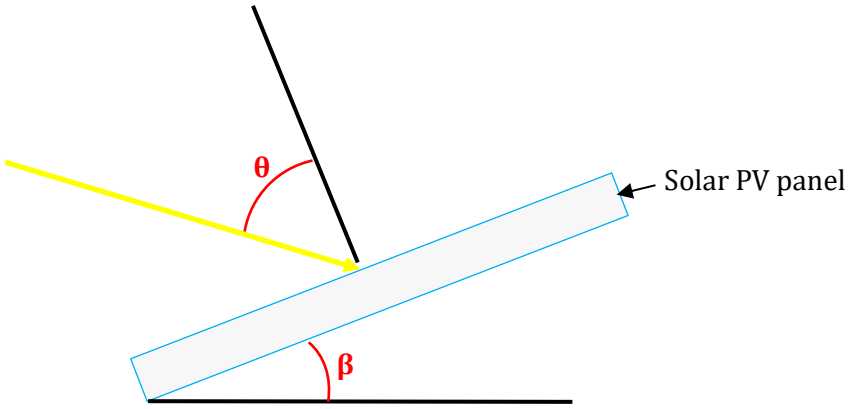

Figure 2.4: The incoming solar radiation (yellow arrow) is at an angle θ relative to the tilt and orientation of the module (here only represented by tilt angle (β) due to figure in two dimentions). θ is called the angle of incidence.

2.2 Optics of solar radiation

This subchapter firstly describes the diffuse and direct solar radiation. Secondly, it presents the physical theory on refraction, under which the Snells law is central. Since the thesis has a focus on transmission of sunlight, this part of the physics on refraction will be given a greater weight.

2.2.1 Direct and diffuse solar radiation

As sunlight goes through the atmosphere, it is not only absorbed, but also scattered by molecular compounds, aerosols and particles. The total solar radiation is thereby split between direct and diffuse light. The direct sunlight beam can be identified as light that can cast shadow from an object, while the diffuse radiation is undirected and so may strike the PV panel from any region. Consequently, diffuse light does not cast any shadow.

Additionally, the total sum of solar radiation that hits a PV module also includes the ground reflected sunlight, which is especially utilized in bifacial solar PV cells[4]. Ground reflected sunlight (I_g) is dependent on the reflectance from the ground (ρ_g) and the tilt angle. Equation 8 defines the total solar radiation (I_T) on a tilted surface:

$$8)\ I_T = I_{DN} \cdot \cos\theta + I_d \cdot \left(\frac{1+\cos\beta}{2}\right) + (I_{DN} \cdot \cos\theta_z + I_d) \cdot \rho_g \cdot \left(\frac{1-\cos\beta}{2}\right), \quad [\mathrm{W/m^2}]$$

where I_{DN} is the direct radiation perpendicular to the plate, I_d represent the diffuse radiation. The total solar radiation on a solar panel is drawn schematically in figure 2.5.

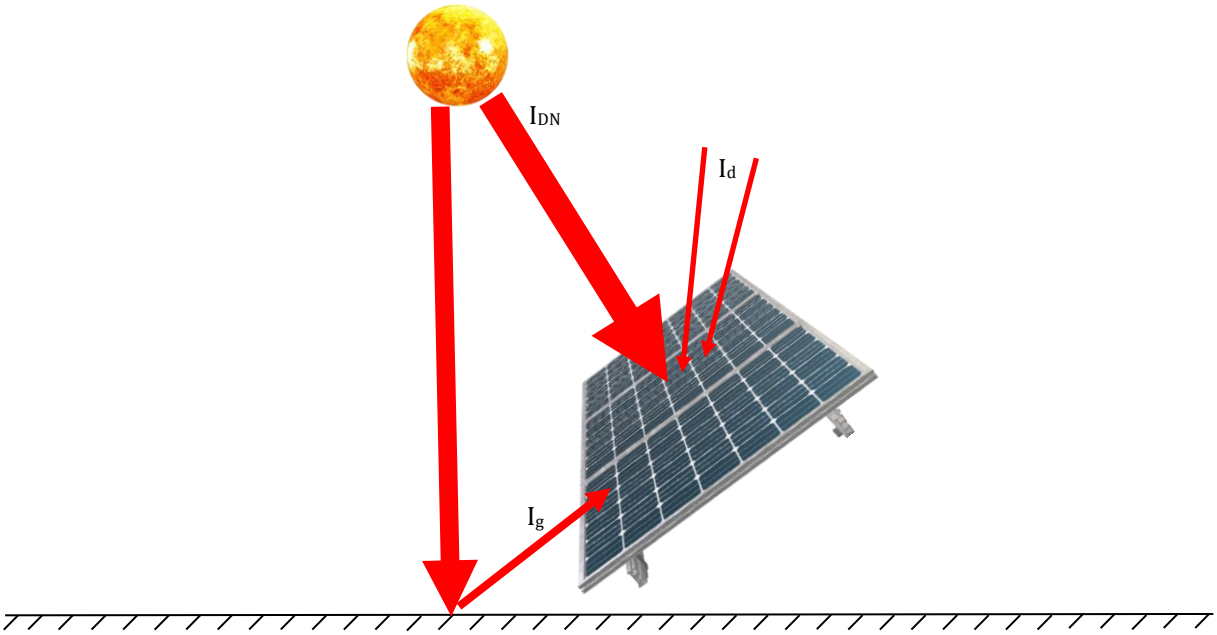

Figure 2.5: Schematic overview of direct normal sunlight (I_{DN}), diffuse irradiance (I_d) and ground reflected light (I_g).

[4] Bifacial solar PV panels can absorb sunlight from the front and back side of the panel.

2.2.2 Absorption/reflection/transmission

When the sunlight encounters and travels through the module glass cover, the total incoming solar insolation (I_T) is devided into reflection (R), transmission (T) and absorption (A), as pictured in figure 2.6.

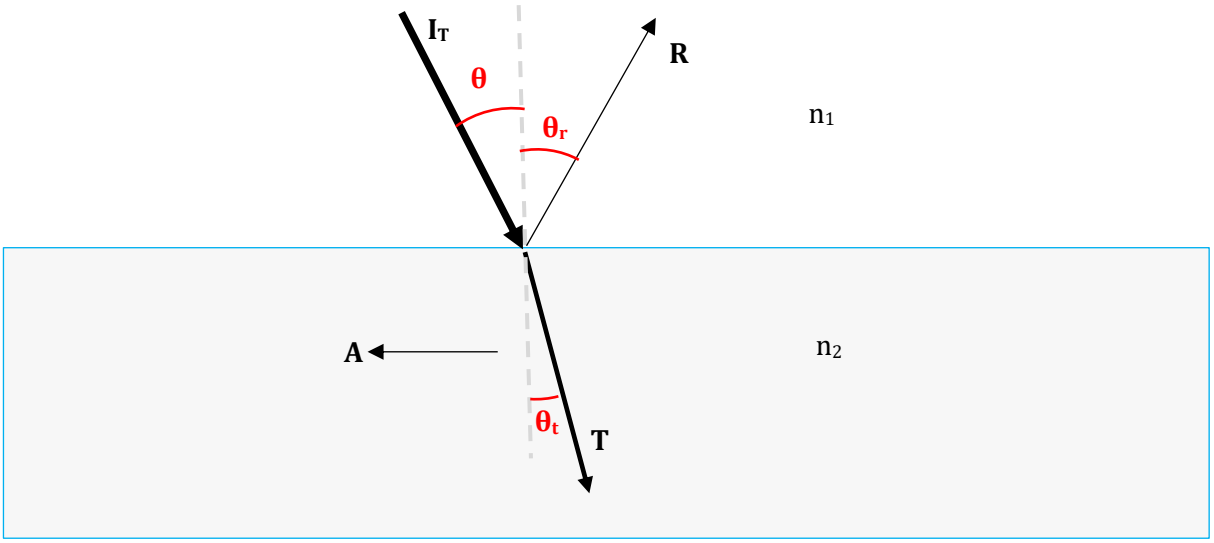

Figure 2.6: When incoming solar radiation (I_T) from one medium (n_1) encounters new material in another medium (n_2) parts of the light will reflect (R) and another fraction will transmit (T). The new medium will have a material specific absorption coefficient. The absorption (A) is undirected, but for simplicity drawn as a line inside the second medium.

To maximize the incoming solar radiation for electricity production, the fraction of transmission should be as high as possible, implying that the absorption and reflection should be kept to a minimum. Scattering and shading of sunlight will decrease the transmission. If I_T is set to unity, equation 9 shows mathematically the linear relationship between the three fractions:

$$9)\ T + A + R = 1 \qquad [-]$$

When the sunlight penetrates another medium the angle of the refracted (transmitted) light (θ_t) relative to the normal deviates from the angle of the incident light (θ) (figure 2.6). The relationship between the angles is dependent on the medium in which the light enters and comes from, and is known as the Snell's law (eq. 10):

$$10)\ n_1 \sin\theta = n_2 \sin\theta_t, \qquad [-]$$

where n_1 and n_2 is the real part of the refractive index of medium 1 and 2 respectively. All refractive indices are set relative to air, which has a value of one. Glass, which is used as glazing in the solar PV parks analyzed in this study, has a refractive index of 1.5.

By combining Fresnel's equations (appendix A) for perpendicular and parallel polarized light with conservation of energy, it is possible to compute the fraction of the sunlight that is transmitted at

different angles. At the intersection between medium 1 and 2, no absorption of light can be assumed, which results in equation 11:

$$11)\ T = 1 - R = \frac{n_2 \cos\theta_t}{2n_1 \cos\theta} \cdot \left(\left(\frac{2n_1 \cos\theta}{n_1 \cos\theta + n_2 \cos\theta_t} \right)^2 + \left(\frac{2n_1 \sin\theta}{n_1 \cos\theta_t + n_2 \cos\theta} \right)^2 \right) \quad [-]$$

For most single axis tracker solar panels located at low latitudes, the angle of incidence is relatively low. For direct sunlight (θ = 0°) equation 11 simplifies to equation 12:

$$12)\ T = \frac{4n_1 n_2}{(n_1 + n_2)^2} \quad [-]$$

From air to a clean non-textured glass plate, the transmission is 96%.

As sunlight passes throung a material, it is also absorbed. The attenuation of the intensity of sunlight is dependent on the thickness of the layer (x) and can be described with the Lambert-Beer law (eq. 13):

$$13)\ I(x) = I_T e^{-\propto x} \quad [W/m^2]$$

I(x) represents the remaining intensity of light at a certain depth into the medium. The absorption coefficient (α) will vary with wavelength of the incoming solar radiation and the material through which the light travels. It determines how far the light penetrates the material before it is absorbed. A low absorption coefficient means that the light can penetrate the material easier.

2.2.3 Albedo

Under the occurrence of soiling on the panels, a layer of dust will add on top of the PV module cover plate. This layer will have its own reflective and absorptive properties, which can be expressed with the term albedo. Strictly speaking, albedo is simply another name for reflectivity, since it is defined as the portion of the light that is reflected by the medium [33, 34]. The value of albedo is also an indicator for absorption of solar radiation. A low albedo indicates a high uptake of light, such as water that has an albedo of 0.1. This value means that 10% of the incoming light is reflected by the water, the rest is absorbed by the medium and stored as heat. Dark surfaces that easily absorbes sunlight exhibit low values of albedo [34]. Investigations of albedo of different types of dust will be a central part of this study.

2.2.4 Scattering of the direct solar irradiation by particles

Scattering of sunlight is defined as dispersal of the direct sunlight beam into a range of various orientations due to physical interactions between a particle and a photon [35]. The redirection of the radiation attenuates the sunlight and thereby increases the loss in electricity production from the solar cell.

Upon elastic scattering, the sunlight gets polarized, but the wavelength remains the same [35]. For elastic scattering, the total energy incident on the particle equals the sum of all scattered waves, which means that no energy is lost to the particle. Depending on the size of the particle that interacts with the light beam, the scattering can be divided into three cathegories [35, 36]:

- Rayleigh scattering
- Mie scattering
- Non-selective, inelastic scattering

All three types of scattering will be relevant for the dust analyzed in this study. It is, however, very difficult to determine which of the cathegories that is more relevant based purely on wavelength of the light and dust particle size distribution. Even though some boundaries between these three scattering types are presented in the following subsections, it is important to remember that these are vague and may deviate according to other factors like dielectric constant and refractive index of the particles [35].

2.2.4.1 Rayleigh scattering

Elastic scattering by spherical molecules, aerosols and particles with a size one-tenth of the wavelength (λ) of the incident light or smaller is often predicted to follow Rayleigh scattering [35, 36] (figure 2.7).

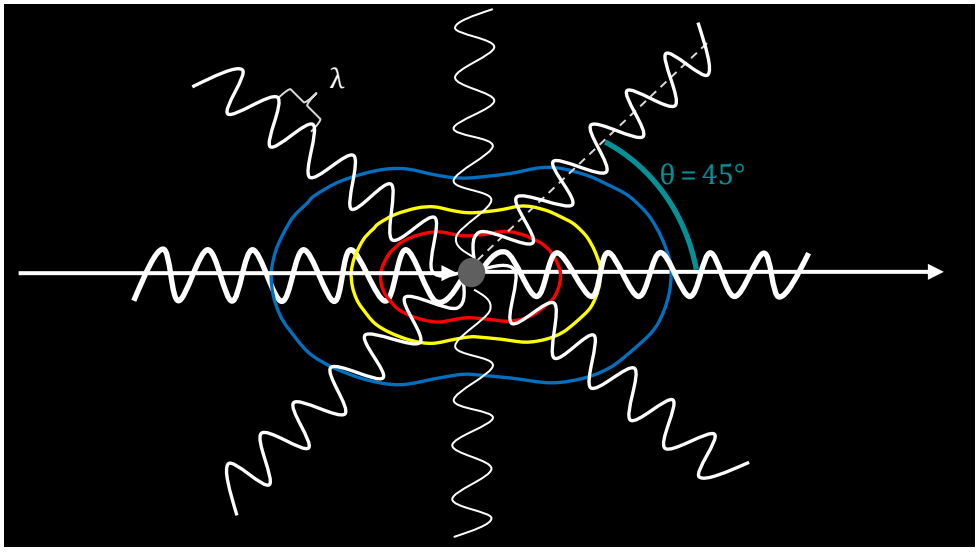

Figure 2.7: Rayleigh scattering of upolarized light (white straight line) that hits a particle with size ca one-tenth the wavelength of light or smaller (greay circle). Some of the incoming light also penetrates and goes through not affected by the particle (white solid line to the right). The colored curves demonstrate the dependency on wavelength of the scattering. The figure is inspired by [37].

As demonstrated in a 2D drawing in figure 2.7, unpolarized light (white, straight arrow) hits a small particle and is partially scattered in every direction (also backwards). It is most likely that

the photon[5] passes straight through the dust particle or bounce straight back (180°) (figure 2.7, marked with the boldest white sinusoidal lines). The intensity of the scattered light in other directions is lower, with the perpendicular direction (θ = 90°) as the lowest. Note that the wavelength of light is not altered in any direction. The intensity of the scattered light varies with wavelength of the photon. This is shown in equation 14, which shows the relationship between the intensity of the Rayleigh scattered light (I_R) and the total incident light on a tilted surface (I_T):

$$14)\ I_R(\lambda, r, \theta_s) \sim I_T \left(\frac{1}{\lambda}\right)^4 r^6\ (1 + \cos^2\theta_s), \qquad [W/m^2]$$

where θ_s is the scattering angle exemplified for one scattering direction in figure 2.7 and I_T is the total incoming intensity of sunlight, defined in equation 8. The radius of the particle and the wavelength of the light is denoted r and λ respectively. Equation 14 implies that Rayleigh scattering is predominantly affecting short wavelengths, due to the dependency of λ^{-4}. This is exemplified in figure 2.7 with three different colors: Blue, yellow and red. Blue has the lowest wavelength, which gives a higher I_R. A higher I_R implies a greater scattering in different directions. Yellow and red colored light have longer wavelengths and so the intensity of the scattered light is lower. This further leads to a higher penetration of light with longer wavelengths compared to short wavelengths.

2.2.4.2 Mie scattering

According to Dick (2018) dust particles with diameters from 1 – 100 μm are responsible for Mie scattering [38]. These particles are about the size of the photon wavelength or somewhat larger [36]. Photons subject to Mie scattering are creating a pattern strongly peaked in a forward lobe, and almost no light is backscattered (figure 2.8). This peak becomes more pronounced with increasing particle size.

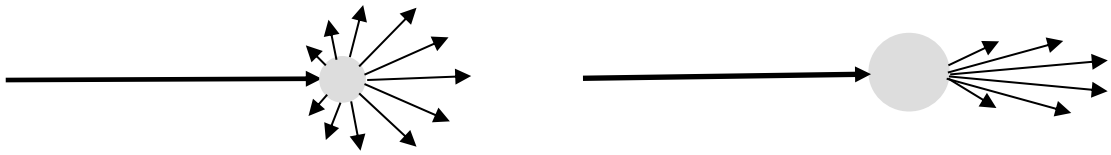

Figure 2.8: Mie scattering of a particle with size about 1 μm – 100 μm. The scattered light forms a pattern with a forward lobe, which is more pronounced the larger the particle.

A mathematical expression of the intensity of the Mie scattered light is not presented in detail, due to the considerable complexity and the reader is instead directed to [39] for further details. However, it is worth noting that the dependency on the wavelength is not strong. All photon wavelengths are therefore experiencing roughly the same scattering pattern.

[5] The probablility of an electron to take a certain path will convert to the intensity of the light at that direction.

2.2.4.3 Non-selective, inelastic scattering

For particles much larger than the wavelength of incident light, the particle no longer only scatters the light once, but multiple scattering inside the particle may occur [36]. This increases the likelihood of absorbing the photon energy and store it as heat in the particles. As a consequence, the incoming photon energy no longer equals the energy of the outgoing scattered light, which is then classified as inelastic scattering. Since this type of scattering does not dependend on the wavelength of the incoming light, it is called non-selective [36].

2.2.5 Absorption of sunlight by dust particles

It is difficult to separate absorption from scattering of sunlight, since they are often used together to explain the reduction in incoming solar radiation, like in section 2.1.3 above. The physical difference is that absorption reduces the total energy of the electromagnetic waves. Absorbing dust particles primarily convert photon energy to vibrations in the lattice, which lead to a rise in temperature [32].

Absorption of dust particles is dependent on albedo and chemical composition. It has been shown that bright particles that lack black carbon or iron oxides, such as quartz (SiO_2) or salt (NaCl), are little or not absorbing sunlight at all [40, 41]. Alfaro et al. 2004 found evidence for a linear dependency on absorption with mass percentage of iron oxide content of the dust [40]. They also showed that the absorption was six times higher for a photon wavelength of 325 nm than for 660 nm, which proved that UV light is more absorbed by dust particles than longer wavelengths [40]. Additionally, pollution of black carbon from incomplete combustion processes into the atmosphere will increase the absorption drastically, due to its dark color.

2.3 The physics of solar cell operation

When the sunlight has travelled from the sun to the Earth, penetrated the atmosphere and the PV module glass cover, it enters the solar cell. In the following paragraphs, the conversion of photon energy to electricity in the solar cell is given a brief introduction. The most commonly used semiconductor material in PV panels is crystalline silicon [8]. All the panels implemented in the utility-scale solar parks examined in this study were c-Si solar cells. Hence, this semiconductor type will be frequently used as an example of how semiconductor materials can utilize sunlight for producing energy.

2.3.1 Semiconductor material characteristics

Semiconductor materials can be built with several elements from different groups in the periodic system, which creates a possibility for many different compositions. The simplest of them are created by single materials from group IV, like crystalline silicon (c-Si) and germanium (Ge). Other

common semiconductors are compounds from groups III and V, like gallium arsenide (GaAs), or from groups II and VI, such as cadmium telluride (CdTe). In search for a higher efficiency, laboratories world wide has continuously been trying to find the optimal set of elements for a semiconductor for solar cells [42]. Most prominent of the more complex semiconductor materals are copper indium gallium diselenide ($CuInGaSe_2$), the so-called CIGS, solar cells.

The atoms in a semiconductor are connected to eachother in covalent bonds, where electrons are shared between two neighbouring atoms. These bonded electrons are called valence electrons and each atom is sourrounded by 8 valence electrons. Under no external energy influence, a semiconductor material has filled up the valence band with electrons and the conduction band is empty. The band gap energy (E_G) between the valence and conduction band is between 0 eV and 4 eV. Metals and isolators cover the materials with overlapping bands and with band gaps above 4 eV respectively.

Under an energy supply higher than the band gap energy, e.g. thermal energy or photon energy (E_{Ph}) from the sun, these covalent bonds may break and electrons are liberated from the valence band to a conduction band. In an ideal semiconductor material, it is not possible for electrons to exist between the two bands. When the electron is in a liberated state in the conduction band it can freely move over the crystal lattice. These charge carriers can be utilized in a circuit and provide electricity. The liberated electron leaves a deficit of negative charge behind, which is referred to as a positive charged hole. A simplified model of the situation is drawn in figure 2.9.

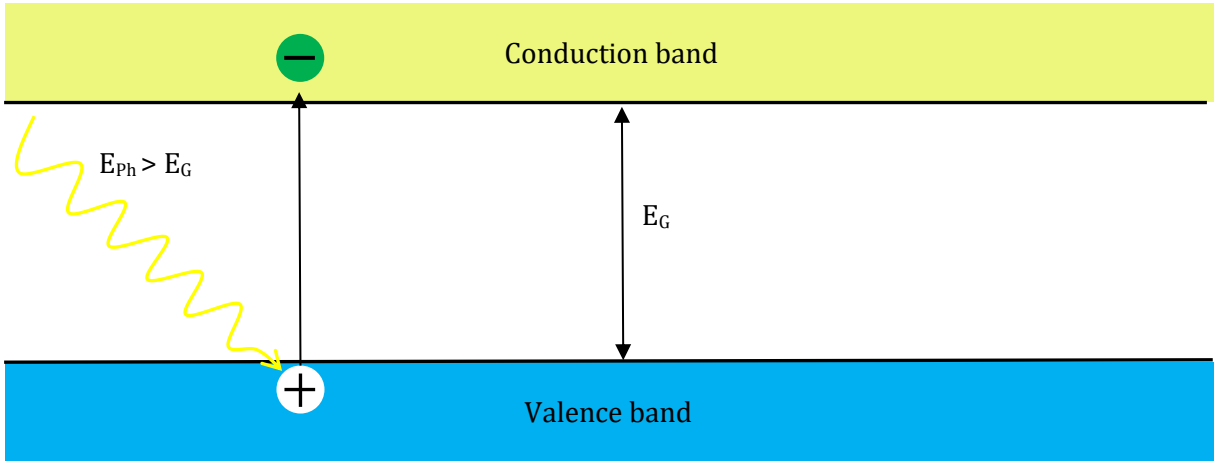

Figure 2.9: When a semiconductor is illuminated, photons that possess an energy higher than the energy gap ($E_{Ph} > E_G$) can excite an electron (depicted as a minus sign) from the valence band (blue) to the conduction band (yellow). A liberated electron leaves a deficit of negative charge, which is denoted as a hole with equal positive charge (depicted as a plus sign)

Note that the valence and conduction bands are not de facto straight lines but vary with peaks and valleys depending on a vector representing momentum. When the highest energy peak of the valence band doesn't correspond to the lowest energy valley of the conduction band, it is referred to as an indirect semiconductor. These materials require both sufficient energy (e.g photons) and

an exchange in momentum with the crystal lattice (phonons) to excite an electron from the valence to the conduction band. Crystalline silicon is an indirect semiconductor material.

2.3.2 Absorption of sunlight in a PV cell

Each semiconductor material has a specific absorption coefficient for every wavelength of the light. Figure 2.10 gives an overview of the absorption coefficients from seven different materials. When close to 100% of the sunlight is taken up by the solar cell, it is called optically thick. Since direct band gap semiconductors have a high absorption coefficient in comparison to indirect band gap semiconductors such as c-Si, it directly implies that these materials can be manufactured very thin and still be near optically thick.

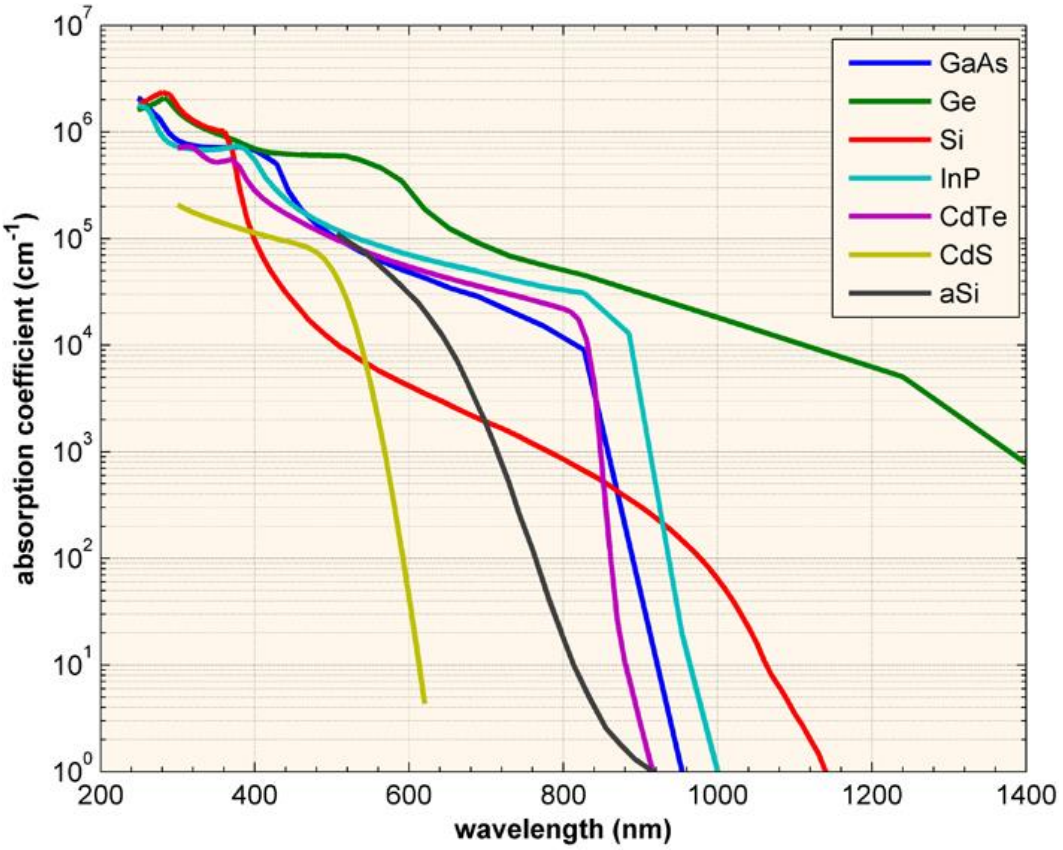

Figure 2.10: The graph shows the absorption coefficient for different semiconductor materials and its dependency on wavelength. Germanium (Ge) and crystalline silicon (Si) are indirect semiconductors, visible by the relatively flat slope. All other materials listed have steep curves and are direct band gap semiconductors. Reprinted with permission of Bowden S. from [8].

Crystalline silicon has an indirect band gap energy of 1.12 eV, which implies that light with wavelength longer than 1107 nm is left unexploited by the semiconductor. Infrared lightwaves that exceed this wavelength travels undisturbed through the silicon wafer. All other photons with an energy higher than 1.12 eV are capable of exciting c-Si electrons to the conduction band. At 364 nm, or 3.4 eV, the photon energy is sufficient for a direct transition of electrons from the valence to the conduction band, hence the sudden increase in the absorption coefficient in the ultraviolet region.

In figure 2.10, it is evident that a higher photon energy increases the absorption coefficient. This can be explained by the energy level of the valence electrons. At a photon energy equal to the band gap energy, only electrons at the valence band edge can absorb the light, whereas for higher energies electrons at lower levels of the valence band may excite to the conduction band.

2.3.3 External quantum efficiency (EQE)

Fundamentally, not every absorbed photon in the solar cell generates electron-hole pairs. The external quantum efficiency represents the fraction of photons that is successfully utilized for creating charge carriers and is dependent on the wavelength (eq. 15).

$$15)\ EQE(\lambda) = \frac{\#electrons\ generated/second}{\#incoming\ photons/second} = \frac{I_{Ph}(\lambda)}{q\Psi(\lambda)}, \qquad [-]$$

where Ψ(λ) is the incoming spectral photon flux to the solar cell and q is the elementary charge. When all photons of a certain wavelength create electrons, the value of EQE(λ) is unity. For light with a photon energy lower than the band gap energy, the EQE(λ) is zero. Ultimately, the EQE includes optical and electrical losses of the PV panel, but does not cover losses due to soiling.

By rearranging equation 15 and integrate over the entire absorption spectrum for crystalline silicon, the total photogenerated current (I_{Ph}) can be found (eq. 16):

$$16)\ I_{Ph} = q \cdot \int_{\lambda_1}^{\lambda_2} EQE(\lambda) \cdot \Psi(\lambda)\, d\lambda \qquad [A]$$

The incoming spectral photon flux, Ψ(λ), will depend on the transmission of solar radiation through the PV cover glass plate. The photon flux at different wavelengths must be measured with a known reference photocurrent and EQE. The highest external quantum efficiency values for c-Si lies between 450 nm and 1000 nm, visible in figure 2.11.

Equation 16 can be extended to include the spectral loss from soiling (eq. 17):

$$17)\ I_{Ph} = q \cdot \int_{\lambda_1}^{\lambda_2} S(\lambda) \cdot EQE(\lambda) \cdot \Psi(\lambda)\, d\lambda \qquad [A]$$

A factor for soiling loss (S), which is a number between 0 and 1, shows explicitly how the photogenerated current relies on soiling: I_{Ph} will be reduced by the dust deposited on PV panels, since it decreases the flux of photons that reaches the PV module. This soiling loss factor can be found through the transmission measurements done in this thesis.

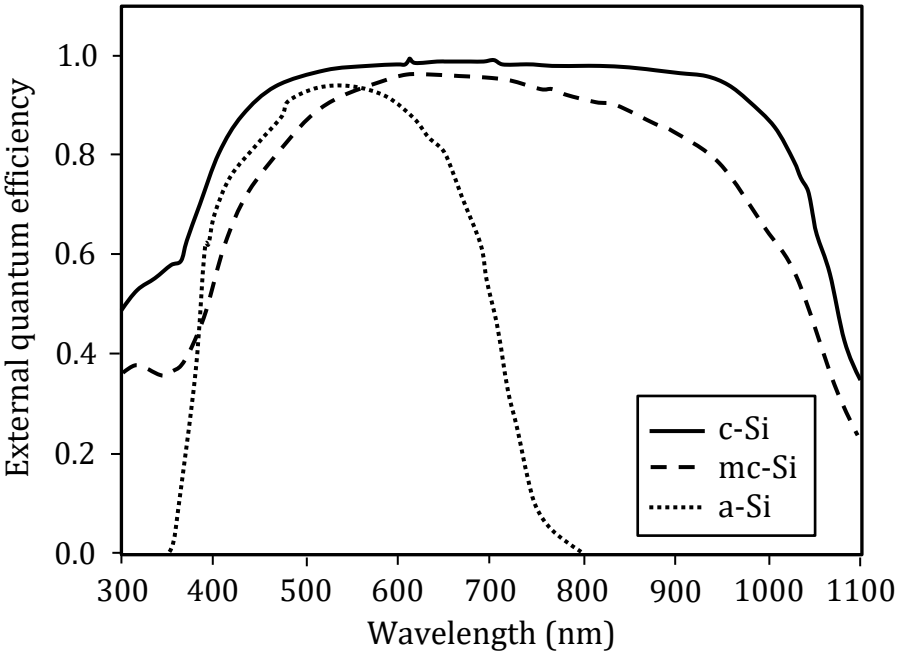

Figure 2.11: The graph shows the external quantum efficiency at wavelengths from 300-1100 nm for three different Silicon materials. An ideal, high quality mono crystalline silicon (c-Si) solar cell follows the solid line. Multi-crystalline and amorphous silicon solar cells are abbreviated mc-Si and a-Si respectively. The graph is inspired from [43].

2.3.4 Doping and the transition from chemical energy to an electrical circuit

Regular c-Si solar cells are doped with elements from neighbouring groups in the periodic system. If for example boron (B) is introduced into the silicon lattice, a deficit of negative charge will arise. This is referred to as positive doping (p-doping), since the wafer will have an abundance of holes. In contrast, if phosphorous (P) is doped into the silicon semiconductor it creates excess electrons that easily excite to the conduction band at room temperature. This is called negative doping (n-doping). Bringing a p-doped (base) and an n-doped (emitter) semiconductor material together will create a pn-junction with built-in potential (V_{bi}) between the sides. A simple set-up of the most vital components is shown in figure 2.12.

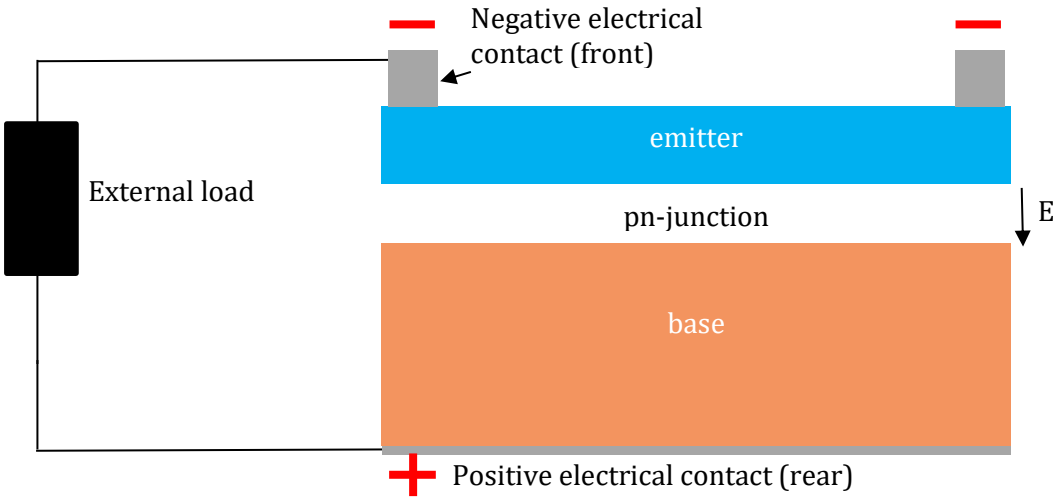

Figure 2.12: A simple model of a solar PV cell. The direction of the electrical field in the space charge region (white) is marked with an arrow and an E.

The build in potential drives the transport of charge carriers in the solar cell: The electrons are led towards the negative pole and the holes towards the positive pole. When an electrical circuit is applied, electrons will travel from the negative pole to the positive in order to equal the deficit of electrons on the positive pole.

When the set-up in figure 2.12 is in open circuit and exposed to sunlight, no electrons flow from the negative to the positive pole through the external circuit to recombine with the holes and hence the measured net current is zero. Excited electrons flow towards the emitter and holes towards the base. The generation of electron-hole pairs has to be equalized by a recombination current, which implies a lower endogenous electrical potential. In other words, at this point the dark current density compensates the photogenerated current density. The difference in the electrical potential is called *open circuit voltage* (V_{OC}). Equation 18 expresses the open circuit voltage (V_{OC}) in mathematical terms:

$$18)\ V_{OC} = \frac{k_B T}{q} \ln\left(\frac{J_{Ph}}{J_0} + 1\right), \qquad [V]$$

where q is the elementary charge, k_B is the Bolzmann constant and T is temperature. The photogenerated current devided by the area equals the photogenerated current density ($J_{Ph} = I_{Ph}/A$). J_0 represents the saturation current density. Further details on the saturation current density can be found in appendix B.

In lack of an external load the electrons on the negative side are short circuited with the positive side. All the generated electrons will recombine immediately with the holes through the external circuit, which means that the voltage across the cell will be zero. At this point the current is at maximum and is named *short circuit current* (I_{SC}).

2.4 Electrical power production from incoming solar radiation

2.4.1 The two-diode model

Under illumination of the solar cell, electron-hole pairs are generated[6] and contribute to a current flowing through an external circuit. Figure 2.13 shows a model of a real solar cell as a two-diode equivalent circuit. The shunt resistance (R_p) represents internal current losses due to defects, such as leakage through the pn-junction, where the electrons have an alternative pathway to recombine with holes. The series resistance (R_s) is designated to resistive losses at various parts of the

[6] More precise would be that the sunlight adds to the thermally generated electron-hole pairs, but since the contribution of the thermally generated current is much lower than from illumination, it is not given great concern in this basic introduction.

solar cell or module architecture, including contacts, cables, interferences and other sources of ohmic losses.

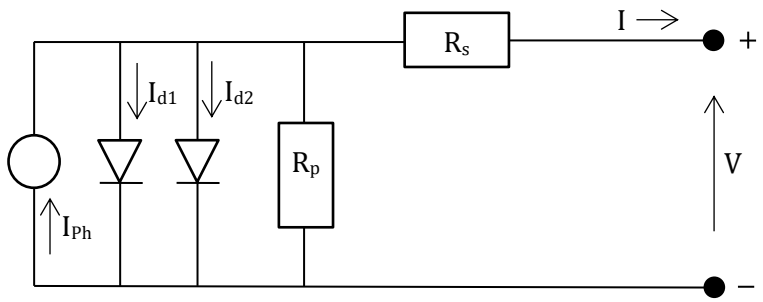

Figure 2.13: A two-diode model representing a solar cell's equivalent circuit. The circle represents the external load. R_p is the shunt resistance and R_s is the series resistance.

The reason for a two-diode model is to implement two different ideality factors, n_1 and n_2 representing an ideal and a non-ideal diode respectively. Therefore, n_1 has the value of unity, whereas n_2 is greater than one (typically a value of two). When the current is defined going from minus to plus, the total current under illumination is described through equation 19:

$$19)\ I = I_{Ph} - I_{01}\left(e^{\frac{q(V-IR_S)}{n_1 k_B T}} - 1\right) - I_{02}\left(e^{\frac{q(V-IR_S)}{n_2 k_B T}} - 1\right) - \frac{V-IR_S}{R_p}, \qquad [A]$$

where the saturation current of the two diodes are denoted I_{01} and I_{02} respectively.

2.4.2 The I-V curve

The power output (P) from a solar cell is the product of current (I) and voltage (V) as shown in equation 20:

$$20)\ P = I \cdot V \qquad [W]$$

Since the power is a product of current and voltage, operating the solar cell at V_{OC} or I_{SC} would simply yield zero power. The point at which the product of current and voltage is at maximum is called the maximal power point (MPP) and is marked in figure 2.14 on a socalled I-V curve (red line). The resulting power has the value of the green area under the curve.

The fill factor is defined in equation 21:

$$21)\ FF = \frac{P_{Max}}{V_{OC} \cdot I_{SC}} = \frac{V_{MPP} \cdot I_{MPP}}{V_{OC} \cdot I_{SC}}, \qquad [-]$$

where V_{MPP} is the voltage at maximum power point, I_{MPP} is the current at maximum power point and the maximal achievable power is denoted P_{Max}. For a best utilization of the produced electricity, the fill factor should be kept as high as possible at all times. This is done with a maximum power point tracker.

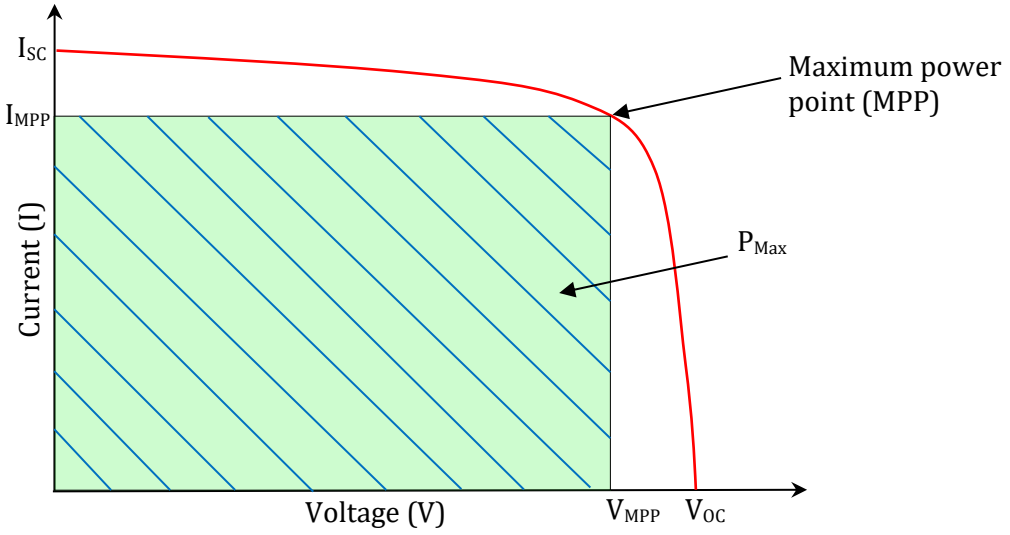

Figure 2.14: I-V curve showing the interdependency of current and voltage. The open circuit voltage (V_{OC}), short circuit current (I_{SC}), voltage at maximum power point (V_{MPP}), current at maximum power point (I_{MPP}) and the maximal achievable power (P_{Max}) can be identified.

The efficiency (η) of the module can be determined through equation 22:

$$22)\ \eta = \frac{P_{Max}}{P_{in}} = \frac{V_{MPP} \cdot I_{MPP}}{P_{in}} = \frac{FF \cdot V_{OC} \cdot I_{SC}}{P_{in}}, \qquad [-]$$

where P_{in} is the incoming power from the solar radiation. In detail, it is the total incoming solar insolation (I_T), defined in equation 8, multiplied with the area of the panel (A).

2.4.3 Reducing effects on solar PV power plant's current and voltage

There are many factors that reduce the performance of a utility-scale solar power plant. In this paragraph, they are briefly presented to provide an overview of the many challenges in PV technology and power plant design. Soiling is the main focus of this thesis and a detailed literature review is presented in chapter 3 and will not be engaged in this subsection.

2.4.3.1 Effect of cell temperature (T_{cell})

The temperature of a solar cell is called cell temperature (T_{cell}) and can be computed with equation 23:

$$23)\ T_{cell} = T_{am} + \left(\left(\frac{9.5}{5.7+3.8 \cdot v}\right) \cdot \left(\frac{NOCT - 20°C}{0.8}\right) \cdot G_{STC}\right), \qquad [°C]$$

where G_{STC} is the incoming sunlight intensity at standard test conditions (usually 1 kW/m²). The nominal operating cell temperature (NOCT) is the temperature of the solar cell at an irradiance level of 800 W/m², an ambient temperature of 20°C and wind velocity of 1 m/s. Furthermore, the cell temperature is dependent on the ambient temperature (T_a) and the wind speed (v).

The cell temperature affects the current and voltage differently. On one hand, an increased T_{cell} will have a slightly positive effect on the current, increasing the I_{SC} as shown in equation 24.

$$24)\ \widetilde{I_{SC}} = I_{SC} \cdot \left(1 + \left(\frac{\varepsilon_{I_{SC}}}{100}\right) \cdot (T_{cell} - T_{STC})\right), \qquad [A]$$

where the correction factor for the short circuit current ($\varepsilon_{I_{SC}}$) is a positive value in %/°C and T_{STC} is the temperature at standard test conditions (normally 25°C). The corrected short circuit current is denoted $\widetilde{I_{SC}}$.

On the other hand, the corrected open circuit voltage ($\widetilde{V_{OC}}$) is affected negatively. Analogously to the corrected short circuit current it can be defined as in equation 25:

$$25)\ \widetilde{V_{OC}} = V_{OC} + \varepsilon_{V_{OC}} \cdot (T_{cell} - T_{STC}) \qquad [V]$$

The correction factor for the open circuit voltage ($\varepsilon_{V_{OC}}$) is a negative number and has the unit V/°C. The correction factor for voltage must be much larger than the correction factor for current, due to the V_{OC} dependency on $1/T_{cell}$, whereas, in comparison, the dependency on T_{cell} for I_{SC} is negligible [7]. A mathematical proof of the dependency on cell temperature exceeds the scope of this thesis.

2.4.3.2 Mismatch losses and hot spots

Mismatch losses occurs when the electrical properties of interconnected cells, modules or arrays are not identical. The discrepancy in current or voltage can be caused by partial shading, manufactural defects or other varying conditions like cell temperature. In terms of soiling, mismatch losses and hot spots occur when a heterogenous layer of dust is deposited on the panels. In the following two paragraphs the two most simple mismatch losses are highlighted: Series and parallel mismatch.

Series mismatch is the most common type of mismatch loss, where for example one cell in a series, denoted *poor cell*, is not producing the same power as the other cells. In this situation, the total voltage from the series experiences only minor changes, since it is the sum over all voltages from every cell. However, the poor cell determines the short circuit current of the entire series of cells, even though all the other cells are capable of producing more current. This can force current in the reverse direction in the poor cell, which may lead to a large dissipation of power. If this is done through a local defect, a shunt, the poor cell experiences local heating. This heating of a cell is called hot spot and may reach very high temperatures. This will furthermore affect the voltage, as seen in the previous section.

For cells in parallel where one cell is damaged and is not producing the same power output, the total voltage will be most affected. In this state, the voltage is determined by the poor cell and the current is added by the cells in parallel. Again, this causes the power to decrease on the overall production of the utility-scale solar power plant.

Mismatch losses can be circumvented by introducing bypass-diodes. A bypass diode leads the electrical current around the damaged cell, module or array that is not producing in accordance with a set parameter. A bypass diode for every single cell would be ideal, but by all means not economically feasible.

2.4.3.3 Effect of light intensity

The incoming sunlight intensity naturally has a decisive effect on the I_{SC} and V_{OC}. In the morning and late afternoon, the sunlight intensity is lower than throughout the middle of the day, as noted in section 2.1.3, and this reduces the power production in these hours. Scattered sunlight on a cloudy day has the same decreasing effect on the solar radiation and the electricity production.

2.4.3.4 Effect of angle of incidence (θ)

A high angle of incidence (θ) will reduce the sunlight intensity. This becomes obvious considering that at high θ the sunlight must be spread over a larger surface, whereas for θ = 0°, the panel captures the most sunlight. Figure 2.15 shows with a simple model how the intensity is reduced.

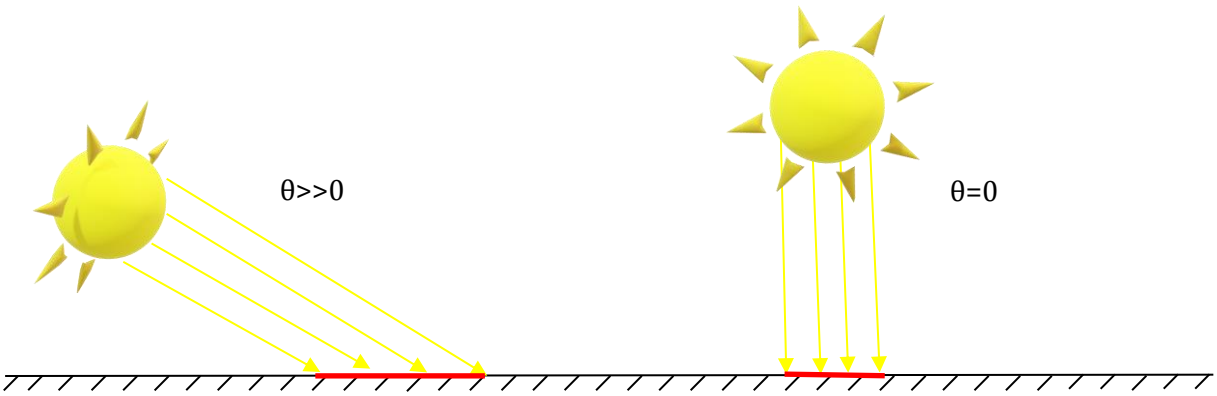

Figure 2.15: Visual explanation of how angle of incidence effects the solar radiation intensity. The red flat lines mark the area where the same solar radiation strikes.

To overcome this effect, a tracking system is required in order to tilt the panels towards the sun at all times.

3 Literature review on soiling

Due to the awareness of the reduction in power production related to soiling, the number of papers on soiling has exploded in recent years, rising from less than ten papers per year in 2008 to around 80 in 2015 [15]. This chapter focuses on giving an overview of the state of the art in the research on dust related issues for PV power production. The term dust will firstly be defined. The second subchapter will explain the different processes that generate, transport, deposit, adhere and remove dust from the panels. The final subchapter explains the impacts dust accumulated on PV panels might have for the power production.

3.1 Dust

This subchapter will give an understanding of the complexity of the term dust, its composition and apperance. As an example of the variety of dust, figure 3.1 shows three different dust samples from distant locations. The different colors are evidence of diversified morphology, albedo and chemical composition of the dust. The dust characteristics (shape, size, albedo and chemical composition) are dependent on local climate, which changes with time. This can cause seasonal and spatial variations in the characteristics of dust particles accumulated on the PV panel [44].

Figure 3.1: Different dust types from Egypt (left), Jordan (middle) and Rwanda (right).

To explain what dust is, this subchapter will concentrate on the size, shape and its chemical composition in the following two paragraphs.

3.1.1 Size and shape

Quite a few authors [44-48] have dared a definition of the term dust (or soil[7]). Common for all definitions is the description of a maximum particle size which is related to the possibility of being lifted by the wind. However, since dust grains are mainly irregular in shape, it must be characterized by its equivalent spherical diameter that possesses the same volume.

According to Picotti et al. (2018) the upper diameter limit of dust particles can be seen in atmospheric or in geologic terms [49]. In geologic terms, dust can be referred to as silt and clay, which have diameters smaller than sand (62.5 μm) [49]. Nonetheless, particles greater than 62.5 μm can naturally be lifted and deposited on PV panels, but research analyses have concluded that particles with a diameter above 500 μm – 1 mm hardly are able to accumulate on PV panels [44, 47, 48, 50]. John et al. (2015) points out that particles with diameter above 500 μm are unlikely to contribute substantially to soiling due to the required lift force from the wind and adherence forces to the surface [47]. However, since these particle sizes in fact exist on the PV modules, they must be included in the definition of dust. As a result, there is a consensus among scientists for the atmospheric term, stating that dust is comprised of particles that naturally can be lifted by into the atmosphere. The geologic term would be insufficient for describing dust particles.

Furthermore, particles above 30 – 50 μm are prone to be blown or washed off the panel by wind and rain [46, 51]. Moreover, the diameter of the dust particles deposited on the panel tends to be smaller the longer they have been exposed to weathering on the panel [46]. Cabanillas & Munguia (2011) found out that tiny particles, less than 1 μm, are the most prevalent in numbers, but in volume fraction, intermediate particles of 1 – 20 μm size are dominant [52].

Seemingly, it is problematic to declare an absolute upper and lower limit of dust particles. Normally, a large percentage of particles have diameters up to 100 μm and the probability shrinks considerably of finding grains above this size on the PV panel. No lower diameter limit can be set for dust particles, but it is difficult to collect and measure finer particles than 0.1 μm, due to agglomeration, equipment limitations and adhesive forces between particle and panel surface.

3.1.2 Chemical composition of dust

The chemical composition of dust particles is heavily reliant on the local ground, vegetation and wind. Wind can carry small dust particles over long distances, but the nearby ground is observed to have a strong impact on coarser particles [19, 26, 53]. During several studies of soiling, scientists have labelled dust in familiar terms like red soil, sand, gypsum, salt, white sand, ash, soot, spores, vegetable fibers, limestone, calcium carbonate, silica, quartz, cement and clay [20-22, 46,

[7] The term soil is in this study used as a synonym to dust.

49, 52]. Particles from rural areas have been found to appear finer and may contain soluble organic minerals, while dust alongside roads or in cities are coarser, inorganic and predominantly insoluble [26]. Utility-scale solar PV parks are often distant from big cities and preferably far away from other industries. The parks analyzed in this study are located either in the desert or in a vegetated area.

As an example of dust composition, Darwish et al. (2014) listed a total of 14 molecular components of dust at four sites in the United Arab Emirates, summarized in table 3.1 [54].

Table 3.1: Molecular composition of soiling in UAE [54].
Site I: Agricultural area relying on salty water wells.
Site II: Agricultural area relying on fresh water wells.
Site III: Desert road.
Site IV: In a city on the coast of the Arabian Sea.

#	Component	Fraction (mass – %)			
		Site I	Site II	Site III	Site IV
1	SiO_2	41.8	45.5	55.8	38.1
2	CaO	25.0	24.6	30.4	21.0
3	Al_2O_3	7.9	10.8	3.8	3.4
4	MgO	6.9	6.3	4.0	17.4
5	Fe_2O_3	12.3	10.5	3.9	16.7
6	SiO_3	2.8	0.2	0.2	0.6
7	K_2O	0.8	0.9	1.2	0.1
8	TiO_2	0.8	0.5	0.3	0.4
9	Cr_2O_3	0.5	0.2	0.1	0.5
10	MnO_2	0.3	0.2	0.1	0.3
11	NiO	0.1	0.1	0.1	0.4
12	SrO	0.1	0.1	0.1	0.0
13	P_2O_3	0.9	-	-	-
14	Cl	-	-	-	1.1

It is visible that silicon, aluminium and calcium dominate the particles from this particular desert region. This may come as no surprise, because of the abundant presence of quartz, feldspars and phyllosilicate in the Earth's crust [49, 53]. In another outdoor soiling experiment conducted by Ilse et al. (2018) in the Atacama desert in Chile, it was found that the majority of the particles contained potassium, aluminium and silicon [55]. In addition, calcium and sulfur were also present in lower ratios. Generally speaking, silicon is the most abundant element in airborne dust [49].

Vegetation can trap particles, leading to a lower dust deposition rate [53]. Nevertheless, in the blooming season, pollen, microbial cells and spores will add to the soiling. Pollen contains carbohydrates, minerals, amino acids, organic acids, metabolites and many other organic substances [56]. A detailed description of the possible grains from pollen would go beyond the outlook of this thesis.

3.2 Dust life cycle

A dust particle that contributes to soiling on a PV panel goes through different stages in its life cycle. It is born when it is cut loose from the topsoil through weathering and lifted above ground from its natural origin. It is then transported to the area where it deposits on the PV panel and adheres to the panel for a certain period of time. By definition, the cycle is complete when the particle has been removed from the surface. Hence, the dust life cycle is divided into five stages called generation, transportation, deposition, adhesion and removal, as shown in figure 3.2.

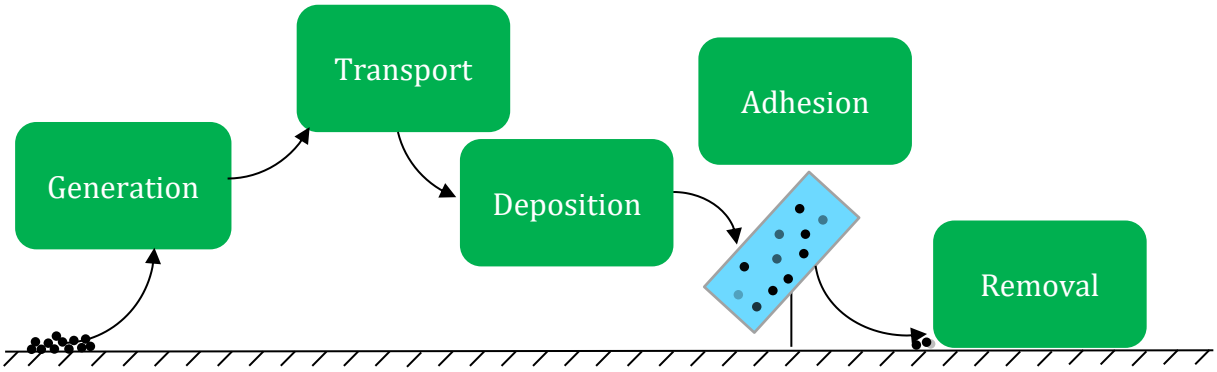

Figure 3.2: Schematical overview of the life cycle of a dust particle. Dust is generated, transported and deposited on the PV panels, adhered to the surface and ultimately removed from the panels.

Local factors that affect these phases can be natural or human induced. The most significant natural factors that influence the dust life cycle are geology, topography, particle concentration in the air (PM), wind speed, wind direction, relative humidity, rain and the morphology and chemical composition of the dust (dust characteristics). Nearby anthropogenic activity[8], obstacles, tilt angle of the modules and surface roughness and type (surface characteristics) are the main human-induced factors that affect the life cycle [30, 57-60]. Figure 3.3 shows all the mentioned factors with connection lines to the parts of the dust life cycle that it clearly affects.

From the diagram it is visible that the dust type, shape and size (geology/dust characteristics) have a significant influence on the dust life cycle. Unquestionably, it is an essential factor for the loss of electricity production due to soiling. This gave a motivation for analyzing the morphology and chemical composition of collected dust from utility-scale solar power plants in this study. Even though the influence of some of these factors is dependent on the presence of others, the following sections try to present the listed natural and anthropogenic factors individually for each of the five aspects in the dust life cycle. However, since dust characteristics are so central in the life cycle and determine the influence of all factors, it is incorporated in the paragraphs of all the other factors.

[8] Antropogenic activity is a term used for human activities such as transportation, plowing farmland and combustion.

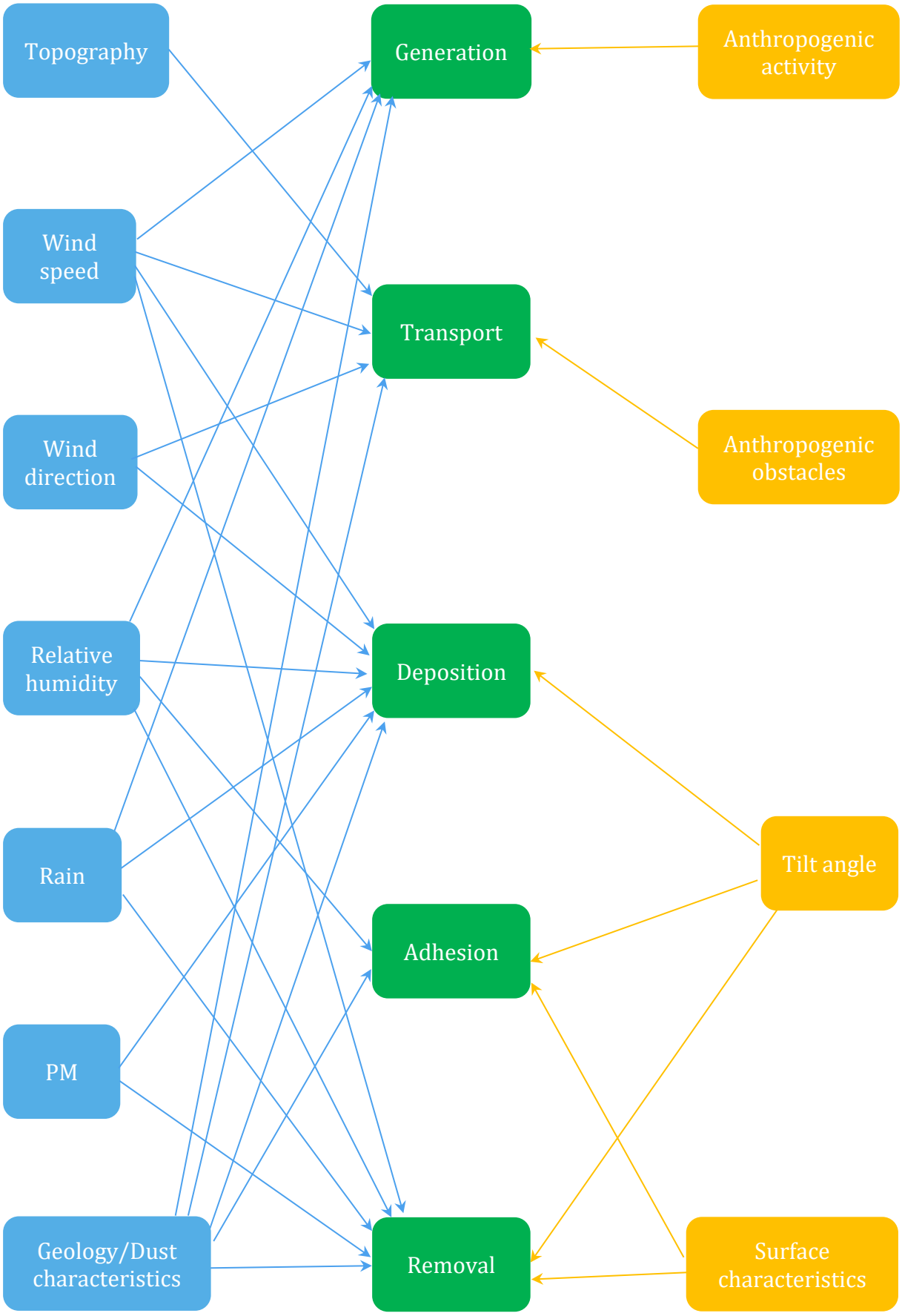

Figure 3.3: The diagram shows the natural (blue boxes) and anthropogenic (orange boxes) factors and how they are linked (lines) to the dust life cycle (green boxes).

3.2.1 Dust generation

Basically, dust generation is a process where particles disconnect from the ground due to weathering and elevate into the air. These two processes depend on geology (type of rock), the natural climate (wind, relative humidity and rain) and human activity in the area (figure 3.4).

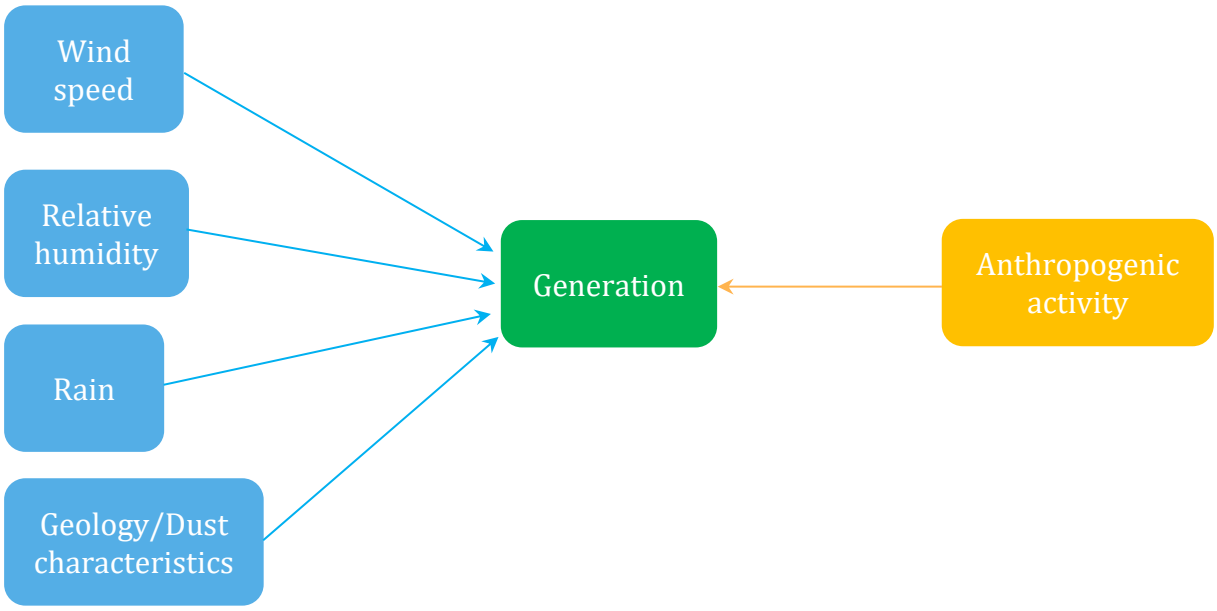

Figure 3.4: Dust generation is dependent on four main natural climatic factors: wind speed, wind direction, relative humidity and rain. The dust characteristics will be determined by the geology in the dust source area. Human induced activity that includes combustion or friction are sources of dust, and other activities that creates wind will impact dust concentration in the air.

Natural dust generation is mainly a consequence of weathering. Weathering is a physical or chemical process that breaks solid rock in the upper continental crust into pieces [49, 61]. Physical weathering is often associated with ice wedging, when water freezes and expands in voids in the ground, resulting in cracks that at last create small particles. However, in the regions studied in this thesis, it is very unlikely that the temperature fluctuates around 0°C at any time of the year. These areas are more prone to another type of physical weathering, abrasion, as a result of aeolian dust colliding into rocks. This is called sandblasting and creates a smooth surface on an obstacle over an extensive time frame.

As opposed to physical weathering, chemical weathering changes the chemical composition of the particle from the rock. This is a consequence of a reaction between the rock and a chemical agent, like for instance acid rain, oxygen or water. Different rock types chemically weather at various rates [61]. Some types, such as granite, are more resistant to weathering, whereas other types, like limestone and dolomite, are partitioned more easily.

Additionally, human induced friction and combustion processes in the society generate and elevate dust [17]. Examples of friction induced dust generation are logging of wood and screeching halt of trains on railroads. The latter emits significant amounts of iron dust particles [44].

The chemical composition of dust particles strongly depends on the sources of dust generation. When elevated into the atmosphere, the particles may or may not be transformed in a reaction with other molecules. Some molecular compounds that rise into the atmosphere can transform and contribute to particulate matter (PM) that later may precipitate [17]. To such compounds counts for instance ammonia (NH_3), volatile organic compounds (VOC), oxides of nitrogen (NO_x) and sulfur (SO_x). Natural sources of dust that don't transform in the atmosphere are pollen from photosynthesis and sand blown from deserts. Moreover, in areas where salt water is present, it can contribute to dust formation and lead to larger particles [46].

3.2.1.1 Influence of rain and relative humidity on dust generation

On one side, rain and relative humidity can facilitate the chemical and physical weathering of rocks, leading to a higher fraction of particles on the ground. On the other side, water also increases the soil moisture content, which leads to a strong capillary force between the grains in the topsoil [29]. In wet conditions, capillary forces dominate the adhesion forces over other mechanisms such as van der Waals and electrostatic forces [29]. The capillary forces are strong enough to prohibit elevation of most particles, since natural wind induced lift or drag force inflicted upon the particles will in comparison be too weak [60]. In short, extensive rain or a humid climate will enforce weathering, but prohibit elevation of dust particles.

3.2.1.2 Influence of wind speed on dust generation

Wind is a momentous factor for dust generation and elevation of particles in particular. Firstly, for an efficient abrasion of rocks a combination of frequent high wind speeds and high PM concentration is essential. Note that the latter de facto depends on the wind as well, since circulation of air must be present to elevate particles and thereby increase the PM concentration. Windy conditions are often equal to dry air, which lowers the capillary adhesion between particles. This means that the lift force from the wind will be sufficient for loading the air with particles from the ground [60]. This leads to higher PM concentration, which in turn can facilitate dust accumulation on the panels. A "sufficient wind speed" is defined as wind velocities that allow for either aerodynamic lifting, saltation or sandblasting [49, 53]. These three suspension mechanisms are visually explained in figure 3.5.

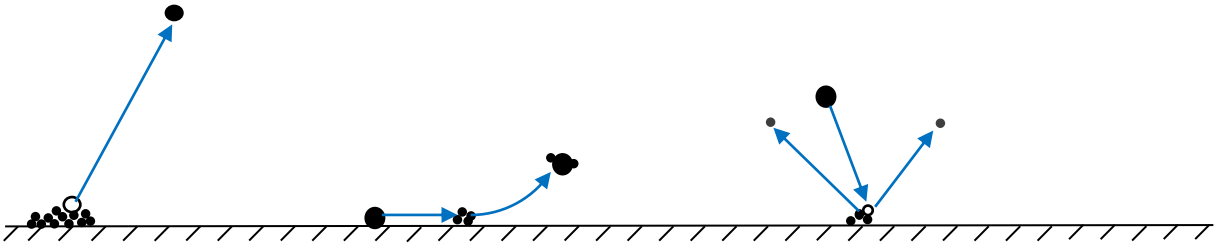

Figure 3.5: Three different mechanisms can initiate suspention of particles: Aerodynamic lifting (left) directly releases particles from the ground. Saltation (middle) indicate that larger particles entrain smaller particles and they are lifted together. Sandblasting occurs when suspended particles crash onto a surface and release other particles from the ground.

Surprisingly, it is evident that intermediate to large (ca. 70 µm – 500 µm) particles are exposed to direct aerodynamic lifting from the ground, despite having a greater mass than finer particles [49, 53]. This can be explained by the fact that silt and clay (< ca. 70 µm) have stronger cohesive forces that bind them together on the ground. Thus, it is difficult to remove them from the ground by direct levitation, but instead, they are mobilized by sandblasting and saltation [53]. Saltation refers to the phenomenon when the wind is moving larger particles horizontally and these particles entrain smaller ones [53]. Sandblasting can occur when intermediate and large particles crash into the ground and break the cohesive bond that keeps the silt and clay to the ground. Once small sized particles are suspended, they tend to travel a long distance from their source area [53].

3.2.2 Dust transport

By dust transport it is meant the horizontal transport of suspended particles from its origin to another location. It is primarily dependent on wind speed and direction, but also obstacles that create a turbulent air flow will affect the transport (figure 3.6).

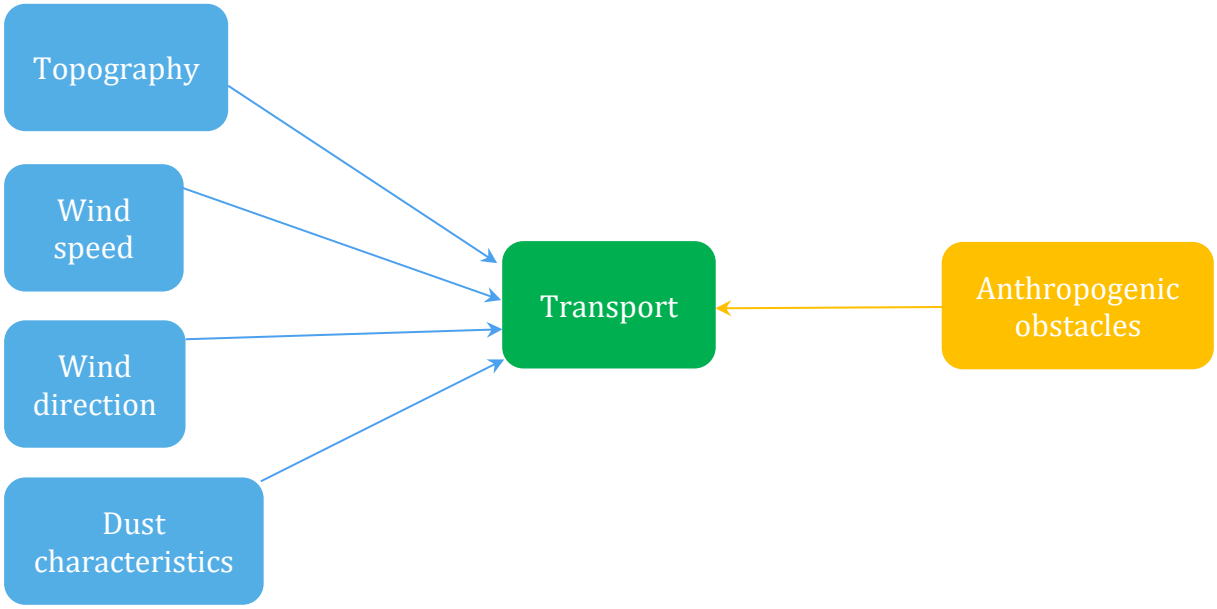

Figure 3.6: The most important factors that influence the transport of suspended dust particles from its origin to the location of the PV panels.

Vertical transport, where particles are brought from the atmosphere down to the panels, is considered dust deposition and is further explained in the next subchapter.

The geology and vegetation are often similar in every direction in close proximity to the solar power parks. This implies that short transported dust particles contain similar chemical and morphological composition regardless of wind direction. For distant transported particles the wind direction may lead to changes in dust characteristics over time [19]. In an example from Portugal, it was demonstrated that dust coming with winds from the Saharan desert showed different properties than European dust coming from other directions [19]. Additionally, a hilly and vegetated area can influence the turbulence in the airflow, creating barriers for the dust transport. This was

evident when exposing two solar parks with different vegetation nearby to the same PM concentration: No vegetation or any other obstacles lead to more dust accumulated on the panel [19]. A further detailed analysis of the dust transport is beyond relevance for a basic understanding of soiling and its impact on the electricity production and is thus excluded in this review.

3.2.3 Dust deposition

The more dust particles that settle on the panel, the thicker the soiling layer will be, and more sunlight attenuates. Dust deposition describes the process of airborne dust that collides with a PV panel. Note that dust deposition does not include the process where particles come to rest on the panel. The factors involved in dust deposition are sketched in figure 3.7.

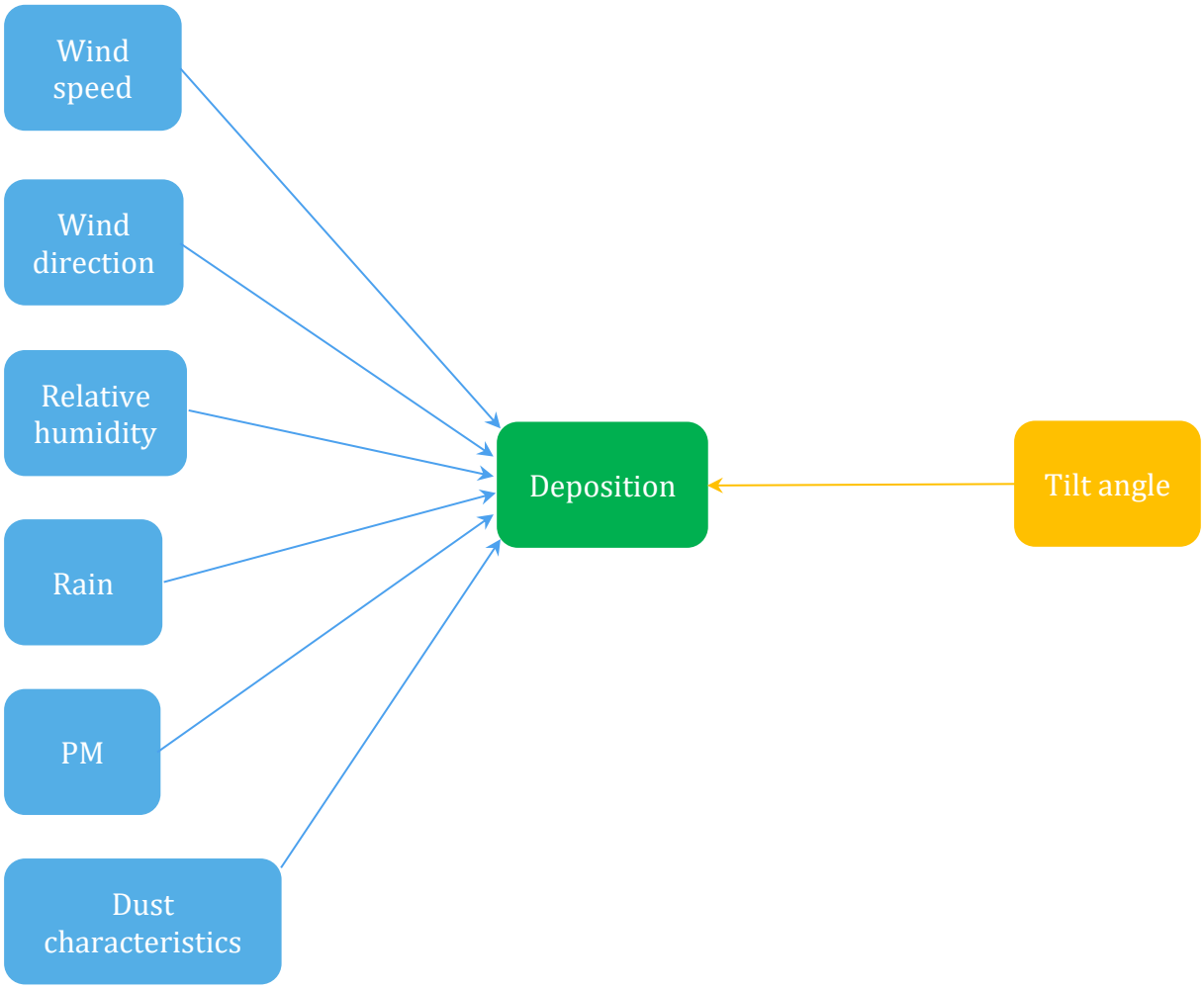

Figure 3.7: Schematic overview of the most important factors influencing the deposition of suspended particles on the solar PV modules.

3.2.3.1 Influence of PM concentration on dust deposition

The most intuitive factor that affects the amount of dust that deposits on the panel is the actual PM concentration in the air. The air must be loaded with airborne dust for particles to deposit on the panel, otherwise no deposition can take place. Generally it applies that a high PM concentration result in a greater deposition rate [45], even though it might not always be the case: In dry

and windy weather conditions, it has been found that a high PM concentration might help to remove particles from the panel, if the initial soiling was high [49, 51].

3.2.3.2 Influence of wind speed on dust deposition

Wind speed determines the upper limit of a particle's mass that can be lifted. Depending on the mass of the particle and the wind speed different depositions may occur. The deposition mechanisms can be divided into three types as depicted in figure 3.8: Sedimentation, turbulent diffusion and Brownian motion [29, 62].

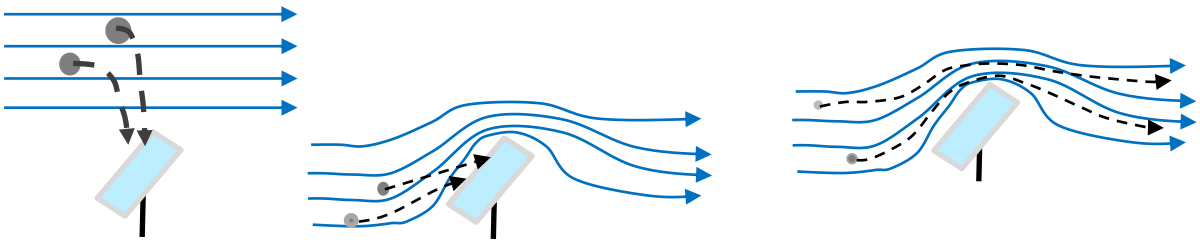

Figure 3.8: Descriptive drawing of the three types of deposition. Blue lines represent streamlines of the wind, whereas black dashed lines indicate the path of a random particle. Particles that follow Brownian motion will diffuse randomly in space, but mainly follow the streamlines of the wind.

Figgis et al. 2017 have tied these deposition mechanisms to size of the grain: Large particles above 10 µm predominantly precipitate by gravitation [29, 49]. Tiny particles below 1 µm will diffuse randomly in space and exhibit Brownian motion [29]. Often these small particles follow the streamlines of the wind. Intermediate size particles (ca 1-10 µm) conduct different behavior at different wind speeds. At low velocity, deposition due to gravity forces dominates. At higher wind velocities, inertial mechanisms trigger deposition: When the wind accelerates in front of an obstacle, the grains won't be able to follow the streamflow and crash into the module [29].

3.2.3.3 Influence of wind direction on dust deposition

Wind direction is highly relevant for the deposition of dust [59]. Over panels that are facing away from the wind, the wind velocity will be turbulent, as shown in figure 3.9. Turbulence causes local halt of the wind over the module and the suspended particles can sediment, which gives a higher deposition rate than for panels facing the wind direction [4].

Figure 3.9: Descriptive drawing showing a photovoltaic module facing the wind (left) and a module facing the opposite direction of the wind (right). Blue lines represent streamlines of the wind, whereas black dotted lines indicate a possible pattern for a dust particle. The turbulent settling, due to gravitational forces, has the highest deposition rate among the two types depicted.

3.2.3.4 Influence of relative humidity on dust deposition

Relative humidity is reported not to have a strong effect on the particle deposition process [29]. Nonetheless, in a wet atmosphere aeolian dust might absorb water vapor, possibly resulting in an increased size and mass [60]. This occurs for instance with particles containing calcite and salt. It may further contribute to agglomeration of particles in the air [63]. A cluster of particles has a higher joint mass, which enhances the likelihood of precipitation compared to individual particles [63]. The increased water content of the precipitating particles may inhibit rebounce effects from the module once the particle collides with the panel [29, 64].

Relative humidity is closely connected to wind velocity. High wind speed increases the probability for dry conditions, whereas low wind speed raises the likelihood for a humid environment [59]. The combination that gives maximal soiling rate is high relative humidity combined with high velocity of particle-loaded air. Particles will then blow into an area where they absorb water, increase their weight and deposit on the panels due to gravity or diffusion. In the study of Javed et al. (2017) they find a low tendency for such conditions when they analyze daily values of relative humidity. However, Figgis (2018) claims that the rapid change in relative humidity makes daily average values ineffective [59, 62]. A peak of 80% for a short period during the day will simply be invisible in the data samples, which Ilse et al. (2018) found in his studies on soiling in Qatar [62, 63]. The temporal solution of the measurement data, Figgis suggests, should be no greater than ten minutes to fully understand how the dust is affected by the local ambient humidity [62].

3.2.3.5 Influence of rain on dust deposition

Normally, heavy rain acts as a cleaning agent, removing dust particles from the panels, whereas light rain has a propensity to facilitate soiling [4, 49]. Naeem et al. (2015) claim that light rain and drizzle have a negative effect on the production due to the enhancement of dust transport from the atmosphere to the panels [60]. Aerosols can be mobilized in the clouds and transformed into droplets (mix of water and dust) that precipitate onto the panels [49]. Another way for rain to bring more dust to the panel is by collision of raindrops with suspended particles in the atmosphere. The raindrop and dust particle are then precipitated together on the PV module. Particles deposited by raindrops tend to be smaller than the mean grain size of the soiling on the panel [26, 65].

3.2.3.6 Influence of tilt angle on dust deposition

One important anthropogenic determinant for dust deposition is the chosen tilt angle for the solar PV module. Boyle et al. (2016) conducted experiments with varying tilted angles and found that horizontal plates exhibit a higher mass accumulation rate than tilted panels, as a consequence of the dominance of gravitational settling compared to turbulent diffusion [65]. Several scientists have found a tendency for larger grains sizes on panels with tilt angles close to the horizontal [44,

51, 66]. Dirt on vertical modules has been deposited through diffusion and are, in general, smaller in size (ref. figure 3.8) [66].

3.2.4 Dust adhesion and removal

When a dust particle hits the surface, it can either attach to the surface or bounce off immediately. The chemical composition of the grains is believed to have a significant influence on the ability to attach and stick to the glazing of the PV modules, since it is decisive for the mechanical and electrostatical properties of the dust [46]. Dust adhesion also contains the ability of a particle to "survive" removing factors, such as gravitation, wind, rain and manual cleaning.

For simplicity reasons, adhesion is here defined as the opposite of removal, implying that net accumulation of dust on the panel surface is a balance between the two processes. Dust removal describes all the mechanisms that cause a particle that once was on the panel to leave. Most of the climatological factors that regulate the adhesion, also have influence on the removal, except rain, PM concentration in the air and wind speed. Consequently, the two last phases of the dust life cycle are treated in one subchapter. Figure 3.10 visualizes the influencing factors for these two processes.

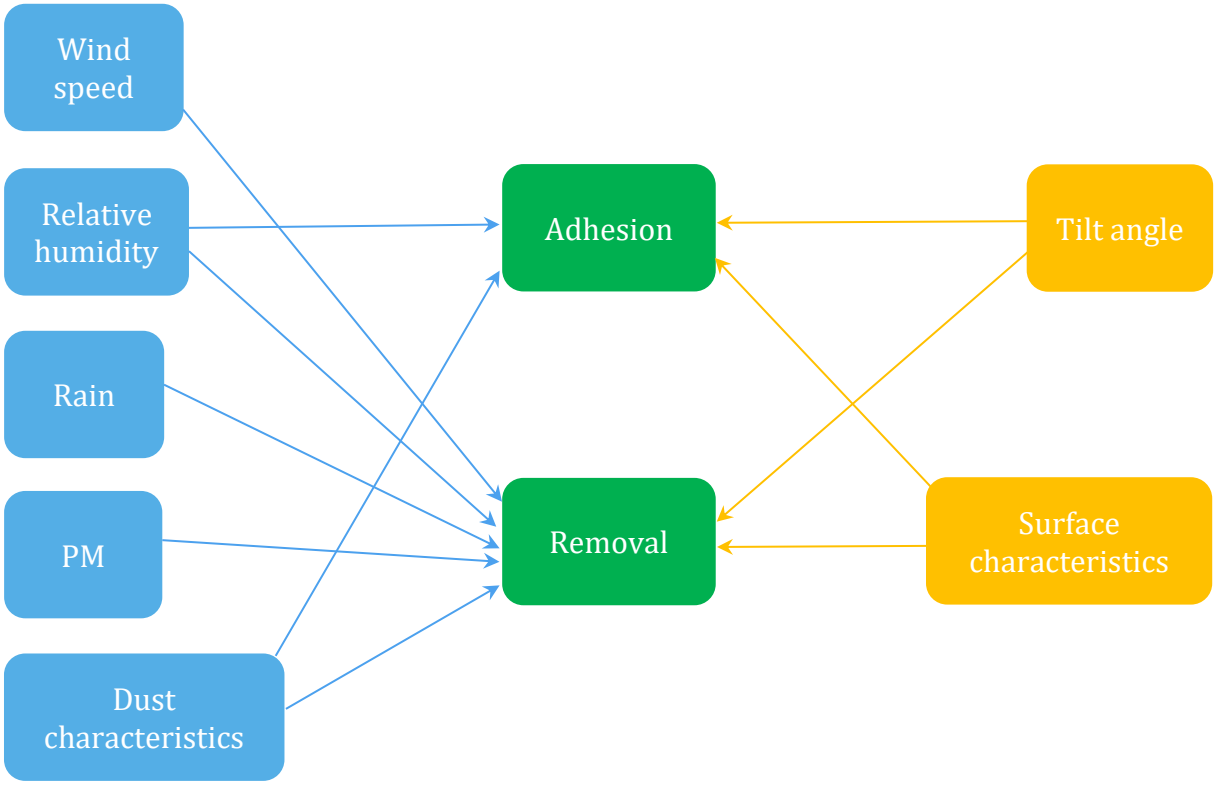

Figure 3.10: Schematic overview of the natural (blue) and antropogenic (orange) factors influencing the adhesion and removal of dust on PV modules.

3.2.4.1 Influence of wind speed and PM on dust removal

Wind speed can have an accumulative (increased dust deposition) or repelling (increased removal) effect, depending mainly on other natural factors like relative humidity, dust characteristics (stickiness) and PM concentration, but also on tilt angle and surface roughness of the panel [45, 60, 64]. Therefore, there is no clear-cut wind speed limit at which dust mainly deposits or is removed [19], but many authors have stated that, in general, low wind velocity increases the dust accumulation, whereas higher velocities remove particles from the panels [44, 46, 48, 57, 67].

Removal of particles from the PV panel requires energy to overcome the frictional force between the particle and the panel [68]. The wind rarely possesses enough power to physically lift particles from the panel up in the air [49, 60]. Instead, in case of tilted panels, particles are dragged or rolled down the surface and entrain other particles [29]. As a result of this, it is understandable that an elevated frame around the solar module acts as a barrier and prohibits particles from being removed completely. Instead they are trapped near the edge of the panel.

At low wind velocity smaller and lighter particles are gently deposited on the panel, not disrupting the already deposited dust particles. However, at high wind velocities particles will crash onto the surface and release grains already in place before the collision [30]. This may lead to a cleaning effect if the surface was substantially loaded with dust prior to the storm and the module is placed at a favorized tilt angle [49, 67]. On one side, Gaier and Perez-Davis (1992) claimed that even on horizontal panels it is observed a cleaning effect during dust storms [51]. On the other side, dust storms don't necessarily have a cleaning effect. Hammad et al. (2018) declare a significant reduction in PV production every spring in Jordan due to the annual sandstorm [6].

Moreover, high wind velocity also reduces the ambient relative humidity, leading to drier conditions [66]. If the relative humidity is low, the adherence forces between panel glazing and grains reduces and the particles can be easier removed by the wind [60]. In a situation of enhanced adherence of dust particles due to high relative humidity, a higher wind velocity is required to remove the dirt [59].

Wind generated removal of dust particles is, in addition, dependent on the size of the aeolian dust and deposited particles. Small particles have a high surface to volume ratio, which means that the frictional forces are greater than for larger grains. By and large most scientists state that wind speeds lower than 50 m/s can't clean any modules for particles less than 50 μm in diameter [60, 66]. Even worse is that at velocities above 25 m/s and high PM concentrations, the panels will be permanently damaged by grain collisions on the surface, a phenomenon which can result in transmission loss [69].

3.2.4.2 Influence of relative humidity on dust adhesion and removal

Relative humidity plays a dual role for the attachment of particles on the panel. It can either enhance or reduce the adhesion, depending on the degree of condensation and dew formation [46]. If the relative humidity rises to almost 100% the particles are not able to absorb all the water and the panels will be flooded [4]. This will result in water running down the panels, which brings dust with it. In this sense relative humidity might have a cleaning effect [70].

Under dry conditions, grains adhere to a surface owing to two frictional forces: van der Waals and electrostatic forces [49]. High relative humidity will strengthen capillary adhesion as a result of the occupation by water droplets of fine voids (capillaries) between grains on the panel, resulting in liquid bridges [29]. At the same time, a tiny water film reduces van der Waals forces with a factor of about 80 and screens the electrostatic forces [29]. High capillary forces will suppress resuspension or rolling of particles off the module [29].

A sufficient value of the relative humidity to enhance the adhesion of the grains resting on PV modules has been reported to be above ca 40 – 60% [4, 49]. The adhesion intensifies proportionally with higher relative humidity, to a certain critical value where water droplets loaded with particles start to run off the panel [29]. For an escalation in the relative humidity from 40% to 80%, adhesion is reported to rise 80% [64].

According to Ilse et al. (2018) and Naeem et al. (2018) agglomeration of particles occurs on the module due to interchanging evaporation and condensation [60, 63]. This is called “caking” and covers the tendency of a compact, rearranged deposition of particles on the panel that can be associated with mud [63, 64]. The appearance of mud can facilitate further dust deposition and also function as a habitat for plants and microorganisms [60, 66]. After the water has reevaporated, the adhesion force is undoubtedly enhanced and it requires, in general, an increased force to remove the dust from the panel compared to dust never exposed to dew [44, 60, 63, 66].

3.2.4.3 Influence of rain on dust removal

There is a large consensus that rain has a positive removal effect on dust accumulated on the panel [64, 70-72]. Nevertheless, results from different works diverge from 1 mm rain being sufficient for a fully rinsed panel [71] to heavy rain showing no significant effect [73]. This could be due to different grain size, since fine particles (2 - 10 µm) are more resistant to rain than coarser ones [21]. It has been found that rain is effective to wash away coarser grains [26, 65]. Rain therefore alters the size composition as it leads to a higher ratio of fine particles.

In the case of a mixture of raindrop and particle that hits the glass cover together, the water may evaporate after deposition and the particle remains strongly attached to the surface [4, 49]. If the

particle also contained salts, it can recrystallize on the panels. These crystals are reported to attach so strongly to the surface, that no subsequent rain can remove them [74].

Heaberlin & Graf (1998) showed that in a wet climate, despite regular flushing of the panels by heavy rainfall, plants started to grow in the soiling on the modules after very long exposure time [75]. This happened in the bottom of the panel along the frame, where the water had been intercepted and eventually evaporated. Experimental studies have made clear that the top of the panel receives cleaner water than the bottom, because as droplets travel down the panel from the top, they get loaded with dust particles [21, 28, 57]. When the contaminated water evaporates at the bottom of the panel, the grains are left behind.

3.2.4.4 Influence of tilt angle on dust adhesion and removal

The tilt angle plays a vital role in the ability of dust particles to attach to the surface [57, 65-67]. A lower tilt angle enhances the ability for larger particles to remain present on the panel despite natural cleaning effects like favorable wind and rain [44, 51, 66]. Small particles, often accumulated on steep tilt angles, tend to agglomerate on the surface. Due to an increased collective surface area and stronger adhesion these fine particles are harder to remove [51, 63, 67].

Single or dual axis tracked solar PV panels not only maximize the incoming direct solar irradiation, but additionally affect dust accumulation on PV panels. As mentioned earlier and shown in figure 3.9, panels oriented away from the wind are prone to experience a higher net accumulation rate. Trackers should orient the panels towards the wind direction in sandstorms with a sufficient tilt angle, in order for particles to easily resuspend or roll off the surface [66]. Evidently, horizontal tilt angle should be avoided during rain events because of the potential of creating a pool of water that later evaporates and enhances the adhesion of particles. Solar parks established in regions close to equator have an optimal tilt angle close to a horizontal plane in order to maximize the utilization of solar insolation. This is especially problematic for regions such as Middle East and North Africa, where the PM concentration is normally quite high [20].

3.2.4.5 Influence of PV surface characterstics on dust adhesion and removal

Specifically with regards to the dust life cycle, the PV surface may only affect the adhesion and removal of particles. PV panels have primarily been tested with two types of glazing: Glass and plastic (epoxy). It has been shown that plastic films can attract more dust due to higher electrostatic charges than glass [4, 58, 76]. Glass is the main PV cover material used today and will be the focus of this thesis.

The most glazings are not significantly textured on the front side of the glass, even though this could have resulted in a higher transmission of sunlight. The reason for having a smooth surface

is predominantly to limit the amount of possible pockets for small-size particles (0.1 – 10 μm) to find shelter where they are protected against cleaning [77]. Patterns and pockets don't automatically stem from intended manufacturing. Sandstorms may lead to erosion and cleaning procedures can scratch the surface. Textured surfaces are hard to rinse totally free of dirt [77, 78]. Moreover, elevated frames should be avoided, for the obvious reason that they extensively raise the likelihood for dust accumulation at the edges of the module [75, 78].

Ilse et al. (2018) claims that relative humidity would support agglomeration of small dust particles if the surface is prepared with hydrophobic anti-soiling product, while a hydrophilic anti-soiling film would, on the other side, provide a more uniform distribution [63]. Currently a lot of research is ongoing related to the possibilities and downsides of using anti-soiling coatings. A detailed description of different anti-soiling materials and their effect on the net dust accumulation is, however, not the aim of this study.

3.3 Impacts of dust accumulation

Dust precipitated on photovoltaic panels reduces the electric power production in an intricate way. It is claimed that these effects are visible from the moment dust accumulation reaches 0.1 g/m^2 [79]. The impacts of dust induced PV power production loss[9] presented in the following paragraphs are not considering suspended particles in the atmosphere. In extremely polluted cities like Beijing, Mexico City and Hong Kong air pollution is so severe that suspended dust particles can attenuate 10–20% of the solar radiation before the sunlight beam reaches the PV module [17, 80, 81]. The focus of this thesis is on the dust that has landed on the PV cover glass plate.

3.3.1 Transmission loss

The transmission of photons through a glass cover contaminated with dirt is visibly lower than for clean panels, due to an increased rate of absorption and reflectance of the light [63] (ref. eq. 9, section 2.2.2). Fewer photons will penetrate the cover plate and reach the PV solar cell, resulting in a decline in photon flux ($\Psi(\lambda)$), due to an increase in the soiling loss coefficient ($S(\lambda)$, eq. 17, section 2.3.3). Kaldellis and Fragos (2011) deposited ash on the panels, and mainly observed enhanced reflection [17]. This was believed to stem from the small particle size distribution of the panel dust. It is important to note that particles don't necessarily block all light over the entire spectrum; they can be more transparent for particular wavelengths and have a higher absorption rate of other wavelengths [52]. As seen in section 2.2.4 dust particles inevitably scatter the sunlight in different directions and consequently, the ratio of diffuse to direct sunlight increases.

[9] Soiling induced PV power production loss will in the following be referred to as "PV soiling loss".

3.3.1.1 Dependency on angle of incidence

Studies have reported a higher transmission loss at higher angles of incidence, due to the fact that grains cast a longer shadow than at normal angles of incidence [73]. Figure 3.11 presents this aspect visually. For solar PV panels with no tracking system of the sun the loss is consequently greater in the early morning and late afternoon due to soiling. These analyses on the dependency of the angle of incidence have led to claims of a higher absorption and reflection rate of diffuse than direct sunlight due to soiling [71, 82].

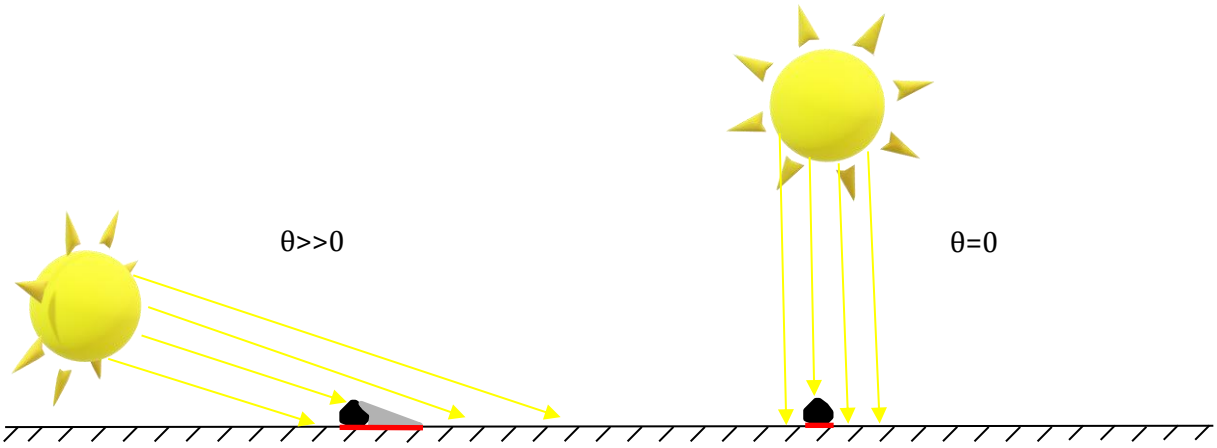

Figure 3.11: Grains resting on a PV panel will cast a long shadow at high angles of incidence (θ). The red flat lines mark the difference in shaded areas for the same particle size.

For utility scale solar parks investigated in this work, all modules are mounted on a single axis east – west tracker. Consequently, the problem is minimized to seasonal differences in the solar zenith angle at noon. Since the parks are located quite close to the equator the small deviations from a normal incident of light beam during the whole year makes this problem negligible.

3.3.1.2 Spectral differences in transmission loss

The reduction in transmission contributed by the dust is spectrally dependent [4]. Interestingly, it has been showed several times that as the density of dust accumulated on the panel increases, the reduction is higher for shorter wavelengths than for longer [25, 57, 66]. Levinson et al. (2005) noted a tendency for UV light waves to extensively be absorbed, rather than reflected [83]. Longer wavelengths, however, tend to be reflected and the loss is not as severe as for shorter wavelengths. Again, this is in line with the assumed dependency on particle size distribution, which was presented in section 2.2.4.

The various spectral response to various types of dust and their density might have implications for an optimal type of solar panel to be installed, at least if cleaning is to be avoided. The absorption spectra in figure 2.10, section 2.3.2 show that c-Si or Ge solar cells have a wide spectral absorption area, whereas others, like CdTe or a-Si, have a narrow region for sunlight uptake at shorter wavelengths [7]. Dust that affects UV light the most will therefore have a greater impact

on the electricity production from the two latter types than from c-Si or Ge solar cells [57, 84]. Consequently, due to spectral differences, there is no linear correlation between average loss in transmission and loss in electricity production of a solar PV module.

3.3.1.3 Non-linear reduction in transmission

The decrease in transmission is typically non-linear. This is visualized in figure 3.12 with data points from two artificial cement dust deposition experiments [21, 22].

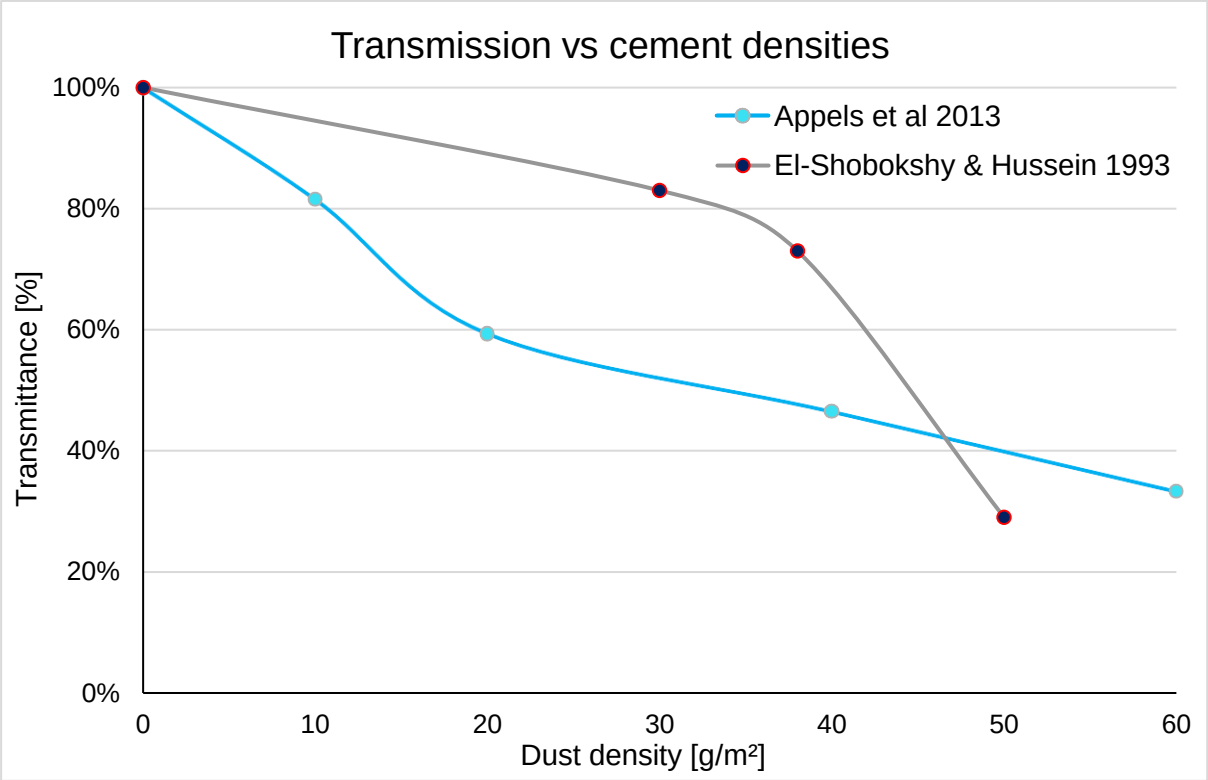

Figure 3.12: Transmission of light as a function of cement dust density. The data were found in [21, 22].

An explanation for non-linearity in the transmission loss is claimed to be related to the behavior of particles. When dust accumulates on a surface, particles tend to pile up and agglomerate on top of each other instead of uniformly distribute over the whole panel [25, 29, 68, 85, 86]. In addition, a mixed grain-size distribution would accelerate the transmission loss over density: Large particles will cover more areas and the smaller fragments will be able to fill the voids between them [46, 68].

3.3.2 Influence on soiling accumulation rate

The dust accumulation rate seems to vary with the already deposited dust density. Some studies have shown that supported by electrostatical charges, particles more likely accumulate where the dust density is already at a high level [4, 26, 66]. Contrarily, others have pointed out the complete opposite effect, stating that panels with a high deposition density experience a lower net dust accumulation rate [26, 46]. Javed et al. (2017) argued that this is not because the deposition rate

declines, but rather as a result of enhanced rebounce and resuspension rate [59]. Ultimately, the accumulation rate in real situations becomes very hard to determine.

3.3.3 Production loss

First and foremost, loss in transmission implies a decline in photon flux, $\Psi(\lambda)$, through the PV cover plate. In accordance with equation 15, section 2.3.3, reduced $\Psi(\lambda)$ will in turn decrease the current generation of the PV modules. In other words, when dust screens the incoming sunlight beam, it has a direct impact on the current [64].

Secondly, soiling would have a less, yet still important, effect on the voltage due to a potential increase in cell temperature [13]. It is not trivial to find the correlation between the soiling and the cell temperature, since in a real environment, other factors such as solar irradiation, wind velocity, ambient temperature, type of PV module and type of surface glazing can influence the temperature to a large degree [64]. Reflected sunlight by dust accumulated on the surface may exhibit a cooling effect [30]. The following two paragraphs shed light on some aspects that complicate the assessments of soiling related production losses.

3.3.3.1 Absorption of heat by dust particles

Direct increase in cell temperature as a consequence of soiling is far more troublesome to ascertain than the transmission loss. When solar irradiance is absorbed by dust particles, it is converted to thermal energy, which subsequently heats up the PV module by thermal conduction. An increased cell temperature has a slightly positive impact on the current, since the band gap is lowered and thermal energy is accessible for excitement of electrons [64]. Nevertheless, it doesn't compensate for the reduced incoming solar radiation and therefore the current drops. Besides, a higher cell temperature reduces voltage, leading to a decreased power production [4, 5, 13].

To find the real production loss due to soiling would therefore include a thorough estimation of the soil-induced effect on cell temperature, which is far from a straight-forward calculation. A changed absorption and reflection rate, a higher tendency to trap exiting IR light and a changed thermal conductivity coefficient may all influence the cell temperature. The values of these parameters are specific for every dust type. For instance, the specific thermal conductivity coefficient is determined by the chemical composition of the dust. The vast majority of dust types are reported to have low thermal conductivity resulting in a heating effect [6, 20]. The only reported dust grain with a high value of thermal conductivity is salt. Salt may therefore have a cooling effect on the panel.

3.3.3.2 Heterogenous soiling creates mismatch losses and hot spots

A non-uniform dust layer on the PV panels would add to the complexity of determining the impact on current and voltage output. Non-uniform dust deposition is not the exception, but rather the

rule in natural conditions [57]. A heterogenous layer of dust causes partial shading of a module or array of modules, which implies that some cells or modules have a lower current than the others, causing mismatch losses. As a consequence, non-uniformity creates a lower correlation between I_{SC} and the maximum power point [4, 19, 20, 62, 78].

As mentioned in section 2.4.3, mismatch losses can furthermore lead to hot spots [4, 20]. The reverse biased electrical energy is then converted to thermal energy (heat) in the shaded cell or module. In addition, if the dust has a low thermal conductivity coefficient, it will isolate like a blanket and further heat up the surface. In extreme cases, the temperature can reach 150 degrees and severely damage the PV module [4]. The hot spots will experience a significant drop in voltage, but in a serie of cells or modules the total potential is only marginally affected.

3.3.4 Justification for using transmission loss as an indicator for soiling effects

First, with hindsight to the irregular variations in the solar insolation at a particular place on the Earth's surface by cause of the motion of the sun and local atmospheric circumstances, it is argued that estimating losses due to soiling from electricity production data is bounded with great uncertainty. To bypass this uncertainty, the transmission of light through a glass plate will give a much more accurate indication of the attenuation of sunlight bounded to soiling.

Second, as indicated above, the attenuation of sunlight is the most relevant indicator of the effect on PV power plants by soiling. Measuring transmission loss in a laboratory instead of analyzing real production loss from utility-scale solar parks would eradicate the uncertainties involved with the voltage drop because of increased cell temperature and current mismatch losses due to partial shading. Arguably, laboratory studies are not representing a real environment, but to achieve a fundamental understanding of the most important effect of soiling (attenuation of sunlight), transmission measurements at different dust densities on PV cover plates is a first step in that direction.

3.4 Artificial, uniform dust deposition

Favorized tilt angles, wind speeds, relative humidity and rain cause dust particles to settle unevenly over the panels and to accumulate on top of each other [46]. For example tilted panels of 30° are likely to facilitate an increased dust settlement in the lower parts of the module [4, 57]. Goossens and van Kerschaever conducted several wind tunnel experiments and found evidence for non-uniform deposition of dust at wind speeds up to 2.5 m/s [45]. Measurements of I-V curves from power production has later also supported the statement of non-uniform dust deposition in natural conditions with wind velocities up to 2.2 m/s [78]. Agglomeration of grain particles and pockets left empty give the panel dust patterns in lieu of a uniform deposition. Additionally, in the

same study by Goossens and van Kershaever it was shown that different wind velocities gives different grain size distribution on the panel [45].

Even though it is widely known that dust mostly settles in a heterogenous way, it is not possible to artificially reproduce this situation, due to the random nature of the heterogeneity. Moreover, agglomeration of dust particles creates a significant challenge during spectrometry measurements; for the same mass of dust, one can identify huge deviations in transmission of sunlight. As a consequence, uniform deposition is required to understand the transmission loss as a function of dust density, even though dust rarely appears uniformly distributed [62].

There have been several attempts to uniformly deposit dust homogenously onto a surface. The various approaches stretch from using an airtight chamber with either a fan [58] or acetonitrile spray gun [79, 84], deposition using dust contaminated water spray over the surface [23], letting dust fall through a cylindrical tube [57, 73] and sieving the dust over a plate [21]. Clearly, there is no common best practice today on how to artificially deposit dust on a surface for a uniform distribution. Based on the simplicity of the method and few tools required, the sieving technique was chosen in this study.

3.5 Summary on soiling

Soiling is a term used on deposited dust particles on a PV cover glass plate. Normally the particles consist of elements that are abundant in the Earth's crust like silicon, aluminum, iron, potassium and calcium in large molecular compounds with oxygen, hydrogen and carbon. The diameter can be up to 1000 μm, but most grains are found between 1 and 100 μm. A particle goes through five phases in its life cycle: Generation, transportation, deposition, adhesion and removal. Several natural and anthropogenic factors influence each of these phases. The most important natural factors are wind, relative humidity, rain, topography, PM and dust characteristics (size, shape and chemical composition). The most influencial anthropogenic factors are human activities, artificial obstacles, tilt angle and surface characteristics. Dust accumulated on the solar PV panel has a detrimental effect on the power production. First and foremost, a soiling layer attenuates the solar radiation, which declines the transmission. The transmission loss can be converted to a loss in the photon flux, which at last has a negative impact on the electrical current. Second, it can lead to mismatched cells and/or modules in series, which leads to reduced production. Finally, it might have a minor impact on the voltage through an increased cell temperature. Concerning all the attenuating factors inherent in electrical production data, it is reasonable to study the transmission rather than the production in order to discover the impact of soiling loss on utility scale solar power parks.

4 Methodology

This chapter firstly introduces the four utility-scale solar power parks investigated in this study. Next, details of the field work at the dust collection sites are explained. The third and last subchapter presents the laboratory methods used to find the dust characteristics and its optical properties. Central identified sources of error in the field and laboratory work are also presented.

4.1 Locations of dust sampling

The utility-scale solar power plants subject for this study are owned and operated by a large scale Norwegian PV company. The company has several solar power plants around the world and is currently expanding to new countries [18]. Samples have been collected at solar power parks in Middle East and Africa: Rwanda, Jordan and Egypt. Jordan and Egypt are located in a region known for high temperatures, very barren vegetation and high PM concentrations in the atmosphere [20]. In contrast, Rwanda is located in a vegetated tropical climate with frequent rain showers.

4.1.1 Jordan

Dust from two power plants in Jordan have been studied. Jordan I solar park is located in South Jordan and has a capacity of 10.5 MW (figure 4.1).

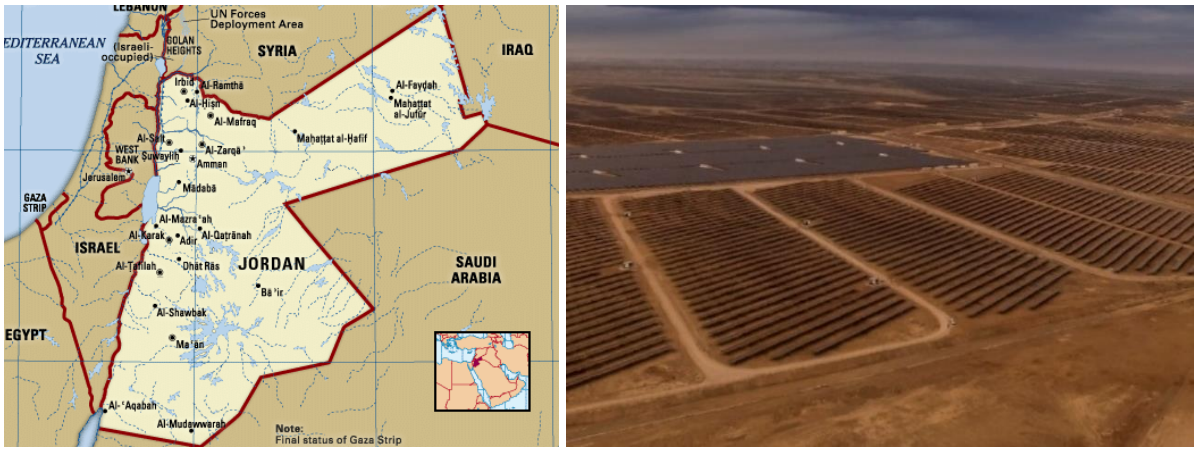

Figure 4.1: Jordan I power plant is located in South Jordan. The images are reprinted with permission: [87] (left picture), [18] (right picture).

The other park, Jordan II, is located in South-West Jordan, and can deliver 10 MW (figure 4.2).

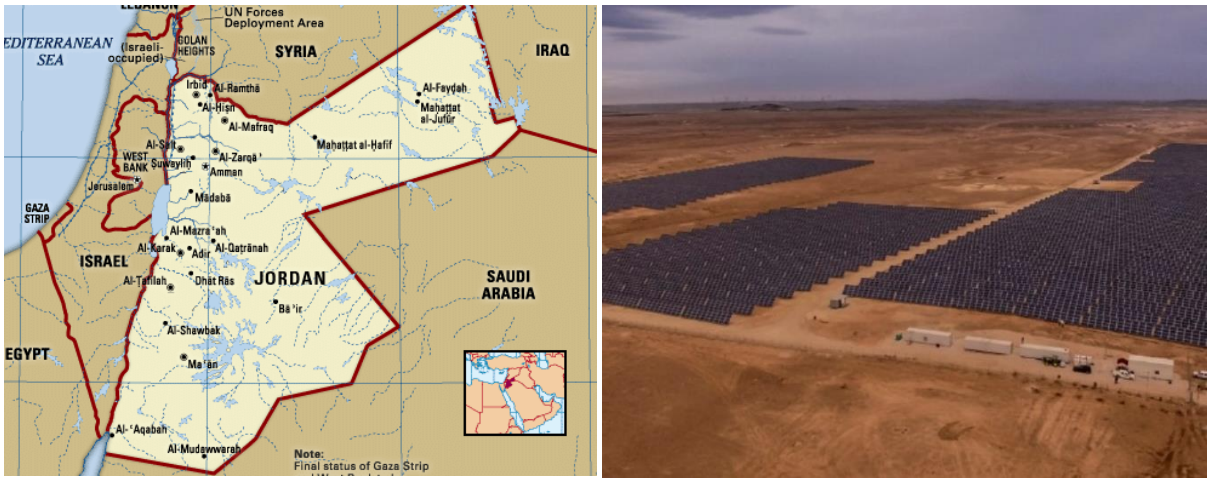

Figure 4.2: Jordan II power plant is located in South West Jordan. The images are reprinted with permission: [87] (left picture), [18] (right picture).

Due to the close proximity of both parks to each other, the vegetation and weather conditions appear similar. The area is barren and flat, favorable for high wind speeds. The mountainous landscape west of Ma'an causes some rain especially in winter time.

4.1.2 Egypt

The Egyptian solar power project in the Saharan desert is a massive PV power park with numerous companies involved (figure 4.3).

Figure 4.3: Egypt I power plant is part of a joint solar PV project in South Egypt. The images are reprinted with permission: [88] (left picture) and [18] (right image).

This part of Egypt is experiencing very limited annual amounts of rain and very high temperatures. The solar farm is 36 km^2 wide and when finished, it will provide ca 1.8 GW solar power to the grid [18]. A norwegian company is the largest developer in the area with 400 MW solar power under construction. Collection of dust samples was done on one of the plots, Egypt I, producing 50 MW when operative. This park has bifacial PV modules, which means that it takes up light from both sides of the panel.

4.1.3 Rwanda

Rwanda I solar power plant is established in Rwamagana district in South-East Rwanda and has a capacity of 8.5 MW (figure 4.4).

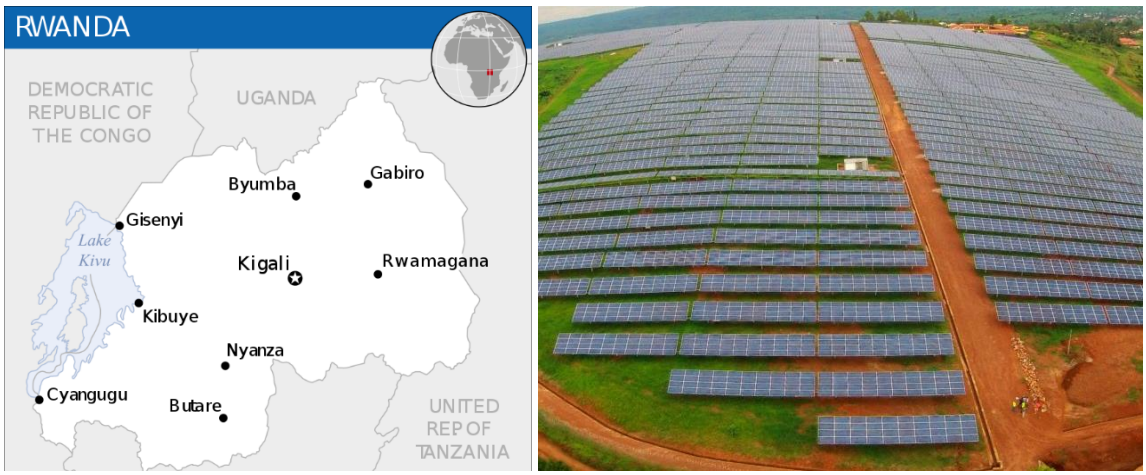

Figure 4.4: Rwanda I power plant is located in the South Eastern part of Rwanda, in Rwamagana district. The images are reprinted with permission from: [89] (left picture), [18] (right picture)

The annual electricity production from this solar power plant makes up 10% of the total electricity production in Rwanda. It is built on a hilltop next to vegetated farmland, where pineapples and other fruits are grown. On the east side of the park, there is moderate traffic on a dirt road, which is a source of increased dust generation. Between the solar PV arrays grass is covering the ground and there are maintenance roads along the outer perimeter of the park and across the middle (figure 4.4, right). The maintenance road is not used on a daily basis.

4.2 Dust sample collection

The goal was to collect enough dust to be able to conduct several experiments in the IFE laboratories in Norway. In order to deposit different dust densities on 8 x 8 cm^2 glass plates, ideally, half a liter (or more) was desired, but table 4.1 and figure 4.5 reveal that this amount was not achieved in every location. A summary of the collected dust samples is given in table 4.1.

Figure 4.5: Collected dust samples from panel and ground at all locations, except panel dust from Rwanda I (insufficient amount). From left: Ground dust Rwanda I, panel dust Jordan I, ground dust Jordan I, panel dust Jordan II, ground dust Jordan II, panel dust Egypt I, ground dust Egypt I.

Table 4.1: Summary of the dust samples collected at the different locations.

Name of power plant	Collected volume (l)		Date collected
	Panel	Ground	
Jordan I	0,10	0,65	16.03.2019
Jordan II	0,70	0,85	17.03.2019
Egypt I	0,35	0,90	19-20.03.2019
Rwanda I	-*	0.55	12-14.03.2019

*From the panels at Rwanda I only dust samples from cotton pieces were collected.

4.2.1 Techniques for dust collection

To remove dust particles from the panels and collect them in a container for analysis purposes, two main techniques were tested: Using a vacuum cleaner and cleaning with a cotton piece.

4.2.1.1 Vacuum cleaner

At sites where the panel dust density is significant and the adhesion of particles to the surface not too strong, it was intended to use a vacuum cleaner. The vacuum cleaner needed to fill several specific criteria:

- It must have filters ensuring that most dust is trapped in a dust collection bag or container.
- It must allow for removing dust from the container without too much loss of particles or contamination of the dust sample.
- It must be easy to carry on site.
- It must be battery-driven, but the battery power must not exceed the limit for batteries carried on airplanes.
- The batteries must be rechargeable.
- It should have a shaft to allow for collection from a larger fraction of the solar panel area.
- It must have a sufficient suction force.
- Possibility of wet cleaning is a plus, but no strict requirement.

Most vacuum cleaners are designed with a filter bag made of cotton. This is not ideal for dust storage, since it is difficult to extract dust from the bag without loosing particles and contaminate the samples with pieces from the filter. Consequently, a storage container without a filter bag is preferrable. This requires a filter after the container and before the sucked air returns to the atmosphere. In order to trap most of the particles, the filter should be as fine as possible. However, the filter must correspond with the battery power and the desired suction force. The most suitable cleaner was found to be Kärcher HV 1/1 Bp Fs, shown in figure 4.6. It failed to fulfill the last point about wet cleaning, so the panels had to be dry before using the vacuum cleaner.

Figure 4.6: Kärcher HV 1/1 Bp Fs (left). The dust is collected in a container right after it is blown through the black cylinder, where it can be collected (right).

4.2.1.2 Cotton piece

In cases where the panels were so clean that using a vacuum cleaner was ineffective, an option was to acquire dust by manually clean the modules with a cotton piece (figure 4.7). This would be enough for characterization analysis, but insufficient with regards to the volume required for the intended optical measurements. This method was used because of a breakdown of the vacuum cleaner in the beginning of the field work, as explained later in this thesis.

Figure 4.7: Whenever the vacuum cleaner was ineffective (or had broken down), cotton pieces were used for dust collection.

4.2.2 Jordan I solar power plant

Sampling from Jordan I took place in the afternoon on March 16th, 2019. Figure 4.8 shows that the dust on the panels was clearly non-uniformly distributed, with piles of dust accumulated near the frame of the panels. It is also visible, that the distribution variates a lot from panel to panel.

Figure 4.8: At Jordan I the dust was clearly non-uniform distributed.

These piles of dust would have been ideal to collect with a vacuum cleaner, but the device was not operative after an early breakdown of the equipment. Instead, the dust was scratched loose with a finger, wearing gloves, and carefully brought into a container. The method proved effective, but due to a limited time available at Jordan I, only about 0.15 liters of panel dust was collected. The ground dust was secured from the soil between the panel rows. The strong winds common to the area had made the ground quite hard, so one had to rub the terrain to collect particles.

4.2.2.1 Sources of error during dust collection from Jordan I

In the time leading up to the sample collection on 16th March 2019, there had been a dust storm in the Ma'an area. The calculated soiling ratio at Jordan I from July 2018 to May 2019 is presented in figure 4.9. Soiling ratio is the relative value of electricity production between a clean and a contaminated PV panel.

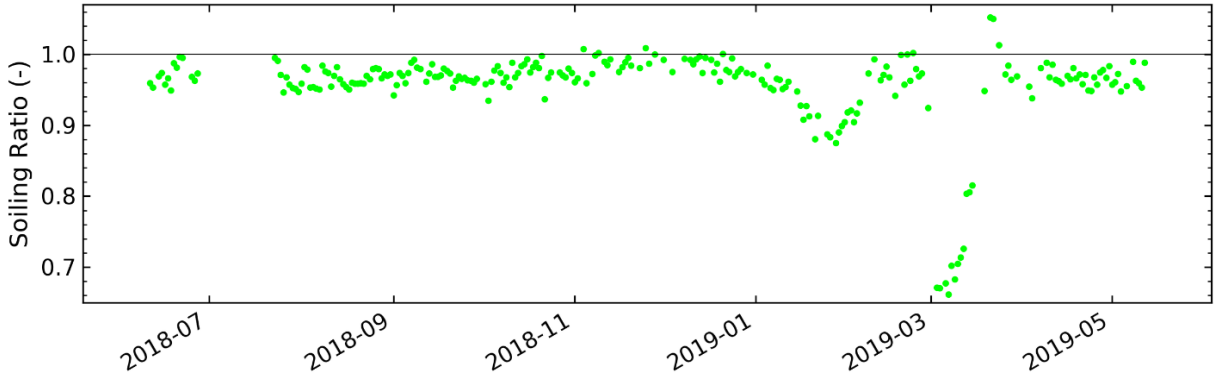

Figure 4.9: Soiling ratio at Jordan I. By the time of dust collection in the middle of March 2019, the panels were still contaminated with dust from the sandstorm earlier that month. The picture is reprinted with permission of Skomedal, Å. [90].

A significant drop in SR (soiling ratio) can easily be identified from the beginning to the middle of March 2019, which corresponds to the dust collection date. The probability for larger grains to suspend in a dust storm is greater than usual, due to the strong force of the wind. Consequently,

the particle size distribution for panel dust, might be biased with a larger fraction of coarse grains than in normal situations.

In addition, heavy rain in the hours before sampling had partially washed the panels and hence altered the particle size distribution and uniformity of the dust layer. Flooded panels may cause lighter particles to escape over the module frame, whereas heavier particles sediment and therefore remain on the module. Therefore, this factor could also increase the likelihood of a larger fraction of coarse particles than what is normal in dry weather, especially at the module frame. Indeed, the dust were only collected from the frame of the panel, which leaves the question open whether this is representative for the panel dust or not.

Lastly, rubbing the soil to receive ground dust particles is not ideal, since these particles are not exposed to dust generation by weathering or levitation from the ground. Consequently, a rougher shape of these particles is expected than the ones from the panel dust.

4.2.3 Jordan II solar power plant

Heavy rainfall in the night from 16 – 17th March had cleaned most of the panels in Jordan II, free of dust, as can be seen in figure 4.10.

Figure 4.10: The rain in the night between March 16-17th had cleaned the panels extensively in Jordan II.

For security reasons, the panels are tilted horizontally in windy conditions, and the rain creates a pool of water on the panel up to the frame height. In the morning on March 17th, when the panels were tilted towards the morning sun at 45°, the water brought the dust to one side of the module, where the frame prevented a portion of the dust not to be washed off the panel. The resulting accumulated dust piles can be seen in figure 4.11.

The same method with gloves and a finger that scratched the dust free into the container was used and proven effective. Similar to Jordan I, the ground dust was collected from the soil between the panels. The ground was very solid, and it was difficult to extract any particles. Furthermore, the ground also contained visible variations in dust size and color, all of which were tried to be included in the sample collection.

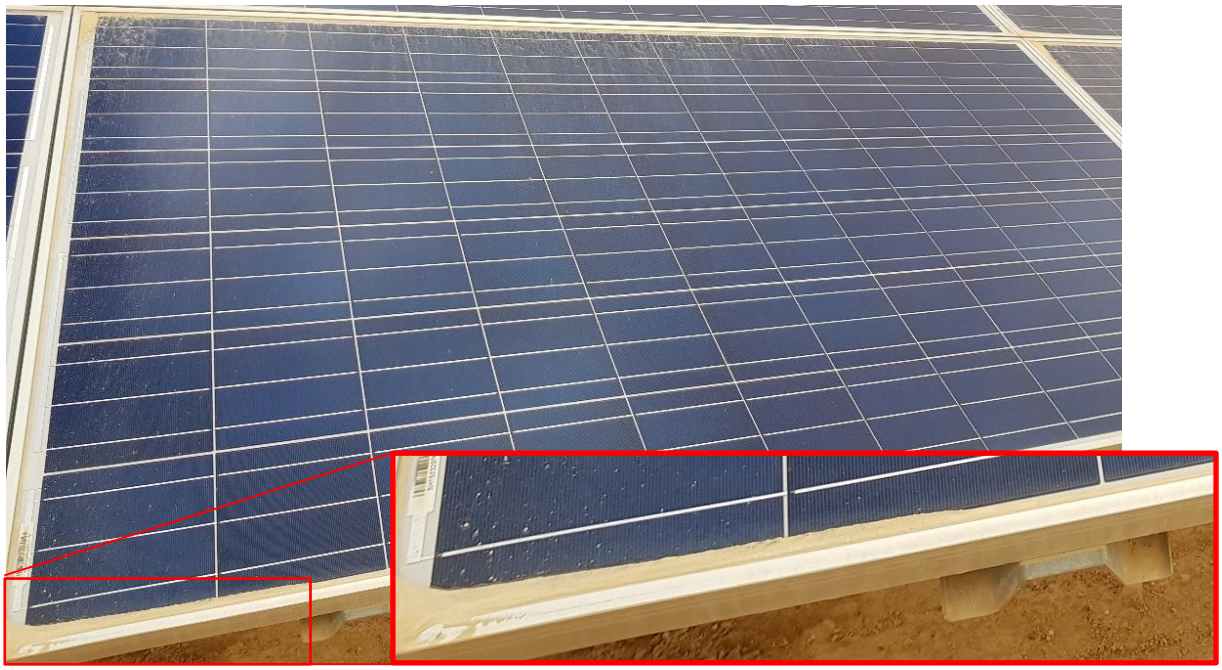

Figure 4.11: The rain had cleaned the panels and left the dust in piles near the frame in Jordan II (see red square).

4.2.3.1 Sources of error during dust collection from Jordan II

The dust storm that polluted Jordan I power plant also reached Jordan II, which may have resulted in a coarser particle size distribution of the panel dust than in a normal case for Jordan II. Figure 4.12 shows the soiling ratio from November 2018 to July 2019, but lacks several datapoints due to filtration of cloudy days. The pyranometer was unfortunately not washed immediately after the sandstorm, which could have resulted in a higher soiling ratio than the de facto attenuation of the sunlight.

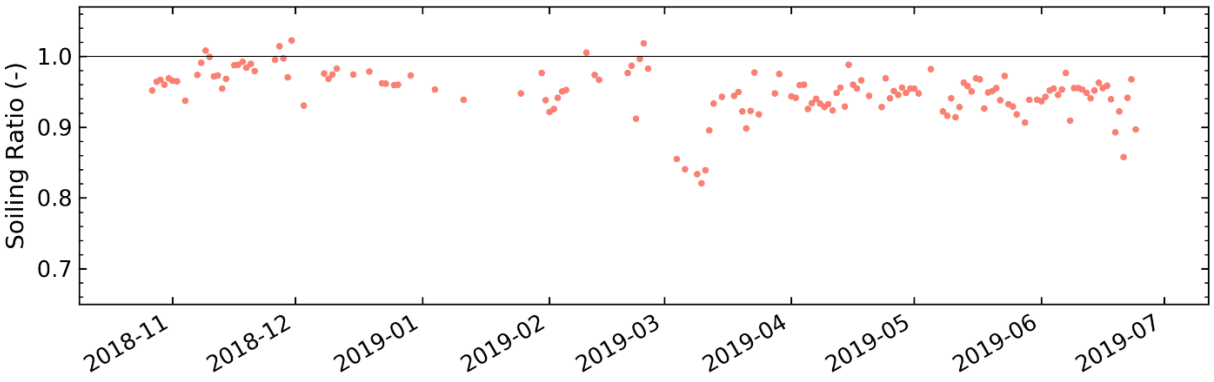

Figure 4.12: Soiling ratio at Jordan II. By the time of dust collection in the middle of March 2019, the panels were still contaminated with dust from the sandstorm earlier that month. The picture is reprinted with permission of Skomedal, Å. [90].

More research is therefore needed to verify the correlation between panel dust and topsoil from both Jordan I and Jordan II power plants under normal soiling situations.

Also similar to Jordan I, the flooding of the panels might have caused an alteration of the particle size distribution. When the panels were tilted in the morning on March 17th it is likely that only

the coarsest grains that quickly sediment will remain close to the frame, while small particles fall off with the water. The rain had cleaned the panels so well, that no other choice was left than to collect panel dust from the frame. It therefore remains unknown weather the panel dust collected from Jordan II is representative for the typical soiling deposited throughout the year.

As mentioned for Jordan I, dust from the hard, compact ground had to be liberated by digging in the topsoil, which meant that subsurface particles were partially included in the sample. Such particles likely have a lower circularity than panel dust, which has been exposed to weathering.

4.2.4 Egypt I solar power plant

Egypt I solar park had been contaminated with dust particles during the construction work, as noted above. The dust was uniformly distributed over the horizontal-tilted panels on the front and back side. The front side contained sufficient dust to be collected using only gloves, visualized in figure 4.13.

Figure 4.13: Collection of dust in Egypt I on March 19th – 20th. The darker part is where the panel was wiped clean with the gloves. The small dots with agglomerations of dust on the panel was a consequence of dew formations or mist that had occurred in the night.

The picture reveals a significant limitation by using gloves: Not all dust particles are alleviated from the surface. Consequently, the morphology of the collected samples may deviate from the real dust deposited on the panels. The dust was gathered on March 19th – 20th, 2019, by wiping 800 panels with bare hands and sliding it down into the container. Conveniently, the modules had no frame, so there was no barrier between the gathered pile of dust and the container. Using the vacuum cleaner would have been very efficient in these circumstances, but it was inaccessible due to equipment failure. The ground dust was collected from loose soil between the panels.

4.2.4.1 Sources of error during dust collection from Egypt I

First, the construction work at the solar power plant in this dry desert area, suspended the ground dust and led to high PM concentration. The artificially suspended particles were then deposited on the panels. This means that the panel dust does not represent natural conditions, which further implies that the likelihood of long transported dust can't be fully understood for Egypt I power plant, since the panel and ground dust most probably are very alike.

Second, collecting dust with bare hands and gloves in such windy conditions as it was in Egypt I March 19th – 20th 2019, can lead to a false conclusion of the particle size distribution, since particles instantly levitated when scratched loose from the panel surface. It is believed that the finest particles were either blown away with the wind or remained attached to the surface instead of being collected in the container.

4.2.5 Rwanda I solar power plant

The sampling at Rwanda I, took place in the long wet season[10] from March 12th – 15th 2019, with one significant tropical rain event on March 14th. The density of dust was very low, but figure 4.14 reveals a thin brown/black dust layer shading the modules.

Figure 4.14: In Rwanda I the uniform-distributed dust was a very thin layer of brown/black color, only visible from high angles of incidence.

The encountered dust density on the panels in Rwanda I in the beginning of March 2019 was representative for the season as a whole, as figure 4.15 displays.

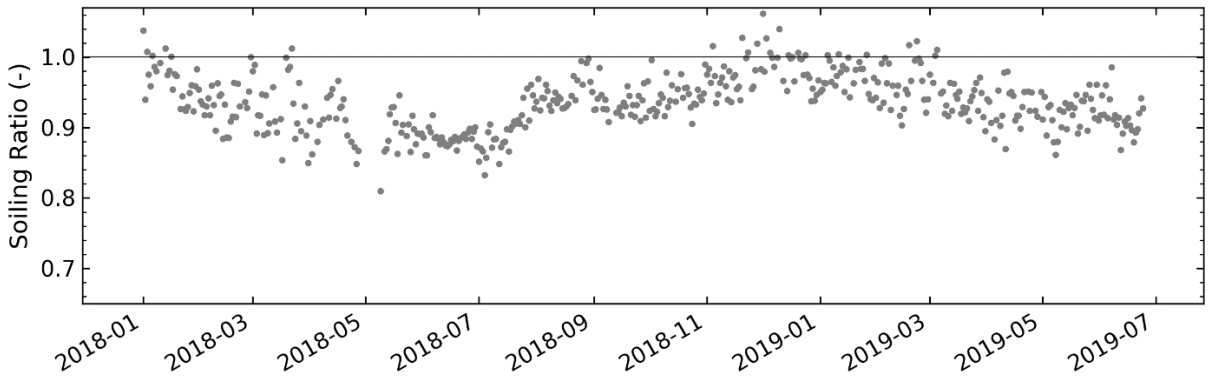

Figure 4.15: Soiling ratio at Rwanda I. The dust collection was executed in the beginning of March 2019, which represented a typical soiling ratio for the season. The picture is reprinted with permission of Skomedal, Å. [90].

[10] The climate in Rwanda can be divided into two wet and two dry seasons. From mid-December to February is a short dry season, and the long dry season is from May to mid-September. March to May is considered a long wet season with heavy and persistent rain. October to November is the short wet season [91]

In general, rain events make the collection of dust from the panels themselves extremely difficult, since only small particles greatly attached to the surface remain after the rain shower (see appendix C for additional observations on rain and Rwandan dust). The strong attachment and the small size of the particles made the initial plan to collect the dust samples from the panels with a vacuum cleaner inefficient. By visual inspection, it was realized that the suction force of the vacuum cleaner was not able to efficiently remove the particles from the panel. Therefore, about 100 panels were cleaned with a cotton piece in order to assess the morphology and chemical composition of dust particles on the panels.

Samples of the soil were collected from the gravel road on the east side of the solar park using the vacuum cleaner. The limited suction force of the vacuum cleaner aided a filtration of the coarsest grains, since they were too heavy to be sucked into the container.

4.2.5.1 Sources of error during dust collection from Rwanda I

Neither the cloth nor the vacuum cleaner was able to remove the particles with high adhesion force to the panel surface at Rwanda I. Due to heavy rainfalls that had washed away coarser grains, the remaining dust on the panels was assessed to be of very small diameter. The filter of the vacuum cleaner had a mesh size of 1 µm. Finer particles than 1 µm could simply flow through the container with the air, which partially explaines why the vacuum cleaner was not useful in Rwanda. Also, it is unknown if the suction force of the vacuum cleaner was sufficient to extract particles that have strong adhesion to the panel.

4.2.6 Artificial dust: Cement

In addition to all the natural dust samples presented above, cement, an artificial dust sample, was also investigated in this thesis (figure 4.16).

Figure 4.16: Hey'di rapid cement.

The chosen cement type was a quick-setting, dry mortar from Hey'di. The main reason for including cement in this thesis was to perform and compare experiments based on the methods in this work with other published results using concrete as an artificial soiling material [21, 22].

4.3 Laboratory analysis

The following paragraphs explain the methods used to find the albedo of the dust, the particles' shape, size and chemical composition, as well as optical measurements. The uncertainties and souces of error are presented towards the end of each measurement tool.

4.3.1 Extraction of particles for dust characterization

Only a small amount of dust is required for morphology and chemical characterization measurements (figure 4.17).

Figure 4.17: Prepared samples of panel dust from the four sites. Note the adhesion of the panel dust from Rwanda I onto the glass surface.

To gain a sufficient amount of dust from Rwanda I, the cloths were carefully rubbed and scraped. On the positive side, this would yield sufficient amounts of dust for chemical and morphological characterization, but it is likely that the finest particles were trapped in the cloth and not removed. Inevitably, small pieces from the cotton were also ripped off and contaminated the samples. The impact of this contamination is evaluated in section 5.5.1 below.

4.3.2 Albedo (ϱ) measurements using ImageJ

The albedo (ϱ) of a dust sample is a crucial parameter that can indicate absorption of sunlight. It was measured using the brightness function in ImageJ. A selected area, that comprised of approximately one million pixels, were averaged for a brightness index (κ_{Dust}) between 0 and 255. This index value was compared with the brightness of a white paper (κ_{WP}) in the same picture, which is known to have an albedo of 65% (ϱ_{WP} = 0.65) [92]. The calculations of the albedo are shown in equations 26.

$$26)\ \varrho = \frac{\kappa_{Dust}}{\kappa_{WP}} \cdot \varrho_{WP} \qquad [-]$$

Figure 4.18 illustrates how the sample is prepared for albedo measurement. It is vital that the selected area, painted in a thin white line, contains no empty pockets of dust, as this would increase the brightness index significantly. Likewise, any small peaks or valleys in the dust sample would create shadows that decrease the brightness index. The sample is spread out on a normal white A4 paper, which is also tested for its brightness in the same picture both on left and right

side of the sample. In case the brightness value of the white paper deviated slightly between left and right side, an average value was chosen.

Figure 4.18: Prepared panel dust sample from Jordan II for albedo measurement by ImageJ. The selected area is marked with a thin white line.

4.3.2.1 Sources of error by albedo measurements

As a consequence of the different shades and voids in the dust pile, which lowers or increases the brightness respectively, the uncertainty had to be calculated for each sample. In order to minimize the uncertainty, the dust was well distributed over the paper, without empty spots, in order to avoid these inconsistencies. The computation of the standard deviation of the brightness resulted in 2% uncertainty in the albedo for all samples.

4.3.3 Dust characterization using Scanning Electron Microscopy (SEM)

The chemical composition and particle shape of the dust could provide answers regarding the correlation between the panel dust and the ground dust, which is one of the main goals of the thesis. A Hitachi S-4800 Scanning Electron Microscope (SEM) was used for to find the chemical components in the dust samples (figure 4.19). In addition, SEM can deliver pictures in high resolution of the dust samples in order to assess the particle shape with ImageJ (section 4.3.4).

Basically, a SEM shoots electrons onto the sample, which subsequently either scatter or result in the release of secondary electrons or excitation of photons from the atoms from the sample. The secondary or backscattered electrons are recorded in sensors and software translates the readings into a picture. As an example, two images of the panel dust from Egypt I are shown in figure 4.20, which were intended for imaging with ImageJ to find the particle shape.

Figure 4.19: Hitachi S-4800 Scanning Electron Microscope (SEM) at Institute for Energy Technique, serial number: 9114-04.

Moreover, the Energy-Dispersive x-ray Spectroscopy (EDS) system, which is connected with SEM, is capable to determine the atoms present in selected grains. X-ray photons will be excited with specific wavelengths depending on the elements they stem from and so the EDS system allows for determining the types of atoms present. More specifically, the SEM point search function was used, meaning that the chemical composition was measured for selected grains in the sample. A minimum of twenty grains with a suitable surface[11] were chosen to attain an average value of the chemical composition of each entire dust sample. The electron beam focuses on a chosen point and the reader collects released X-rays for a certain amount of time. Only measurements where above 1000 counts were detected by the reader were included in the further analysis.

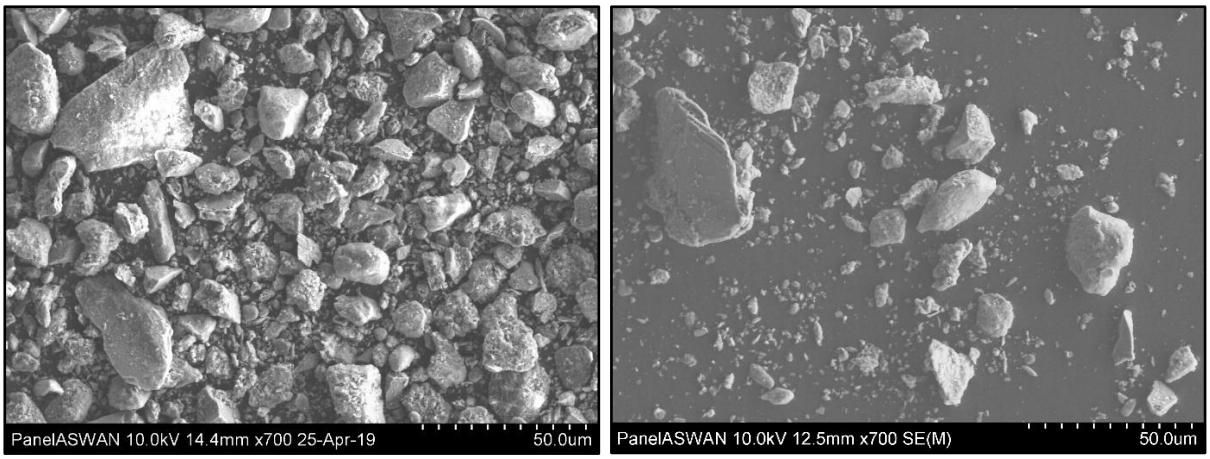

Figure 4.20: Two different rawdata images captured with SEM, subject for imaging in figure 4.21. The dust sample stems from panels at Egypt I power plant.

[11] For the electrons to hit the target and to be read by the sensor, the particle had to be relatively flat and not lay in the shadow of other particles.

4.3.3.1 Sources of error during chemical analysis

The x-rays read by the detector have wavelengths, which are unique for an electron dropping down from a higher energetic, electron shell to a lower. However, some of these peaks can be very close to each other and lead to peak overlaps, which confuse the reading of the signals. As an example, boron and carbon are very close to each other. Unless it is known that no minerals in the dust contain boron or carbon, it sometimes can't be ruled out that the computer is mistaking. This would yield erroneous results to the chemical composition and was unfortunately the case for the last measurement of cement. Thus, the cement dust sample couldn't be properly measured.

4.3.4 Particle shape analysis using ImageJ

The particle shape is believed to be rougher for ground based dust than for panel dust. To shed light on this hypothesis, the circularity function in ImageJ is employed. For a precise estimation of the dust particle shape, the images captured with SEM had to display separate grains (figure 4.20 above). Whenever the grains were resting in contact with each other, it was impossible to achieve a satisfying separation of the particles with ImageJ, as the left image in figure 4.21 demonstrate.

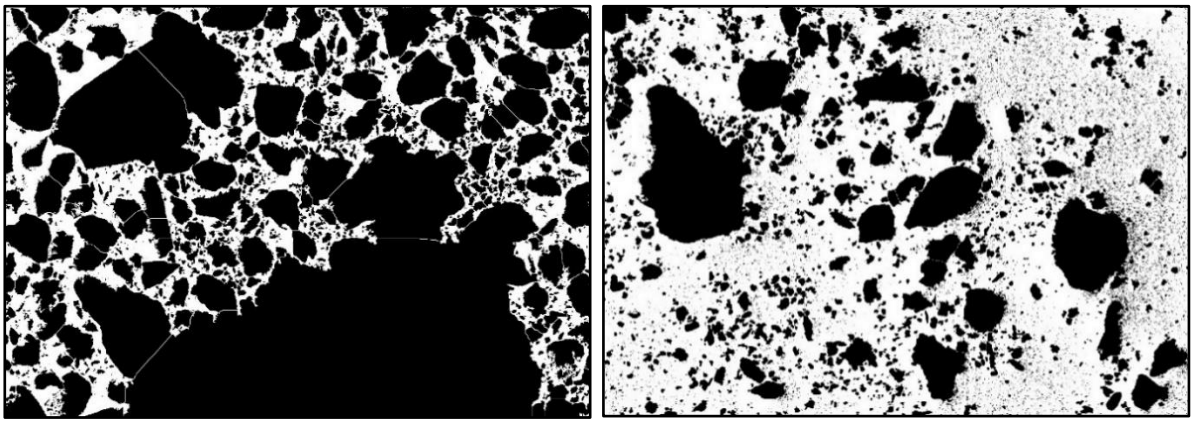

Figure 4.21: Precise imaging required rawdata images that showed separate grains (right). Grains resting in contact with each other were impossible to separate in a satisfying way (left). The respective rawdata images were presented in figure 4.20.

Due to the lack of accuracy in the left image in figure 4.21, it couldn't be used for evaluation of the particle shape. Only treated pictures clearly correlating with the raw image (figure 4.20), such as the right image in figure 4.21, were kept for further analysis. By further comparison of the raw images in figure 4.20 with the treated images in figure 4.21 several small black dots in the latter can be identified that rather represent differences in the shadow than particles. To exclude these dots in the image analysis, a minimum of 150 continuous black pixels was required for it to be considered a particle. In the example of the rightmost image from figure 4.20 and 4.21, it gives a total of 772 identified particles (figure 4.22).

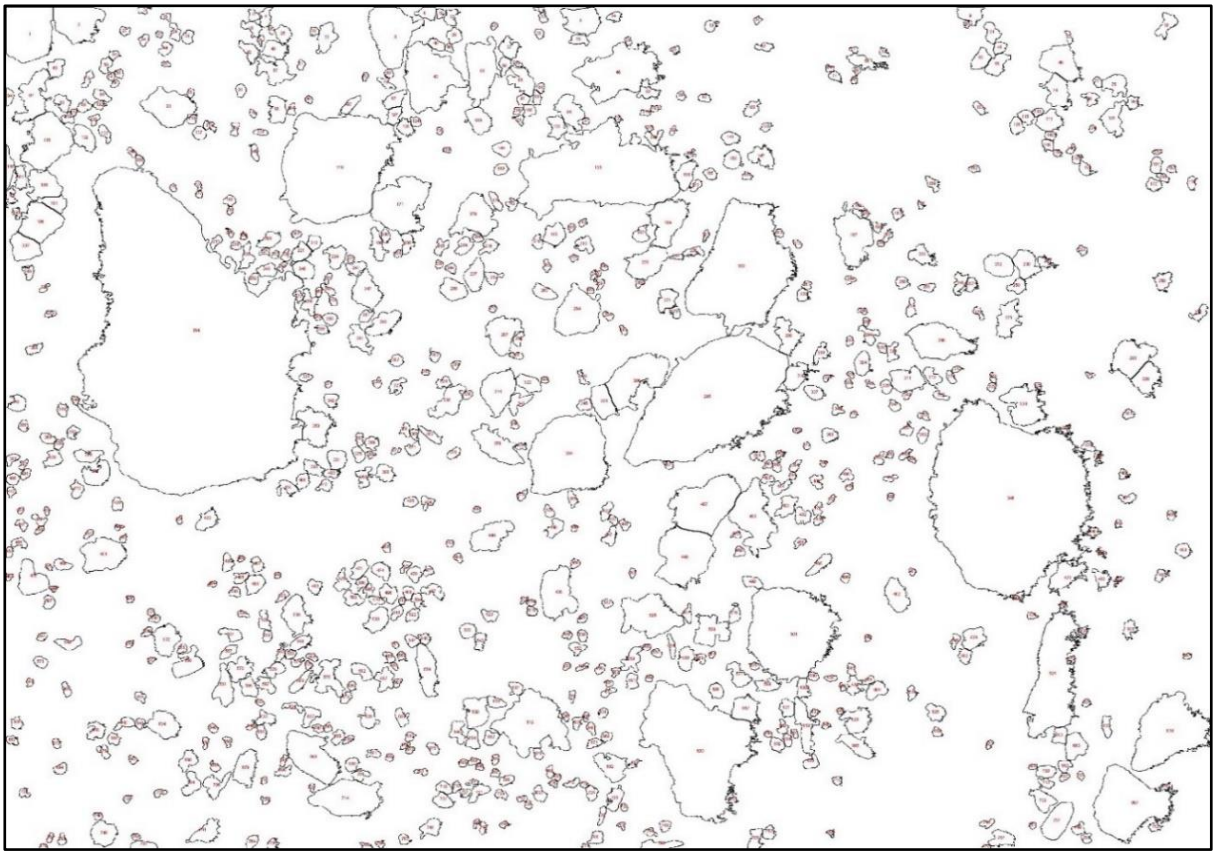

Figure 4.22: 772 particles were identified after excluding all black dots with a lower pixel number than 150 in the example from Egypt I panel dust. Only outlines and numbering of the particles are drawn.

The identified grains in the images were tested for their circularity (ω). Equation 27 defines the mathematical expression that ImageJ uses to calculate the circularity of a particle.

$$27) \qquad \omega = \frac{4\pi(Area)}{Circumference^2} \cdot 100\% \qquad [-]$$

Evidently, solved for a perfectly round particle, the circularity factor has to be 100%. The particles were tested for 40%, 50%, 60%, 70% and 80% circularity and a minimum of seven different images and 1500 particles were analyzed from each sample. Figure 4.23 shows the decrease in particle counts with ascending circularity limit.

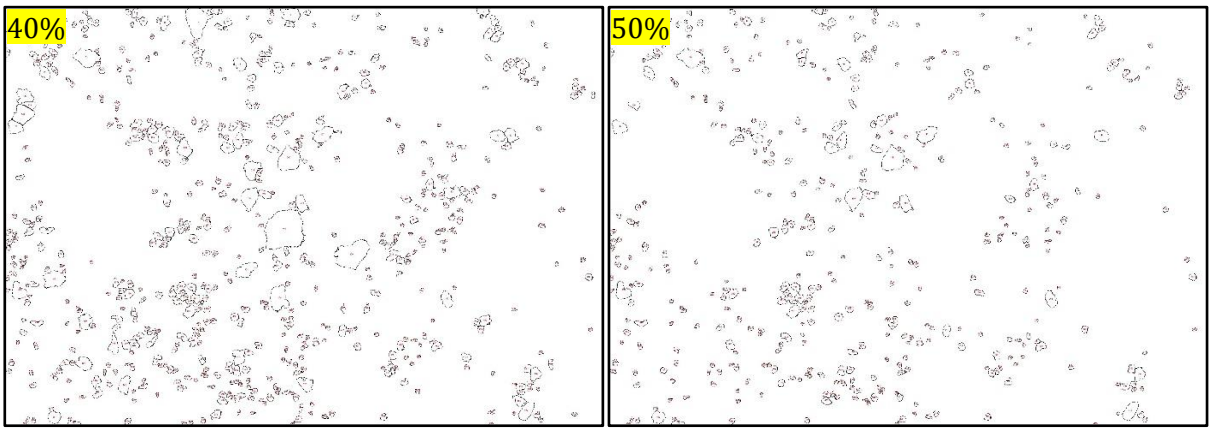

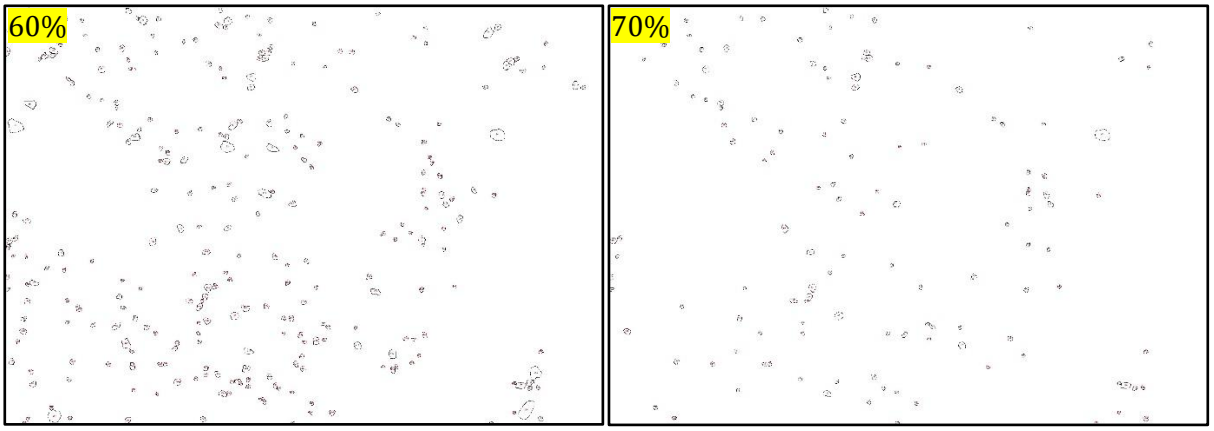

Figure 4.23: The identified grains were tested for their circularity at 40% (previous page, left), 50% (previous page, right), 60% (left), 70% (right) and 80% (not included). The circularity fractions in this particular example from Egypt I panel dust were 78.0%, 55.7%, 36.0%, 16.6% and 3.8% in ascending circularity order respectively.

4.3.4.1 Sources of error by particle shape analysis

One particular challenge with the determination of particle shape was the required resolution of the pictures taken with SEM for analysis in ImageJ. For sufficient identification of the grains, both reading sensors for backscattered and secondary electrons had to be used to produce clear pictures with good identification of grains, as both images in figure 4.20 show. Nevertheless, using the secondary electron detector induced an internal brightness difference on every grain, since this detector is placed at the side of the sample. At a closer look at the raw images in figure 4.20, the right side of the grains is brighter than the left side of the grains, which altered the circularity analysis. Evidently, the borderline on the bright side became much more neatly measured and longer than the dark side, which resulted in a larger circumference in total. This can be easily identified when comparing the right image in figure 4.20 with figure 4.22. The effect of this error is that the circularity appears lower than in reality, and especially for larger grains or zoomed in pictures.

4.3.5 Size distribution measurements using Dynamic Light Scattering (DLS)

The particle size distribution is previously been reported to have a crucial influence on the transmission of sunlight [17]. The size distribution was analyzed with a Malvern Mastersizer 2000 Dynamic Light Scattering (DLS) device (figure 4.24), which has a measuring range between 0.05 and 3000 µm. The samples were mixed with water and stirred at a speed of 3000 rpm during measurement. A Helium-Neon laser light is directed onto the medium and the light beam is scattered by the particles [93]. The resulting intensity of the scattered light is distinct for the particle size that the laser beam encountered and is detected by signal readers.

Due to the coarse grain size in some of the samples, the particles in the solution had a tendency to settle with time, which required swift work after the insertion of the sample. This measurement was conducted by Serkan Kelesoglu at IFE, because of the strict regulations of using the device. A

minimum of six executions of the eight samples were conducted to avoid great outliers. Only three measurements were conducted at a time due to the risk of sedimentation.

Figure 4.24: Dynamic Light Scatter at Institute for Energy Technique.

For comparative porposes, it was desired to calculate one single value for the particle size distribution for every dust sample. Labelled PDS, it was computed by multiplying the volumetric percentage with the particle diameter at each size interval and summarized over the entire size distribution. The total sum is then divided by 1000.

4.3.5.1 Sources of error by particle size measurements

The DLS device assumes all particles to be spherical. From figure 4.20 it can easily be identified, however, that few particles are close to be a perfect sphere. Without a perfect sphere, the scattering of the light will depend on the angle of incidence from the light source on the particle. Since the particles in the solution are arbitrarily floating around, this error source is random in nature: A particle might be struck by light at any orientation and scatter the light differently depending on its orientation. This implies that for instance a grain with a thin, long cylindric shape causes either small or large intensity of the scattered light beam, depending on the particle's orientation. Consequently, the DLS results may deviate from the real particle size distribution.

4.3.6 Sieving of ground dust and cement

The ground dust collected from the four sites clearly exhibited a particle size distribution much larger than the panel dust. A large fraction of these particles was above 1 mm in diameter and clearly would neither replicate the results from the panel dust, nor is it likely to find these particle sizes on the PV modules. It was thus necessary to sieve the samples. Based on the maximum particle diameter found with the DLS measurements for the panel dust, a minimum mesh size was determined for the filtration of the ground dust. Table 4.2 gives an overview of the lowest mesh sizes used for each ground dust sample. Additionally, the cement dust was sieved with a 20 µm sieve for experimental purposes.

Table 4.2: Overview of the smallest sieve mesh size used in preparing the ground dust samples.

Sample #	Sieve mesh size [µm]
Jordan I	80
Jordan II	80
Rwanda I	80
Egypt I	63
Cement	20

The sieving was done with a Retsch AS200 Tap device, which shakes and taps the sieves for an efficient filtering of the dust (figure 4.25). Every filtration had a minimum time lapse of 20 minutes and several sieve mesh sizes were used to create an efficient process.

Figure 4.25: Retsch AS200 Tap sieving device was used for filtering the ground dust samples to replicate the panel dust size distribution.

As can be identified in figure 4.25, a significant portion of the dust escaped the sieves and was lost during the filtration. Out of ca 1 l of ground dust sample, roughly 0,1 l percolated the smallest mesh size given in table 4.2. The rest was filtered out and not used for further analyses.

4.3.6.1 Sources of error by sieving ground dust

There is a discrepancy between the particle size measurement with DLS and the maximum desired particle size done with sieving. When sieving the sample with e.g. a mesh size of 80 µm, a thin, long cylindric particle comes through the mesh opening in one specific orientation, whereas the DLS might not measure this particle in the same orientation. The sieve will always favorize the lowest possible diameter, whereas for the DLS device, this is random. The maximum particle size is therefore expected to have been measured higher by DLS than the mesh size of the sieve.

4.3.7 Uniform dust deposition on glass plates for transmission measurements

To be able to conduct transmission measurements of different dust densities with a spectrometer it is necessary to deposit the dust uniformly over glass plates. The glass plates are 8 x 8 cm^2; small enough to use a circular sieve with diameter 20 cm for the deposition (figure 4.26). An 80 µm sieve was chosen for the natural dust samples, while 20 µm was used for the cement. A coarser mesh-size would allow large agglomerated dust piles to come through the mesh opening. Additionally, a mesh size of >80 µm would be challenging to use for deposition of low densities, since the particles would penetrate the sieve very quickly.

Figure 4.26: Sieving of dust for uniform deposition on 8 x 8 cm^2 glass plate. The sieve has a diameter of 20 cm and mesh size 80 µm (20 µm for cement).

The validation of uniform distribution was first done qualitatively with naked eye (figure 4.27). In cases where dust particles clearly had a heterogenous distribution, the sieving was terminated, the plate was cleaned, and the deposition had to start over again.

Figure 4.27: Example of non-uniform (left) and uniform (right) deposition of dust on glass plates. The validation was done qualitatively with a naked eye.

Furthermore, a second validation of the homogeneity of the dust deposition was quantitatively computed: For each sample, four locations were selected on the contaminated glass plate and optically measured for its transmission (figure 4.28). The difference in transmission of the four measurements gave a quantitative indicator of the homogeneity of the dust deposition.

Figure 4.28: Four points (in yellow) on each sample were selected for transmission measurements with the spectrometer, in order to quantitatively assess the homogeneity of the dust layer.

The density of deposited dust (ρ) was found by the difference in the mass of the glass plate before and after dust deposition divided by the glass surface area (figure 4.29 and eq. 28).

Figure 4.29: Density measurements calculated from the difference in mass weighed before (left) and after (right) dust deposition. In this particular example the mass difference is 39.9 mg, resulting in a density of ca 6.23 g/m^2.

28) $$\rho = \frac{\Delta m}{A} = \frac{m_{con} - m_{clean}}{A}, \qquad [g/m^2]$$

where m_{con} and m_{clean} represent the mass of the dust contaminated and clean glass plate respectively and the area (A) is 64 cm^2.

For every natural dust sample[12] 30 different densities were uniformly deposited on the glass plate for transmission measurements, while cement was tested for 33 densities (see appendix D, table D.1 for details).

4.3.7.1 Sources of error during dust deposition

To uniformly deposit dust on a glass plate was not a straightforward operation. First of all, the laboratory was well ventilated, which means that particles may have been blown away during and after deposition, which alters the particle size distribution of the deposited dust in comparison to the sample itself and the homogeneity of the distribution. Next, the glass plates with the deposited dust were brought from the deposition area to the characterization lab, being extensively exposed to circulation of air. One had to be extremely careful when opening doors and walking around with the plate. This possibly led to loss of fine dust particles and disturbed homogeneity of the particle distribution on the plate.

Lastly, not all dust particles were finer than the mesh size of 80 µm, as can be seen in the right image of figure 4.30. Larger particles than 80 µm were held back, which consequently led to a deviation of the transmission value in comparison to the real situation for panel dust.

Figure 4.30: The initial amount of dust (left) and the rest after sieving (right). The picture represents panel dust from Jordan II.

[12] The amount of panel dust from Rwanda was insufficient to conduct transmission measurements.

4.3.8 Transmission measurements

Finally, transmission measurements of the dust contaminated glass plates will provide the essential results of the entire thesis. Through these results, it may be possible to understand the impact that the different dust types have on the incoming sunlight at the four utility scale solar power parks studied in this thesis. The spectrometer used for transmission measurements was Ocean Optics, shown in figure 4.31.

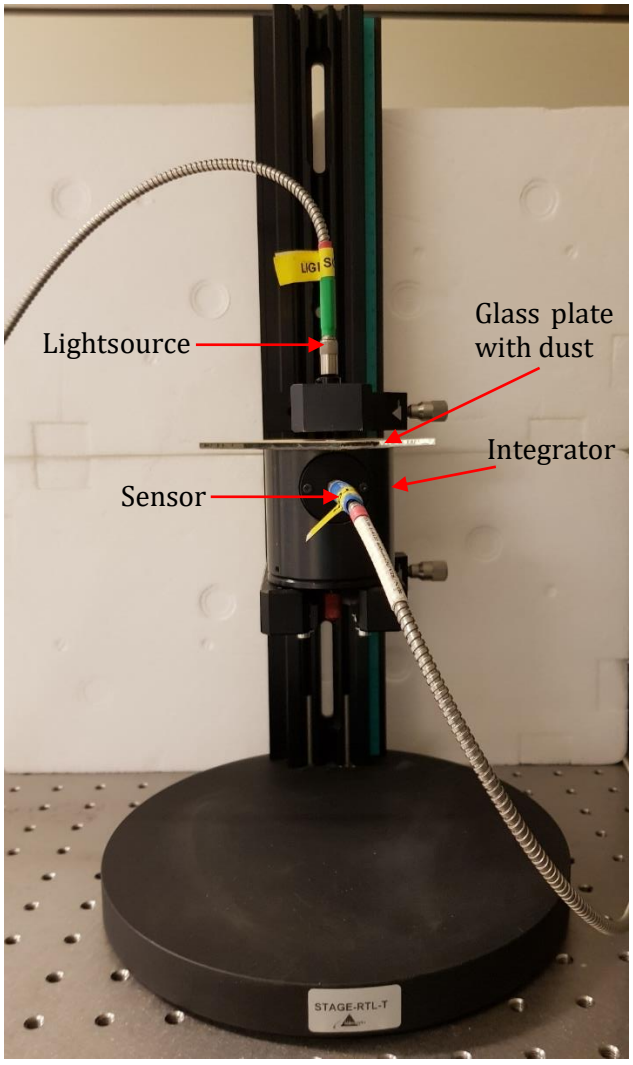

Figure 4.31: Ocean Optics spectrometer was used for transmission measurements. Light hits the top of the plate and the sensor reads the light signal that is transmitted through the plate.

The working principle of the spectrometer is as follows: A source emits light with wavelengths of 350 – 1000 nm that hits the glass plate above a cylinder-shaped integrator with a small hole. Light that passes through the plate is reflected inside the cylinder in every direction, due to white walls with a high albedo. At one location there is an opening for reading light signals (marked “sensor” in figure 4.31). The device has to be calibrated for a normal, unhindered light beam before the

plate is placed in between the light source and the integrator. A clean plate was measured to normalize all the 30 measurements. The reduction in transmission of light from a cleaned to a contaminated glass plate can be assigned to the density of dust.

An Ocean optics spectrometer provides the transmission values in dependency of wavelength. Due to the amount of data the transmission had to be calculated using Python. The full length of the code is given in appendix E.

5 Results and discussion

The first section of this chapter evaluates the relationship between the panel and ground dust for each location sequentially by comparing four main dust characteristics: Visual appearance, chemical composition, particle shape and particle size distribution. Next, the chapter compares the same four dust characteristics between the four power plants Jordan I, Jordan II, Egypt I and Rwanda I. Additionally, the comparison includes cement as an artificial dust sample. In the third subchapter, the main results from the transmission measurements are presented and discussed. It is concentrated on explaining deviations seen in the transmission curves between the different samples and correlates the trends with the presented dust characteristics. Then, the most important identified sources of error are analyzed in the fourth section. The last subchapter proposes a standardized and improved method for field collection and laboratory analysis for future soiling research.

5.1 Comparison of dust characteristics between panel dust and soil

A central goal of this study is to reveal the correlation between the dust that accumulates on a panel and the topsoil around the panel. If the dust deposited on PV modules to a large extent is comparable with the topsoil, this would imply that a study of the ground dust nearby could provide estimates of the soiling loss on PV panels. To answer this question, the following paragraphs will compare the visual difference, chemical composition, particle shape and size distribution between panel and ground based dust.

5.1.1 Jordan I

5.1.1.1 Visual comparison

The dust samples collected on March 16th, 2019, at the Jordan I solar power plant in Jordan are shown in figure 5.1. The panel dust is displayed to the right, whereas the sieved ground dust is presented to the left. The ground dust sample has been sieved with 80 μm mesh size. Both dust samples have a brown appearance, with a brighter color of the panel dust than the ground dust.

This is also supported by the albedo measurement, which showed an albedo of 0.50 for panel dust and 0.36 for ground dust. Seemingly, the panel dust also tends to agglomerate easier.

Figure 5.1: Dust found at Jordan I power plant in Jordan March 16th, 2019. The right picture visualizes the panel dust and the left image shows the sieved ground dust.

5.1.1.2 Chemical composition

An overview of the most important chemical elements of the ground dust and the panel dust is given in figure 5.2. The correlation between the two sector diagrams is strong, with only minor deviations. Carbon is deviating with 2.7%, but note that the dust sample is spread over a carbon plate for examination, which means that the result of this element in particular might have been influenced by the carbonaceous background.

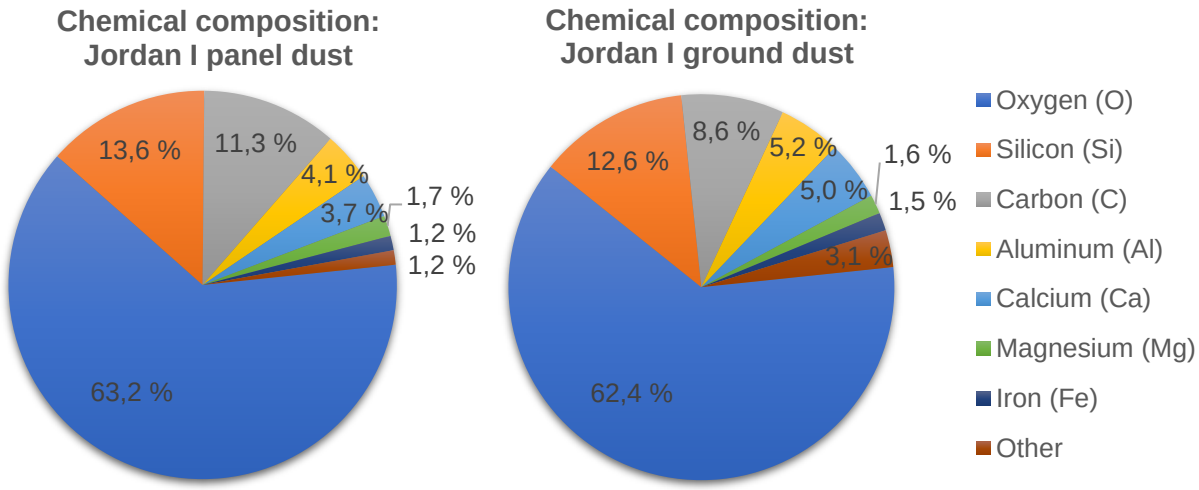

Figure 5.2: The sector diagrams compares the panel dust with the ground dust from Jordan I. The graphs reveal a good correlation in chemical composition between the two samples.

5.1.1.3 Particle shape

The fraction of circular particles in the panel and ground dust at various circularity factors is given in figure 5.3. There is no significant difference between the samples for a circularity factor of less than 70%. Nevertheless, for a circularity factor of 70 – 80%, panel dust has a higher percentage of circular grains than ground dust.

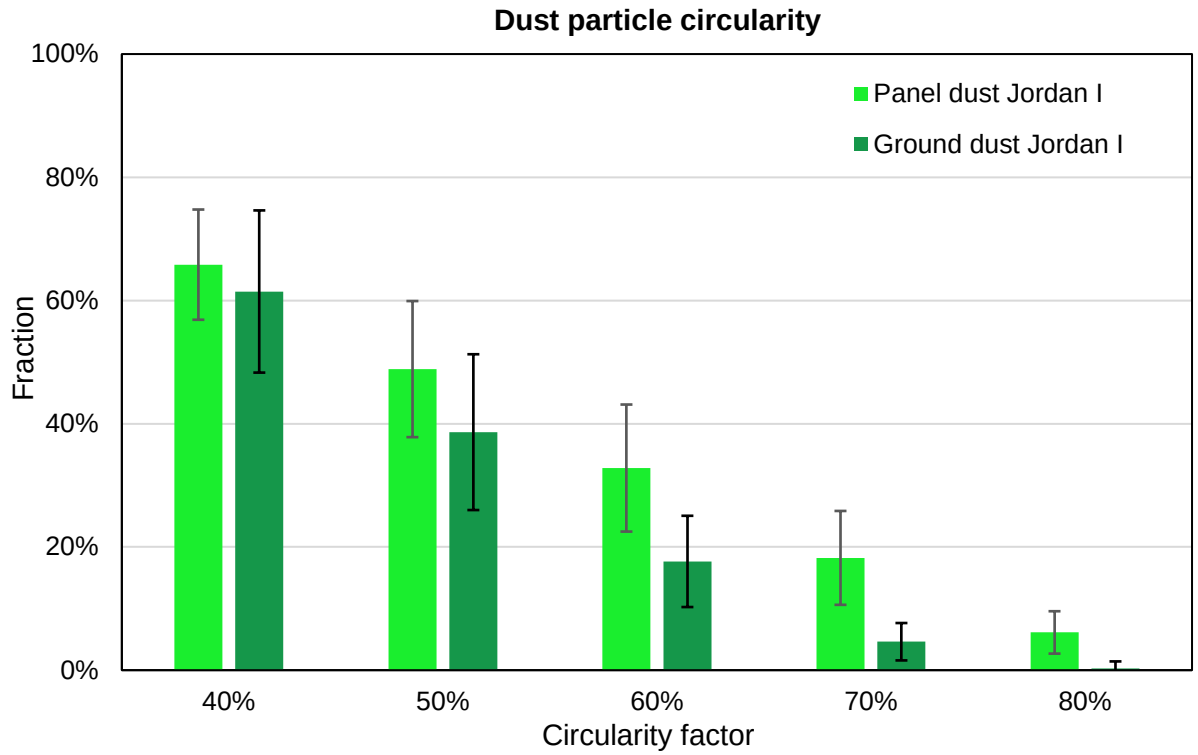

Figure 5.3: Comparison of the circularity factor between the panel and ground dust from Jordan I.

5.1.1.4 Particle size distribution

The particle size distribution of the sieved ground dust and panel dust is shown in figure 5.4.

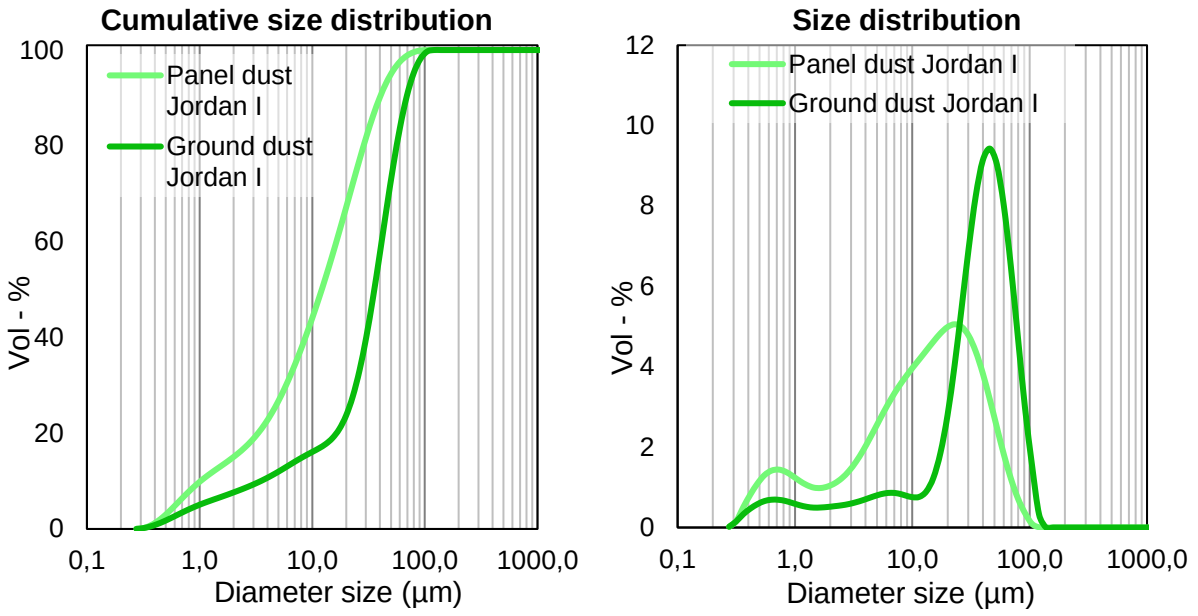

Figure 5.4: Particle size distribution (right) and cumulative size distribution (left) of the panel dust (light green) and sieved ground dust (dark green) from Jordan I.

It is visible that the ground dust has a higher fraction of particles from 30 µm to 100 µm, whereas the panel dust has more fine grains up to 20 µm. Both samples show that the lowest particle size is approximately 0.3 µm. It is important to bear in mind that in terms of numbers of particles, the

fraction of small particles is much higher. Larger particles are fewer in numbers, but contribute more to the total volume.

5.1.1.5 Comparison of ground and panel dust at Jordan I

The clear deviation in albedo between panel and ground dust might indicate that long transported dust has accumulated on the panel. However, the chemical composition of the two samples showed no significant difference. A plausible explanation for the variation in brightness might also rise from deviation in particle size distribution, which can cause different scattering patterns (section 2.2.4). The dependency on scattering pattern for visual appearance of the samples is further supported by the brighter color of the ground dust after sieving (appendix F, figure F.2). This allows for the possibility of panel dust to originate from the soil nearby despite a clear difference in albedo. Furthermore, the presented deviation in particle circularity of the samples reveals little evidence for long-transported dust. Naturally, when airborne dust has been resting on the panel, it becomes exposed to physical weathering, which tends to make the particles more spherical.

The factors above suggest that there is reason to believe that most of the panel dust at Jordan I on March 16th could, in fact, stem from the ground nearby or from sources with similar soil characteristics as the ground at Jordan I power plant. Nonetheless, due to the difference in color and a great uncertainty in the chemical composition and particle circularity, long-transported dust cannot be ruled out.

5.1.2 Jordan II

5.1.2.1 Visual comparison

Panel dust and topsoil from Jordan II collected on March 17th, 2019, is visually compared in figure 5.5.

Figure 5.5: Dust collected at Jordan II on March 17th, 2019. The left picture shows sieved ground dust from between the panel rows. The rightmost picture visualizes the panel dust.

The raw ground dust was dried and sieved with an 80 µm sieve (figure 5.5, left). The panel dust is pictured to the right and shows a somewhat higher agglomerative behavior than the ground dust. The color of both samples is very similar and they have an equal albedo of 0.45.

5.1.2.2 Chemical composition

The chemical composition of ground dust and panel dust is given in figure 5.6.

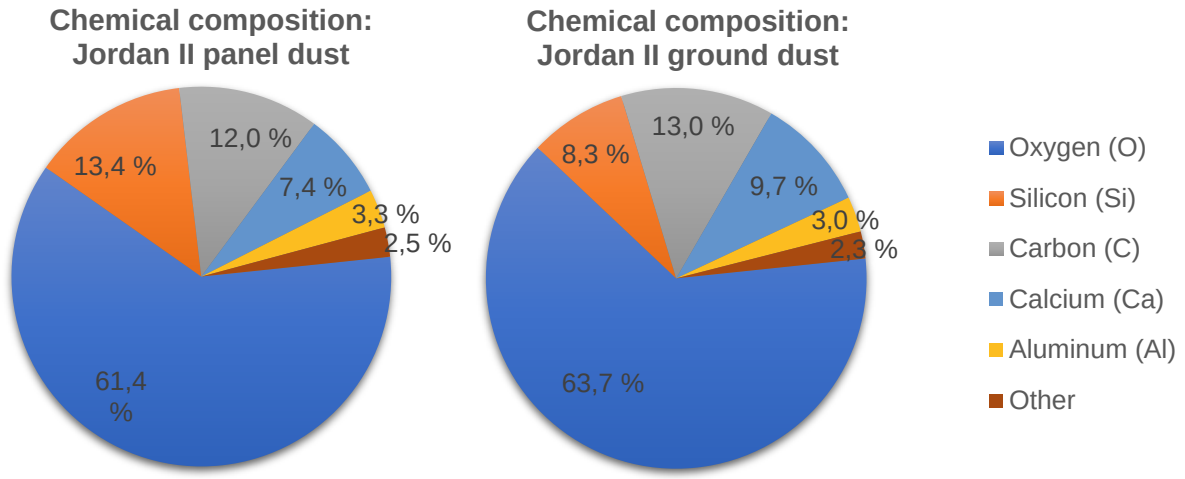

Figure 5.6: Chemical composition of panel and ground dust at Jordan II. The samples had few statistically significant elements.

The relative content of silicon is on average 5%-points lower in the ground dust than the panel dust. Apart from the deviation in silicon, no significant variations between the two samples are identified. Both the panel dust and the ground dust show only five statistically significant elements present, which is, compared to the other sites, the lowest number.

5.1.2.3 Particle shape

The particle shape of the sieved ground dust is compared with the panel dust in figure 5.7.

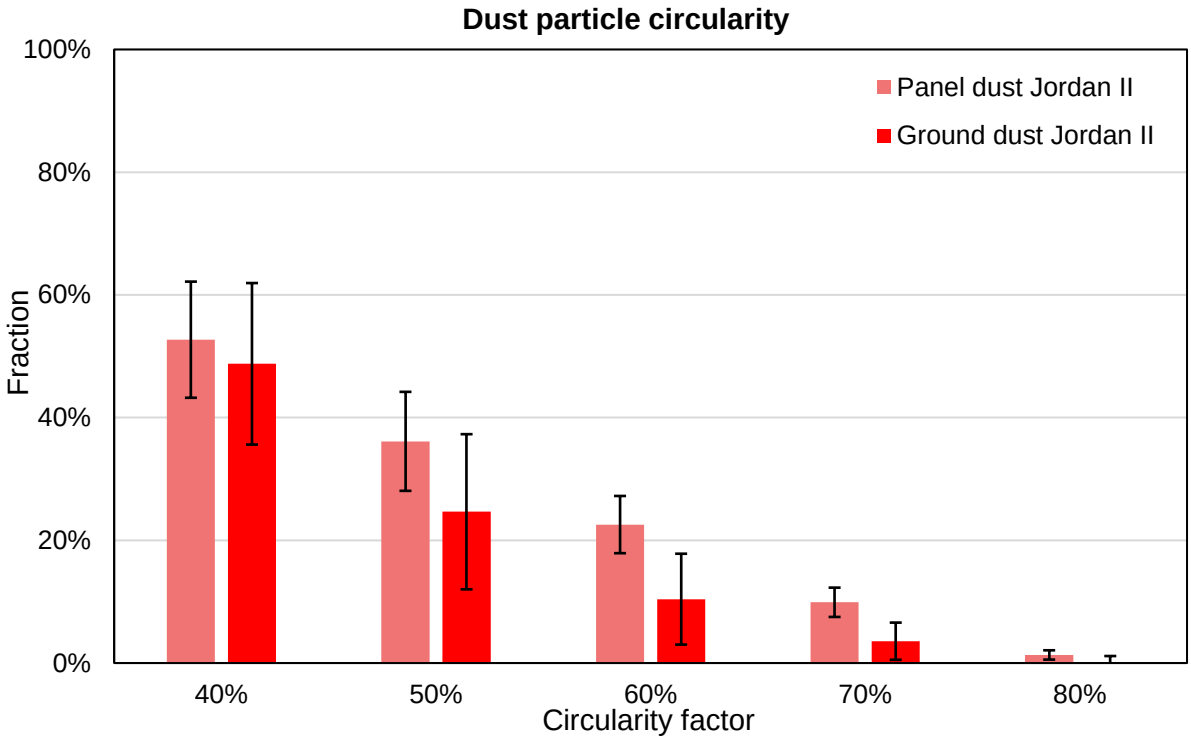

Figure 5.7: Particle circularity for ground (dark red) and panel dust (light red) at Jordan II.

Even though the average fraction of particles at every circularity factor is higher for panel dust, the graph reveals that the uncertainty is too large for a statistically significant difference between the two samples.

5.1.2.4 Particle size distribution

The particle size distribution of the panel and ground dust is presented in figure 5.8. There is a good correlation between the two curves in the volumetric fraction of particles with diameter up to 3 µm. The panel dust contains a high fraction of particles with diameter of ca. 5 – 80 µm, while the sieved ground dust is dominated in volume by particles with diameters between 20 and 100 µm. Both samples have particles down to 0.25 µm.

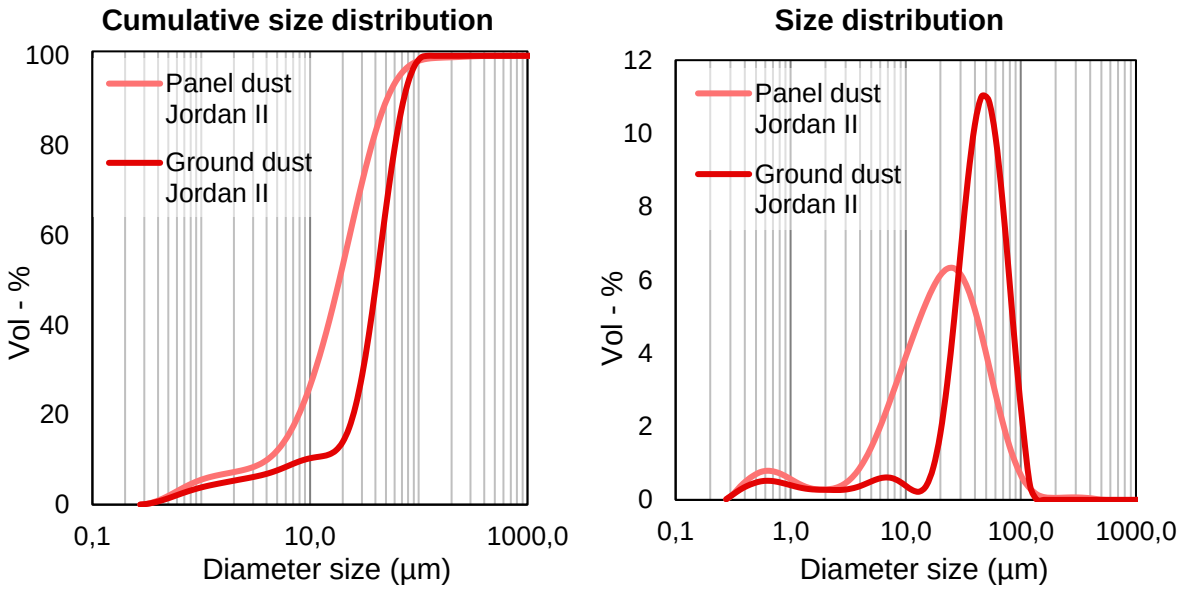

Figure 5.8: Particle size distribution (right) and cumulative size distribution (left) of the panel dust (light red) and sieved ground dust (dark red) from Jordan II.

5.1.2.5 Comparison of ground and panel dust at Jordan II

The visual comparison of the sieved topsoil and the panel dust from Jordan II power plant showed no significant difference in neither color, albedo nor particle shape. Surprisingly, also the chemical composition proved very similar, despite the distinct variation in ground dust at site (ref. section 4.2.3). All the elements present in the panel dust were also found in the ground dust. The visibly lower agglomeration of particles in the ground dust most likely stems from a higher fraction of large particle sizes. In conclusion, it is most likely that the panel dust collected at Jordan II on March 17th stem from the ground nearby or from sources with similar soil characteristics.

5.1.3 Egypt I

5.1.3.1 Visual comparison

The dust samples collected on March 19th and 20th 2019, from the Egypt I solar park are displayed in figure 5.9. The pictures show strong visual correlation between the panel (right) and the sieved

ground dust (left). The agglomeration of particles seems equal and it is impossible to identify any variation in color. The albedo of sieved ground dust and panel dust was measured to be 0.40 and 0.42 respectively, which demonstrate the equal visual appearance.

Figure 5.9: Dust collected at Egypt I on March 19th – 20th, 2019. The left picture shows sieved ground dust (63 µm mesh size). The right picture visualizes the panel dust.

5.1.3.2 Chemical composition

The ground and panel dust were tested for their chemical composition, shown in figure 5.10.

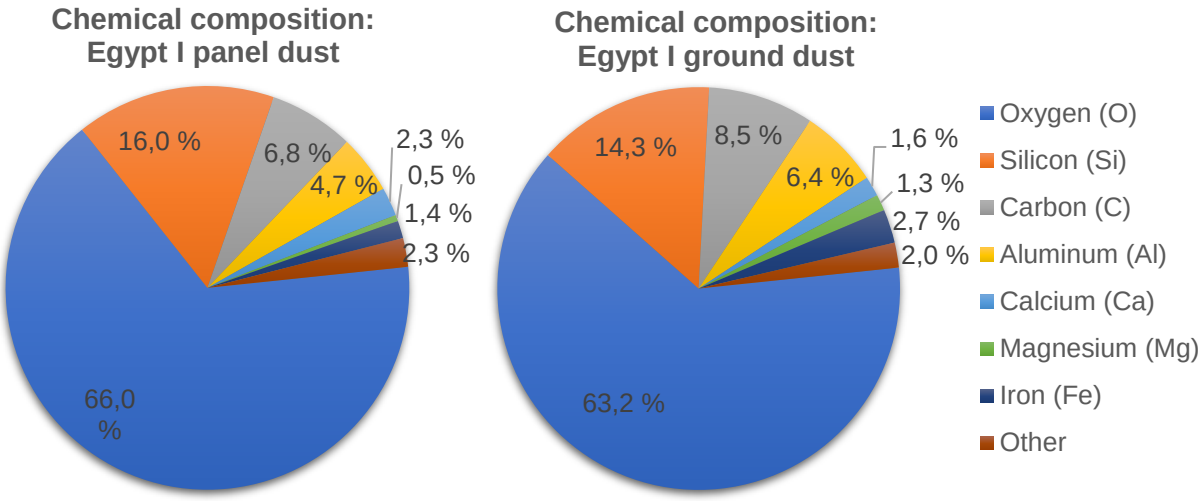

Figure 5.10: The chemical composition of the panel (left) and ground dust (right) at Egypt I. There are no significant differences between the two samples.

There are minor differences of about 1 – 3% in the ratios of almost every element, but these deviations are not statistically significant.

5.1.3.3 Particle shape

Figure 5.11 shows the fractions of the panel and ground dust samples at different circularity factors. Even though the average ratio is higher for panel dust at all circularity percentages, the uncertainty is too large for any firm conclusions. Therefore, no statistically significant difference is detected in particle shape between sieved ground dust and panel dust.

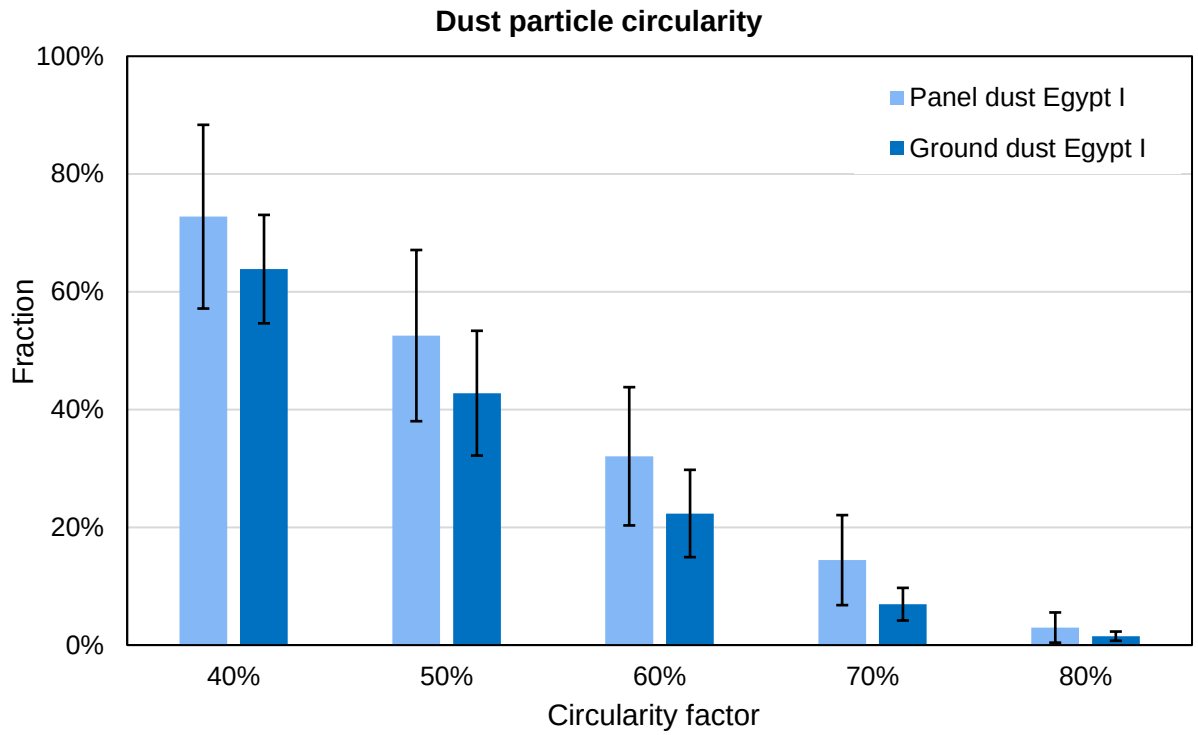

Figure 5.11: Particle circularity for ground (dark blue) and panel dust (light blue) at Egypt I.

5.1.3.4 Particle size distribution

The particle size distribution of the sieved ground and panel dust is given in figure 5.12.

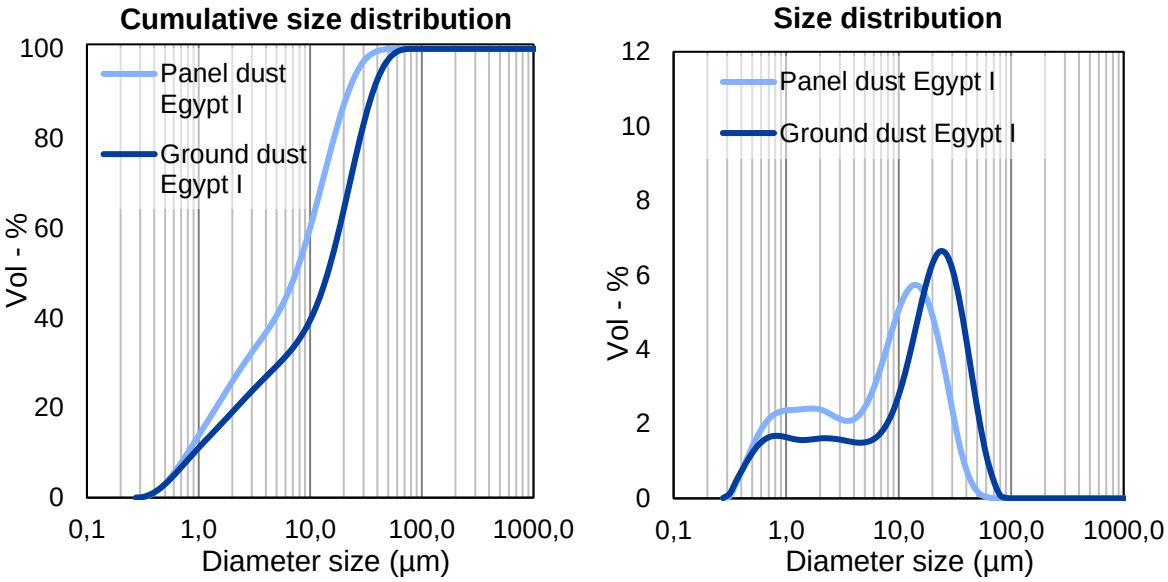

Figure 5.12: Particle size distribution (right) and cumulative size distribution (left) of the panel dust (light blue) and sieved ground dust (dark blue) from Egypt I.

The shape of the two curves is very similar, but the ground dust has a slightly larger size distribution, peaking at 25 µm. The panel dust has the largest volumetric fraction at ca 15 µm. The curves are identical up to 0.4 µm. Thereafter, the panel dust has a higher fraction of particles with diameter 0.5 – 10 µm, whereas particles with diameter 20 – 70 µm dominate the ground dust.

5.1.3.5 Comparison ground and panel dust at Egypt I

The analyses of the dust samples collected from Egypt I have revealed a large correlation between the topsoil and the panel dust in every measured parameter. The particle size distribution curves don't match entirely, which highlights the need for a better sieving technique of the topsoil (elaborated in section 5.4.2.4). Nevertheless, there are strong reasons to believe that the panel dust is coming directly from the topsoil nearby or soil equal to the ground at the power plant.

With hindsight to the recent establishment of the park last months, with extensive construction work that has suspended particulate matter, this was an expected result. The power plant should be reinvestigated after the construction work has finished and the panels have been exposed to natural soiling over a long timeframe, to discover if the correlation between panel and ground dust changes.

5.1.4 Rwanda I

5.1.4.1 Visual comparison

Figure 5.13 compares the ground and panel dust from Rwanda I, collected on March 11th – 14th 2019. Most prominent is the difference in color between the two samples. The sieved ground dust (left image) appears in a very dark red color. In contrast to everything seen so far, the panel dust turned out darker than the ground dust with its deep brown, almost black, color. The measured albedo of the sieved ground and panel dust obtained values of 0.18 and 0.14 respectively.

Figure 5.13: Visual comparison of dust from Rwanda I. The sieved (80 µm) ground dust (left image) was collected from a road east of the power plant. The right picture shows the panel dust.

In addition to the mentioned differences above, the panel dust was very sticky to surfaces (e.g. figure 4.17), as opposed to the ground dust which didn't exhibit this property. A high adhesion factor could also explain the difference in collection of panel dust with wet and dry cleaning, shown in figure C.1 in appendix C. Cleaning in dry conditions is far less efficient than using a wet cloth due to the strong attachment of the dust to the panel. However, the noticeable higher stickiness of this sample compared to the other samples, could have also been a result of contamination by cotton pieces in the sample (ref. section 5.5.1).

5.1.4.2 Chemical composition

Due to the clear difference in color, albedo and stickiness between the samples, distinct differences in the chemical composition were expected. Strangely however, no large deviations can be detected in figure 5.14. Primarily, panel dust has a higher percentage of carbon and silicon. For ground dust, aluminum and iron are stronger represented than in the panel dust. Nevertheless, the chemical composition between the two samples correlates to a large extent and, interestingly, both samples lack calcium.

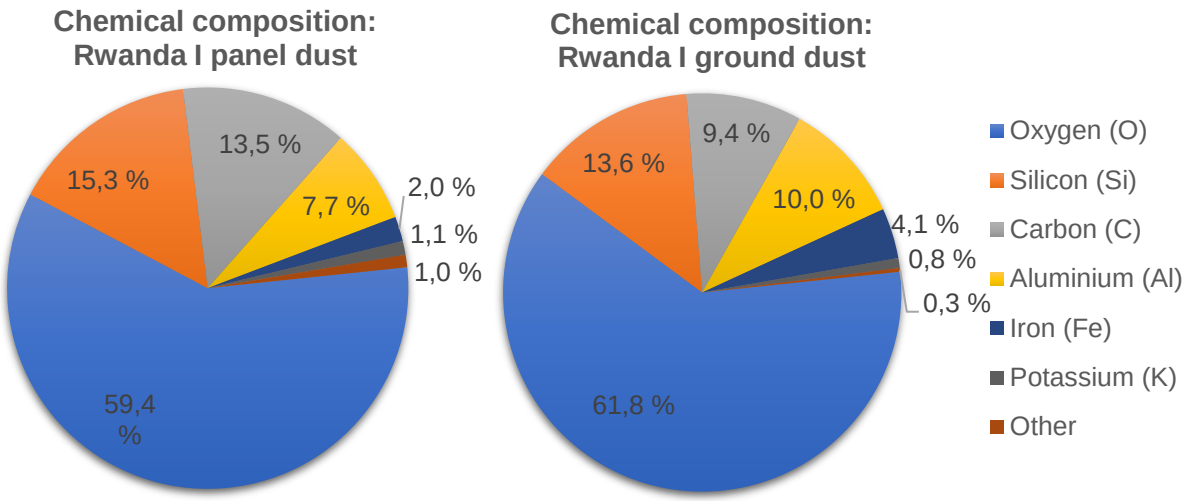

Figure 5.14: The chemical composition of the panel (left) and ground dust (right) from Rwanda I.

5.1.4.3 Particle shape

A comparison of the particle shape between the panel and ground dust is displayed in figure 5.15.

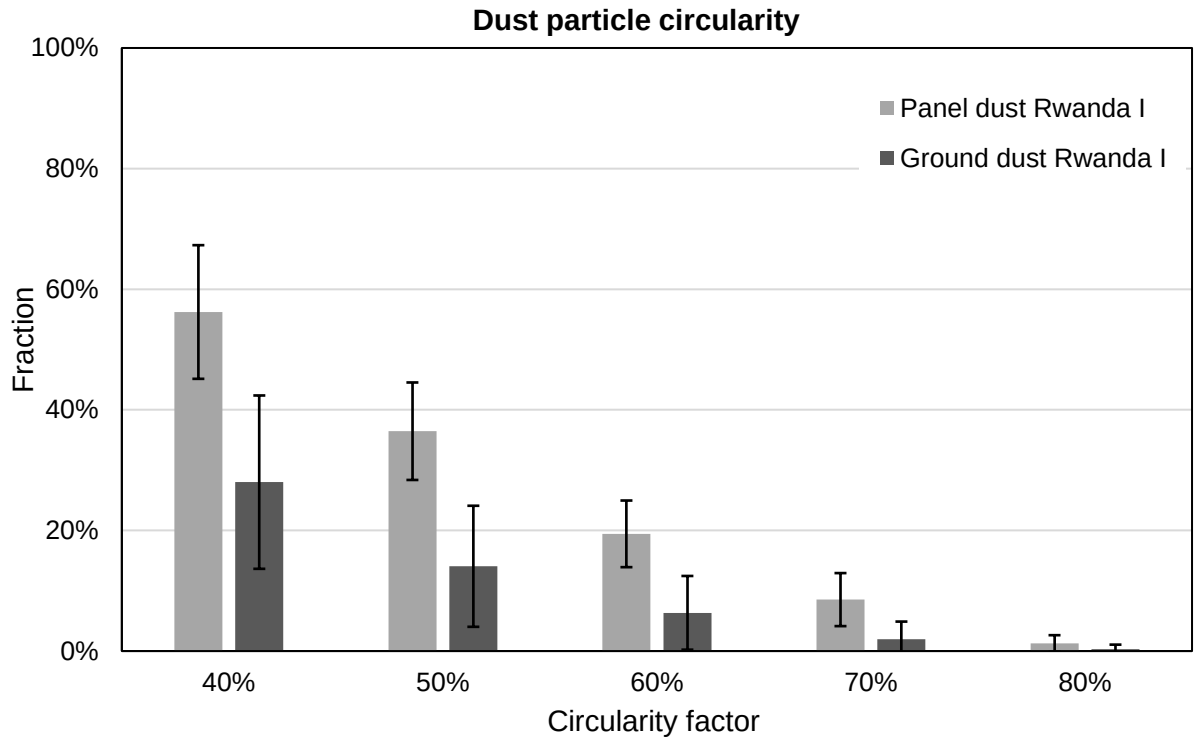

Figure 5.15: Particle circularity for ground (dark grey) and panel dust (light grey) at Rwanda I.

The panel dust has significantly higher percentages of particles at 40 – 60% circularity than ground dust, indicating that the panel dust has a higher proportion of semi-spherical particles. It is no statistically significant difference between the dust types at higher circularity factors.

5.1.4.4 Particle size distribution

The particle size distribution for the panel and ground dust is compared in figure 5.16. The shape of the two curves strongly correlates, but above 5 µm the curve for ground dust seems offset by 30 µm: It is peaking at 55 µm, whereas the panel dust has its peak at 25 µm.

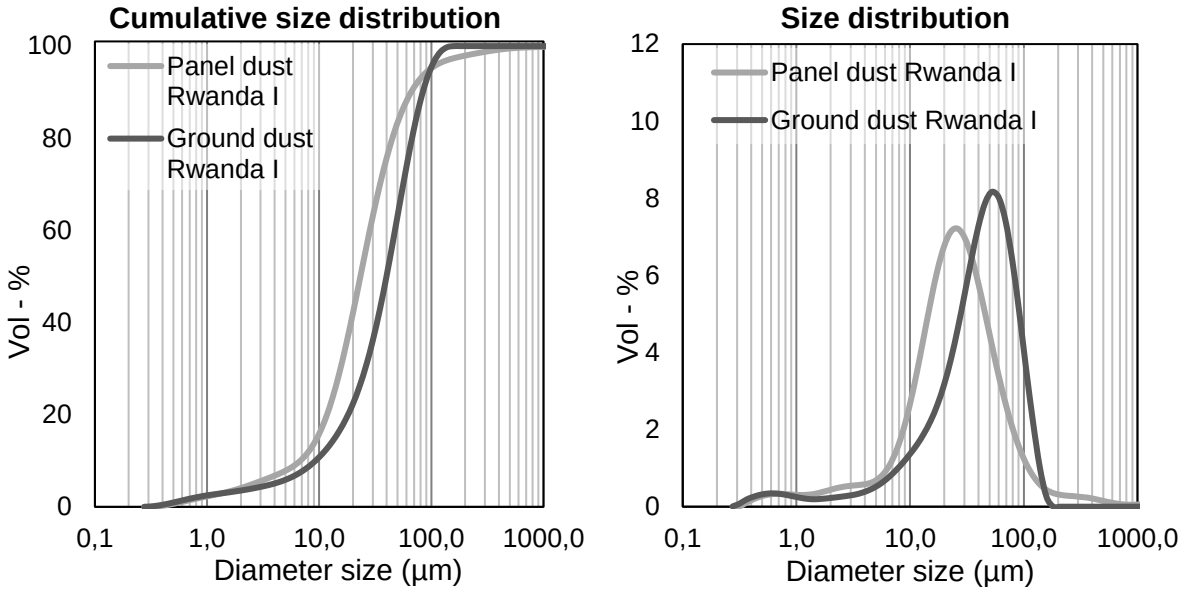

Figure 5.16: Particle size distribution (right) and cumulative size distribution (left) of the panel dust (light grey) and sieved ground dust (dark grey) from Rwanda I.

By a closer look at the two graphs for panel dust, it is visible that particles as large as 1000 µm have been detected. It is very unlikely to find such coarse particles on a PV module, especially during the rainy season in Rwanda. These coarse particles can be ascribed to the extraction process of dust from the cloth, an error that is further discussed in section 5.5.1 below.

5.1.4.5 Comparison of ground and panel dust at Rwanda I

The strong contrasts in color, albedo, stickiness and particle shape between the topsoil and panel dust indicate a different dust source than the ground nearby for the soiling of the PV panels at Rwanda I. At the time of collection, the vegetation was blooming and consequently, the atmosphere was loaded with pollen. The larger amount of carbon in the panel dust compared to ground dust may signalize content of organic matter in the dust. This is further supported by the lack of calcium in the chemical analysis result, since carbon mostly builds minerals with calcium, like calcite ($CaCO_3$) and dolomite ($CaMg(CO_3)_2$). The assessed content of organic carbon in the panel dust is the most probable reason for the dark color of the panel dust and could possibly be the reason for the high stickiness of the dust.

Nonetheless, the similar chemical composition and close albedo value between the topsoil and panel dust may indicate that ground-based dust most probably contributes to the soiling on the panels. However, this effect is believed to be secondary to pollen, microbial cells and spores during the blooming season. The lower impact of the ground dust can be explained by the fact that the vegetation probably traps a large portion of the suspended ground dust before it reaches the panels. Additionally, grains from the ground are believed to have a lower adhesion force than organic matter and are therefore washed off the panels during tropical rain. Lastly, there are less open, barren landscapes for dust to be generated and suspended.

5.1.5 Discussion on the relationship between ground dust and panel dust

This subsection has compared the dust from the panels and ground nearby at four different solar PV parks. The focus has been to discover the possibility of using topsoil as a representative dust sample for evaluating the soiling loss. On one side, the results have shown that in open, barren landscapes, the panel and ground dust exhibit very similar characteristics. In the vegetated area, on the other side, the correlation between panel dust and soil is much more unclear, especially regarding difference in color, albedo, particle adhesion and shape. It is likely that pollen and other airborne organic matter plays a bigger role in the dust deposition during the blooming season.

Generally, the panel dust had a higher ratio of circular grains than the ground dust from the same location. This was expected due to a greater exposure of physical weathering than the more protected dust on the ground. A particle on the panel is continuously exposed to high wind speeds, extensive bombardment of other particles, rain and humidity, through which the particle is shaped to a more spherical form.

Furthermore, the results have shown that a simple method by sieving out the particle sizes in the ground dust that wasn't found in the panel dust proved insufficient. Although the size distribution curves for panel and sieved ground dust show similar shape and are close to each other, the logarithmic scale of the graphs reveals that the sieved topsoil dust clearly contains coarser particles, which requires a more elaborate sieving technique (ref. section 5.4.2.4 below).

Unfortunately, only one measurement at each location has been made at one specific time slot throughout the year, which implies that precautions should be taken when concluding the relationship between the panel and ground dust. The results presented above are specific for dust that was stored on the panels in March 2019. The specific wind direction, wind speed and other natural factors presented in chapter 3.2 may variate inter-annually and, in particular, intra-annually (ref. figure 4.9, 4.12 and 4.15 in section 4.2). A natural continuation of this work is therefore to evaluate the correlation between panel dust and ground dust at another time of the year.

5.2 Comparison of dust characteristics between the four locations and cement

The different dust characteristics, which were compared between panel dust and soil in the previous section, are in the succeeding passage compared between the four different locations. In order to have a reproducible sample type for correlation and validation, an artificial dust sample with cement was added to the comparative analyses.

5.2.1 Visual comparison

Cement dust is presented alongside an overview of all the other eight natural dust samples in figure 5.17. The left column of natural dust represents sieved ground dust, while the panel dust is in the right column.

Figure 5.17: Visual comparison of cement dust (left) and the eight natural dust samples, with ground dust left and panel dust right.

Like the black panel dust and dark red ground dust from Rwanda I, the grey color of cement visually stands out from the rest of the samples. Furthermore, on one hand the panel dust from Jordan I appears in similar bright color pattern as the Jordan II panel and ground dust. On the other hand, the sieved ground dust from Jordan I is very alike the two Egypt I dust samples.

Cement has an equally high agglomerative behavior as the ground and panel dust from Egypt I and panel dust from Jordan I. Very small particles with a high surface-to-volume ratio can easier stick to each other than larger particles due to contact electrification and van der Waals forces. The former is especially pronounced for very small particles [62]. Electrons can transfer over such small particles and build attractive electrostatic forces, bonding the particles together [62].

The quantitative measurements of albedo of the dust samples are summarized in table 5.1.

Table 5.1: Measured albedo of the nine dust samples.

Location	Albedo
Jordan I, Panel	0.50
Jordan I, Ground	0.36
Jordan II, Panel	0.45
Jordan II, Ground	0.45
Egypt I, Panel	0.42
Egypt I, Ground	0.40
Rwanda I, Panel	0.14
Rwanda I, Ground	0.18
Cement	0.36

The overview reveals that black panel dust from Rwanda I has the lowest albedo among the tested dust types, followed by red ground dust from the same location. Cement has been reported in the literature to have a wide range of albedo (0.20 – 0.60) [94]. The value of 0.36 lies in the middle of this range. Desert soil normally has albedo in the range 0.37 – 0.49 [95]. When considering the uncertainty of 2%, these results comply very well with the literature.

5.2.2 Chemical composition

The chemical composition of the eight natural dust samples is presented in figure 5.18.

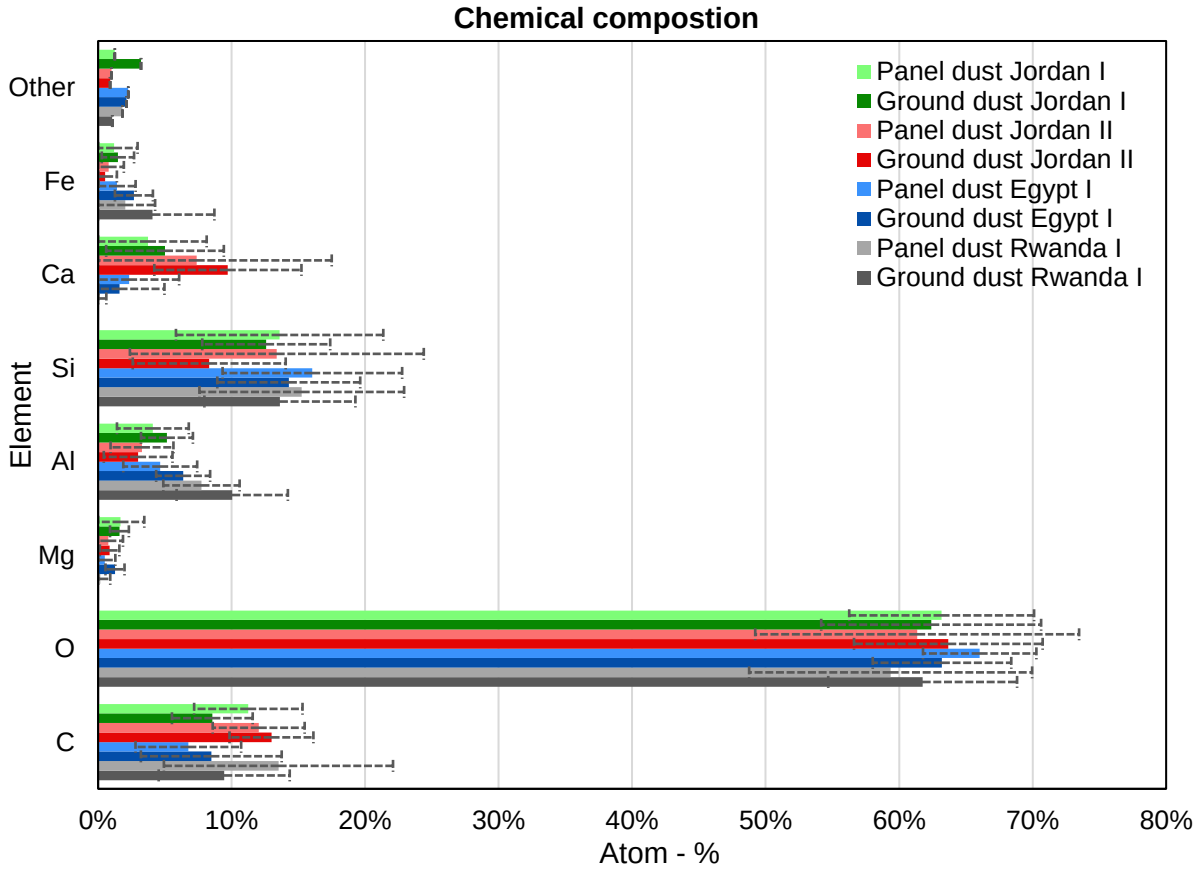

Figure 5.18: Chemical composition of every collected dust sample. Note the considerable uncertainty.

The reason for the large fraction of oxygen (O) is because it is encompassed in almost every mineral. Generally, there are very small mean differences between the samples and the standard deviation is high. The only substantial divergence is the lack of magnesium (Mg) and calcium (Ca) in the Rwandan samples. Particularly interesting with hindsight to absorption is that panel and ground dust from Rwanda I and ground dust from Egypt I seem to contain more iron (Fe) than in the samples from Jordan I and II, yet the uncertainty is very high.

A mineral is classified by its chemical composition and crystalline structure [96]. The presented elements in figure 5.18 can lead to several different types of minerals, which cannot be determined by this simple overview. The most common minerals that possess elements from the graph above is given in table 5.2, which indicates that at least 16 prevalent minerals can be formed by 11 elements found in the samples.[13] Breaking the chemical analyses down to single elements is consequently not beneficial, since an investigation of minerals could possibly separate different locations from each other. This would furthermore improve the assessment of the correlation between ground and panel dust.

Table 5.2: An overview of the most common minerals in the world [96]. Two or more elements enclosed in parentheses with comma in between implies that the composition of the mineral can variate over a limited range expressed by the individual atoms in the parentheses.

Mineral	Chemical composition
Quartz	SiO_2
Calcite	$CaCO_3$
Potassium feldspar	$KAlSi_3O_8$
Dolomite	$CaMg(CO_3)_2$
Hematite	Fe_2O_3
Magnetite	Fe_3O_4
Pyrite	FeS_2
Plagioclase feldspar	$(Na, Ca)(Al,Si)_4O_8$*
Olivine	$(Mg, Fe)_2SiO_4$
Garnet	$(Mg, Fe, Ca)_3Al_2Si_3O_{12}$
Muscovite	$KAl_2(AlSi_3)O_{10}(OH)_2$
Hornblende	$NaCa_2(Mg, Fe, Al)_5(Al, Si)_8O_{22}(OH)_2$
Augite	$Ca(Mg, Fe)Si_2O_6$
Epidote	$Ca_2FeAl_2Si_3O_{12}(OH)$
Biotite	$K(Fe, Mg)_3AlSi_3O_{10}(OH)_2$
Chlorite	$(Mg, Fe)_6Si_4O_{10}(OH)_8$

*For plagioclase feldspar Na>Ca

Due to equipment failure, the chemical composition of cement dust was not conducted, but was given on the container label: CaO, SiO_2, Al_2O_3, Fe_2O_3, H_2O and SO_3. Apart from sulfur, this content of elements is very similar to the other dust samples, yet the relative amount of each element remains unknown.

[13] The low percentages of 3 elements (Na, S and K) is added up in the category ''Other''. Hydrogen cannot be measured by the scanning electron microscope device.

5.2.3 Particle shape

All nine dust samples are compared for particle circularity in figure 5.19.

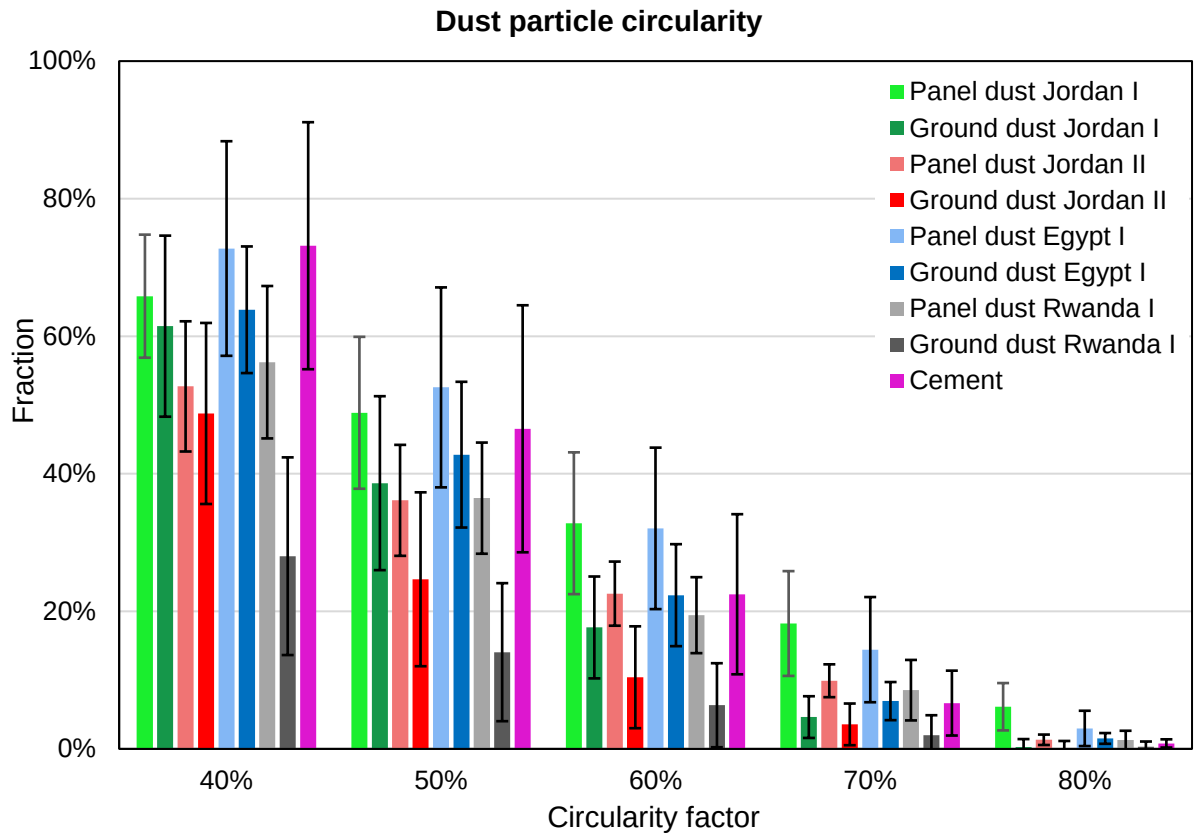

Figure 5.19: Comparison of particle circularity of nine dust samples. The ground dust samples have been sieved according to table 4.2.

The graph indicates that, on average, cement and panel dust from Egypt I and Jordan I seem to contain more circular particles than the rest. In general, the circularity for the panel and ground dust from Egypt I greatly correlates with that of the respective samples from Jordan I. However, the considerable uncertainty makes it difficult to establish firm conclusions from this graph and more pictures should be analyzed in order to decrease the standard deviation.

The poor representation of spherical particles in the ground dust from Rwanda I compared to the other dust samples is a somewhat challenging result: The circularity of the Rwanda I ground dust sample is clearly lower for 40 – 70% circularity factor. As mentioned in section 4.3.5.1 above, the dynamic light scattering method used to find the particle size distribution assumes round particles, which is very far from the case for this type of dust. Complete spherical particles can, in general, not be expected for any dust type, but the problem rest on the significant mismatch compared to the other samples. As a result, the analysis of the particle size distribution of Rwanda I ground dust may yield a greater deviation from the de facto grain size than all the other samples.

5.2.4 Particle size distribution

The panel dust collected from the four different sites contains the particle sizes that have been lifted by the wind, deposited on the panel and adhered to the surface. These samples are of most analytical value and thus, the particle size distribution curves of panel dust are firstly presented. Next, the size distribution of all nine dust samples is compared with each other.

5.2.4.1 Comparison of panel dust

The panel dust from Jordan I, Jordan II, Egypt I and Rwanda I are compared in figure 5.20. In the graph over cumulative size distribution (left graph) it can be easily identified that the Egypt I panel dust has the smallest particle size distribution, followed by Jordan I and then Jordan II. Panel dust from Rwanda I exhibit largest particle size distribution, but note that the cloth might have contaminated the sample and disturbed the particle size distribution measurement as discussed below (paragraph 5.5.1).

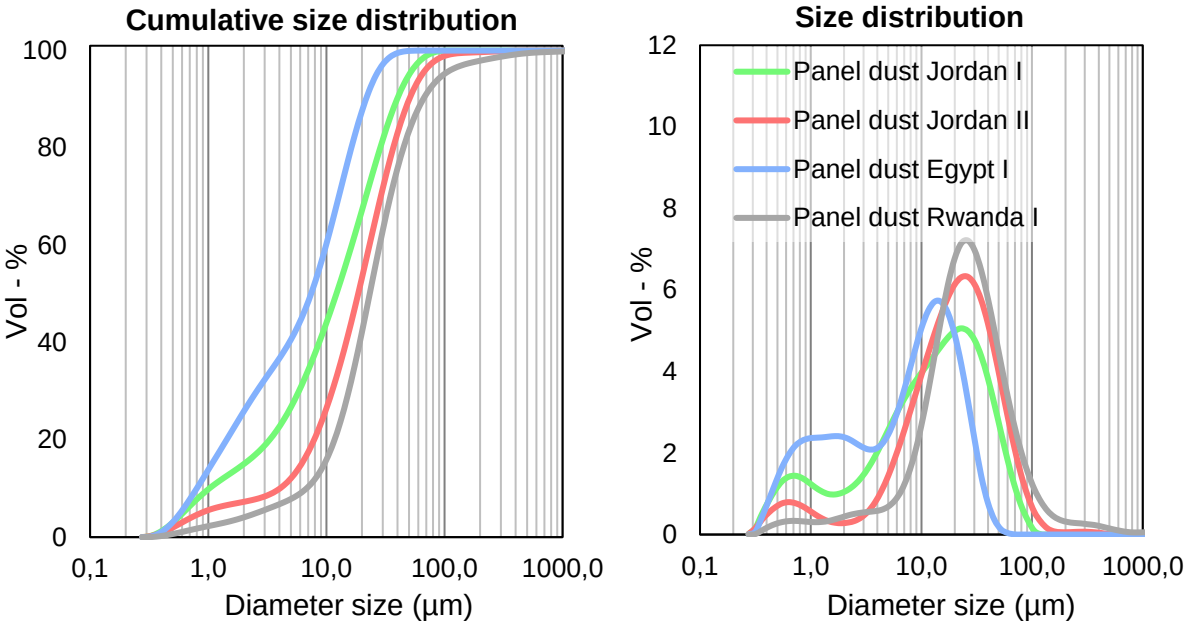

Figure 5.20: Particle size distribution (right) and cumulative size distribution (left) of the panel dust from Jordan I (light green), Jordan II (light red), Egypt I (light blue) and Rwanda I (light grey).

Particles with a diameter of 10 – 30 µm seem to be responsible for a large volumetric response for all samples. The samples from Jordan I, Jordan II and Rwanda I peak at approximately 25 µm, while Egypt I panel dust peaks at ca 15 µm.

5.2.4.2 Comparison of all nine dust samples

Bringing all nine particle size distribution curves together in one graph may at first glance look a bit chaotic. Dark colors represent the sieved ground dust from the same site as panel dust painted in same, but lighter colors. The pink curve shows the size distribution of the sieved cement dust. The particle size distribution curve is shown in figure 5.21 followed by the cumulative size distribution in figure 5.22.

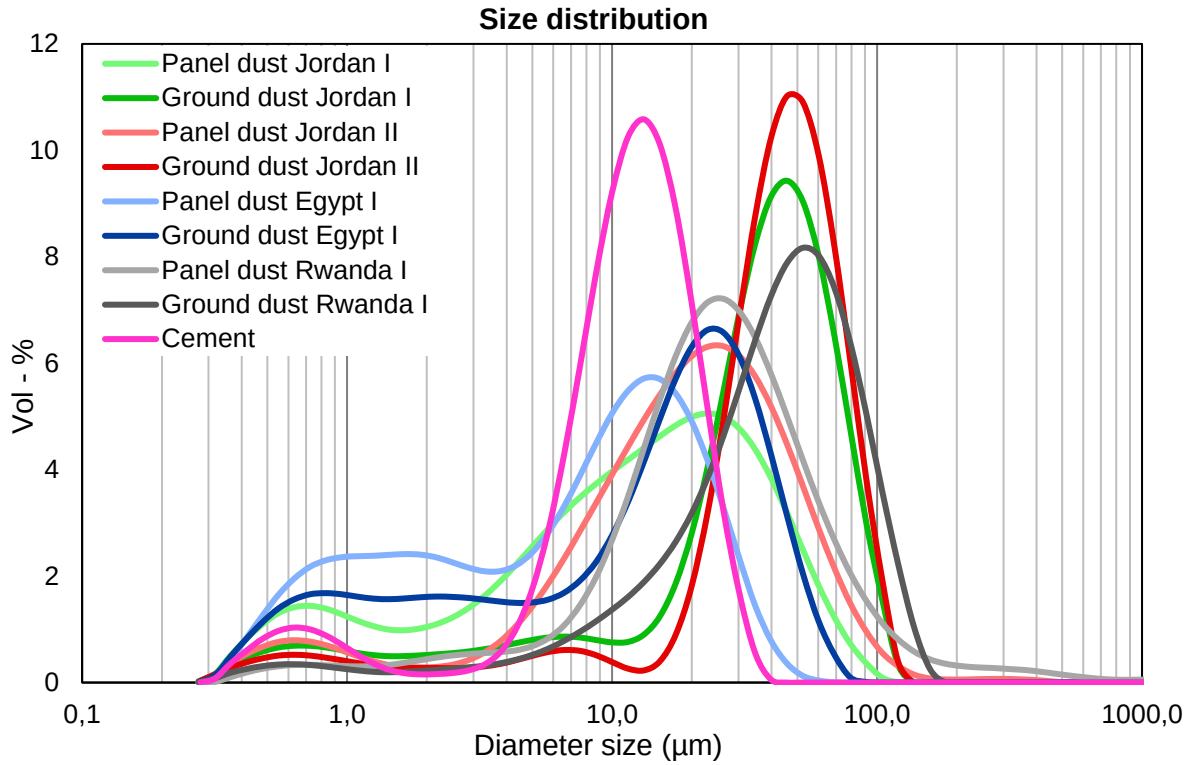

Figure 5.21: Particle size distribution for all the nine dust samples.

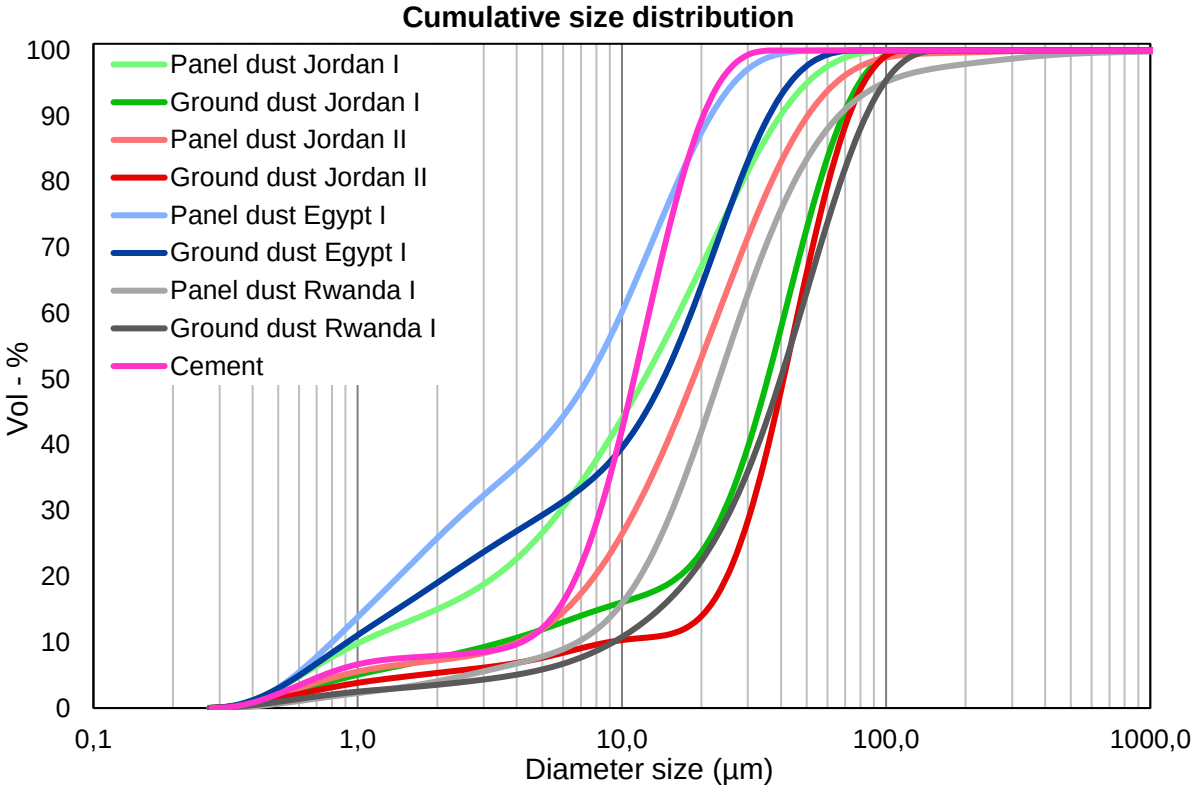

Figure 5.22: The cumulative size distribution of all nine dust samples.

The cement dust sample is mainly comprised of particles from 5 µm to 25 µm, besides a smaller fraction of fine particles between 0.4 µm and 1 µm. This creates a very steep cumulative curve for cement dust. In addition, notice specifically the similar cumulative size distribution curves of

ground dust from Egypt I (dark blue) and the panel dust from Jordan I (light green). Coincidently, the cumulative curves of these two samples are intersecting four times and particles around 25 μm have the highest volume percentage.

Likewise, the three ground dust samples from Jordan I (dark green), Jordan II (dark red) and Rwanda I (dark grey) also consist of very similar particle size distribution with several intersecting points between the cumulative distribution curves. The ground dust from Jordan I has a somewhat higher amount of grains with size 0.5 – 7 μm, whereas Jordan II has a bit higher fraction of particles with diameter 35 – 80 μm. The Rwanda I ground dust sample consists of a larger fraction of grains at 8 – 20 μm. However, the shape of the curves is almost identical; particles with a diameter around 45 – 50 μm dominate the volume of both dust samples. Neither sieved topsoil from Jordan I nor Jordan II contain grains larger than 120 μm, but the ground dust sample from Rwanda I has grains above 150 μm.

5.2.5 Discussion on correlations between dust characteristics

As pointed out above, the cement dust, panel dust from Jordan I and panel and ground dust from Egypt I all exhibited a higher degree of agglomeration than the other dust samples. The very same four samples also have the smallest particle size distribution (figure 5.21 and 5.22), which indicates a correlation between agglomeration and particle size.

The correlation between particle size distribution and particle shape is also striking. Cement dust, panel dust from Jordan I and Egypt I all exhibit the highest average fraction of particles with circularity factors up to 70% according to figure 5.19, and these samples have the finest particle size distribution curves. Similarly, according to figure 5.22, ground dust samples from Jordan II and Rwanda I have the coarsest particle composition and they seemingly also have the lowest circularity of all the samples (figure 5.19).

If this argument holds, the particle shape should not be severely different between panel dust from Jordan I and ground dust from Egypt I. However, at a closer look at figure 5.19 above, there may be an evidence for a lower particle circularity of ground dust than for panel dust despite similar particle size distribution curves. Even though the uncertainty is considerable, ground dust from Egypt I has lower mean percentage of circular particles at all factors from 40 – 80%. Particularly interesting is this result when recalling of the particle size distribution curves for the two samples in figure 5.21. Ground dust from Egypt I has a higher fraction of fine particles (0.6 μm to 3 μm), which should be an advantage in measuring the circularity factor with ImageJ. This leads to a firmer conclusion of the circularity difference between panel and ground dust, indicating that the panel dust has been grinded through weathering.

5.3 Effect of dust on transmission

The following subchapter focuses on answering the second and third goal of the thesis. The second goal, which aimed at developing an overview of the decrease in transmission by miscellaneous types of soiling, is tackled by quantifying and comparing the transmission of sunlight through PV cover glass contaminated with different types of dust. The first section discusses the transmission of light through panel dust. Thereafter, the transmission through ground dust is presented, followed by a comparison of all the samples in the third paragraph. In the end of each of the first three sections, the different transmission curves are compared and discussed in light of the dust characteristics presented in the section 5.2 above.

The fourth paragraph highlights the spectral differences in the transmission loss. Three intervals in the ultraviolet, visual and near infrared spectrum are selected and the resulting transmission curves are compared. The fifth and last paragraph summarizes the subsection in order to answer the third goal of this thesis, which is directed at finding the most important dust characteristics for the transmission loss. A regression analysis is presented to support the discussion.

The spectrometer used for transmission measurements provides spectral data shown in the example of panel dust from Jordan I given in figure 5.23. The other seven analyzed samples are given in appendix F, figures F.3 – F.9. Between 350 nm and 1000 nm, 852 data points are averaged to a single value for the transmission of sunlight for one particular dust density.

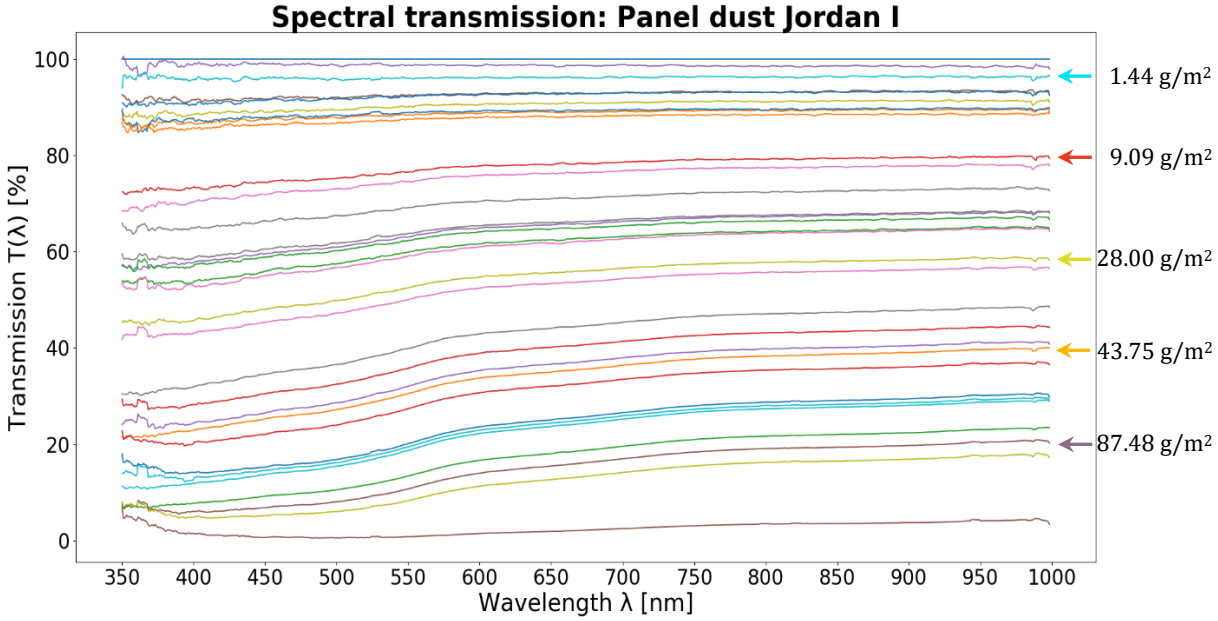

Figure 5.23: Spectral transmission of light through 31 different densities of panel dust from Jordan I deposited on a PV cover plate. Every colored curve represents a certain dust density given in table D.1, appendix D. Five selected densities are marked in the graph. The spectrometer measures from UV light at 350 nm to NIR light at 1000 nm.

5.3.1 Transmission through panel dust

The mean spectral transmission curves of different densities of panel dust from Jordan I, Jordan II and Egypt I are given in figure 5.24. The collected dust from the PV panels at Rwanda I was insufficient for deposition on glass plates and couldn't be evaluated.

The mean spectral transmission decreases approximately exponentially as the dust density increases. By the time a panel has reached 25 g/m² of dust, the sunlight is attenuated by approximately 40 – 50%. The graph reveals a clear difference between the three types of panel dust: The loss in sunlight that penetrates the glass plate is, in general, more severe with Saharan panel dust from Egypt I, while the panel dust from Jordan I is second worst. The panel dust that attenuates the sunlight the least stems from Jordan II. At 50 g/m² the loss in solar radiation is 80% for Egypt I panel dust, whereas panel dust from Jordan II "only" has a loss of about 65%.

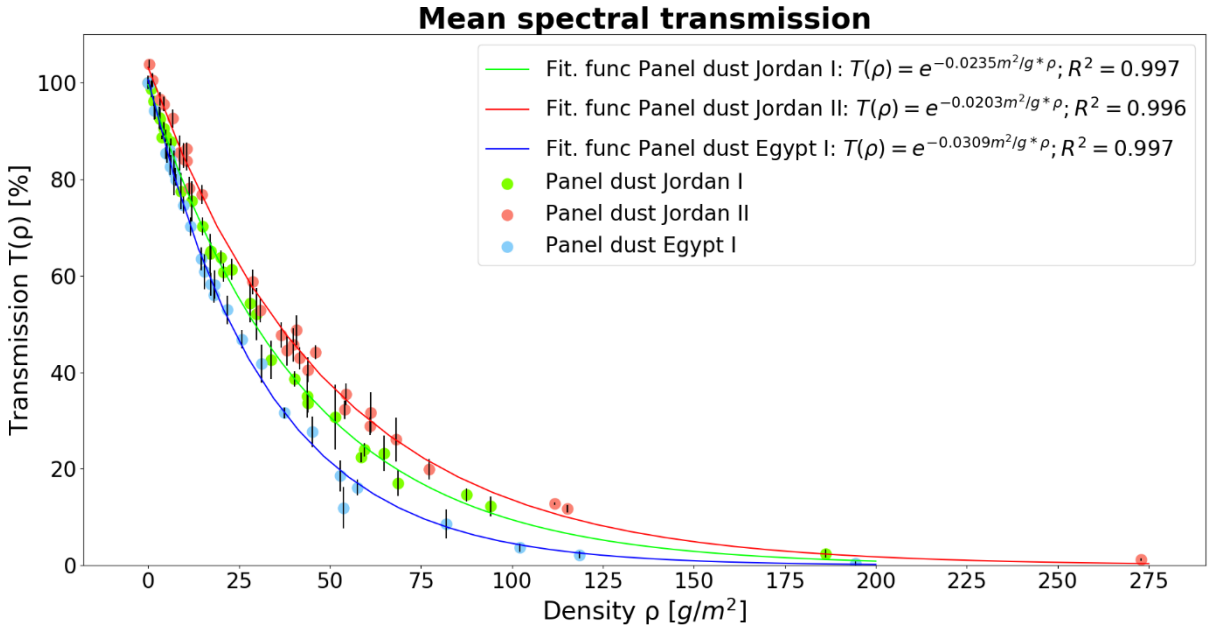

Figure 5.24: Mean spectral transmission of light (350 nm – 1000 nm) through PV cover glass plate contaminated with various panel dust densities from Jordan I (green), Jordan II (red) and Egypt I (blue). The line marks the respective fitted exponential function. The uncertainty in y-direction represent the heterogeneity of the dust deposition. The weighing uncertainty in x-direction is only 0.1 g/m², which is too small to be visible.

The reduction in transmission can also be portrayed with the slope coefficient (α) of an exponential fit function. The α-coefficients for the three plotted functions are shown in the legend of figure 5.24. A high value of α represents a steep curve, implying strong attenuation of sunlight. Contrarily, more gradual loss in transmission versus dust density exhibits a low α-coefficient. The slope coefficients for natural panel dust fluctuate between 0.0309 m²/g and 0.0203 m²/g. The fitted functions for all three samples give very high R^2 values, confirming a good fit of the datapoints to an exponential function.

In a real situation, it is very unlikely to find PV panels contaminated with above 25 g/m² of dust, as this would result in a tremendous loss in electricity production. Before PV cover plates reach such soiling levels, they are washed clean by the cleaning personnel. To take a closer look at the transmission loss at low densities of dust, figure 5.25 concentrates on the contaminations of dust up to 30 g/m².

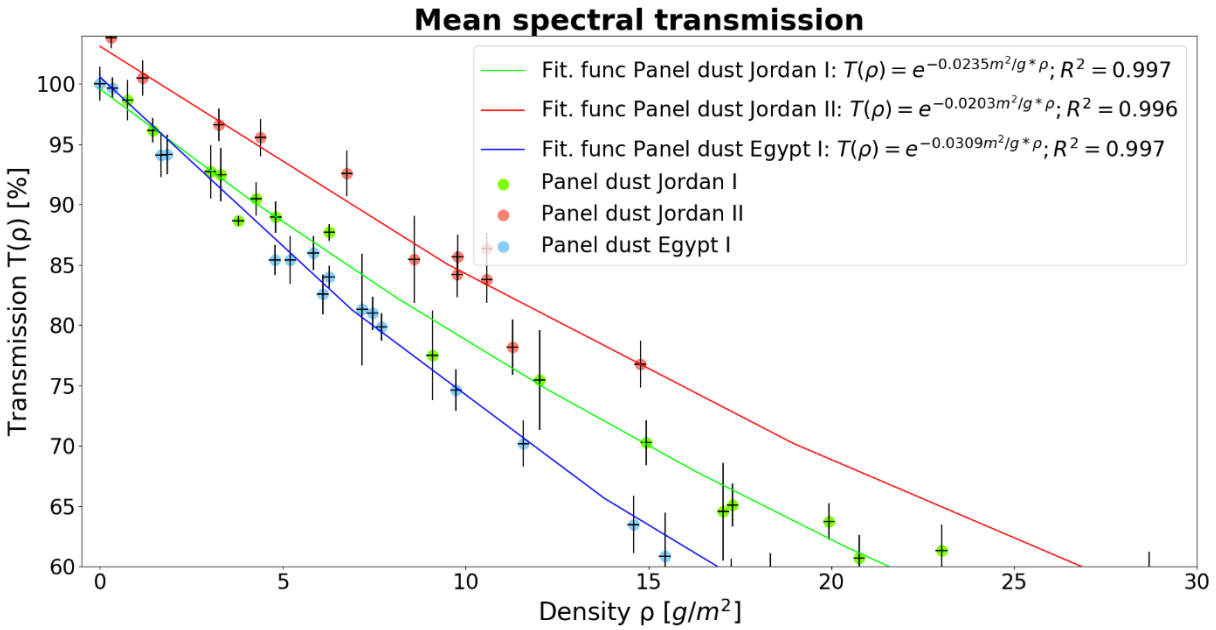

Figure 5.25: Transmission of light (350 nm – 1000 nm) through a PV cover glass plate at different panel dust densities from Jordan I (green), Jordan II (red) and Egypt I (blue). The uncertainty in y-direction represent the heterogeneity of the dust deposition and the uncertainty in x-direction is considering the weighing uncertainty of 0.1 g/m².

The graph shows the same order between the three samples: Egypt I panel dust attenuates the sunlight the most even at low densities, with Jordan I in the middle. Jordan II again shows less attenuation than the other two. Notice that the graph surprisingly indicates that a bit of soiling with panel dust from Jordan II might have a positive effect. This might be due to an increased roughness of the surface which better transmit the light than a smooth cover plate. It could, however, also stem from device or calibration error.

The resulting range of α-coefficient implies that a natural soiling layer of 5 g/m² would lead to a transmission loss of approximately 14.3% in in the worst case (Egypt I power plant) compared to ca 9.7% in the best case (Jordan II power plant). A difference of almost 5% is far from unimportant for a utility-scale power plant: Given equal climatological situations, it implies a more frequent cleaning or an increased reduction in the electricity produced, which in either case leads to lower revenue from the power plant.

5.3.1.1 Discussion on panel dust characteristics and transmission loss

The PDS value is meant to represent the particle size distribution with one single value. In the following, the identified deviations in the α-coefficients, i.e. transmission, between the panel dust

samples are seen in light of the different dust characteristics. Table 5.3 summarizes the most important dust characteristics and the transmission loss. The transmission loss is expressed through the α-coefficient of the fitted exponential function and the PDS value is meant to represent the particle size distribution with one single value. In the following, the identified deviations in the α-coefficients, i.e. transmission, between the panel dust samples are seen in light of the different dust characteristics.

Table 5.3: Differences in transmission loss (represented by α-coefficient) and dust characteristics between panel dust from Jordan I, Jordan II and Egypt I. The value for 50% circularity has been selected from the data for comparative purposes.

	α-coefficient [m^2/g]	PSD [-]	Albedo (ϱ) [-]	Iron (Fe) content * [%]	Fraction of 50% circularity * [%]
Jordan I, Panel	0.0235	2.09	0.50	1.2	48.9
Jordan II, Panel	0.0203	3.03	0.45	0.8	36.1
Egypt I, Panel	0.0309	1.17	0.42	1.4	52.6

* The difference between the three panel dust samples is not statistically significant.

On one hand, the transmission loss correlates perfectly with the different cumulative particle size distribution curves in figure 5.20, which revealed that Egypt I panel dust comprises of the finest particles, followed by panel dust from Jordan I. Lastly, panel dust from Jordan II has the coarsest grain composition, not considering panel dust from Rwanda I. It is therefore likely that the particle size distribution is a significant factor for the amount of sunlight that penetrates the dust layer and the results indicate that small particles contribute to a higher transmission loss than coarser ones at same dust density.

On the second hand, the values for the albedo effect, presented in table 5.1, showed that the brightest panel dust sample was from Jordan I (ϱ = 0.50), followed by Jordan II (ϱ = 0.45) and Egypt I panel dust, which contained the darkest color and lowest albedo (ϱ = 0.42). This indicates a different absorption rate, where Egypt I is absorbing more sunlight then Jordan I and Jordan II. If reflection from the brighter dust samples doesn't compensate for the lower absorption, it means that panel dust from Jordan I must have the lowest transmission loss of sunlight in a situation where the particle size distribution is identical for all three samples (ref. eq. 9, section 2.2.2).

The iron oxide content and particle shape of the dust types are unfortunately not significantly deviating from each other, due to the high uncertainty in the data material. Based on the comparative study on panel dust, the particle size distribution is likely the main contributor to the different mean transmission of sunlight, while the results are insufficient for an assessment on albedo, iron oxide content and particle shape.

5.3.2 Transmission through ground dust

The transmission of light through different densities of ground dust from Jordan I, Jordan II, Egypt I and Rwanda I with respective exponential trend lines is given in figure 5.26.

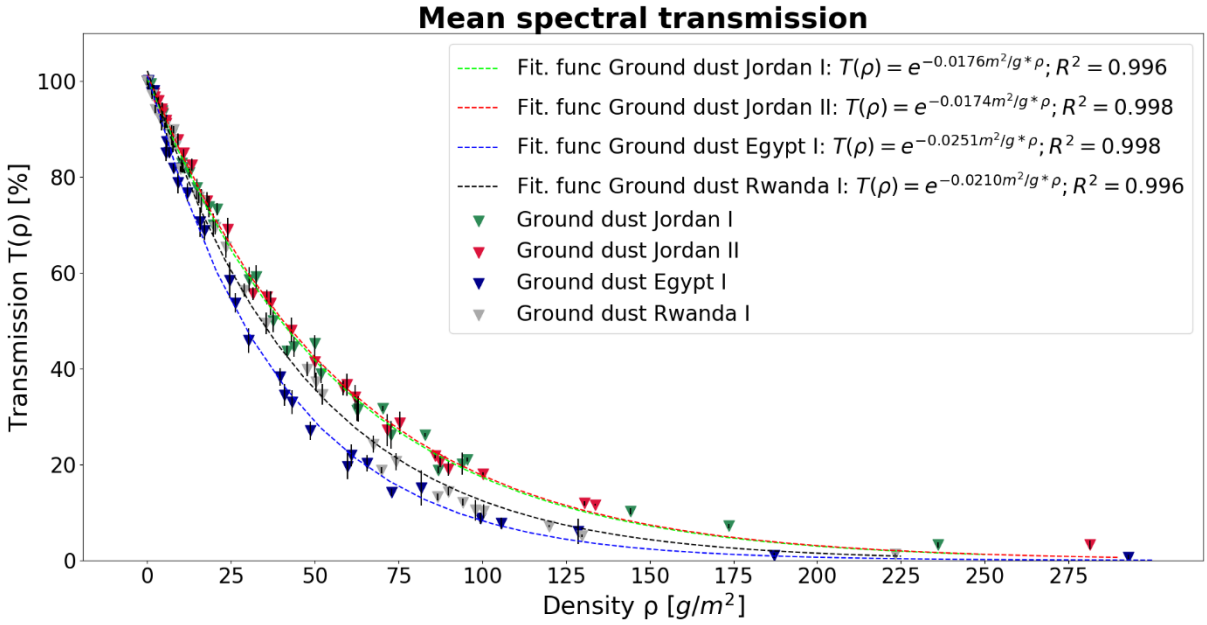

Figure 5.26: Transmission of light (350 nm – 1000 µm) through a glass plate contaminated with ground dust at different densities from Jordan I (dark green), Jordan II (dark red), Egypt I (dark blue) and Rwanda I (grey) with exponential trend lines.

The first interesting point to highlight is the close similarity between ground dust from Jordan I and Jordan II. By looking at the trend line, it is almost impossible to separate them. Their α-coefficients are deviating by only 0,0002 m^2/g, showing 0.0174 m^2/g and 0.0176 m^2/g for ground dust from Jordan II and Jordan I respectively. In terms of reduction of sunlight, the topsoil dust from Jordan I and Jordan II have the lowest reducing effect on the transmission: At 50 g/m^2 the loss in transmission is roughly 58%, while for the same density with ground dust from Rwanda I and Egypt I the transmission loss is 65% and 71% respectively.

The ground dust from Egypt I features the largest negative effect on the transmission of sunlight with an α-coefficient of 0.0251 m^2/g, whereas the transmission curve representing the dark red topsoil dust from Rwanda I is positioned between the ground dust from Egypt I and Jordan I/II and has an α-coefficient of 0.0210 m^2/g. The slope coefficients for natural ground dust vary between 0.0251 m^2/g and 0.0174 m^2/g. The R^2 values show acceptable goodness of fit.

5.3.2.1 Discussion on ground dust characteristics and transmission loss

The following paragraphs aim to explain the deviations and similarities in transmission of light through ground dust by comparisons with the differences in dust characteristics. Table 5.4 highlights the most important parameters and is based on figure 5.26 and the general trend on dust characteristics.

As indicated in the previous section for panel dust, the most influential parameter for the transmission of light through dust again seems to be the particle size distribution: Ground dust from Egypt I, which has the highest transmission loss, also comprise of the finest grain sizes. Compared with ground dust from Jordan I, which has a lower albedo than topsoil from Egypt I and no large difference in particle circularity or iron content, the substantial discrepancy in transmission is highly likely a result of the dissimilarity in particle size distribution.

Table 5.4: Differences in transmission loss (represented by α-coefficient) and dust characteristics between ground dust from Jordan I, Jordan II, Egypt I and Rwanda I. The value for 50% circularity has been selected from the data for for comparative purposes.

	α-coefficient [m^2/g]	PSD [-]	Albedo (ϱ) [-]	Iron (Fe) content [%]	Fraction of 50% circularity * [%]
Jordan I, Ground	0.0176	4,55	0.36	1.5	38.6
Jordan II, Ground	0.0174	5,20	0.45	0.5	24.7
Egypt I, Ground	0.0251	2,02	0.40	2.7	42.8
Rwanda I, Ground	0.0210	5,40	0.18	4.1	14.1

* The difference in circularity is only statistically significant between ground dust from Egypt I and Rwanda I.

The summary in table 5.4 further provides evidence that the transmission of sunlight is dependent on albedo of the dust. Even though figure 5.21 and 5.22 reveal quite similar size distribution curves among ground dust from Jordan I, Jordan II and Rwanda I, the transmission loss is clearly higher for ground dust from Rwanda I (figure 5.26). This lower transmission through dust from Rwanda I likely mirrors the distinct dark red color of Rwanda I ground dust that has an albedo of 0.18, compared to 0.36 and 0.45 for Jordan I and Jordan II respectively. Topsoil dust from Rwanda I therefore absorbs more sunlight than ground dust from Jordan I and Jordan II, resulting in a lower transmission, despite having similar particle size distribution curves.

Additionally, albeit a high uncertainty is involved in the chemical analyses, the higher transmission loss of sunlight through a layer of ground dust from Rwanda I compared to Jordan I and Jordan II might also arise out of a higher iron oxide content. As described in section 2.2.5, a high iron oxide content is reported to increase the absorption of sunlight. The iron content, presented in figure 5.19, might therefore indicate the impact of this parameter on transmission of sunlight.

Following the assessment about albedo being a determinant of transmission loss, ground dust from Jordan I should have a somewhat higher transmission loss than ground dust from Jordan II. By reexamining figure 5.21 and 5.22, which show the particle size distribution, only minor discrepancies were pinpointed between the ground dust from Jordan I and Jordan II. Visually, the ground dust from Jordan I appears considerably darker and has an albedo 0.09 lower than the ground dust from Jordan II, which results in a higher absorption rate in favor of the topsoil dust

from Jordan I. There are no other significant differences between these two types of dust with regards to iron content, chemical composition or circularity.

As a consequence of a higher absorption rate and somewhat smaller particle size distribution, it was expected that ground dust from Jordan I would have a higher α-coefficient than ground dust from Jordan II. This is however not the case, which mainly relates to the DLS measurement. The fraction of particles that fulfills 40 – 60% circularity is on average ten percentage points lower for ground dust from Jordan II than from Jordan I (figure 5.19). It can therefore not be ruled out that the size distribution measurements with the DLS device have been equal for both samples. Rather, there is a chance that ground dust particles from Jordan II were determined to have a lower or higher diameter than in reality. A higher estimated particle size distribution for ground dust from Jordan II would cohere stronger with the assumed correlation between a large particle size distribution and a lower transmission loss.

5.3.3 Comparison of transmission of all dust samples

In figure 5.27 all analyzed samples for transmission of light are merged into one graph. This includes cement, which evidently reduces the sunlight much more than any of the other dust types.

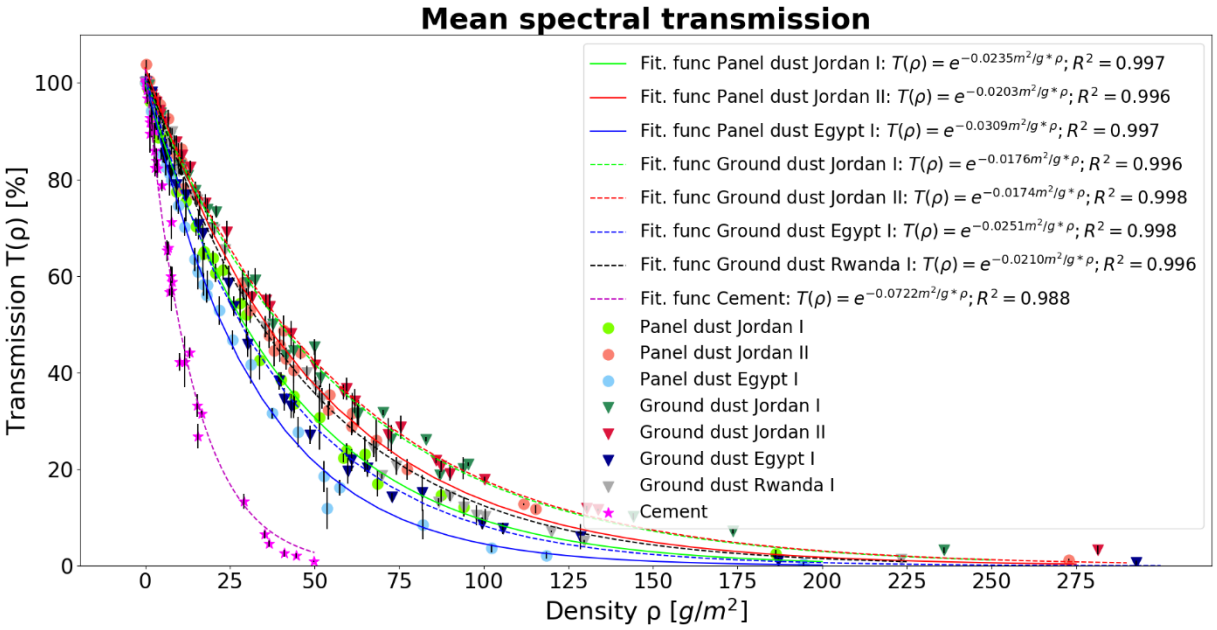

Figure 5.27: Transmission of light (350 nm – 1000 µm) through a glass plate contaminated with dust at different densities from eight locations: Panel and ground dust from Jordan I (light and dark green), panel and ground dust from Jordan II (light and dark red), panel and ground dust from Egypt I (light and dark blue), ground dust from Rwanda I (grey) and cement (pink) with exponential trend lines.

At 50 g/m² of cement dust, approximately all incoming sunlight is blocked, resulting in an α-coefficient of cement dust significantly higher than any other dust type (α = 0.0722 m²/g). Furthermore, figure 5.27 also reveals two other interesting factors. First, the transmission curves of panel dust from Jordan I and ground dust from Egypt I are very close to each other, with a difference in the slope coefficient of only 0.0016 m²/g. Second, the transmission curves representing ground

dust from Rwanda I and panel dust from Jordan II are even more adjacent, with α-coefficients of 0.0210 m^2/g and 0.0203 m^2/g respectively.

5.3.3.1 Discussion on dust characteristics and transmission loss

A summary of the transmission (described with the α-coefficients) and dust characteristics is presented in table 5.5 for all dust samples.

Table 5.5: Selected values to highlight differences in transmission loss and dust characteristics between all dust types.

	α-coefficient [m^2/g]	PSD [-]	Albedo (ϱ) [-]	Iron (Fe) content [%]	Fraction of 50% circularity* [%]
Jordan I, Panel	0.0235	2.09	0.50	1.2	48.9
Jordan I, Ground	0.0176	4.55	0.36	1.5	38.6
Jordan II, Panel	0.0203	3.03	0.45	0.8	36.1
Jordan II, Ground	0.0174	5.20	0.45	0.5	24.7
Egypt I, Panel	0.0309	1.17	0.42	1.4	52.6
Egypt I, Ground	0.0251	2.02	0.40	2.7	42.8
Rwanda I, Panel	-**	4.73	0.14	2.0	36.5
Rwanda I, Ground	0.0210	5.40	0.18	4.1	14.1
Cement	0.0722	1.26	0.36	-***	46.5

* The difference in circularity at 50% is only statistically significant for ground dust from Rwanda I.
**The transmission of Rwanda I panel dust could not be measured due insufficient amount of dust collected.
*** The chemical composition of cement was not analyzed, but the content clarification showed Fe_2O_3.

The reason for the very effective decrease in transmission with increasing cement dust density is due to a very fine particle size distribution combined with iron oxide content and a low albedo. Although several other dust types have a higher fraction of particles with diameter 0.5 – 5 μm (figure 5.21) and panel dust from Egypt I has a lower value of PSD (table 5.5), cement dust can still be considered to have the finest particle size distribution. Figure 5.22 illustrated that no other sample has a maximum size at 40 μm, like cement, resulting in a cumulative curve that reaches 100% before any other dust sample. The low albedo effect of 0.36 combined with Fe_2O_3 minerals likely results in an increased absorption, which intensifies the decrease in transmission of sunlight through cement dust. Consequently, Hey'di Rapid cement dust that is sieved with 20 μm mesh size attenuates the solar insolation the most among all tested dust types.

Comparing ground dust from Egypt I and panel dust from Jordan I to each other in figure 5.27 reveals additional interesting points. In section 5.2.4 the close correlation in particle size distribution between these dust samples was specifically mentioned. Table 5.5 also shows very equal PSD values, with 2.09 and 2.02 for panel dust from Jordan I and ground dust from Egypt I respectively. Even if the collected ground dust from Egypt I has a lower maximum particle size (80 μm contra 100 μm for panel dust from Jordan I), it can still be claimed that the particle size distribution between the samples correlates to a large extent. The small deviation in transmission loss

might therefore instead stem from dissimilarities is albedo and iron oxide content. Egypt I ground dust is believed to have a higher absorption rate, due to the deviation of 0.1 in albedo and a higher, although uncertain, iron oxide content. Taking all these factors into account, it is reasonable that the data points over transmission are very close to each other, as figure 5.27 discloses, yet that Egypt I ground dust has a slightly larger deteriorating effect on transmission of light than panel dust from Jordan I.

Another proof of the relationship between albedo and iron oxide content with transmission of sunlight is found by a closer look at ground dust from Rwanda I. It has a low albedo ($\varrho = 0.18$), but a coarse particle size distribution in comparison to the other samples. By comparing ground dust from Rwanda I with panel dust from Jordan II, two dust samples that are closely connected on the transmission plot in figure 5.27, it is apparent that these two samples don't have a similar particle size distribution (figure 5.21). However, the anticipated lower transmission loss as a result of coarser grains in the ground dust sample from Rwanda I can be cancelled out by a higher absorption rate, due to a difference in albedo of 0.27 and a clearly higher iron oxide content.

5.3.4 Spectral differences in transmission loss

The attenuation of sunlight by a layer of dust varies over the light spectrum, as declared in section 3.3.1. To illustrate the spectral difference in transmission loss, which was introduced in figure 5.23, five selected densities of panel dust from Jordan II are compared in wavelength intervals of 50 nm in figure 5.28.

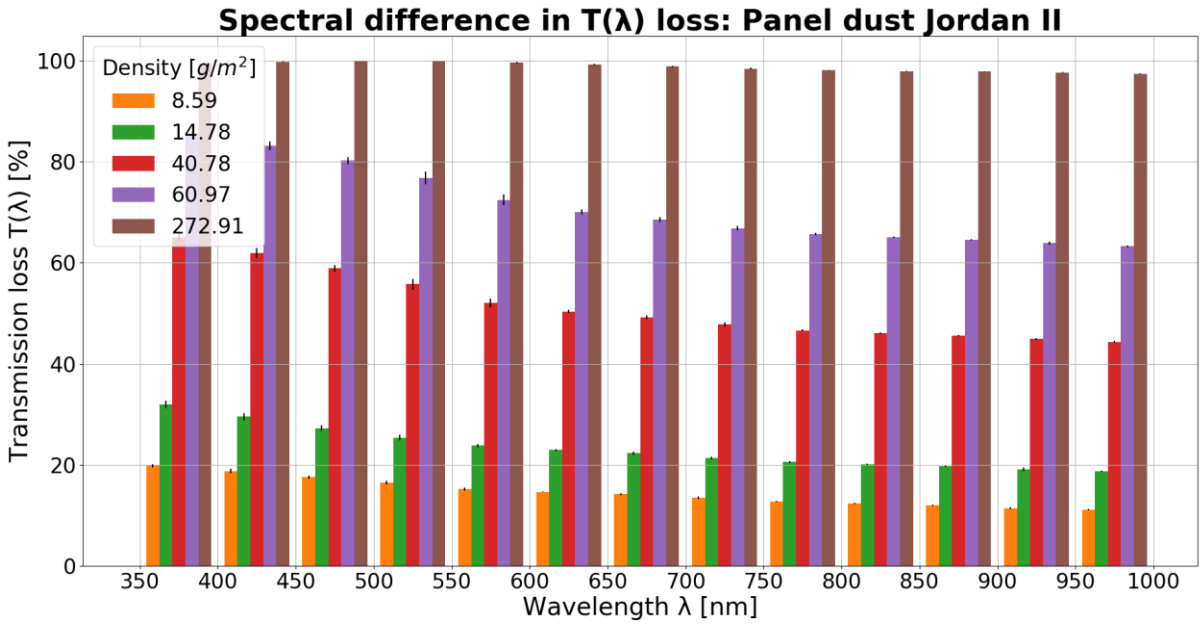

Figure 5.28: Spectral differences in attenuation of sunlight. The graph shows the average transmission loss for five selected densities of panel dust from Jordan II in wavelength intervals of 50 nm from 350 – 1000 nm. Spectral differences of the other dust types can be found in appendix F.

When the dust almost blocks all light, like at 272.9 g/m^2, the spectral difference is only a few per cent and obviously unimportant. At 40 – 60 g/m^2 the difference between light at 350 – 400 nm and at 950 – 1000 nm can be as much as 20%. However, the soiling is rarely at such high levels, which means that the two lowest selected densities of 8.6 g/m^2 and 14.8 g/m^2 are more often realized in natural conditions. For these densities the spectral difference is not as severe, but still deviates approximately 10% from the lowest to the highest wavelength considered. All the other dust samples show similar characteristics and are shown in appendix F (figure F.10 – F.16).

5.3.4.1 Alfa coefficient

Another way to demonstrate the spectral variation in transmission of sunlight is to consider the slope coefficient (α) of the fitted functions for UV, visual and NIR spectrum. Table 5.6 compares the α-coefficient for all the samples, except panel dust from Rwanda I, due to the insufficient amount collected for transmission measurements. The R^2 identifies the goodness of fit of the function, which for all samples is satisfying. For all samples, the attenuation of sunlight is more severe the shorter the wavelength. This is in line with previously reported results in the literature on soiling [57, 84].

Table 5.6: Comparison of the spectral difference in transmission at three intervals of wavelength: UV/VIS, VIS and NIR. Last column shows the percentage change in average α-coefficient from UV/VIS to NIR spectrum.

	UV/VIS 350-500nm		VIS 500-800nm		NIR 800-1000nm		Percentage change
	α [m^2/g]	R^2	α [m^2/g]	R^2	α [m^2/g]	R^2	UV/VIS -> NIR
Jordan I, Panel	0.0303	99,5%	0.0231	99,7%	0.0201	99,7%	33.7%
Jordan I, Ground	0.0232	99,5%	0.0175	99,6%	0.0144	99,4%	37.9%
Jordan II, Panel	0.0276	99,5%	0.0197	99,6%	0.0171	99,5%	38.0%
Jordan II, Ground	0.0232	99,6%	0.0172	99,8%	0.0144	99,7%	37.9%
Egypt I, Panel	0.0373	99,7%	0.0309	99,7%	0.0271	99,7%	27.3%
Egypt I, Ground	0.0309	99,7%	0.0253	99,7%	0.0213	99,8%	31.1%
Rwanda I, Ground	0.0232	99,6%	0.0213	99,6%	0.0193	99,6%	16.8%
Cement	0.0773	98,7%	0.0722	98,7%	0.0688	98,8%	11.0%

In detail, table 5.6 lifts an interesting assessment. The ground dust from Jordan I, Jordan II and Rwanda I has an equal α-coefficient of 0.0232 m^2/g for 350 – 500 μm. For the NIR wavelength area the dust types from Jordan I and Jordan II have a slope coefficient of 0.0144 m^2/g; in other words, a drop by 37.9%. Ground dust from Rwanda I, however, only drops 16.8% down to 0.0193 m^2/g. The most distinct divergence between these three dust types is the albedo and iron oxide content, leading to a higher absorption for ground dust from Rwanda I. Ground dust from Jordan I and Jordan II are far brighter than the dark red ground dust from Rwanda I (figure 5.17). Mirrored in a higher slope coefficient for VIS and NIR spectrum for ground dust from Rwanda I, a red colored dust will reflect light around 700 nm, since this is the wavelength of red electromagnetic radiation.

5.3.5 Summary on transmission loss

This subchapter has found a distinct dependency between transmission of light and the particle size distribution of the dust. Additionally, the albedo of a sample also seems to play a secondary, yet significant role. Vague indications of a dependency on the iron oxide content have also been addressed.

Firstly, for a perpendicular angle of light incidence with the solar panel ($\theta = 0°$) and an equal density of dust layer on a PV panel, the soiling will result in a more severe drop in transmission if the dust comprises of grains with a low diameter. To explain this further, figure 5.29 visualizes how the small grains can spread over the surface are more equally distributed over the panel than larger grains at equal dust density.

Figure 5.29: Two panels with equal density of dust, but different grain size distribution, will have dissimilar effect on the transmission of sunlight. The situation to the right clearly will transmit more sunlight than in the left situation.

At equal density, dust samples that comprise of coarser particles leave voids for light to penetrate the layer (figure 5.29, right), while for samples with mainly fine particles the sunlight is attenuated over the entire area (figure 5.29, left). This is the reason why the dust samples with low particle size distribution (e.g. cement) have the lowest transmission of light. Equally, coarser dust samples (for instance ground dust from Jordan II) tend to have a higher transmission rate.

It is also important to remember the tendency for agglomeration of dust with a very fine particle size distribution, which can be well identified for cement and panel dust from Egypt I and Jordan I in figure 5.17. This agglomeration will counteract the ability to fill emerged voids between the particles and rather deposit on top of other grains. The effect of agglomeration seems to be comparatively subordinate to the impact of filling voids by small grains, since the results have demonstrated such a strong dependency on the particle size distribution.

The tall grains to the right in figure 5.29 may cast longer shadows when the incident light is not perpendicular on the panel and cancel out this effect, as illustrated in figure 3.11. Nevertheless, since all the PV power parks assessed in this study have a single axis tracker and are located close to equator, shadow casting of particles is a negligible problem.

The second most important determinant of sunlight transmission is the albedo of the dust. In figure 5.29 some grains are painted with a brighter color than the others to remind the reader that the dust can have different colors and be partially transparent [52]. If the dust appears black or very dark, it will obviously have a lower albedo and thus a higher absorption rate than a bright

dust sample. Introduced in section 2.2.4, reflection of the dust between 1 – 100 μm essentially follows Mie scattering, which has a dominant forward lobe (figure 2.8). This means that the light primarily goes through the dust when the grain size is about the same size as the wavelength, and the albedo is high.

In general, Saharan dust has previously been reported to have very low absorption of sunlight due to low content of iron, while south of Sahara – Sahel – has a more red colored soil, due to a higher content of iron oxides [40, 41]. Figure 5.18 above, which compared the chemical composition of all the dust types, reveals that ground dust from Rwanda I indeed has higher iron content, even though the uncertainty is high. Note that the graph shows iron content in atomic percentage, which in mass would be much higher, due to a higher molar value of iron compared to all the other elements discovered in the dust. The iron oxide content might explain a lower transmission of light than what could be anticipated through the particle size distribution as the only known parameter.

In a simple attempt to quantify the relationship between transmission loss and these three mentioned parameters, regression analysis was conducted (table 5.7). The dependent variables were the α-coefficients from the natural dust samples[14]. These variables were compared with the respective independent variables for particle size distribution (PSD) and albedo (ϱ). The level of confindence was set to 90%. The regression revealed no statistical significance for a dependency on iron oxide content due to a very high p-value of 0.71 (appendix F, table F.2).

Table 5.7: Regression analysis on the influence of particle size distribution and albedo on the α-coefficient of the exponential fit function from figure 5.27.

	Coefficients	Std error	p-value	Confidence interval
Intercept	0.0415 m^2/g	0.0055 m^2/g	0.0017	[0.0297 – 0.0532 m^2/g]
Particle size (PSD)	-0.0031 $m^2/(g{\cdot}mm)$	0.0006 $m^2/(g{\cdot}mm)$	0.0072	[-0.0044 – -0.0018 $m^2/(g{\cdot}mm)$]
Albedo (ϱ)	-0.0220 m^2/g	0.0101 m^2/g	0.0946	[-0.0435 – -0.0005 m^2/g]

Table 5.7 supports the general conclusion from above: Firstly, it shows that particle size distribution has a very low p-value (0.72%), which means that it highly likely correlates strongly with the α-coefficient, i.e. the transmission loss. Secondly, the regression results indicate that the contribution by albedo is still significant, yet more uncertain, with a p-value of 9.46% just within the confidence limit (below 10%). This reflects the subordinate role that albedo is playing on the determination of the α-coefficient in comparison to the particle size distribution. Likewise, the fact that the regression analysis couldn't find a statistically significant relationship between the iron oxide content and the transmission loss is clear, since the effect is believed to be overshadowed by the

[14] The cement dust sample and panel dust from ASYV were obviously not included due to lack of information on iron oxide content and transmission respectively.

strong effect from the particle size distribution in particular and the albedo. It might also relate to an interdependency between albedo and iron oxide content in this small dataset.

Based on the regression analysis, a linear formula for computing the α-coefficient is suggested in equation 29.

$$29)\ \alpha = 0.0415 - 0.0031PSD - 0.0220\wp, \qquad [-]$$
$$for\ PSD = [1.15 - 5.50]$$
$$\wp = [0.15 - 0.50]$$

This formula should be seen as a first estimate and a motivation for more data analysis to establish a model for transmission loss, rather than given formula for the slope coefficient that can be used world wide for all dust types. Recall that only seven datapoints have been used for this regression analysis, which is a very small number for statistical analysis.

5.4 A standardized method for dust collection and laboratory analyses

The fourth and last goal has been to establish a replicable, simple and fast method for collection of dust samples and characterization analyses for future work. If researchers studying other locations are able to conduct the entire process in a similar way, a wide overview of transmission curves of different dust types could be implemented as a valuable tool for decision-makers. Additionally, if industry companies can conduct simple and fast measurements, that can determine the particle size distribution, iron oxide content and albedo, a proposed model for transmission loss dependent on density of dust can give a first estimation on the severity of soiling at a given location of interest. The proposed standard procedure, which builds on the methodology presented in chapter 4, is elaborated in the following paragraphs and consists of:

- Collection of dust with either vacuum cleaner, bare hands or squeegee with water spray gun, depending on the dust accumulation on the panels.
- Chemical composition analysis with XRD to attain mineral content of the dust.
- Particle shape and size measurements using a focused beam reflectance device or DLS with polyphosphate.
- Development of a model for transmission loss versus density of dust.
- A more sophisticated, optimized sieving technique if ground dust is to be used as a basis for transmission loss estimations.

5.4.1 Optimized methodology for dust collection

The initial prospect to collect dust with a vacuum cleaner, sucking it off the panel, was unfortunately not thoroughly tested, because of the equipment failure early into the fieldwork. Nevertheless, it is evident that the device would have been of considerable benefit where the dust density on the panel was clearly visible at low angles of incidence, like at Jordan I and Egypt I shown in figure 4.8 and 4.13 respectively (sections 4.2.2 and 4.2.4).

Especially in the Egypt I solar power park, a uniform, medium-thick layer of dust was present, which a vacuum cleaner effectively could have collected. In case the dust in addition is fairly adherent to the surface, as in Egypt I (figure 4.13), a brush could help removing it (figure 5.30), but should not contaminate the sample with pieces from the brush.

Figure 5.30: A vacuum cleaner brush.

Additionally, collection with a vacuum cleaner would have been little affected by the windy weather condition which was present at the time of the sampling. To sum up, at a high level of soiling, and medium to high level of uniform deposition, a vacuum cleaner with similar properties (ref. section 4.2.1.1) as Kärcher HV 1/1 Bp Fs is recommended (table 5.8).

Particularly when the dust is uniformly distributed over the module, sweeping panels with bare hands to collect a sufficient amount of dust is ineffective. Cleaning 800 panels to get 0.35 l panel dust in Egypt I consumed two full working days. However, when the dust is stored along the frame of the panel, best exemplified at Jordan II in figure 4.11 (section 4.2.3), it is preferable to rub the particles free with a finger and bring them into a container. At Jordan II it took only about three hours to gather 0.70 l dust. In general, at high levels of dust density and a very heterogenous distribution, a vacuum cleaner is not necessary. To scratch it free with a finger is more efficient in this situation, since no dust would be lost in the vacuum container and filter (table 5.8).

To collect dust samples from the modules in Rwanda I power plant with a vacuum cleaner turned out unsuccessful due to the low density and high level of uniform distribution. After several hours of vacuum cleaning no dust particles could be identified in the container of the device. To get a few particles for shape, size and chemical measurements, a cloth was used instead, yet this technique contaminates the sample severely, as discussed in section 5.5.1 below.

One might argue that for a clear heterogeneous layer of dust, a vacuum cleaner might be useful even for low densities, since it would be possible to focus the device on certain areas of the module. Nevertheless, this work proposes a new method for collection of dust from panels where the density is very low, presented below: Squeegee and water spray gun.

Table 5.8: The proposed methods for collecting dust at different densities of dust and uniformity.

Panel dust density	Uniformity	Preferred cleaning method
High (clearly visible at any angle of incidence)	High	Vacuum cleaner
	Medium	Vacuum cleaner
	Low	Scratch dust loose with (gloved) finger
Low (only visible at high angles of incidence)	High	Squeegee with water spray
	Medium	Squeegee with water spray
	Low	Squeegee with water spray / (Vacuum cleaner)

5.4.1.1 A new method for collecting particles from panels at low densities of dust: Squeegee, water spray gun and funnel

Most power plants experience a thin layer of dust at all times which is difficult to extract without some sort of contamination of the sample. Inspired by the technique of cleaning windows on a building with a squeegee, a similar method for solar panels is proposed (figure 5.31).

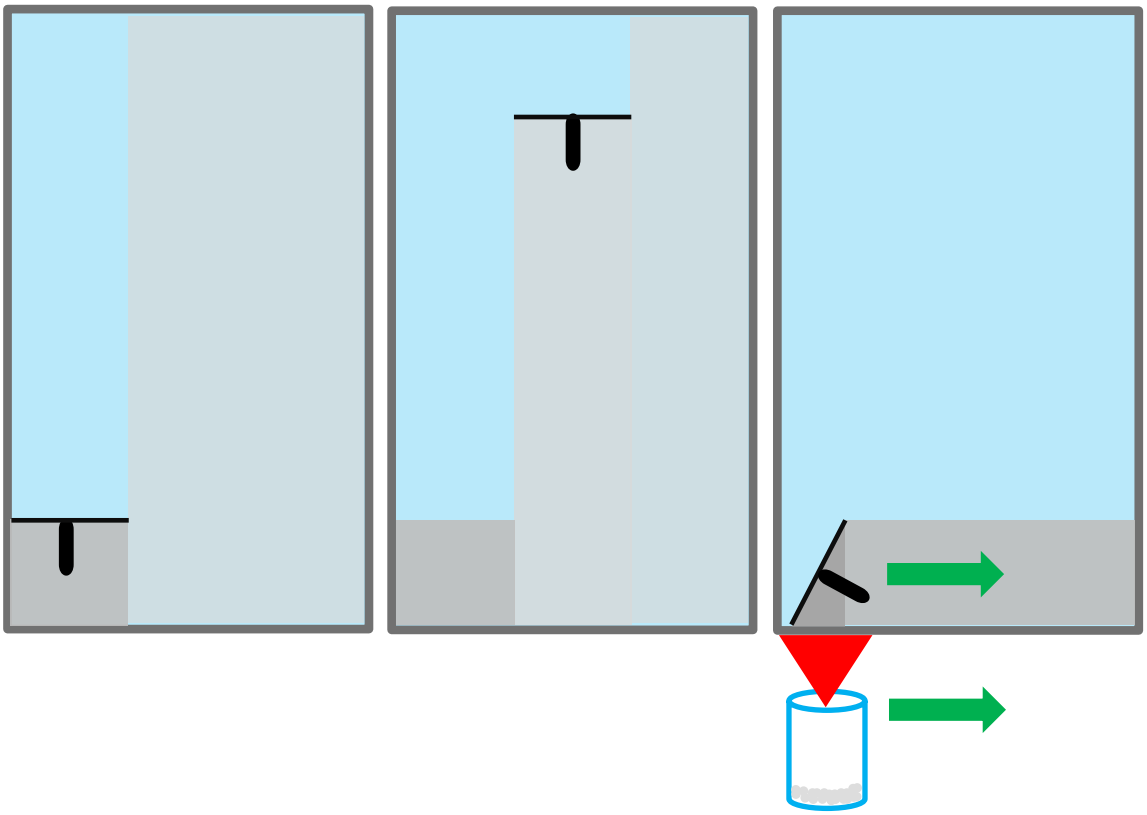

Figure 5.31: The proposed method for collection of particles at low densities of dust on the module. Water is sprayed on the surface and a squeegee wipes the dust to the lower end of the panel. In this case, the frame will intercept the water and dust. When all the dust is brought to the bottom, the squeegee sweeps horizontally with a funnel (red triangle) and a container underneath that collects the samples.

In detail, a spray gun pours water onto the glass and a squeegee sweeps the surface downwards. At the bottom of the panel, the water with dust is collected in a can with help of a funnel. The method is illustrated in figure 5.31 for framed PV panels. If the panel lacks a frame, the squeegee is brought to the bottom with the funnel and container underneath the panel at all times. After collection of the dusty water, the container is left in a dry room for evaporation of the water.

Unfortunately, the method was not tested in the field, due to the risk assessment prior to the travel, which had stated that scratches and other permanent marks on the glass surface of the module were by no means to be caused. Clearly, it is understandable to avoid this method if the dust density is high, but when the density is low, this risk of scratches is probably negligible.

5.4.1.2 Collection of ground dust with vacuum cleaner

The cheapest, fastest and easiest way to collect ground dust is to gather loose particles by rubbing the can on the ground surface and collect loose particles. One issue with this method is the possibility of gathering particles in the subsurface that are not exposed to dust generation. It might contain a lower particle circularity and the method has no filtration of the coarsest sand particles and stones. For this reason, only about 0.1 l out of 0.85 l of ground dust from Jordan II was left after sieving. By using a vacuum cleaner instead, the limited suction force facilitates a natural filtration of small stones in the sample. Even though it takes longer time, the vacuum cleaner could acquire fine particle sized ground dust, since coarse sand particles and stones are not collected due to the limited suction force. For all types of ground dust tested in this work, using a vacuum cleaner similar to Kärcher HV 1/1 Bp Fs is assessed to be the best choice.

5.4.2 Optimizing laboratory measurements

This pioneer study of dust characteristics and optical properties is meant to pave the way for future work. Thus, several improvements with regards to determination of chemical composition, assessments of particle shape and size distribution, transmission estimation and sieving for later laboratory studies were identified. They are discussed in the following subsections.

5.4.2.1 Improvements for chemical analysis: X-Ray powder Diffraction (XRD)

As the discussion in section 5.2.2 highlighted, it is difficult to base conclusions on the correlation between panel dust and ground dust as long as only element ratios and no minerals are known. With knowledge over minerals present in the panel dust and in the ground, better assessments could be made on the correlation between them. It is proposed to use an X-Ray powder Diffraction (XRD) device, with which it is possible to determine the chemical composition and, if needed, the crystalline structure of the minerals [97]. It can provide an unambiguous mineral determination in less than 20 minutes [97].

5.4.2.2 Optimized particle size distribution measurements

In the way the DLS device was used to find the particle size distribution gave inadequate results. Since this parameter is proven to be the most important determinant for transmission loss, an improvement of the grain size assessments is required. To combat the sedimentation during particle size measurements water soluble dispersants, such as polyphosphate, polymers or surfactants could enhance the dissolvement of particles. These disperants are able to prevent dust particles to agglomerate and enable them to remain suspended in the stirred solution throughout the duration of the measurement. Ultimately, this will decrease the sedimentation and give improved results.

A focused beam reflectance measurement (FBRM) device is another option for dust particle size distribution. A "ParticleTrack" device by Mettler Toledo is constructed in a way that easily can be lowered into a stirred solution and measure the particle size distribution over time [98]. It can measure particles in a range from 0.5 – 1000 μm, which agrees to the normal size distribution of the presented dust types above. In addition, this device ostensibly also measures the particle shape. It has therefore the potential of providing values on particle shape with a lower uncertainty than presented above. Finally, "ParticleTrack" can also be deployed in situ, which is a great advantage with regards to a fast response of soiling in combination with a model that can predict effects on transmission based on particle size distribution and other parameters.

5.4.2.3 A model for estimation of transmission loss by soiling

This pioneer study has been able to determine two statistically significant parameters for computation of the transmission loss. In addition, the iron oxide content might play a subordinate role. Through more data from other dust types a robust model can be established, that can compute the transmission of sunlight purely based on particle size distribution, albedo and other possible influencing factors, like iron oxide content. This model would provide a better approximation of the α-coefficient. By using Lambert-Beers law (ref. eq. 13) and the estimated α-coefficient, a transmission curve of new collected dust samples can be modelled. This could save both time and money, since a transmission measurement is a time-consuming experiment. In addition, it could deliver a fast response to the decision makers with regards to the severity of the potential soiling loss in a region.

5.4.2.4 Sieving optimization

Results from the proposed model mentioned above could be verified with ground dust in locations with barren vegetation. However, due to the strong dependency on particle size distribution, a verification with ground dust requires a better sieving technique. In this work, it has been tried to use a simple sieving method, with only one sieve that was supposed to exclude all ground dust

particles above the largest particle size found in the panel dust. This proved, however, to be inaccurate, as seen in all particle size distribution curves: None of the ground dust samples duplicated the particle size distribution of the panel dust from the same location. The identified particle size distribution of the panel dust in mass percentage should lay the baseline for sieving topsoil dust. The resulting correlation between the size distributions of the ground and panel dust depends on how fine the sieving intervals are selected.

5.4.3 Summary on a standard procedure for evaluating new potential locations

For an intended new establishment of a solar power plant, a PV module cover plate should be set up for investigation of the deposited dust for a certain duration. Only about 5 ml of dust is required for size distribution measurements alongside visual and chemical analysis. By benefitting from the proposed standard collection method for low dust densities (section 5.4.1.1) the required time frame could be down to weeks or days depending on the size of the panel, weather conditions and PM concentration in the air. Before evaporation of the water during sampling, the particle size distribution can be measured with a focused beam reflectance device. When the dust has been dried, the albedo can be calculated using ImageJ and the chemical composition is found by XRD. Values on particle size, albedo and iron oxide could then be fed into a model, which gives a first estimate of the transmission loss due to soiling. The model could be verified with sieved topsoil from the ground nearby if the power plant is to be established in an open, barren landscape.

One might think that a PV cover plate for collection of panel dust could be replaced with simple PM measurements to understand what particles that would deposit on the panel. This method has unfortunately proved insufficient, since the PM measurement devices are often constructed for particles up to 10 μm in diameter [62]. This study, however, has uncovered that particles above 10 μm are responsible for the largest volume fraction for all the dust types analyzed. When tried to modify the PM measurement apparatus for higher dust particle sizes, a problem with particles stuck in the device has been encountered [62]. Therefore, PM measurements are still immature for panel dust particle size estimations.

5.5 Error analysis

During the field- and laboratory work, several errors have been identified that should be accounted for in future studies of dust characteristics and transmission effects. Some of the known concerns prior to the measurements have already been listed in chapter 4. In the following subchapter the most severe errors discovered during the laboratory work are assessed including suggestions for solutions to the problems.

5.5.1 Contamination of Rwanda I panel dust

Due to the low density of dust on the PV panels in Rwanda, a cotton piece was used to collect particles for characterization. Upon extraction of the dust from the cloth in the laboratory, textile pieces were also scratched free alongside the dust (figure 5.32).

Figure 5.32: The collected dust with cloths from Rwanda I contaminated the samples significantly. The two large particles visible in the picture are clearly from a cloth and has a high value of carbon compared to the identified dust particles. Also, other particles with irregular shape is believed to be pieces of cotton.

When introduced in the sample, it was impossible to separate these loose pieces from the dust at a later point in time. The contamination of cotton pieces disturbed the entire dust characterization analysis, yet the particle size distribution was most severely affected. Without any chance of excluding the textile pieces in the analysis, it followed that the dynamic light scattering (DLS) device found evidence of particles up to 2 mm in diameter. This is way coarser than any other panel dust sample, and not possible considering the weather conditions at the time of collection: The tropical rain showers that frequently occurred during the rainy season would easily have washed such coarse particles off the cover plate. Consequently, the de facto particle size distribution of panel dust from Rwanda I remains unknown and the results above give only a vague indication of the composition. Since the particle size distribution of the panel dust from Rwanda I couldn't be identified, this had implications for the sieving of the ground dust from Rwanda I as well. Without knowing the maximal particle size of the panel dust, a best guess of 80 μm was decided. In short, the contamination of textile pieces in the panel dust from Rwanda I had huge implications for the size distribution.

Moreover, the pollution of cloth pieces had also a significant effect on the analyses of the chemical composition. Some of the images taken with SEM clearly contained particles that looked like originating from textile substance and these were easy to exclude in the analyses. Yet other particles were hard to determine whether they were real dust particles or from the cloth. Whenever the

point analyses with EDS showed an abnormally high content of carbon, it was suspected to be a cotton piece and excluded in the further analysis. However, it is possible that natural dust from the vegetation like pollen, fibers and spores were avoided in fear of analyzing a cotton piece. Consequently, the carbon content of panel dust could, in reality, be either higher or lower than shown in figure 5.14.

The particle shape analysis of the contaminated panel dust from Rwanda I was also challenging to master. An image had to be taken with SEM that showed a significant number of particles, but at the same time contained as few pieces as possible, that were assumed to be extracted from the cloth. Figure 5.33 shows an example of one SEM image of panel dust from Rwanda I that was used for shape analysis. Contamination of cotton pieces in this picture cannot be ruled out, but if present, they appear with similar shape as the dust particles. In this way it would not alter the shape analysis result in a very significant way.

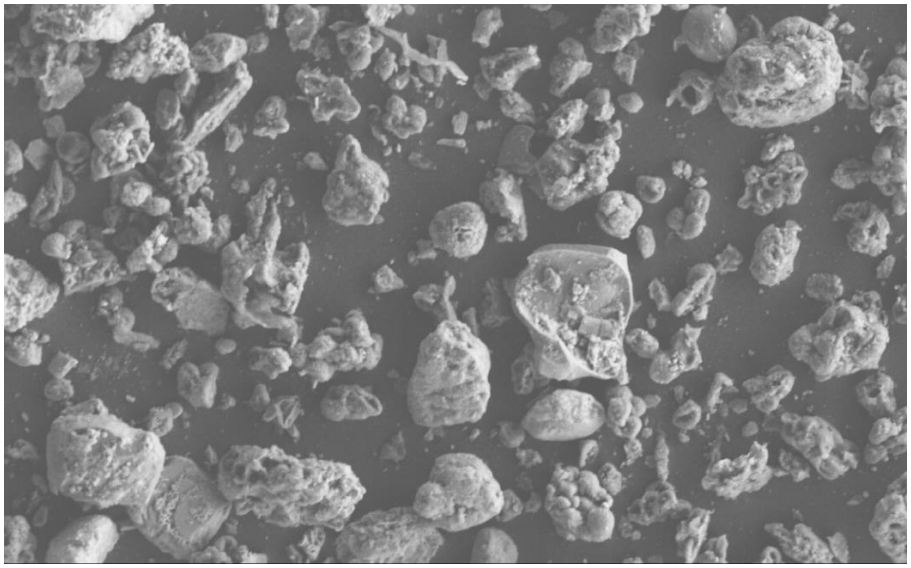

Figure 5.33: An example of one picture of Rwanda I panel dust that was processed further with ImageJ to analyze the particle shape

5.5.2 Errors related to particle size distribution analysis with DLS

The DLS device is based on light that is polarized by particles dissolved in water. This device assumes spherical particles, which is a crucial source of failure that has already been thoroughly discussed in section 4.3.5.1 above and will not be further elaborated.

There are two additional major error sources related to this device when examining dust particles. Firstly, larger grains have problems with sedimentation during the analysis despite the continuous mixing of the sample. Each of the three consecutive measurements needs approximately 30 seconds, which adds up to a total of at least 1.5 minutes. This is enough time for the largest particles to sediment throughout the experiment and a drop in volume percentage of the largest particles can be identified between the three measurements. Furthermore, a decrease in percentage of

large particles leads to an increase in the content of the smaller particles. For this reason, no more than 3 measurements were done after the stirring of the sample, and for most of the dust types only minor changes were identified. Nevertheless, ground dust from Jordan I and Jordan II had clear drops in volume percentage for particles above 40 µm and the measurement had to be repeated several times to reach a satisfying result.

Second, agglomeration of particles can affect the results, since the device would read clusters of particles as one big particle. This could mean that the share of large particles would go up and lead to a lower percentage of small particles than in reality. Moreover, formed clusters would additionally have a higher likelihood of sedimentation, which again would affect the results as described above.

Due to the significant uncertainties with DLS and the strong correlation between the particle size distribution of a dust sample and its transmission of light, ameliorations were suggested above (section 5.4.2.2).

5.5.3 Errors related to particle shape analysis in ImageJ

A significant problem with the particle shape analysis of SEM pictures with ImageJ was related to the selected zoom of the image and the particle size distribution of the dust sample. In general, ImageJ undoubtedly assesses small particles on a picture to be more circular by than larger ones. The reason for this inconsistency is due to the much finer resolved border lines of large particles compared to small particles (example in figure 5.34), which leads to a high value for circumference in comparison to its surface area. Consequently, the circularity will go down for images with a large portion of coarse particles. As a result of this error, it is no surprise that the finest dust samples, like cement and panel dust from Jordan I and Egypt I, have the highest measured circularity ratios.

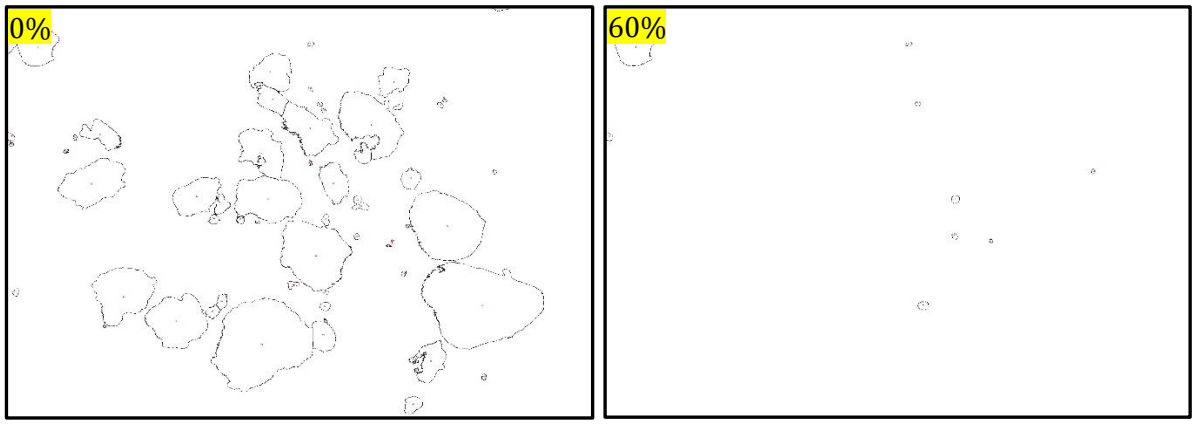

Figure 5.34: The circumference of large particles is finer resoluted than the small particles and so they are assessed to be less circular. The left picture shows all particles present in ImageJ, and the right image has excluded all particles with less than 60% circularity.

Unfortunately, this error is impossible to quantify, and should therefore be avoided in precise measurements of the particle shape. Since big particles on images can be achieved by either a large particle size or an enlarged image, the outcomes from this analysis are therefore heavily dependent on both of these inputs. It further implies that it could be possible to use the zooming feature in SEM to adjust the images so that particles with different size appear similar on the images. This would require a very time consuming, neat work, but likely still be prone to error. It could be better accomplished with the focused beam reflector device presented in section 5.4.2.2 above.

6 Conclusions

Soiling on the PV cover glass plate leads to unwanted attenuation of the total solar irradiation. This comprehensive study of soiling effects on solar electricity production in utility scale solar power parks raises awareness of the important characteristics of dust particles that deposit on solar modules and their impact on transmission of sunlight. The literature review on soiling defined dust as particles with diameters mainly in the range between 1 µm and 100 µm. They often contain elements from minerals most abundant in nature such as silicon, oxygen, carbon, calcium, aluminum, potassium and iron. The review further structured the complex interactions of particulate matter with natural and anthropogenic factors into five steps in a dust life cycle: Generation, transport, deposition, adhesion and removal. It is obvious that the local climate has a huge impact on the entire life cycle. The review concluded that soiling mainly affects current through attenuated direct solar insolation alongside an indirect reduction in voltage through an increased cell temperature.

The results from the experimental part of the study have shown evidence for a strong correlation between topsoil and panel dust in open, barren and arid landscapes. In the blooming season in vegetated areas, the picture is more unclear, but the chemical analyses indicated a higher carbon content in the panel dust than in the topsoil. This was further supported by a deviation in visual appearance: A dark brown, almost black color of panel dust could indicate contamination of organic matter. Additionally, the suspended topsoil dust is likely intercepted by the vegetation and instead, the accumulated soiling on the panels is dominated by pollen and spores.

The dust characterization analyses of the soiling have indicated a range in particle size distribution of approximately 0.3 – 120 µm, where particles between 10 – 30 µm dominate the volumetric response for all samples. Values for albedo are varying between 0.36 – 0.50 in desert areas, whereas a considerably lower value of 0.14 was obtained for panel dust in a vegetated location. The transmission measurements of soiling have been expressed through the slope coefficient of a fitted exponential function to the data points. Panel dust from arid landscapes exhibited α-coefficients in the range 0.0309 – 0.0203 m^2/g. This implies that a common soiling layer of 5 g/m^2

would lead to a transmission loss of approximately 14.3% in in the worst case compared to ca 9.7% in the best case. Such a difference of almost 5% is substantial for a utility-scale power plant. Under equal weather conditions a dust type with a high α-coefficient connotes a higher frequency of cleaning the modules in order not to lose income due to increased attenuation of the sunlight. Additionally, cleaning fine particles is more cumbersome than coarser ones, due to the higher adhesion of fine grains. Water is then most probably required in order to wash the panels successfully, which in a desert area is a highly valuable resource. In either case, the non-trivial increased costs on the basis of a strong attenuating dust type should boost the motivation for an assessment of the local dust type prior to an establishment of a PV power station.

The analysis of the correlation between dust characteristics and transmission of sunlight has revealed a strong dependency on the particle size distribution. The smaller the particles, the more efficient they fill the voids between the grains and attenuate the sunlight. Larger particles rather tend to build up higher and leave pockets for the sunlight to penetrate the PV cover glass. Additionally, the transmission of light through soiling depends on the albedo and iron content. Darker dust types will absorb more light than brighter colors, which rather scatter the sunlight by Mie scattering pattern. A higher iron oxide content is also believed to increase the absorption, but this research is insufficient to firmly conclude a significant impact by this parameter and more data is required. The study has also revealed a spectral difference in the attenuation of sunlight for all dust types considered: Higher energetic light at wavelengths of about 400 nm are more attenuated than near infrared light.

Lastly, the thesis suggested a standard method for estimation of a potential solar power plant ex ante establishment. A panel should be set up for roughly a week and panel dust can be collected with a squeegee and a water spray gun. Focused beam reflectance measurements (FBRM) can be conducted in situ, which provides the particle size distribution of the dust collected. Next, the albedo and iron oxide content can be measured using ImageJ and XRD respectively. Feeding these three parameters into a transmission model developed on the basis of this and future research on transmission can give an assessment of the attenuation of sunlight as a function of dust density. The model could be verified with ground dust, if the park is to be established in an open, barren landscape. What remains is to identify what the normal dust density (soiling ratio) is for a given location, which must be estimated by evaluating all the influencing factors of the dust life cycle described in chapter 3.

7 Future work

The purpose of this dissertation was to understand the relationship between ground dust and panel dust, as well as detecting which dust characteristics that are correlated with transmission loss of sunlight. The research has established a standard proposed method for collection of dust and evaluation of soiling loss prior to installation of a utility scale solar power park. The following themes are proposed based on the outcome of this thesis:

- Field work: Verifying the new proposed collection method for low densities of dust.
- Conduct the same dust characteristics and transmission analyses to attain more data for establishment of a model which can predict transmission loss as a function of density of dust for all dust types.
- Discover and quantify the dependency on albedo and iron oxide content for transmission loss by using artificial dust samples with equal particle size distribution.
- Study of the impact on heterogeneity in the particle size distribution and impacts on the transmission loss.

References

1. IPCC, *Summary for Policymakers*, in: MASSON-DELMOTTE V./ZHAI P./PÖRTNER H.-O./ROBERTS D./SKEA J./SHUKLA P. R./PIRANI A./MOUFOUMA-OKIA W./PÉAN R. P., C./CONNORS S./MATTHEWS J. B. R./CHEN Y./ZHOU X./GOMIS M. I./LONNOY E./MAYCOCK T./TIGNOR M./WATERFIELD T. (eds.), Global Warming of 1.5°C. An IPCC Special Report on the impacts of global warming of 1.5°C above pre-industrial levels and related global greenhouse gas emission pathways, in the context of strengthening the global response to the threat of climate change, sustainable development, and efforts to eradicate poverty, Geneva: World Meteorological Organization,2018, pp. 32.

2. IEA, *World Energy Outlook 2018, Executive Summary,* France, 2018.

3. BEYOND PETROLIUM, *BP Energy Outlook,* London, 2019.

4. ZAIHIDEE F. M., MEKHILEF S., SEYEDMAHMOUDIAN M. and HORAN B., *Dust as an unalterable deteriorative factor affecting PV panel's efficiency: Why and how,* Renewable and Sustainable Energy Reviews, 2016, **65**(1): p. 1267-1278.

5. MERAL M. E. & DINÇER F., *A review of the factors affecting operation and efficiency of photovoltaic based electricity generation systems,* Renewable and Sustainable Energy Reviews, 2011, **15**(5): p. 2176-2184.

6. HAMMAD B., AL–ABED M., AL–GHANDOOR A., AL–SARDEAH A. and AL–BASHIR A., *Modeling and analysis of dust and temperature effects on photovoltaic systems' performance and optimal cleaning frequency: Jordan case study,* Renewable and Sustainable Energy Reviews, 2018, **82**(1): p. 2218-2234.

7. SMEETS A., JÄGER K., OLINDO I., VAN SWAAIJ R. and ZEMAN M., *Solar Energy: The Physics and Engineering of Photovoltaic Conversion Technologies and Systems,* Cambridge: UIT Cambridge, 2016.

8. HONSBERG C. & BOWDEN S., *PV Education*, 2013, last updated: 28.02.2019, available from: https://www.pveducation.org/ (cited: 23.04.2019).

9. IEA, *Solar Energy*, 2019, last updated: 19.02.2019, available from: https://www.iea.org/topics/renewables/solar/ (cited: 20.02.2019).

10. MUNSELL M., *Global Solar PV Installations to Surpass 104GW in 2018* 2018, last updated: 16.04.2018, available from: https://www.greentechmedia.com/articles/read/global-solar-pv-installations-to-surpass-104-gw-in-2018#gs.a9r9SZTM (cited: 20.02.2019).

11. IEA, *Renewables 2018 - Analysis and Forecasts to 2023,* France, 2018.

12. SHOCKLEY W. & QUEISSER H. J., *Detailed Balance Limit of Efficiency of p-n Junction Solar Cells,* Journal of Applied Physics, 1961, **32**(3): p. 510-519.

13. MAGHAMI M. R., HIZAM H., GOMES C., RADZI M. A., REZADAD M. I. and HAJIGHORBANI S., *Power loss due to soiling on solar panel: A review,* Renewable and Sustainable Energy Reviews, 2016, **59**(1): p. 1307-1316.

14. LAWSON B., *Hydroelectric Power*, Encyclopedia: Electropedia, 2005, last updated: 21.11.2018, available from: https://www.mpoweruk.com/hydro_power.htm#top (cited: 20.07.2018).

15. COSTA S. C. S., DINIZ A. S. A. C. and KAZMERSKI L. L., *Dust and soiling issues and impacts relating to solar energy systems: Literature review update for 2012–2015,* Renewable and Sustainable Energy Reviews, 2016, **63**(1): p. 33-61.

16. GHAZI S., SAYIGH A. and KENNETH I., *Dust effecton flat surfaces - A review paper,* Renewable and Sustainable Energy Reviews, 2014, **33**(1): p. 742–751.

17. KALDELLIS J. K. & FRAGOS P., *Ash deposition impact on the energy performance of photovoltaic generators,* Journal of Cleaner Production, 2011, **19**(4): p. 311-317.

18. SCATEC SOLAR, *Our portfolio*, 2019, available from: https://www.scatecsolar.com/Portfolio (cited: 15.03.2019).

19. CONCEIÇÃO R., SILVA H. G., MIRÃO J., GOSTEIN M., FIALHO L., NARVARTE L. and COLLARES-PEREIRA M., *Saharan dust transport to Europe and its impact on photovoltaic performance: A case study of soiling in Portugal,* Solar Energy, 2018, **160**(1): p. 94-102.

20. ABDERREZEK M. & FATHI M., *Experimental study of the dust effect on photovoltaic panels' energy yield,* Solar Energy, 2017, **142**(1): p. 308-320.

21. APPELS R., LEFEVRE B., HERTELEER B., GOVERDE H., BEERTEN A., PAESEN R., DE MEDTS K., DRIESEN J. and POORTMANS J., *Effect of soiling on photovoltaic modules,* Solar Energy, 2013, **96**(1): p. 283-291.

22. EL-SHOBOKSHY M. S. & HUSSEIN F. M., *Effect of dust with different physical properties on the performance of photovoltaic cells,* Solar Energy, 1993, **51**(6): p. 505-511.

23. KALDELLIS J. K., FRAGOS P. and KAPSALI M., *Systematic experimental study of the pollution deposition impact on the energy yield of photovoltaic installations,* Renewable Energy, 2011, **36**(10): p. 2717-2724.

24. ADINOYI M. J. & SAID S. A. M., *Effect of dust accumulation on the power outputs of solar photovoltaic modules,* Renewable Energy, 2013, **60**(1): p. 633-636.

25. AL-HASAN A. Y., *A new correlation for direct beam solar radiation received by photovoltaic panel with sand dust accumulated on its surface,* Solar Energy, 1998, **63**(5): p. 323-333.

26. ALFARO S. C., CHABAS A., LOMBARDO T., VERNEY-CARRON A. and AUSSET P., *Predicting the soiling of modern glass in urban environments: A new physically-based model,* Atmospheric Environment, 2012, **60**(1): p. 348-357.

27. SMITH M. K., WAMSER C. C., JAMES K. E., MOODY S., SAILOR D. J. and ROSENSTIEL T. N., *Effects of Natural and Manual Cleaning on Photovoltaic Output,* Journal of Solar Energy Engineering, 2013, **135**(3): p. 034505.

28. HEE J. Y., KUMAR L. V., DANNER A. J., YANG H. and BHATIA C. S., *The Effect of Dust on Transmission and Self-cleaning Property of Solar Panels,* Energy Procedia, 2012, **15**(1): p. 421-427.

29. FIGGIS B., ENNAOUI A., AHZI S. and RÉMOND Y., *Review of PV soiling particle mechanics in desert environments,* Renewable and Sustainable Energy Reviews, 2017, **76**(1): p. 872-881.

30. GUO B., FIGGIS B., JAVED W. and MIRZA T., *Effect of Dust and Weather Conditions on Photovoltaic Performance in Doha, Qatar*, in: IEEE, 2015 First Workshop on Smart Grid and Renewable Energy (SGRE), Doha, Qatar, 2015, pp. 7.

31. SANDSTAD J., *Elektromagnetisk stråling*, 2018, last updated: 13.11.2018, available from: https://snl.no/elektromagnetisk_str%C3%A5ling (cited: 17.04.2019).

32. MCINTOSH K., ABBOTT M. and SUDBURY B., *The solar spectrum: Atmospheric influences*, 2011, available from: https://www2.pvlighthouse.com.au/resources/courses/altermatt/The%20Solar%20Spectrum/Two%20mechanisms%20for%20atmospheric%20absorption%20of%20sunlight.aspx (cited: 09.07.2019).

33. NORTH CAROLINA CLIMATE OFFICE, *Albedo*, 2013, available from: https://climate.ncsu.edu/edu/Albedo (cited: 04.08.2019).

34. TAHA H., SAILOR D. and AKBARI H., *High-Albedo Materials for Reducing Building Cooling Energy Use,* Lawrence Berkeley Laboratory, University of California, Berkeley, CA, 1992.

35. ABDULSALAM G. A. & KHALEEL S. A., *Free Space Optical Communications - Theory and Practices*, in: MUTAMED K. (eds.), Wireless Communication, London: IntechOpen,2014, pp. 54.

36. LOCKWOOD D. J., *Rayleigh and Mie Scattering*, Encyclopedia: Encyclopedia of Color Science and Technology, 2016, last updated: 05.07.2016, available from: https://link.springer.com/content/pdf/10.1007%2F978-3-642-27851-8_218-2.pdf (cited: 24.06.2019).

37. ZUCCONI A., *The Mathematics of Rayleigh Scattering*, 2017, last updated: 10.10.2017, available from: https://www.alanzucconi.com/2017/10/10/atmospheric-scattering-3/ (cited: 25.06.2019).

38. DICK Ø. B., *Mie-spredning*, Encyclopedia: Store Norske Leksikon, 2018, last updated: 20.02.2018, available from: https://snl.no/mie-spredning (cited: 25.06.2019).

39. GISLÉN L., *Mie Theory*, Lund: University L., 2007, available from: http://home.thep.lu.se/~larsg/Site/MieTheory.pdf (cited: 25.06.2019).

40. ALFARO S. C., LAFON S., RAJOT J. L., FORMENTI P., GAUDICHET A. and MAILLE M., *Iron oxides and light absorption by pure desert dust: An experimental study,* Journal of geological research, 2004, **109**(D8): p. 8208-8217.

41. KAUFMANN Y. J., TANRÉ D., DUBOVIK O., KARNIELI A. and REMER L. A., *Absorption of sunlight by dust as inferred from satellite and ground-based remote sensing,* Geophysical research letters, 2001, **28**(8): p. 4.

42. NREL, *Best Research-Cell Efficiencies*, 2018, last updated: 26.11.2018, available from: https://www.nrel.gov/pv/assets/images/efficiency-chart.png (cited: 15.04.2019).

43. JESTIN Y., *Down-Shifting of the Incident Light for Photovoltaic Applications,* Comprehensive Renewable Energy, 2012, **1**(1): p. 563-585.

44. KUMAR E. S., SARKAR D. B. and BEHERA D. K., *Soiling and Dust Impact on the Efficiency and the Maximum Power Point in the Photovoltaic Modules,* International Journal of Engineering Research & Technology (IJERT), 2013, **2**(2): p. 1-9.

45. GOOSSENS D. & VAN KERSCHAEVER E., *Aeolian dust deposition on photovoltaic solar cells: The effects of wind velocity and airborne dust concentration on cell performance,* Solar Energy, 1999, **66**(4): p. 277-289.

46. JAVED W., WUBULIKASIMU Y., FIGGIS B. and GUO B., *Characterization of dust accumulated on photovoltaic panels in Doha, Qatar,* Solar Energy, 2017, **142**(1): p. 123-135.

47. JOHN J. J., WARADE S., KUMAR A. and KOTTANTHARAYIL A., *Evaluation and Prediction of Soiling Loss on PV modules with Artificially Deposited Dust*, in: IEEE, 42nd Photovoltaic Specialist Conference, New Orleans, 2015, pp. 3.

48. MANI M. & PILLAI R., *Impact of dust on solar photovoltaic (PV) performance: Research status, challenges and recommendations,* Renewable and Sustainable Energy Reviews, 2010, **14**(9): p. 3124-3131.

49. PICOTTI G., BORGHESANI P., CHOLETTE M. E. and MANZOLINI G., *Soiling of solar collectors – Modelling approaches for airborne dust and its interactions with surfaces,* Renewable and Sustainable Energy Reviews, 2018, **81**(1): p. 2343-2357.

50. MASTEKBAYEVA G. A. & KUMAR S., *Effect of dust on the transmittance of low density polyethylene glazing in a tropical climate,* Solar Energy, 2000, **68**(2): p. 135-141.

51. GAIER J. R. & PEREZ-DAVIS M. E., *Effect of Particle Size of Martian Dust on the Degradation of Photovoltaic Cell Performance*, in: NASA LEWIS RESEARCH CENTER CLEVELAND, Solar Energy Conference, Hawaii, USA, 1992, pp. 17.

52. CABANILLAS R. E. & MUNGUÍA H., *Dust accumulation effect on efficiency of Si photovoltaic modules,* Journal of Renewable and Sustainable Energy, 2011, **3**(4): p. 043114.043111 - 043114.043110.

53. LAWRENCE C. R. & NEFF J. C., *The contemporary physical and chemical flux of aeolian dust: A synthesis of direct measurements of dust deposition,* Chemical Geology, 2009, **267**(1): p. 46–63.

54. DARWISH Z. A., KAZEM H. A., SOPIAN K., AL-GOUL M. A. and ALAWADHI H., *Effect of dust pollutant type on photovoltaic performance,* Renewable and Sustainable Energy Reviews, 2015, **41**(1): p. 735-744.

55. ILSE K. K., RABANAL J., SCHONLEBER L., KHAN M. Z., NAUMANN V., HAGENDORF C. and BAGDAHN J., *Comparing Indoor and Outdoor Soiling Experiments for Different Glass Coatings and Microstructural Analysis of Particle Caking Processes,* Ieee Journal of Photovoltaics, 2018, **8**(1): p. 203-209.

56. SUGANDHA G., *9 Main Chemical Constituents of Pollen | Palynology*, 2018, available from: http://www.biologydiscussion.com/palynology/9-main-chemical-constituents-of-pollen-palynology/64405 (cited: 28.02.2019).

57. QASEM H., BETTS T. R., MÜLLEJANS H., ALBUSAIRI H. and GOTTSCHALG R., *Dust-induced shading on photovoltaic modules,* Progress in Photovoltaics: Research and Applications, 2014, **22**(2): p. 218-226.

58. JIANG H., LU L. and SUN K., *Experimental investigation of the impact of airborne dust deposition on the performance of solar photovoltaic (PV) modules,* Atmospheric Environment, 2011, **45**(25): p. 4299-4304.

59. JAVED W., GUO B. and FIGGIS B., *Modeling of photovoltaic soiling loss as a function of environmental variables,* Solar Energy, 2017, **157**(1): p. 397-407.

60. NAEEM M. & TAMIZHMANI G., *Climatological Relevance to the Soiling Loss of Photovoltaic Modules*, in: IEEE, 2015 Saudi Arabia Smart Grid Conference, Jeddah, Saudi-Arabia, 2015, pp. 5.

61. LUMEN LEARNING, *Weathering and Erosion*, 2018, available from: https://courses.lumenlearning.com/wmopen-geology/chapter/outcome-weathering-and-erosion/ (cited: 07.04.2019).

62. FIGGIS B., *Investigation of PV Soiling and Condensation in Desert Environments via Outdoor Microscopy,* Diss., Strasbourg: University of Strasbourg, 2018.

63. ILSE K. K., FIGGIS B. W., WERNER M., NAUMANN V., HAGENDORF C., PÖLLMANN H. and BAGDAHN J., *Comprehensive analysis of soiling and cementation processes on PV modules in Qatar,* Solar Energy Materials and Solar Cells, 2018, **186**(1): p. 309-323.

64. SAID S. A. M., HASSAN G., WALWIL H. M. and AL-AQEELI N., *The effect of environmental factors and dust accumulation on photovoltaic modules and dust-accumulation mitigation strategies,* Renewable and Sustainable Energy Reviews, 2018, **82**(1): p. 743-760.

65. BOYLE L., FLINCHPAUGH H. and HANNIGAN M., *Assessment of PM dry deposition on solar energy harvesting systems: Measurement–model comparison,* Aerosol Science and Technology, 2016, **50**(4): p. 380-391.

66. SAYYAH A., HORENSTEIN M. N. and MAZUMDER M. K., *Energy yield loss caused by dust deposition on photovoltaic panels,* Solar Energy, 2014, **107**(1): p. 576-604.

67. HEGAZY A. A., *Effect of dust accumulation on solar transmittance through glass covers of plate-type collectors,* Renewable Energy, 2001, **22**(4): p. 525-540.

68. BEATTIE N. S., MOIR R. S., CHACKO C., BUFFONI G., ROBERTS S. H. and PEARSALL N. M., *Understanding the effects of sand and dust accumulation on photovoltaic modules,* Renewable Energy, 2012, **48**(1): p. 448-452.

69. MAROUANI A., BOUAOUADJA N., CASTRO Y. and DURAN A., *Effect of the Sandstorms on the Solar Panels*, 2013, last updated: 25.02.2016, available from: http://www.isites.info/PastConferences/ISITES2013/ISITES2013/papers/A1-ISITES13089.pdf (cited: 23.04.2019).

70. CARON J. R. & LITTMANN B., *Direct Monitoring of Energy Lost Due to Soiling on First Solar Modules in California,* Ieee Journal of Photovoltaics, 2013, **3**(1): p. 336-340.

71. ZORRILLA-CASANOVA J., PILIOUGINE M., CARRETERO J., BERNAOLA P., CARPENA P., MORA-LÓPEZ L. and SIDRACH-DE-CARDONA M., *Analysis of dust losses in photovoltaic modules*, in: World Renewable Energy Congress, Linköping, Sweden, 2011, pp. 8.

72. ØGAARD M. B., *Effect of Soiling on the Performance of Photovoltaic Modules in Kalkbult, South Africa,* Diss., Grimenes A. A./Selj J., Ås: NMBU, 2016.

73. PEDERSEN H. B., *Experimental study of soiling on photovoltaic modules in a Nordic climate,* Diss., Grimenes A. A./Selj J., Ås: NMBU, 2015.

74. ELMINIR H. K., GHITAS A. E., HAMID R. H., EL-HUSSAINY F., BEHEARY M. M. and ABDEL-MONEIM K. M., *Effect of dust on the transparent cover of solar collectors,* Energy Conversion and Management, 2006, **47**(18): p. 3192-3203.

75. HAEBERLIN H. & GRAF J. D., *Gradual Reduction of PV Generator Yield due to Pollution*, in: 2nd World Conference on Photovoltaic Solar Energy Conversion, Vienna, Austria, 1998, pp. 4.

76. GARG H. P., *Effect of dirt on transparent covers in flat plate solar energy collectors. ,* Solar Energy, 1974, **15**(1): p. 299-302.

77. JIANG Y., LU L., FERRO A. R. and AHMADI G., *Analyzing wind cleaning process on the accumulated dust on solar photovoltaic (PV) modules on flat surfaces,* Solar Energy, 2018, **159**(1): p. 1031-1036.

78. LOPEZ-GARCIA J., POZZA A. and SAMPLE T., *Long-term soiling of silicon PV modules in a moderate subtropical climate,* Solar Energy, 2016, **130**(1): p. 174-183.

79. BURTON P. D., BOYLE L., GRIEGO J. J. M. and KING B. H., *Quantification of a Minimum Detectable Soiling Level to Affect Photovoltaic Devices by Natural and Simulated Soils,* Ieee Journal of Photovoltaics, 2015, **5**(4): p. 1143-1149.

80. TIAN W., WANG Y., REN J. and ZHU L., *Effect of urban climate on building integrated photovoltaics performance,* Energy Conversion and Management, 2007, **48**(1): p. 1-8.

81. PANG H., CLOSE J. and LAM K.-H., *Study on Effect of Urban Pollution to Performance of Commercial Copper Indium Diselenide Modules*, in: IEEE, 4th World Conference on Photovoltaic Energy Conference, Waikoloa, USA 2006, pp. 4.

82. BOYLE L., FLINCHPAUGH H. and HANNIGAN M., *Impact of Natural Soiling on the Transmission of PV Cover Plates*, in: IEEE, 39th Photovoltaic Specialists Conference (PVSC), Tampa, USA, 2013, pp. 3.

83. LEVINSON R., BERDAHL P., ASEFAWBERHE A. and AKBARI H., *Effects of soiling and cleaning on the reflectance and solar heat gain of a light-colored roofing membrane,* Atmospheric Environment, 2005, **39**(40): p. 7807-7824.

84. JOHN J. J., WARADE S., TAMIZHMANI G. and KOTTANTHARAYIL A., *Study of Soiling Loss on Photovoltaic Modules With Artificially Deposited Dust of Different Gravimetric Densities and Compositions Collected From Different Locations in India,* Ieee Journal of Photovoltaics, 2016, **6**(1): p. 236-243.

85. AL-HASAN A. Y. & GHONEIM A. A., *A new correlation between photovoltaic panel's efficiency and amount of sand dust accumulated on their surface,* International Journal of Sustainable Energy, 2005, **24**(4): p. 187-197.

86. BURTON P. D. & KING B. H., *Spectral Sensitivity of Simulated Photovoltaic Module Soiling for a Variety of Synthesized Soil Types,* Ieee Journal of Photovoltaics, 2014, **4**(3): p. 890 - 898.

87. IRVINE V. E., BICKERTON I. J. and JABER K. S. A., *Jordan*, 2019, last updated: 30.05.2019, available from: https://www.britannica.com/place/Jordan/media/1/306128/61343 (cited: 12.06.2019).

88. KONOPKA B., *Cairo on world map*, 2016, available from: https://pasarelapr.com/detail/cairo-on-world-map-21.html# (cited: 12.06.2019).

89. BRATBERG K. L. R., *Rwandas brutale historie*, 2019, last updated: 10.04.2019, available from: https://www.folkogforsvar.no/rwandas-brutale-historie/ (cited: 12.06.2019).

90. SKOMEDAL Å., HAUG H. and MARSTEIN E. S., *Endogenous Soiling Rate Determination and Detection of Cleaning Events in Utility-Scale PV Plants,* Ieee Journal of Photovoltaics, 2019, **9**(3): p. 858 - 863.

91. EXPERT AFRICA, *Rwanda Information - Weather & climate*, available from: https://www.expertafrica.com/rwanda/weather-and-climate (cited: 15.03.2019).

92. KESKI-KORSU M., *How to calculate albedo yourself?*, 2012, available from: http://albedodreams.info/how_to/how-to-calculate-albedo-yourself/ (cited: 18.07.2019).

93. PARTICLE ANALYTICAL, *Laserbeugung*, 2019, available from: https://particle.dk/de/laserbeugung/ (cited: 26.04.2019).

94. SWEENEY A., WEST R. P. and O'CONNOR C., *Parameters affecting the albedo effect in concrete* Dublin: Trinity College, 2011, **2**: p. 1-8.

95. PERLIN J., *Keeping cool with the albedo effect*, Pacific Standard, 2009, available from: https://psmag.com/environment/keeping-cool-with-the-albedo-effect-3837 (cited: 15.07.2019).

96. ABBOTT R. N. J., CALLAHAN J. E., COWAN E. A., MCKINNEY F. K., MCKINNEY M., RAYMOND L. A. and WEBB F., *Common Rock-Forming Minerals: Identification*, 2000, available from: http://www.appstate.edu/~abbottrn/mnrl-id/ (cited: 19.06.2019).

97. DUTROW B. L. & CLARK C. M., *X-ray Powder Diffraction (XRD)*, 2019, last updated: 05.04.2019, available from: https://serc.carleton.edu/research_education/geochemsheets/techniques/XRD.html (cited: 19.06.2019).

98. METTLER TOLEDO, *Real Time Particle Size & Count Analysis*, 2016, last updated: 12.01.2016, available from: https://www.mt.com/es/en/home/products/L1_AutochemProducts/FBRM-PVM-Particle-System-Characterization/FBRM.html (cited: 31.07.2019).

Appendix

A Fresnel's equations and reflectivity

The Fresnel's equations on polarized light are given in equations 30 – 33:

30) $t_s = \frac{2n_1 \sin\theta}{n_1 \cos\theta + n_2 \cos\theta_t}$

31) $r_s = \frac{n_1 \sin\theta - n_2 \cos\theta_t}{n_1 \cos\theta + n_2 \cos\theta_t}$

32) $t_p = \frac{2n_1 \sin\theta}{n_1 \cos\theta_t + n_2 \cos\theta}$

33) $r_p = \frac{n_1 \sin\theta_t - n_2 \cos\theta}{n_1 \cos\theta_t + n_2 \cos\theta}$,

where n_1 and n_2 represent the refractive index from medium 1 and 2 respectively. θ and θ_t is the angles of incoming and transmitted light respectively. For unpolarized light, the reflectivity (R) equals the mean of the two polarizations:

34) $R = \frac{1}{2}\left(r_s^2 + r_p^2\right)$

B Saturation current density (J_0)

The saturation current density (J_0) is given by

$$35)\ J_0 = qn_i^2\left(\frac{D_N}{L_N+N_A}+\frac{D_P}{L_P N_D}\right),$$

and has the unit A/m^2. q is the elementary charge, n_i is the intrinsic carrier concentration. Important is the minority carrier diffusion coefficient (D) and the diffusion length (L) for electrons and holes respectively. N_A and N_D denote the density of acceptor and donor atoms respectively.

C Rwandan dust collection

A particulary interesting collection of Rwandan dust took place before and after the significant rain event that occurred on March 14th, 2019. The visual difference in figure C.1 likely indicates that water was needed for an efficient cleaning of the modules. The adhesion force was probably so high, that dry cleaning of the panels didn't yield a large amount of dust on the cloth.

Figure C.1: Difference between dust cleaned with a cloth before (left) and after (right) the rainfall on March 14th at Rwanda I power plant.

D Densities for transmission measurement

The densities for every transmission measurement are given in table D.1.

Table D.1: Overview of the different deposited densities of dust of all 7 dust types during transmission measurements. The uncertainty is 0.16 g/m² for each density.

Sample	Rwanda I	Jordan I		Jordan II		Egypt I		Cement
	Ground [g/m²]	Panel [g/m²]	Ground [g/m²]	Panel [g/m²]	Ground [g/m²]	Panel [g/m²]	Ground [g/m²]	[g/m²]
1	1.42	0.75	0.30	0.30	1.91	0.34	0.31	0.14
2	2.31	1.44	0.98	1.16	2.28	1.67	1.31	0.39
3	3.94	3.02	4.47	3.25	2.73	1.84	1.36	0.41
4	5.28	3.30	4.64	4.39	3.25	4.78	1.94	0.70
5	7.25	3.78	7.36	6.75	4.17	5.20	4.33	1.33
6	7.62	4.27	10.22	8.59	4.38	5.83	5.56	1.36
7	7.83	4.81	10.67	9.77	5.52	6.09	5.80	1.36
8	8.33	6.27	12.47	9.78	5.63	6.27	6.47	1.91
9	9.95	9.09	14.78	10.58	9.23	7.17	7.92	2.66
10	14.77	12.02	18.33	10.58	10.91	7.45	9.11	2.73
11	15.36	14.94	19.78	11.28	13.27	7.70	11.95	2.83
12	16.13	17.05	20.83	14.78	17.77	9.73	15.66	3.13
13	20.28	17.30	30.33	28.69	24.09	11.58	17.00	3.58
14	23.44	19.94	32.44	30.89	31.59	14.59	24.67	4.84
15	28.83	20.77	37.58	36.50	35.69	15.45	26.20	6.42
16	35.50	23.02	41.64	38.08	36.75	17.27	30.31	6.72
17	47.81	28.00	43.86	39.81	42.98	18.08	39.55	7.05
18	50.41	29.78	50.02	40.78	50.06	18.33	40.98	7.53
19	52.22	33.72	51.86	41.64	58.45	21.81	43.13	7.77
20	67.55	40.16	62.61	43.83	59.53	25.77	48.62	7.78
21	69.91	43.75	62.91	45.94	61.97	31.14	59.77	7.94
22	74.19	43.97	70.31	54.02	71.67	37.44	60.97	10.13
23	86.63	51.36	72.75	54.39	75.45	45.13	65.52	11.61
24	89.92	58.58	82.95	60.97	85.84	52.72	72.95	13.13
25	94.17	59.48	86.94	61.22	87.39	53.67	81.84	15.30
26	97.89	64.91	93.94	68.16	89.91	57.50	99.41	15.56
27	100.42	68.59	95.41	77.28	100.17	81.91	105.72	16.67
28	119.98	87.48	144.27	111.70	130.42	102.23	128.52	29.16
29	129.73	94.08	173.55	115.28	133.77	118.48	187.03	35.25
30	223.31	186.22	236.02	272.91	281.44	194.47	292.78	36.62
31								41.03
32								44.50
33								49.72

E Calculation of transmission loss

Ocean optics spectrometer yields 852 data points for one measurement ranging from 350 to 1000 µm wavelength. As visualized in figure 4.28, section 4.3.7, four measurements per deposited density were conducted. 30 different densities per dust sample in addition to one clean glass plate were measured from all 8 dust samples from the four locations. In addition, 33 densities of cement were measured, which gave a total of 961 000 data points. Needless to say, this had to be computed with a program designed for handling large data and Python was selected. The computation of the rawdata was done to create the graphs shown in the transmission results in subchapter 5.3 and in appendix F. In the following, the code from Python is given in full length:

```
from os import path
import numpy as np
import matplotlib.pyplot as plt
from matplotlib.ticker import ScalarFormatter
from scipy.optimize import curve_fit
from sklearn.metrics import r2_score

tms_aswan = []
tms_ejre = []
tms_oryx = []
tms_ground_aswan = []
tms_ground_ejre=[]
tms_ground_oryx=[]
tms_ground_asyv = []
tms_cement=[]

#open first files
rawdata_aswan = path.relpath("C:/Users/oysteino/Desktop/Solenergi/Rådata/
                             Transmisjon/ASWAN/20170922_1_ASWAN_
                             Transmission_Transmission_01.txt")
with open(rawdata_aswan, "r") as file:
    for line in file:
        tms_aswan.append(line.strip().split("\t"))
rawdata_ejre = path.relpath("C:/Users/oysteino/Desktop/Solenergi/Rådata/
                             Transmisjon/EJRE/20170922_1_EJRE_
                             Transmission_Transmission_01.txt")
with open(rawdata_ejre, "r") as file:
    for line in file:
        tms_ejre.append(line.strip().split("\t"))
rawdata_oryx = path.relpath("C:/Users/oysteino/Desktop/Solenergi/Rådata/
                             Transmisjon/ORYX/20170922_1_ORYX_
                             Transmission_Transmission_01.txt")
with open(rawdata_oryx, "r") as file:
    for line in file:
        tms_oryx.append(line.strip().split("\t"))
rawdata_ground_aswan = path.relpath("C:/Users/oysteino/Desktop/
                                    Solenergi/Rådata/Transmisjon/
                                    ASWAN_GROUND/20170922_1_
                                    ASWAN_GROUND_Transmission_
                                    Transmission_01.txt")
with open(rawdata_ground_aswan, "r") as file:
    for line in file:
        tms_ground_aswan.append(line.strip().split("\t"))
rawdata_ground_ejre = path.relpath("C:/Users/oysteino/Desktop/
```

```
                                        Solenergi/Rådata/Transmisjon/
                                        EJRE_GROUND/20170922_1_EJRE_GROUND_
                                        Transmission_Transmission_01.txt")
with open(rawdata_ground_ejre, "r") as file:
    for line in file:
        tms_ground_ejre.append(line.strip().split("\t"))
rawdata_ground_oryx = path.relpath("C:/Users/oysteino/Desktop/
                                        Solenergi/Rådata/Transmisjon/
                                        ORYX_GROUND/20170922_1_ORYX_GROUND_
                                        Transmission_Transmission_01.txt")
with open(rawdata_ground_oryx, "r") as file:
    for line in file:
        tms_ground_oryx.append(line.strip().split("\t"))
rawdata_ground_asyv = path.relpath("C:/Users/oysteino/Desktop/
                                        Solenergi/Rådata/Transmisjon/
                                        ASYV_GROUND/20170922_1_ASYV_GROUND_
                                        Transmission_Transmission_01.txt")
with open(rawdata_ground_asyv, "r") as file:
    for line in file:
        tms_ground_asyv.append(line.strip().split("\t"))
rawdata_cement=path.relpath("C:/Users/oysteino/Desktop/Solenergi/Rådata/
                            Transmisjon/Cement/20170922_1_CEMENT_
                            Transmission_Transmission_01.txt")
with open(rawdata_cement, "r") as file:
    for line in file:
        tms_cement.append(line.strip().split("\t"))


#Delete the first rows up to 350 nm
ind=tms_aswan.index(['350,115', '102,16'])
ind2=tms_aswan.index(['987,437', '1192,6'])-ind
for i in range((ind-1),-1,-1):
    tms_aswan.pop(i)
    tms_ejre.pop(i)
    tms_oryx.pop(i)
    tms_ground_aswan.pop(i)
    tms_ground_ejre.pop(i)
    tms_ground_oryx.pop(i)
    tms_ground_asyv.pop(i)
    tms_cement.pop(i)

# from string to float and replace comma with dot
for i in range (0,len(tms_aswan),1):
    for j in range (0, len(tms_aswan[i]),1):
        tms_aswan[i][j]=float(tms_aswan[i][j].replace(",","."))
        tms_ejre[i][j] = float(tms_ejre[i][j].replace(",", "."))
        tms_oryx[i][j] = float(tms_oryx[i][j].replace(",", "."))
        tms_ground_aswan[i][j] = float(tms_ground_aswan[i][j].replace(",",
                                        "."))
        tms_ground_ejre[i][j] = float(tms_ground_ejre[i][j].replace(",",
                                        "."))
        tms_ground_oryx[i][j] = float(tms_ground_oryx[i][j].replace(",",
                                        "."))
        tms_ground_asyv[i][j] = float(tms_ground_asyv[i][j].replace(",",
                                        "."))
        tms_cement[i][j] = float(tms_cement[i][j].replace(",", "."))


#adding all data from transmission measurements
for v in range (1,32,1):
    for u in range (1,5,1):
```

```
if v==1 and u==1:
    continue
else:
    temp=[]
    temp2=[]
    temp3=[]
    temp4=[]
    temp5=[]
    temp6=[]
    temp7=[]

    #open data as text files, and save them as strings
    x=["C:/Users/oysteino/Desktop/Solenergi/Rådata/Transmisjon/
       ASWAN/20170922_",v,"_ASWAN_Transmission_Transmission_0",
       u,".txt"]
    x[1]=str(x[1])
    x[3]=str(x[3])
    x=''.join(x)
    op=path.relpath(x)
    with open(op,"r") as fi:
        for li in fi:
            temp.append(li.strip().split("\t"))

    x=["C:/Users/oysteino/Desktop/Solenergi/Rådata/Transmisjon/
       EJRE/20170922_",v,"_EJRE_Transmission_Transmission_0",
       u,".txt"]
    x[1]=str(x[1])
    x[3]=str(x[3])
    x=''.join(x)
    op=path.relpath(x)
    with open(op,"r") as fi:
        for li in fi:
            temp2.append(li.strip().split("\t"))

    x=["C:/Users/oysteino/Desktop/Solenergi/Rådata/
       Transmisjon/ORYX/20170922_",v,"_ORYX_Transmission_
       Transmission_0",u,".txt"]
    x[1]=str(x[1])
    x[3]=str(x[3])
    x=''.join(x)
    op=path.relpath(x)
    with open(op,"r") as fi:
        for li in fi:
            temp3.append(li.strip().split("\t"))

    x=["C:/Users/oysteino/Desktop/Solenergi/Rådata/Transmisjon/
       ASWAN_GROUND/20170922_",v,"_ASWAN_GROUND_Transmission_
       Transmission_0",u,".txt"]
    x[1]=str(x[1])
    x[3]=str(x[3])
    x=''.join(x)
    op=path.relpath(x)
    with open(op,"r") as fi:
        for li in fi:
            temp4.append(li.strip().split("\t"))

    x=["C:/Users/oysteino/Desktop/Solenergi/Rådata/Transmisjon/
       EJRE_GROUND/20170922_",v,"_EJRE_GROUND_Transmission_
       Transmission_0",u,".txt"]
    x[1]=str(x[1])
    x[3]=str(x[3])
```

```
            x=''.join(x)
            op=path.relpath(x)
            with open(op,"r") as fi:
                for li in fi:
                    temp5.append(li.strip().split("\t"))

            x=["C:/Users/oysteino/Desktop/Solenergi/Rådata/Transmisjon/
               ORYX_GROUND/20170922_",v,"_ORYX_GROUND_Transmission_
               Transmission_0",u,".txt"]
            x[1]=str(x[1])
            x[3]=str(x[3])
            x=''.join(x)
            op=path.relpath(x)
            with open(op,"r") as fi:
                for li in fi:
                    temp6.append(li.strip().split("\t"))

            x=["C:/Users/oysteino/Desktop/Solenergi/Rådata/Transmisjon/
               ASYV_GROUND/20170922_",v,"_ASYV_GROUND_Transmission_
               Transmission_0",u,".txt"]
            x[1]=str(x[1])
            x[3]=str(x[3])
            x=''.join(x)
            op=path.relpath(x)
            with open(op,"r") as fi:
                for li in fi:
                    temp7.append(li.strip().split("\t"))

            # Delete the first rows up to 350 nm
            for i in range((ind - 1), -1, -1):
                temp.pop(i)
                temp2.pop(i)
                temp3.pop(i)
                temp4.pop(i)
                temp5.pop(i)
                temp6.pop(i)
                temp7.pop(i)

            # from string to float and replace comma with dot
            for i in range(0, len(temp), 1):
                for j in range(0, len(temp[i]), 1):
                    temp[i][j] = float(temp[i][j].replace(",", "."))
                    temp2[i][j] = float(temp2[i][j].replace(",", "."))
                    temp3[i][j] = float(temp3[i][j].replace(",", "."))
                    temp4[i][j] = float(temp4[i][j].replace(",", "."))
                    temp5[i][j] = float(temp5[i][j].replace(",", "."))
                    temp6[i][j] = float(temp6[i][j].replace(",", "."))
                    temp7[i][j] = float(temp7[i][j].replace(",", "."))

        # the data from all measurements in one array
        for i in range(0, len(tms_aswan), 1):
            tms_aswan[i].append(temp[i][1])
            tms_ejre[i].append(temp2[i][1])
            tms_oryx[i].append(temp3[i][1])
            tms_ground_aswan[i].append(temp4[i][1])
            tms_ground_ejre[i].append(temp5[i][1])
            tms_ground_oryx[i].append(temp6[i][1])
            tms_ground_asyv[i].append(temp7[i][1])

# since cement has 34 measurements and 13 measurements of a clean plate, it
must be treated separately
```

```
for v in range (1,35,1):
    if v==1:
        for u in range(2,14,1):
            temp=[]

            # open data as text files, and save them as strings
            x = ["C:/Users/oysteino/Desktop/Solenergi/Rådata/Transmi
                 sjon/Cement/20170922_", v,"_CEMENT_Transmission_Transmis
                 sion_0", u, ".txt"]
            x[1] = str(x[1])
            x[3] = str(x[3])
            x = ''.join(x)
            op = path.relpath(x)
            with open(op, "r") as fi:
                for li in fi:
                    temp.append(li.strip().split("\t"))
            #Delete first rows up to 350 nm
            for i in range((ind - 1), -1, -1):
                temp.pop(i)
            #From string to float and replace comma with dot
            for i in range(0, len(temp), 1):
                for j in range(0, len(temp[i]), 1):
                    temp[i][j] = float(temp[i][j].replace(",", "."))

            # the data from all measurements in one array
            for i in range(0, len(tms_cement), 1):
                tms_cement[i].append(temp[i][1])
    else:
        for u in range (1,5,1):

            temp=[]

            #open data as text files, and save them as strings
            x=["C:/Users/oysteino/Desktop/Solenergi/Rådata/Transmi
               sjon/Cement/20170922_", v,"_CEMENT_Transmission_Transmis
               sion_0", u, ".txt"]
            x[1]=str(x[1])
            x[3]=str(x[3])
            x=''.join(x)
            op=path.relpath(x)
            with open(op,"r") as fi:
                for li in fi:
                    temp.append(li.strip().split("\t"))

            #Delete first rows up to 350 nm
            for i in range((ind - 1), -1, -1):
                temp.pop(i)
            #From string to float and replace comma with dot
            for i in range(0, len(temp), 1):
                for j in range(0, len(temp[i]), 1):
                    temp[i][j] = float(temp[i][j].replace(",", "."))

            # the data from all measurements in one array
            for i in range(0, len(tms_cement), 1):
                tms_cement[i].append(temp[i][1])



#Take out 2 values that is disrupted in the data for all measurements
tms_aswan.pop(ind2)
tms_aswan.pop(ind2)
```

```
tms_ejre.pop(ind2)
tms_ejre.pop(ind2)
tms_oryx.pop(ind2)
tms_oryx.pop(ind2)
tms_ground_aswan.pop(ind2)
tms_ground_aswan.pop(ind2)
tms_ground_ejre.pop(ind2)
tms_ground_ejre.pop(ind2)
tms_ground_oryx.pop(ind2)
tms_ground_oryx.pop(ind2)
tms_ground_asyv.pop(ind2)
tms_ground_asyv.pop(ind2)
tms_cement.pop(ind2)
tms_cement.pop(ind2)

#---- tms is now a matrix with a vector of wavelengths on first column and
then raw data for all measurements on following
#---- columns. This means that four transmission measurements for a spe-
cific density is stacked up in columns after each other

# Take out wavelength and find indexes for bar charts
wavlen = []
temp=np.transpose(tms_aswan)
wavlen.append(temp[0][0:len(temp[0])])
wavlen=wavlen[0].tolist()
ind_wavlen400=wavlen.index(400.676)
ind_wavlen450=wavlen.index(450.154)
ind_wavlen500=wavlen.index(500.116)
ind_wavlen550=wavlen.index(550.546)
ind_wavlen600=wavlen.index(600.656)
ind_wavlen650=wavlen.index(650.442)
ind_wavlen700=wavlen.index(700.661)
ind_wavlen750=wavlen.index(750.54)
ind_wavlen800=wavlen.index(800.075)
ind_wavlen850=wavlen.index(850.005)
ind_wavlen900=wavlen.index(900.311)
ind_wavlen950=wavlen.index(950.24)
ind_wavlen998=wavlen.index(998.337)

# Averaging and finding standard deviation of the four transmission meas-
urements
avg_tms_aswan = np.zeros([len(tms_aswan),31])
std_tms_aswan = np.zeros([len(tms_aswan),31])
avg_tms_ejre = np.zeros([len(tms_ejre),31])
std_tms_ejre = np.zeros([len(tms_ejre),31])
avg_tms_oryx = np.zeros([len(tms_oryx),31])
std_tms_oryx = np.zeros([len(tms_oryx),31])
avg_tms_ground_aswan = np.zeros([len(tms_ground_aswan),31])
std_tms_ground_aswan = np.zeros([len(tms_ground_aswan),31])
avg_tms_ground_ejre = np.zeros([len(tms_ground_ejre),31])
std_tms_ground_ejre = np.zeros([len(tms_ground_ejre),31])
avg_tms_ground_oryx = np.zeros([len(tms_ground_oryx),31])
std_tms_ground_oryx = np.zeros([len(tms_ground_oryx),31])
avg_tms_ground_asyv = np.zeros([len(tms_ground_asyv),31])
std_tms_ground_asyv = np.zeros([len(tms_ground_asyv),31])
avg_tms_cement = np.zeros([len(tms_cement),34])
std_tms_cement = np.zeros([len(tms_cement),34])

for i in range(0, len(tms_aswan), 1):
    k = 0
    for j in range(1, len(tms_aswan[0]) - 3, 4):
```

```
        avg_tms_aswan[i][k] = sum(tms_aswan[i][j:j+4])/4
        std_tms_aswan[i][k] = np.std(tms_aswan[i][j:j+4])
        avg_tms_ejre[i][k] = sum(tms_ejre[i][j:j+4]) / 4
        std_tms_ejre[i][k] = np.std(tms_ejre[i][j:j+4])
        avg_tms_oryx[i][k] = sum(tms_oryx[i][j:j+4]) / 4
        std_tms_oryx[i][k] = np.std(tms_oryx[i][j:j+4])
        avg_tms_ground_aswan[i][k] = sum(tms_ground_aswan[i][j:j+4]) / 4
        std_tms_ground_aswan[i][k] = np.std(tms_ground_aswan[i][j:j+4])
        avg_tms_ground_ejre[i][k] = sum(tms_ground_ejre[i][j:j+4]) / 4
        std_tms_ground_ejre[i][k] = np.std(tms_ground_ejre[i][j:j+4])
        avg_tms_ground_oryx[i][k] = sum(tms_ground_oryx[i][j:j+4]) / 4
        std_tms_ground_oryx[i][k] = np.std(tms_ground_oryx[i][j:j+4])
        avg_tms_ground_asyv[i][k] = sum(tms_ground_asyv[i][j:j+4]) / 4
        std_tms_ground_asyv[i][k] = np.std(tms_ground_asyv[i][j:j+4])
        k = k+1

    avg_tms_cement[i][0]=sum(tms_cement[i][1:14])/13
    std_tms_cement[i][0]=np.std(tms_cement[i][1:14])

    q=1
    for p in range (14,len(tms_cement[0])-3,4):
        avg_tms_cement[i][q]=sum(tms_cement[i][p:p+4])/4
        std_tms_cement[i][q]=np.std(tms_cement[i][p:p+4])

        q=q+1


#---- avg_tms is now a matrix of the 30 density measurements AND the ini-
tial measurement of the clean glass plate,
#---- which is the first column of avg_tms (except tms_cement that consists
of 33 density measurements


# normalizing the transmission measurements to a clean glass plate
for i in range(0,len(avg_tms_aswan),1):
    for j in range (1,len(avg_tms_aswan[i]),1):
        avg_tms_aswan[i][j]=(avg_tms_aswan[i][j]*100)/avg_tms_aswan[i][0]
        avg_tms_ejre[i][j]=(avg_tms_ejre[i][j]*100)/avg_tms_ejre[i][0]
        avg_tms_oryx[i][j]=(avg_tms_oryx[i][j]*100)/avg_tms_oryx[i][0]
        avg_tms_ground_aswan[i][j]=(avg_tms_ground_aswan[i][j]*100)/
                                    avg_tms_ground_aswan[i][0]
        avg_tms_ground_ejre[i][j]=(avg_tms_ground_ejre[i][j]*100)/
                                    avg_tms_ground_ejre[i][0]
        avg_tms_ground_oryx[i][j]=(avg_tms_ground_oryx[i][j]*100/
                                    avg_tms_ground_oryx[i][0]
        avg_tms_ground_asyv[i][j]=(avg_tms_ground_asyv[i][j]*100)/
                                    avg_tms_ground_asyv[i][0]
    avg_tms_aswan[i][0]=avg_tms_aswan[i][0]*100/avg_tms_aswan[i][0]
    avg_tms_ejre[i][0]=avg_tms_ejre[i][0]*100/avg_tms_ejre[i][0]
    avg_tms_oryx[i][0]=avg_tms_oryx[i][0]*100/avg_tms_oryx[i][0]
    avg_tms_ground_aswan[i][0]=avg_tms_ground_aswan[i][0]*100/
                                    avg_tms_ground_aswan[i][0]
    avg_tms_ground_ejre[i][0]=avg_tms_ground_ejre[i][0]*100/
                                    avg_tms_ground_ejre[i][0]
    avg_tms_ground_oryx[i][0]=avg_tms_ground_oryx[i][0]*100/
                                    avg_tms_ground_oryx[i][0]
    avg_tms_ground_asyv[i][0]=avg_tms_ground_asyv[i][0]*100/
                                    avg_tms_ground_asyv[i][0]

    #normalizing for cement
```

```
    for p in range (1,len(avg_tms_cement[i]),1):
        avg_tms_cement[i][p]=(avg_tms_cement[i][p]*100)/
                                avg_tms_cement[i][0]
    avg_tms_cement[i][0]=avg_tms_cement[i][0]*100/avg_tms_cement[i][0]

#drop in transmission depending on wavelength and density
diff_tms_aswan=np.zeros([len(avg_tms_aswan),len(avg_tms_aswan[0])-1])
diff_tms_ejre=np.zeros([len(avg_tms_ejre),len(avg_tms_ejre[0])-1])
diff_tms_oryx=np.zeros([len(avg_tms_oryx),len(avg_tms_oryx[0])-1])
diff_tms_ground_aswan=np.zeros([len(avg_tms_ground_aswan),
                                len(avg_tms_ground_aswan[0])-1])
diff_tms_ground_ejre=np.zeros([len(avg_tms_ground_ejre),
                                len(avg_tms_ground_ejre[0])-1])
diff_tms_ground_oryx=np.zeros([len(avg_tms_ground_oryx),
                                len(avg_tms_ground_oryx[0])-1])
diff_tms_ground_asyv=np.zeros([len(avg_tms_ground_asyv),
                                len(avg_tms_ground_asyv[0])-1])
diff_tms_cement=np.zeros([len(avg_tms_cement),len(avg_tms_cement[0])-1])
for i in range(0,len(avg_tms_aswan),1):
    for j in range(1,len(avg_tms_aswan[0]),1):
        diff_tms_aswan[i][j-1]=avg_tms_aswan[i][0]-avg_tms_aswan[i][j]
        diff_tms_ejre[i][j-1]=avg_tms_ejre[i][0]-avg_tms_ejre[i][j]
        diff_tms_oryx[i][j-1]=avg_tms_oryx[i][0]-avg_tms_oryx[i][j]
        diff_tms_ground_aswan[i][j-1]=avg_tms_ground_aswan[i][0]-
                                      avg_tms_ground_aswan[i][j]
        diff_tms_ground_ejre[i][j-1]=avg_tms_ground_ejre[i][0]-
                                      avg_tms_ground_ejre[i][j]
        diff_tms_ground_oryx[i][j-1]=avg_tms_ground_oryx[i][0]-
                                      avg_tms_ground_oryx[i][j]
        diff_tms_ground_asyv[i][j-1]=avg_tms_ground_asyv[i][0]-
                                      avg_tms_ground_asyv[i][j]
    for p in range(1, len(avg_tms_cement[0]),1):
        diff_tms_cement[i][p-1]=avg_tms_cement[i][0]-avg_tms_cement[i][p]

# Density arrays for the different transmission measurements
den_aswan=[0, 4.78, 45.13, 1.67, 18.33, 6.27, 31.14, 25.77, 118.48, 1.84,
           102.23, 5.83, 18.08, 81.91, 7.17, 21.81, 17.27, 7.45, 6.09,
           52.72, 37.44, 53.67, 15.45, 14.59, 0.34, 57.50, 7.70, 194.47,
           11.58, 9.73, 5.20]
den_ejre=[0, 43.97, 68.59, 9.09, 17.05, 3.02, 12.02, 33.72, 4.27, 58.58,
          3.30, 3.78, 19.94, 40.16, 43.75, 87.48, 29.78, 17.30, 28.00,
          64.91, 4.81, 6.27, 23.02, 51.36, 0.75, 186.22, 20.77, 14.94,
          94.08, 1.44, 59.48]
den_oryx=[0, 0.30, 68.16, 9.78, 8.59, 40.78, 3.25, 10.58, 28.69, 43.83,
          54.02, 77.28, 41.64, 10.58, 9.77, 6.75, 45.94, 36.50, 54.39,
          60.97, 30.89, 111.70, 115.28, 39.81, 14.78, 272.91, 1.16, 11.28,
          38.08, 4.39, 61.22]
den_ground_aswan=[0, 26.20, 7.92, 15.66, 72.95, 187.03, 48.62, 59.77,
                  99.41, 30.31, 1.94, 1.31, 4.33, 17.00, 6.47, 1.36,
                  60.97, 105.72, 0.31, 5.80, 11.95, 128.52, 24.67, 65.52,
                  292.78, 81.84, 43.13, 39.55, 40.98, 5.56, 9.11]
den_ground_ejre=[0, 10.67, 0.30, 62.91, 41.64, 86.94, 72.75, 12.47, 18.33,
                 43.86, 0.98, 20.83, 50.02, 70.31, 82.95, 95.41, 144.27,
                 173.55, 236.02, 4.47, 7.36, 32.44, 62.61, 19.78, 30.33,
                 4.64, 10.22, 37.58, 14.78, 51.86, 93.94]
den_ground_oryx=[0, 89.91, 17.77, 10.91, 130.42, 35.69, 71.67, 87.39, 4.17,
                 50.06, 5.52, 58.45, 100.17, 281.44, 75.45, 3.25, 9.23,
                 2.73, 31.59, 24.09, 4.38, 2.28, 1.91, 42.98, 85.84,
                 133.77, 13.27, 59.53, 5.63, 61.97, 36.75]
den_ground_asyv=[0, 97.89, 5.28, 100.42, 8.33, 15.36, 74.19, 7.62, 52.22,
                 35.50, 14.77, 28.83, 2.31, 9.95, 47.81, 94.17, 129.73,
```

```
                223.31, 7.25, 20.28, 23.44, 50.41, 67.55, 89.92, 119.98,
                1.42, 3.94, 69.91, 86.63, 7.83, 16.13]
den_cement=[0, 36.62, 41.03, 29.16, 16.67, 35.25, 15.30, 6.72, 1.33, 7.53,
            44.50, 49.72, 1.36, 0.39, 0.70, 1.91, 7.77, 6.42, 4.84, 1.36,
            0.41, 2.66, 3.58, 2.73, 11.61, 7.78, 13.13, 3.13, 7.94, 2.83,
            15.56, 7.05, 0.14, 10.13]
den_uncertainty=0.16

#Ordering the drop in transmission with ascending dust density
sorted_den_aswan=[]
sorted_den_ejre=[]
sorted_den_oryx=[]
sorted_den_ground_aswan=[]
sorted_den_ground_ejre=[]
sorted_den_ground_oryx=[]
sorted_den_ground_asyv=[]
sorted_den_cement=[]
ind_den_aswan_asc=np.argsort(den_aswan[1:len(den_aswan)])
ind_den_ejre_asc=np.argsort(den_ejre[1:len(den_ejre)])
ind_den_oryx_asc=np.argsort(den_oryx[1:len(den_oryx)])
ind_den_ground_aswan_asc=np.argsort(den_ground_aswan[1:len
                                                    (den_ground_aswan)])
ind_den_ground_ejre_asc=np.argsort(den_ground_ejre[1:len(den_ground_ejre)])
ind_den_ground_oryx_asc=np.argsort(den_ground_oryx[1:len(den_ground_oryx)])
ind_den_ground_asyv_asc=np.argsort(den_ground_asyv[1:len(den_ground_asyv)])
ind_den_cement_asc=np.argsort(den_cement[1:len(den_cement)])

temp=np.zeros([len(diff_tms_aswan),len(diff_tms_aswan[0])])
for j in ind_den_aswan_asc:
    sorted_den_aswan.append(den_aswan[j+1])
for i in range(0, len(diff_tms_aswan),1):
    k=0
    for j in ind_den_aswan_asc:
        temp[i][k]=diff_tms_aswan[i][j]
        k=k+1
diff_tms_aswan=temp

temp=np.zeros([len(diff_tms_ejre),len(diff_tms_ejre[0])])
for j in ind_den_ejre_asc:
    sorted_den_ejre.append(den_ejre[j+1])
for i in range(0, len(diff_tms_ejre),1):
    k=0
    for j in ind_den_ejre_asc:
        temp[i][k]=diff_tms_ejre[i][j]
        k=k+1
diff_tms_ejre=temp

temp=np.zeros([len(diff_tms_oryx),len(diff_tms_oryx[0])])
for j in ind_den_oryx_asc:
    sorted_den_oryx.append(den_oryx[j+1])
for i in range(0, len(diff_tms_ejre),1):
    k=0
    for j in ind_den_oryx_asc:
        temp[i][k]=diff_tms_oryx[i][j]
        k=k+1
diff_tms_oryx=temp

temp=np.zeros([len(diff_tms_ground_aswan),len(diff_tms_ground_aswan[0])])
for j in ind_den_ground_aswan_asc:
    sorted_den_ground_aswan.append(den_ground_aswan[j+1])
for i in range(0, len(diff_tms_ground_aswan),1):
```

```
    k=0
    for j in ind_den_ground_aswan_asc:
        temp[i][k]=diff_tms_ground_aswan[i][j]
        k=k+1
diff_tms_ground_aswan=temp

temp=np.zeros([len(diff_tms_ground_ejre),len(diff_tms_ground_ejre[0])])
for j in ind_den_ground_ejre_asc:
    sorted_den_ground_ejre.append(den_ground_ejre[j+1])
for i in range(0, len(diff_tms_ground_ejre),1):
    k=0
    for j in ind_den_ground_ejre_asc:
        temp[i][k]=diff_tms_ground_ejre[i][j]
        k=k+1
diff_tms_ground_ejre=temp

temp=np.zeros([len(diff_tms_ground_oryx),len(diff_tms_ground_oryx[0])])
for j in ind_den_ground_oryx_asc:
    sorted_den_ground_oryx.append(den_ground_oryx[j+1])
for i in range(0, len(diff_tms_ground_oryx),1):
    k=0
    for j in ind_den_ground_oryx_asc:
        temp[i][k]=diff_tms_ground_oryx[i][j]
        k=k+1
diff_tms_ground_oryx=temp

temp=np.zeros([len(diff_tms_ground_asyv),len(diff_tms_ground_asyv[0])])
for j in ind_den_ground_asyv_asc:
    sorted_den_ground_asyv.append(den_ground_asyv[j+1])
for i in range(0, len(diff_tms_ground_asyv),1):
    k=0
    for j in ind_den_ground_asyv_asc:
        temp[i][k]=diff_tms_ground_asyv[i][j]
        k=k+1
diff_tms_ground_asyv=temp

temp=np.zeros([len(diff_tms_cement),len(diff_tms_cement[0])])
for j in ind_den_cement_asc:
    sorted_den_cement.append(den_cement[j+1])
for i in range(0, len(diff_tms_cement),1):
    k=0
    for j in ind_den_cement_asc:
        temp[i][k]=diff_tms_cement[i][j]
        k=k+1
diff_tms_cement=temp

#----diff_tms is now a matrix (852,30) with ascending dust density on col-
umns.

#Averaging over 50 nm and taking out only 5 of the 30 densities for a good
looking bar plot
temp=np.transpose(diff_tms_aswan)
temp2=np.transpose(diff_tms_ejre)
temp3=np.transpose(diff_tms_oryx)
temp4=np.transpose(diff_tms_ground_aswan)
temp5=np.transpose(diff_tms_ground_ejre)
temp6=np.transpose(diff_tms_ground_oryx)
temp7=np.transpose(diff_tms_ground_asyv)
temp8=np.transpose(diff_tms_cement)

chosen_den_aswan=np.zeros([5])
```

```
chosen_den_ejre=np.zeros([5])
chosen_den_oryx=np.zeros([5])
chosen_den_ground_aswan=np.zeros([5])
chosen_den_ground_ejre=np.zeros([5])
chosen_den_ground_oryx=np.zeros([5])
chosen_den_ground_asyv=np.zeros([5])
chosen_den_cement=np.zeros([5])

avg_diff_tms_aswan=np.zeros([6,13])
std_diff_tms_aswan=np.zeros([6,13])
avg_diff_tms_ejre=np.zeros([6,13])
std_diff_tms_ejre=np.zeros([6,13])
avg_diff_tms_oryx=np.zeros([6,13])
std_diff_tms_oryx=np.zeros([6,13])
avg_diff_tms_ground_aswan=np.zeros([6,13])
std_diff_tms_ground_aswan=np.zeros([6,13])
avg_diff_tms_ground_ejre=np.zeros([6,13])
std_diff_tms_ground_ejre=np.zeros([6,13])
avg_diff_tms_ground_oryx=np.zeros([6,13])
std_diff_tms_ground_oryx=np.zeros([6,13])
avg_diff_tms_ground_asyv=np.zeros([6,13])
std_diff_tms_ground_asyv=np.zeros([6,13])
avg_diff_tms_cement=np.zeros([6,13])
std_diff_tms_cement=np.zeros([6,13])
k=1
for i in range (5,len(temp),6):
    chosen_den_aswan[k-1]=sorted_den_aswan[i]
    chosen_den_ejre[k-1]=sorted_den_ejre[i]
    chosen_den_oryx[k-1]=sorted_den_oryx[i]
    chosen_den_ground_aswan[k-1]=sorted_den_ground_aswan[i]
    chosen_den_ground_ejre[k-1] = sorted_den_ground_ejre[i]
    chosen_den_ground_oryx[k-1] = sorted_den_ground_oryx[i]
    chosen_den_ground_asyv[k-1]=sorted_den_ground_asyv[i]
    chosen_den_cement[k-1]=sorted_den_cement[i]

    avg_diff_tms_aswan[k][0]=np.average(temp[i][0:ind_wavlen400])
    std_diff_tms_aswan[k][0]=np.std(temp[i][0:ind_wavlen400])
    avg_diff_tms_aswan[k][1]=np.average(temp[i][ind_wavlen400:
                                                ind_wavlen450])
    std_diff_tms_aswan[k][1]=np.std(temp[i][ind_wavlen400:ind_wavlen450])
    avg_diff_tms_aswan[k][2]=np.average(temp[i][ind_wavlen450:
                                                ind_wavlen500])
    std_diff_tms_aswan[k][2]=np.std(temp[i][ind_wavlen450:ind_wavlen500])
    avg_diff_tms_aswan[k][3]=np.average(temp[i][ind_wavlen500:
                                                ind_wavlen550])
    std_diff_tms_aswan[k][3]=np.std(temp[i][ind_wavlen500:ind_wavlen550])
    avg_diff_tms_aswan[k][4]=np.average(temp[i][ind_wavlen550:
                                                ind_wavlen600])
    std_diff_tms_aswan[k][4]=np.std(temp[i][ind_wavlen550:ind_wavlen600])
    avg_diff_tms_aswan[k][5]=np.average(temp[i][ind_wavlen600:
                                                ind_wavlen650])
    std_diff_tms_aswan[k][5]=np.std(temp[i][ind_wavlen600:ind_wavlen650])
    avg_diff_tms_aswan[k][6]=np.average(temp[i][ind_wavlen650:
                                                ind_wavlen700])
    std_diff_tms_aswan[k][6]=np.std(temp[i][ind_wavlen650:ind_wavlen700])
    avg_diff_tms_aswan[k][7]=np.average(temp[i][ind_wavlen700:
                                                ind_wavlen750])
    std_diff_tms_aswan[k][7]=np.std(temp[i][ind_wavlen700:ind_wavlen750])
    avg_diff_tms_aswan[k][8]=np.average(temp[i][ind_wavlen750:
```

```
                                                    ind_wavlen800])
    std_diff_tms_aswan[k][8]=np.std(temp[i][ind_wavlen750:ind_wavlen800])
    avg_diff_tms_aswan[k][9]=np.average(temp[i][ind_wavlen800:
                                                    ind_wavlen850])
    std_diff_tms_aswan[k][9]=np.std(temp[i][ind_wavlen800:ind_wavlen850])
    avg_diff_tms_aswan[k][10]=np.average(temp[i][ind_wavlen850:
                                                    ind_wavlen900])
    std_diff_tms_aswan[k][10]=np.std(temp[i][ind_wavlen850:ind_wavlen900])
    avg_diff_tms_aswan[k][11]=np.average(temp[i][ind_wavlen900:
                                                    ind_wavlen950])
    std_diff_tms_aswan[k][11]=np.std(temp[i][ind_wavlen900:ind_wavlen950])
    avg_diff_tms_aswan[k][12]=np.average(temp[i][ind_wavlen950:
                                                    ind_wavlen998])
    std_diff_tms_aswan[k][12]=np.std(temp[i][ind_wavlen950:ind_wavlen998])

    avg_diff_tms_ejre[k][0]=np.average(temp2[i][0:ind_wavlen400])
    std_diff_tms_ejre[k][0]=np.std(temp2[i][0:ind_wavlen400])
    avg_diff_tms_ejre[k][1]=np.average(temp2[i][ind_wavlen400:
                                                    ind_wavlen450])
    std_diff_tms_ejre[k][1]=np.std(temp2[i][ind_wavlen400:ind_wavlen450])
    avg_diff_tms_ejre[k][2]=np.average(temp2[i][ind_wavlen450:
                                                    ind_wavlen500])
    std_diff_tms_ejre[k][2]=np.std(temp2[i][ind_wavlen450:ind_wavlen500])
    avg_diff_tms_ejre[k][3]=np.average(temp2[i][ind_wavlen500:
                                                    ind_wavlen550])
    std_diff_tms_ejre[k][3]=np.std(temp2[i][ind_wavlen500:ind_wavlen550])
    avg_diff_tms_ejre[k][4]=np.average(temp2[i][ind_wavlen550:
                                                    ind_wavlen600])
    std_diff_tms_ejre[k][4]=np.std(temp2[i][ind_wavlen550:ind_wavlen600])
    avg_diff_tms_ejre[k][5]=np.average(temp2[i][ind_wavlen600:
                                                    ind_wavlen650])
    std_diff_tms_ejre[k][5]=np.std(temp2[i][ind_wavlen600:ind_wavlen650])
    avg_diff_tms_ejre[k][6]=np.average(temp2[i][ind_wavlen650:
                                                    ind_wavlen700])
    std_diff_tms_ejre[k][6]= np.std(temp2[i][ind_wavlen650:ind_wavlen700])
    avg_diff_tms_ejre[k][7]= np.average(temp2[i][ind_wavlen700:
                                                    ind_wavlen750])
    std_diff_tms_ejre[k][7]=np.std(temp2[i][ind_wavlen700:ind_wavlen750])
    avg_diff_tms_ejre[k][8]=np.average(temp2[i][ind_wavlen750:
                                                    ind_wavlen800])
    std_diff_tms_ejre[k][8]=np.std(temp2[i][ind_wavlen750:ind_wavlen800])
    avg_diff_tms_ejre[k][9]=np.average(temp2[i][ind_wavlen800:
                                                    ind_wavlen850])
    std_diff_tms_ejre[k][9]=np.std(temp2[i][ind_wavlen800:ind_wavlen850])
    avg_diff_tms_ejre[k][10]=np.average(temp2[i][ind_wavlen850:
                                                    ind_wavlen900])
    std_diff_tms_ejre[k][10]=np.std(temp2[i][ind_wavlen850:ind_wavlen900])
    avg_diff_tms_ejre[k][11]=np.average(temp2[i][ind_wavlen900:
                                                    ind_wavlen950])
    std_diff_tms_ejre[k][11]=np.std(temp2[i][ind_wavlen900:ind_wavlen950])
    avg_diff_tms_ejre[k][12]=np.average(temp2[i][ind_wavlen950:
                                                    ind_wavlen998])
    std_diff_tms_ejre[k][12]=np.std(temp2[i][ind_wavlen950:ind_wavlen998])

    avg_diff_tms_oryx[k][0]=np.average(temp3[i][0:ind_wavlen400])
    std_diff_tms_oryx[k][0]=np.std(temp3[i][0:ind_wavlen400])
    avg_diff_tms_oryx[k][1]=np.average(temp3[i][ind_wavlen400:
                                                    ind_wavlen450])
    std_diff_tms_oryx[k][1]=np.std(temp3[i][ind_wavlen400:ind_wavlen450])
    avg_diff_tms_oryx[k][2]=np.average(temp3[i][ind_wavlen450:
```

```
                                                    ind_wavlen500])
std_diff_tms_oryx[k][2]= np.std(temp3[i][ind_wavlen450:ind_wavlen500])
avg_diff_tms_oryx[k][3]= np.average(temp3[i][ind_wavlen500:
                                                    ind_wavlen550])
std_diff_tms_oryx[k][3]= np.std(temp3[i][ind_wavlen500:ind_wavlen550])
avg_diff_tms_oryx[k][4]= np.average(temp3[i][ind_wavlen550:
                                                    ind_wavlen600])
std_diff_tms_oryx[k][4]= np.std(temp3[i][ind_wavlen550:ind_wavlen600])
avg_diff_tms_oryx[k][5]= np.average(temp3[i][ind_wavlen600:
                                                    ind_wavlen650])
std_diff_tms_oryx[k][5]= np.std(temp3[i][ind_wavlen600:ind_wavlen650])
avg_diff_tms_oryx[k][6]= np.average(temp3[i][ind_wavlen650:
                                                    ind_wavlen700])
std_diff_tms_oryx[k][6]= np.std(temp3[i][ind_wavlen650:ind_wavlen700])
avg_diff_tms_oryx[k][7]= np.average(temp3[i][ind_wavlen700:
                                                    ind_wavlen750])
std_diff_tms_oryx[k][7]= np.std(temp3[i][ind_wavlen700:ind_wavlen750])
avg_diff_tms_oryx[k][8]= np.average(temp3[i][ind_wavlen750:
                                                    ind_wavlen800])
std_diff_tms_oryx[k][8]= np.std(temp3[i][ind_wavlen750:ind_wavlen800])
avg_diff_tms_oryx[k][9]= np.average(temp3[i][ind_wavlen800:
                                                    ind_wavlen850])
std_diff_tms_oryx[k][9]= np.std(temp3[i][ind_wavlen800:ind_wavlen850])
avg_diff_tms_oryx[k][10]= np.average(temp3[i][ind_wavlen850:
                                                    ind_wavlen900])
std_diff_tms_oryx[k][10]= np.std(temp3[i][ind_wavlen850:ind_wavlen900])
avg_diff_tms_oryx[k][11]= np.average(temp3[i][ind_wavlen900:
                                                    ind_wavlen950])
std_diff_tms_oryx[k][11]= np.std(temp3[i][ind_wavlen900:ind_wavlen950])
avg_diff_tms_oryx[k][12]= np.average(temp3[i][ind_wavlen950:
                                                    ind_wavlen998])
std_diff_tms_oryx[k][12]= np.std(temp3[i][ind_wavlen950:ind_wavlen998])

avg_diff_tms_ground_aswan[k][0]= np.average(temp4[i][0:ind_wavlen400])
std_diff_tms_ground_aswan[k][0]= np.std(temp4[i][0:ind_wavlen400])
avg_diff_tms_ground_aswan[k][1]= np.average(temp4[i][ind_wavlen400:
                                                    ind_wavlen450])
std_diff_tms_ground_aswan[k][1]=np.std(temp4[i][ind_wavlen400:
                                                    ind_wavlen450])
avg_diff_tms_ground_aswan[k][2]= np.average(temp4[i][ind_wavlen450:
                                                    ind_wavlen500])
std_diff_tms_ground_aswan[k][2]=np.std(temp4[i][ind_wavlen450:
                                                    ind_wavlen500])
avg_diff_tms_ground_aswan[k][3]=np.average(temp4[i][ind_wavlen500:
                                                    ind_wavlen550])
std_diff_tms_ground_aswan[k][3]=np.std(temp4[i][ind_wavlen500:
                                                    ind_wavlen550])
avg_diff_tms_ground_aswan[k][4]=np.average(temp4[i][ind_wavlen550:
                                                    ind_wavlen600])
std_diff_tms_ground_aswan[k][4]=np.std(temp4[i][ind_wavlen550:
                                                    ind_wavlen600])
avg_diff_tms_ground_aswan[k][5]=np.average(temp4[i][ind_wavlen600:
                                                    ind_wavlen650])
std_diff_tms_ground_aswan[k][5]=np.std(temp4[i][ind_wavlen600:
                                                    ind_wavlen650])
avg_diff_tms_ground_aswan[k][6]=np.average(temp4[i][ind_wavlen650:
                                                    ind_wavlen700])
std_diff_tms_ground_aswan[k][6]=np.std(temp4[i][ind_wavlen650:
                                                    ind_wavlen700])
avg_diff_tms_ground_aswan[k][7]=np.average(temp4[i][ind_wavlen700:
```

```
                                                    ind_wavlen750])
    std_diff_tms_ground_aswan[k][7]=np.std(temp4[i][ind_wavlen700:
                                                    ind_wavlen750])
    avg_diff_tms_ground_aswan[k][8]=np.average(temp4[i][ind_wavlen750:
                                                    ind_wavlen800])
    std_diff_tms_ground_aswan[k][8]=np.std(temp4[i][ind_wavlen750:
                                                    ind_wavlen800])
    avg_diff_tms_ground_aswan[k][9]=np.average(temp4[i][ind_wavlen800:
                                                    ind_wavlen850])
    std_diff_tms_ground_aswan[k][9]=np.std(temp4[i][ind_wavlen800:
                                                    ind_wavlen850])
    avg_diff_tms_ground_aswan[k][10]=np.average(temp4[i][ind_wavlen850:
                                                    ind_wavlen900])
    std_diff_tms_ground_aswan[k][10]=np.std(temp4[i][ind_wavlen850:
                                                    ind_wavlen900])
    avg_diff_tms_ground_aswan[k][11]=np.average(temp4[i][ind_wavlen900:
                                                    ind_wavlen950])
    std_diff_tms_ground_aswan[k][11]=np.std(temp4[i][ind_wavlen900:
                                                    ind_wavlen950])
    avg_diff_tms_ground_aswan[k][12]=np.average(temp4[i][ind_wavlen950:
                                                    ind_wavlen998])
    std_diff_tms_ground_aswan[k][12]=np.std(temp4[i][ind_wavlen950:
                                                    ind_wavlen998])

    avg_diff_tms_ground_ejre[k][0]=np.average(temp5[i][0:ind_wavlen400])
    std_diff_tms_ground_ejre[k][0]=np.std(temp5[i][0:ind_wavlen400])
    avg_diff_tms_ground_ejre[k][1]=np.average(temp5[i][ind_wavlen400:
                                                    ind_wavlen450])
    std_diff_tms_ground_ejre[k][1]=np.std(temp5[i][ind_wavlen400:
                                                    ind_wavlen450])
    avg_diff_tms_ground_ejre[k][2]=np.average(temp5[i][ind_wavlen450:
                                                    ind_wavlen500])
    std_diff_tms_ground_ejre[k][2]=np.std(temp5[i][ind_wavlen450:
                                                    ind_wavlen500])
    avg_diff_tms_ground_ejre[k][3]=np.average(temp5[i][ind_wavlen500:
                                                    ind_wavlen550])
    std_diff_tms_ground_ejre[k][3]=np.std(temp5[i][ind_wavlen500:
                                                    ind_wavlen550])
    avg_diff_tms_ground_ejre[k][4]=np.average(temp5[i][ind_wavlen550:
                                                    ind_wavlen600])
    std_diff_tms_ground_ejre[k][4]=np.std(temp5[i][ind_wavlen550:
                                                    ind_wavlen600])
    avg_diff_tms_ground_ejre[k][5]=np.average(temp5[i][ind_wavlen600:
                                                    ind_wavlen650])
    std_diff_tms_ground_ejre[k][5]=np.std(temp5[i][ind_wavlen600:
                                                    ind_wavlen650])
    avg_diff_tms_ground_ejre[k][6]=np.average(temp5[i][ind_wavlen650:
                                                    ind_wavlen700])
    std_diff_tms_ground_ejre[k][6]=np.std(temp5[i][ind_wavlen650:
                                                    ind_wavlen700])
    avg_diff_tms_ground_ejre[k][7]=np.average(temp5[i][ind_wavlen700:
                                                    ind_wavlen750])
    std_diff_tms_ground_ejre[k][7]= np.std(temp5[i][ind_wavlen700:
                                                    ind_wavlen750])
    avg_diff_tms_ground_ejre[k][8]=np.average(temp5[i][ind_wavlen750:
                                                    ind_wavlen800])
    std_diff_tms_ground_ejre[k][8]=np.std(temp5[i][ind_wavlen750:
                                                    ind_wavlen800])
    avg_diff_tms_ground_ejre[k][9]=np.average(temp5[i][ind_wavlen800:
                                                    ind_wavlen850])
    std_diff_tms_ground_ejre[k][9]=np.std(temp5[i][ind_wavlen800:
```

```
                                                    ind_wavlen850])
avg_diff_tms_ground_ejre[k][10]=np.average(temp5[i][ind_wavlen850:
                                                    ind_wavlen900])
std_diff_tms_ground_ejre[k][10]=np.std(temp5[i][ind_wavlen850:
                                                    ind_wavlen900])
avg_diff_tms_ground_ejre[k][11]=np.average(temp5[i][ind_wavlen900:
                                                    ind_wavlen950])
std_diff_tms_ground_ejre[k][11]=np.std(temp5[i][ind_wavlen900:
                                                    ind_wavlen950])
avg_diff_tms_ground_ejre[k][12]=np.average(temp5[i][ind_wavlen950:
                                                    ind_wavlen998])
std_diff_tms_ground_ejre[k][12]=np.std(temp5[i][ind_wavlen950:
                                                    ind_wavlen998])

avg_diff_tms_ground_oryx[k][0]=np.average(temp6[i][0:ind_wavlen400])
std_diff_tms_ground_oryx[k][0]=np.std(temp6[i][0:ind_wavlen400])
avg_diff_tms_ground_oryx[k][1]=np.average(temp6[i][ind_wavlen400:
                                                    ind_wavlen450])
std_diff_tms_ground_oryx[k][1]=np.std(temp6[i][ind_wavlen400:
                                                    ind_wavlen450])
avg_diff_tms_ground_oryx[k][2]=np.average(temp6[i][ind_wavlen450:
                                                    ind_wavlen500])
std_diff_tms_ground_oryx[k][2]=np.std(temp6[i][ind_wavlen450:
                                                    ind_wavlen500])
avg_diff_tms_ground_oryx[k][3]=np.average(temp6[i][ind_wavlen500:
                                                    ind_wavlen550])
std_diff_tms_ground_oryx[k][3]=np.std(temp6[i][ind_wavlen500:
                                                    ind_wavlen550])
avg_diff_tms_ground_oryx[k][4]=np.average(temp6[i][ind_wavlen550:
                                                    ind_wavlen600])
std_diff_tms_ground_oryx[k][4]=np.std(temp6[i][ind_wavlen550:
                                                    ind_wavlen600])
avg_diff_tms_ground_oryx[k][5]=np.average(temp6[i][ind_wavlen600:
                                                    ind_wavlen650])
std_diff_tms_ground_oryx[k][5]=np.std(temp6[i][ind_wavlen600:
                                                    ind_wavlen650])
avg_diff_tms_ground_oryx[k][6]=np.average(temp6[i][ind_wavlen650:
                                                    ind_wavlen700])
std_diff_tms_ground_oryx[k][6]=np.std(temp6[i][ind_wavlen650:
                                                    ind_wavlen700])
avg_diff_tms_ground_oryx[k][7]=np.average(temp6[i][ind_wavlen700:
                                                    ind_wavlen750])
std_diff_tms_ground_oryx[k][7]=np.std(temp6[i][ind_wavlen700:
                                                    ind_wavlen750])
avg_diff_tms_ground_oryx[k][8]=np.average(temp6[i][ind_wavlen750:
                                                    ind_wavlen800])
std_diff_tms_ground_oryx[k][8]=np.std(temp6[i][ind_wavlen750:
                                                    ind_wavlen800])
avg_diff_tms_ground_oryx[k][9]=np.average(temp6[i][ind_wavlen800:
                                                    ind_wavlen850])
std_diff_tms_ground_oryx[k][9]=np.std(temp6[i][ind_wavlen800:
                                                    ind_wavlen850])
avg_diff_tms_ground_oryx[k][10]=np.average(temp6[i][ind_wavlen850:
                                                    ind_wavlen900])
std_diff_tms_ground_oryx[k][10]=np.std(temp6[i][ind_wavlen850:
                                                    ind_wavlen900])
avg_diff_tms_ground_oryx[k][11]=np.average(temp6[i][ind_wavlen900:
                                                    ind_wavlen950])
std_diff_tms_ground_oryx[k][11]=np.std(temp6[i][ind_wavlen900:
                                                    ind_wavlen950])
avg_diff_tms_ground_oryx[k][12]=np.average(temp6[i][ind_wavlen950:
```

```
                                                    ind_wavlen998])
    std_diff_tms_ground_oryx[k][12]=np.std(temp6[i][ind_wavlen950:
                                                    ind_wavlen998])

    avg_diff_tms_ground_asyv[k][0]=np.average(temp7[i][0:ind_wavlen400])
    std_diff_tms_ground_asyv[k][0]=np.std(temp7[i][0:ind_wavlen400])
    avg_diff_tms_ground_asyv[k][1]=np.average(temp7[i][ind_wavlen400:
                                                    ind_wavlen450])
    std_diff_tms_ground_asyv[k][1]=np.std(temp7[i][ind_wavlen400:
                                                    ind_wavlen450])
    avg_diff_tms_ground_asyv[k][2]=np.average(temp7[i][ind_wavlen450:
                                                    ind_wavlen500])
    std_diff_tms_ground_asyv[k][2]=np.std(temp7[i][ind_wavlen450:
                                                    ind_wavlen500])
    avg_diff_tms_ground_asyv[k][3]=np.average(temp7[i][ind_wavlen500:
                                                    ind_wavlen550])
    std_diff_tms_ground_asyv[k][3]=np.std(temp7[i][ind_wavlen500:
                                                    ind_wavlen550])
    avg_diff_tms_ground_asyv[k][4]=np.average(temp7[i][ind_wavlen550:
                                                    ind_wavlen600])
    std_diff_tms_ground_asyv[k][4]=np.std(temp7[i][ind_wavlen550:
                                                    ind_wavlen600])
    avg_diff_tms_ground_asyv[k][5]=np.average(temp7[i][ind_wavlen600:
                                                    ind_wavlen650])
    std_diff_tms_ground_asyv[k][5]=np.std(temp7[i][ind_wavlen600:
                                                    ind_wavlen650])
    avg_diff_tms_ground_asyv[k][6]=np.average(temp7[i][ind_wavlen650:
                                                    ind_wavlen700])
    std_diff_tms_ground_asyv[k][6]=np.std(temp7[i][ind_wavlen650:
                                                    ind_wavlen700])
    avg_diff_tms_ground_asyv[k][7]=np.average(temp7[i][ind_wavlen700:
                                                    ind_wavlen750])
    std_diff_tms_ground_asyv[k][7]=np.std(temp7[i][ind_wavlen700:
                                                    ind_wavlen750])
    avg_diff_tms_ground_asyv[k][8]=np.average(temp7[i][ind_wavlen750:
                                                    ind_wavlen800])
    std_diff_tms_ground_asyv[k][8]=np.std(temp7[i][ind_wavlen750:
                                                    ind_wavlen800])
    avg_diff_tms_ground_asyv[k][9]=np.average(temp7[i][ind_wavlen800:
                                                    ind_wavlen850])
    std_diff_tms_ground_asyv[k][9]=np.std(temp7[i][ind_wavlen800:
                                                    ind_wavlen850])
    avg_diff_tms_ground_asyv[k][10]=np.average(temp7[i][ind_wavlen850:
                                                    ind_wavlen900])
    std_diff_tms_ground_asyv[k][10]=np.std(temp7[i][ind_wavlen850:
                                                    ind_wavlen900])
    avg_diff_tms_ground_asyv[k][11]=np.average(temp7[i][ind_wavlen900:
                                                    ind_wavlen950])
    std_diff_tms_ground_asyv[k][11]=np.std(temp7[i][ind_wavlen900:
                                                    ind_wavlen950])
    avg_diff_tms_ground_asyv[k][12]=np.average(temp7[i][ind_wavlen950:
                                                    ind_wavlen998])
    std_diff_tms_ground_asyv[k][12]=np.std(temp7[i][ind_wavlen950:
                                                    ind_wavlen998])

    avg_diff_tms_cement[k][0]=np.average(temp8[i][0:ind_wavlen400])
    std_diff_tms_cement[k][0]=np.std(temp8[i][0:ind_wavlen400])
    avg_diff_tms_cement[k][1]=np.average(temp8[i][ind_wavlen400:
                                                    ind_wavlen450])
    std_diff_tms_cement[k][1]=np.std(temp8[i][ind_wavlen400:ind_wavlen450])
    avg_diff_tms_cement[k][2]=np.average(temp8[i][ind_wavlen450:
```

```
                                                        ind_wavlen500])
    std_diff_tms_cement[k][2]=np.std(temp8[i][ind_wavlen450:ind_wavlen500])
    avg_diff_tms_cement[k][3]=np.average(temp8[i][ind_wavlen500:
                                                        ind_wavlen550])
    std_diff_tms_cement[k][3]=np.std(temp8[i][ind_wavlen500:ind_wavlen550])
    avg_diff_tms_cement[k][4]=np.average(temp8[i][ind_wavlen550:
                                                        ind_wavlen600])
    std_diff_tms_cement[k][4]=np.std(temp8[i][ind_wavlen550:ind_wavlen600])
    avg_diff_tms_cement[k][5]=np.average(temp8[i][ind_wavlen600:
                                                        ind_wavlen650])
    std_diff_tms_cement[k][5]=np.std(temp8[i][ind_wavlen600:ind_wavlen650])
    avg_diff_tms_cement[k][6]=np.average(temp8[i][ind_wavlen650:
                                                        ind_wavlen700])
    std_diff_tms_cement[k][6]=np.std(temp8[i][ind_wavlen650:ind_wavlen700])
    avg_diff_tms_cement[k][7]=np.average(temp8[i][ind_wavlen700:
                                                        ind_wavlen750])
    std_diff_tms_cement[k][7]=np.std(temp8[i][ind_wavlen700:ind_wavlen750])
    avg_diff_tms_cement[k][8]=np.average(temp8[i][ind_wavlen750:
                                                        ind_wavlen800])
    std_diff_tms_cement[k][8]=np.std(temp8[i][ind_wavlen750:ind_wavlen800])
    avg_diff_tms_cement[k][9]=np.average(temp8[i][ind_wavlen800:
                                                        ind_wavlen850])
    std_diff_tms_cement[k][9]=np.std(temp8[i][ind_wavlen800:ind_wavlen850])
    avg_diff_tms_cement[k][10]=np.average(temp8[i][ind_wavlen850:
                                                        ind_wavlen900])
    std_diff_tms_cement[k][10]=np.std(temp8[i][ind_wavlen850:
                                                        ind_wavlen900])
    avg_diff_tms_cement[k][11]=np.average(temp8[i][ind_wavlen900:
                                                        ind_wavlen950])
    std_diff_tms_cement[k][11]=np.std(temp8[i][ind_wavlen900:
                                                        ind_wavlen950])
    avg_diff_tms_cement[k][12]=np.average(temp8[i][ind_wavlen950:
                                                        ind_wavlen998])
    std_diff_tms_cement[k][12]=np.std(temp8[i][ind_wavlen950:
                                                        ind_wavlen998])
    k=k+1

# Average and standard deviation of transmission over entire spectrum
tot_avg_tms_aswan=[]
tot_std_tms_aswan=[]
temp=np.transpose(avg_tms_aswan)
temp2=np.transpose(std_tms_aswan)
tot_avg_tms_ejre=[]
tot_std_tms_ejre=[]
temp3=np.transpose(avg_tms_ejre)
temp4=np.transpose(std_tms_ejre)
tot_avg_tms_oryx=[]
tot_std_tms_oryx=[]
temp5=np.transpose(avg_tms_oryx)
temp6=np.transpose(std_tms_oryx)
tot_avg_tms_ground_aswan=[]
tot_std_tms_ground_aswan=[]
temp7=np.transpose(avg_tms_ground_aswan)
temp8=np.transpose(std_tms_ground_aswan)
tot_avg_tms_ground_ejre=[]
tot_std_tms_ground_ejre=[]
temp9=np.transpose(avg_tms_ground_ejre)
temp10=np.transpose(std_tms_ground_ejre)
tot_avg_tms_ground_oryx=[]
tot_std_tms_ground_oryx=[]
temp11=np.transpose(avg_tms_ground_oryx)
```

```
temp12=np.transpose(std_tms_ground_oryx)
tot_avg_tms_ground_asyv=[]
tot_std_tms_ground_asyv=[]
temp13=np.transpose(avg_tms_ground_asyv)
temp14=np.transpose(std_tms_ground_asyv)
tot_avg_tms_cement=[]
tot_std_tms_cement=[]
temp15=np.transpose(avg_tms_cement)
temp16=np.transpose(std_tms_cement)
for i in range(0,len(avg_tms_aswan[0]),1):
    tot_avg_tms_aswan.append(np.average(temp[i][0:len(avg_tms_aswan)]))
    tot_std_tms_aswan.append(np.average(temp2[i][0:len(std_tms_aswan)]))
    tot_avg_tms_ejre.append(np.average(temp3[i][0:len(avg_tms_ejre)]))
    tot_std_tms_ejre.append(np.average(temp4[i][0:len(std_tms_ejre)]))
    tot_avg_tms_oryx.append(np.average(temp5[i][0:len(avg_tms_oryx)]))
    tot_std_tms_oryx.append(np.average(temp6[i][0:len(std_tms_oryx)]))
    tot_avg_tms_ground_aswan.append(np.average(temp7[i][0:
                                                len(avg_tms_ground_aswan)]))
    tot_std_tms_ground_aswan.append(np.average(temp8[i][0:
                                                len(std_tms_ground_aswan)]))
    tot_avg_tms_ground_ejre.append(np.average(temp9[i][0:
                                                len(avg_tms_ground_ejre)]))
    tot_std_tms_ground_ejre.append(np.average(temp10[i][0:
                                                len(std_tms_ground_ejre)]))
    tot_avg_tms_ground_oryx.append(np.average(temp11[i][0:
                                                len(avg_tms_ground_oryx)]))
    tot_std_tms_ground_oryx.append(np.average(temp12[i][0:
                                                len(std_tms_ground_oryx)]))
    tot_avg_tms_ground_asyv.append(np.average(temp13[i][0:
                                                len(avg_tms_ground_asyv)]))
    tot_std_tms_ground_asyv.append(np.average(temp14[i][0:
                                                len(std_tms_ground_asyv)]))
for p in range(0,len(avg_tms_cement[0]),1):
    tot_avg_tms_cement.append(np.average(temp15[p][0:len(avg_tms_cement)]))
    tot_std_tms_cement.append(np.average(temp16[p][0:len(std_tms_cement)]))

# Average and standard deviation of transmission 350-500nm
UV_VIS_avg_tms_aswan=[]
UV_VIS_std_tms_aswan=[]
UV_VIS_avg_tms_ejre=[]
UV_VIS_std_tms_ejre=[]
UV_VIS_avg_tms_oryx=[]
UV_VIS_std_tms_oryx=[]
UV_VIS_avg_tms_ground_aswan=[]
UV_VIS_std_tms_ground_aswan=[]
UV_VIS_avg_tms_ground_ejre=[]
UV_VIS_std_tms_ground_ejre=[]
UV_VIS_avg_tms_ground_oryx=[]
UV_VIS_std_tms_ground_oryx=[]
UV_VIS_avg_tms_ground_asyv=[]
UV_VIS_std_tms_ground_asyv=[]
UV_VIS_avg_tms_cement=[]
UV_VIS_std_tms_cement=[]
for i in range(0,len(avg_tms_aswan[0]),1):
    UV_VIS_avg_tms_aswan.append(np.average(temp[i][0:ind_wavlen500]))
    UV_VIS_std_tms_aswan.append(np.average(temp2[i][0:ind_wavlen500]))
    UV_VIS_avg_tms_ejre.append(np.average(temp3[i][0:ind_wavlen500]))
    UV_VIS_std_tms_ejre.append(np.average(temp4[i][0:ind_wavlen500]))
    UV_VIS_avg_tms_oryx.append(np.average(temp5[i][0:ind_wavlen500]))
    UV_VIS_std_tms_oryx.append(np.average(temp6[i][0:ind_wavlen500]))
    UV_VIS_avg_tms_ground_aswan.append(np.average(temp7[i][0:
```

```
                                                        ind_wavlen500]))
    UV_VIS_std_tms_ground_aswan.append(np.average(temp8[i][0:
                                                        ind_wavlen500]))
    UV_VIS_avg_tms_ground_ejre.append(np.average(temp9[i][0:
                                                        ind_wavlen500]))
    UV_VIS_std_tms_ground_ejre.append(np.average(temp10[i][0:
                                                        ind_wavlen500]))
    UV_VIS_avg_tms_ground_oryx.append(np.average(temp11[i][0:
                                                        ind_wavlen500]))
    UV_VIS_std_tms_ground_oryx.append(np.average(temp12[i][0:
                                                        ind_wavlen500]))
    UV_VIS_avg_tms_ground_asyv.append(np.average(temp13[i][0:
                                                        ind_wavlen500]))
    UV_VIS_std_tms_ground_asyv.append(np.average(temp14[i][0:
                                                        ind_wavlen500]))
for p in range(0, len(avg_tms_cement[0]), 1):
    UV_VIS_avg_tms_cement.append(np.average(temp15[p][0:ind_wavlen500]))
    UV_VIS_std_tms_cement.append(np.average(temp16[p][0:ind_wavlen500]))


# Average and standard deviation of transmission 500-800nm
VIS_avg_tms_aswan=[]
VIS_std_tms_aswan=[]
VIS_avg_tms_ejre=[]
VIS_std_tms_ejre=[]
VIS_avg_tms_oryx=[]
VIS_std_tms_oryx=[]
VIS_avg_tms_ground_aswan=[]
VIS_std_tms_ground_aswan=[]
VIS_avg_tms_ground_ejre=[]
VIS_std_tms_ground_ejre=[]
VIS_avg_tms_ground_oryx=[]
VIS_std_tms_ground_oryx=[]
VIS_avg_tms_ground_asyv=[]
VIS_std_tms_ground_asyv=[]
VIS_avg_tms_cement=[]
VIS_std_tms_cement=[]
for i in range(0,len(avg_tms_aswan[0]),1):
    VIS_avg_tms_aswan.append(np.average(temp[i][ind_wavlen500:
                                                        ind_wavlen800]))
    VIS_std_tms_aswan.append(np.average(temp2[i][ind_wavlen500:
                                                        ind_wavlen800]))
    VIS_avg_tms_ejre.append(np.average(temp3[i][ind_wavlen500:
                                                        ind_wavlen800]))
    VIS_std_tms_ejre.append(np.average(temp4[i][ind_wavlen500:
                                                        ind_wavlen800]))
    VIS_avg_tms_oryx.append(np.average(temp5[i][ind_wavlen500:
                                                        ind_wavlen800]))
    VIS_std_tms_oryx.append(np.average(temp6[i][ind_wavlen500:
                                                        ind_wavlen800]))
    VIS_avg_tms_ground_aswan.append(np.average(temp7[i][ind_wavlen500:
                                                        ind_wavlen800]))
    VIS_std_tms_ground_aswan.append(np.average(temp8[i][ind_wavlen500:
                                                        ind_wavlen800]))
    VIS_avg_tms_ground_ejre.append(np.average(temp9[i][ind_wavlen500:
                                                        ind_wavlen800]))
    VIS_std_tms_ground_ejre.append(np.average(temp10[i][ind_wavlen500:
                                                        ind_wavlen800]))
    VIS_avg_tms_ground_oryx.append(np.average(temp11[i][ind_wavlen500:
                                                        ind_wavlen800]))
    VIS_std_tms_ground_oryx.append(np.average(temp12[i][ind_wavlen500:
```

```
                                                        ind_wavlen800]))
    VIS_avg_tms_ground_asyv.append(np.average(temp13[i][ind_wavlen500:
                                                        ind_wavlen800]))
    VIS_std_tms_ground_asyv.append(np.average(temp14[i][ind_wavlen500:
                                                        ind_wavlen800]))
for p in range(0, len(avg_tms_cement[0]), 1):
    VIS_avg_tms_cement.append(np.average(temp15[p][ind_wavlen500:
                                                        ind_wavlen800]))
    VIS_std_tms_cement.append(np.average(temp16[p][ind_wavlen500:
                                                        ind_wavlen800]))

# Average and standard deviation of transmission 800-1000nm
VIS_NIR_avg_tms_aswan=[]
VIS_NIR_std_tms_aswan=[]
VIS_NIR_avg_tms_ejre=[]
VIS_NIR_std_tms_ejre=[]
VIS_NIR_avg_tms_oryx=[]
VIS_NIR_std_tms_oryx=[]
VIS_NIR_avg_tms_ground_aswan=[]
VIS_NIR_std_tms_ground_aswan=[]
VIS_NIR_avg_tms_ground_ejre=[]
VIS_NIR_std_tms_ground_ejre=[]
VIS_NIR_avg_tms_ground_oryx=[]
VIS_NIR_std_tms_ground_oryx=[]
VIS_NIR_avg_tms_ground_asyv=[]
VIS_NIR_std_tms_ground_asyv=[]
VIS_NIR_avg_tms_cement=[]
VIS_NIR_std_tms_cement=[]
for i in range(0,len(avg_tms_aswan[0]),1):
    VIS_NIR_avg_tms_aswan.append(np.average(temp[i][ind_wavlen800:
                                                        ind_wavlen998]))
    VIS_NIR_std_tms_aswan.append(np.average(temp2[i][ind_wavlen800:
                                                        ind_wavlen998]))
    VIS_NIR_avg_tms_ejre.append(np.average(temp3[i][ind_wavlen800:
                                                        ind_wavlen998]))
    VIS_NIR_std_tms_ejre.append(np.average(temp4[i][ind_wavlen800:
                                                        ind_wavlen998]))
    VIS_NIR_avg_tms_oryx.append(np.average(temp5[i][ind_wavlen800:
                                                        ind_wavlen998]))
    VIS_NIR_std_tms_oryx.append(np.average(temp6[i][ind_wavlen800:
                                                        ind_wavlen998]))
    VIS_NIR_avg_tms_ground_aswan.append(np.average(temp7[i][ind_wavlen800:
                                                        ind_wavlen998]))
    VIS_NIR_std_tms_ground_aswan.append(np.average(temp8[i][ind_wavlen800:
                                                        ind_wavlen998]))
    VIS_NIR_avg_tms_ground_ejre.append(np.average(temp9[i][ind_wavlen800:
                                                        ind_wavlen998]))
    VIS_NIR_std_tms_ground_ejre.append(np.average(temp10[i][ind_wavlen800:
                                                        ind_wavlen998]))
    VIS_NIR_avg_tms_ground_oryx.append(np.average(temp11[i][ind_wavlen800:
                                                        ind_wavlen998]))
    VIS_NIR_std_tms_ground_oryx.append(np.average(temp12[i][ind_wavlen800:
                                                        ind_wavlen998]))
    VIS_NIR_avg_tms_ground_asyv.append(np.average(temp13[i][ind_wavlen800:
                                                        ind_wavlen998]))
    VIS_NIR_std_tms_ground_asyv.append(np.average(temp14[i][ind_wavlen800:
                                                        ind_wavlen998]))
for p in range(0, len(avg_tms_cement[0]), 1):
    VIS_NIR_avg_tms_cement.append(np.average(temp15[p][ind_wavlen800:
                                                        ind_wavlen998]))
    VIS_NIR_std_tms_cement.append(np.average(temp16[p][ind_wavlen800:
```

```
                                                    ind_wavlen998]))


#plotting different figures


#decrease in transmission bar chart
positions = np.linspace(350,950,13)
plt.figure(1)
for i in range(0,len(avg_diff_tms_aswan),1):
    if i==0:
        plt.bar(positions + (i* 50)/len(avg_diff_tms_aswan),
                avg_diff_tms_aswan[i], width=8.33,
                yerr=std_diff_tms_aswan[i], label='_nolegend_')
    else:
        plt.bar(positions + (i * 50) / len(avg_diff_tms_aswan), avg_
                diff_tms_aswan[i], width=8.33, yerr=std_diff_tms_aswan[i])
plt.title("Paneldust Egypt I", fontsize=30)
leg = plt.legend(chosen_den_aswan,fontsize=16, loc=2)
leg.set_title("Density [$g/m^2$]", prop={'size':'18'})
plt.xlabel('Wavelength [nm]',size=18)
plt.xticks([350,400,450,500,550,600,650,700,750,800,850,900,950,1000],
               fontsize=16)
plt.ylabel('Transmission loss [%]', size=18)
plt.yticks(fontsize=16)
plt.grid(True)

plt.figure(2)
for i in range(0,len(avg_diff_tms_ejre),1):
    if i==0:
        plt.bar(positions + (i* 50)/len(avg_diff_tms_ejre),
                avg_diff_tms_ejre[i], width=8.33,
                yerr=std_diff_tms_ejre[i], label='_nolegend_')
    else:
        plt.bar(positions + (i * 50) / len(avg_diff_tms_ejre),
                avg_diff_tms_ejre[i], width=8.33,
                yerr=std_diff_tms_ejre[i])
plt.title("Paneldust Jordan I", fontsize=30)
leg = plt.legend(chosen_den_ejre,fontsize=16, loc=2)
leg.set_title("Density [$g/m^2$]", prop={'size':'18'})
plt.xlabel('Wavelength [nm]',size=18)
plt.xticks([350,400,450,500,550,600,650,700,750,800,850,900,950,1000],
              fontsize=16)
plt.ylabel('Transmission loss [%]', size=18)
plt.yticks(fontsize=16)
plt.grid(True)

plt.figure(3)
for i in range(0,len(avg_diff_tms_oryx),1):
    if i==0:
        plt.bar(positions + (i* 50)/len(avg_diff_tms_oryx),
                avg_diff_tms_oryx[i], width=8.33,
                yerr=std_diff_tms_oryx[i], label='_nolegend_')
    else:
        plt.bar(positions + (i * 50) / len(avg_diff_tms_oryx),
                avg_diff_tms_oryx[i], width=8.33,
                yerr=std_diff_tms_oryx[i])
plt.title("Paneldust Jordan II", fontsize=30)
leg = plt.legend(chosen_den_oryx,fontsize=16, loc=2)
leg.set_title("Density [$g/m^2$]", prop={'size':'18'})
```

```
plt.xlabel('Wavelength [nm]',size=18)
plt.xticks([350,400,450,500,550,600,650,700,750,800,850,900,950,1000],
               fontsize=16)
plt.ylabel('Transmission loss [%]', size=18)
plt.yticks(fontsize=16)
plt.grid(True)

plt.figure(4)
for i in range(0,len(avg_diff_tms_ground_aswan),1):
    if i==0:
        plt.bar(positions + (i* 50)/len(avg_diff_tms_ground_aswan),
                avg_diff_tms_ground_aswan[i], width=8.33,
                yerr=std_diff_tms_ground_aswan[i], label='_nolegend_')
    else:
        plt.bar(positions + (i * 50) / len(avg_diff_tms_ground_aswan),
                avg_diff_tms_ground_aswan[i], width=8.33,
                yerr=std_diff_tms_ground_aswan[i])
plt.title("Grounddust Egypt I", fontsize=30)
leg = plt.legend(chosen_den_ground_aswan,fontsize=16, loc=2)
leg.set_title("Density [$g/m^2$]", prop={'size':'18'})
plt.xlabel('Wavelength [nm]',size=18)
plt.xticks([350,400,450,500,550,600,650,700,750,800,850,900,950,1000],
               fontsize=16)
plt.ylabel('Transmission loss [%]', size=18)
plt.yticks(fontsize=16)
plt.grid(True)

plt.figure(5)
for i in range(0,len(avg_diff_tms_ground_ejre),1):
    if i==0:
        plt.bar(positions + (i* 50)/len(avg_diff_tms_ground_ejre),
                avg_diff_tms_ground_ejre[i], width=8.33,
                yerr=std_diff_tms_ground_ejre[i], label='_nolegend_')
    else:
        plt.bar(positions + (i * 50) / len(avg_diff_tms_ground_ejre),
                avg_diff_tms_ground_ejre[i], width=8.33,
                yerr=std_diff_tms_ground_ejre[i])
plt.title("Grounddust Jordan I", fontsize=30)
leg = plt.legend(chosen_den_ground_ejre,fontsize=16, loc=2)
leg.set_title("Density [$g/m^2$]", prop={'size':'18'})
plt.xlabel('Wavelength [nm]',size=18)
plt.xticks([350,400,450,500,550,600,650,700,750,800,850,900,950,1000],
               fontsize=16)
plt.ylabel('Transmission loss [%]', size=18)
plt.yticks(fontsize=16)
plt.grid(True)

plt.figure(6)
for i in range(0,len(avg_diff_tms_ground_oryx),1):
    if i==0:
        plt.bar(positions + (i* 50)/len(avg_diff_tms_ground_oryx),
                avg_diff_tms_ground_oryx[i], width=8.33,
                yerr=std_diff_tms_ground_oryx[i], label='_nolegend_')
    else:
        plt.bar(positions + (i * 50) / len(avg_diff_tms_ground_oryx),
                avg_diff_tms_ground_oryx[i], width=8.33,
                yerr=std_diff_tms_ground_oryx[i])
plt.title("Grounddust Jordan II", fontsize=30)
leg = plt.legend(chosen_den_ground_oryx,fontsize=16, loc=2)
leg.set_title("Density [$g/m^2$]", prop={'size':'18'})
```

```
plt.xlabel('Wavelength [nm]',size=18)
plt.xticks([350,400,450,500,550,600,650,700,750,800,850,900,950,1000],
               fontsize=16)
plt.ylabel('Transmission loss [%]', size=18)
plt.yticks(fontsize=16)
plt.grid(True)

plt.figure(7)
for i in range(0,len(avg_diff_tms_ground_asyv),1):
    if i==0:
        plt.bar(positions + (i* 50)/len(avg_diff_tms_ground_asyv),
                avg_diff_tms_ground_asyv[i], width=8.33,
                yerr=std_diff_tms_ground_asyv[i], label='_nolegend_')
    else:
        plt.bar(positions + (i * 50) / len(avg_diff_tms_ground_asyv),
                avg_diff_tms_ground_asyv[i], width=8.33,
                yerr=std_diff_tms_ground_asyv[i])
plt.title("Grounddust Rwanda I", fontsize=30)
leg = plt.legend(chosen_den_ground_asyv,fontsize=16, loc=2)
leg.set_title("Density [$g/m^2$]", prop={'size':'18'})
plt.xlabel('Wavelength [nm]',size=18)
plt.xticks([350,400,450,500,550,600,650,700,750,800,850,900,950,1000],
               fontsize=16)
plt.ylabel('Transmission loss [%]', size=18)
plt.yticks(fontsize=16)
plt.grid(True)

plt.figure(8)
for i in range(0,len(avg_diff_tms_cement),1):
    if i==0:
        plt.bar(positions + (i* 50)/len(avg_diff_tms_cement),
                avg_diff_tms_cement[i], width=8.33,
                yerr=std_diff_tms_cement[i], label='_nolegend_')
    else:
        plt.bar(positions + (i * 50) / len(avg_diff_tms_cement),
                avg_diff_tms_cement[i], width=8.33,
                yerr=std_diff_tms_cement[i])
plt.title("Cement dust", fontsize=30)
leg = plt.legend(chosen_den_cement,fontsize=16, loc=2)
leg.set_title("Density [$g/m^2$]", prop={'size':'18'})
plt.xlabel('Wavelength [nm]',size=18)
plt.xticks([350,400,450,500,550,600,650,700,750,800,850,900,950,1000],
               fontsize=16)
plt.ylabel('Transmission loss [%]', size=18)
plt.yticks(fontsize=16)
plt.grid(True)

plt.show()
'''
'''
#Plot Transmission spectral soluted, for appendix
plt.figure(1)
plt.title('Spectral transmission: Paneldust Egypt I', fontsize=30)
plt.plot(wavlen,avg_tms_aswan)
plt.xlabel('Wavelength [nm]',size=18)
plt.ylabel('Transmission [%]', size=18)
plt.xticks([350,400,450,500,550,600,650,700,750,800,850,900,950,1000],
               fontsize=16)
plt.yticks(fontsize=16)

plt.figure(2)
```

```
plt.title('Spectral transmission: Paneldust Jordan I', fontsize=30)
plt.plot(wavlen,avg_tms_ejre)
plt.xlabel('Wavelength [nm]',size=18)
plt.ylabel('Transmission [%]', size=18)
plt.xticks([350,400,450,500,550,600,650,700,750,800,850,900,950,1000],
               fontsize=16)
plt.yticks(fontsize=16)

plt.figure(3)
plt.title('Spectral transmission: Paneldust Jordan II', fontsize=30)
plt.plot(wavlen,avg_tms_oryx)
plt.xlabel('Wavelength [nm]',size=18)
plt.ylabel('Transmission [%]', size=18)
plt.xticks([350,400,450,500,550,600,650,700,750,800,850,900,950,1000],
               fontsize=16)
plt.yticks(fontsize=16)

plt.figure(4)
plt.title('Spectral transmission: Grounddust Egypt I', fontsize=30)
plt.plot(wavlen,avg_tms_ground_aswan)
plt.xlabel('Wavelength [nm]',size=18)
plt.ylabel('Transmission [%]', size=18)
plt.xticks([350,400,450,500,550,600,650,700,750,800,850,900,950,1000],
               fontsize=16)
plt.yticks(fontsize=16)

plt.figure(5)
plt.title('Spectral transmission: Grounddust Jordan I', fontsize=30)
plt.plot(wavlen,avg_tms_ground_ejre)
plt.xlabel('Wavelength [nm]',size=18)
plt.ylabel('Transmission [%]', size=18)
plt.xticks([350,400,450,500,550,600,650,700,750,800,850,900,950,1000],
               fontsize=16)
plt.yticks(fontsize=16)

plt.figure(6)
plt.title('Spectral transmission: Grounddust Jordan II', fontsize=30)
plt.plot(wavlen,avg_tms_ground_oryx)
plt.xlabel('Wavelength [nm]',size=18)
plt.ylabel('Transmission [%]', size=18)
plt.xticks([350,400,450,500,550,600,650,700,750,800,850,900,950,1000],
               fontsize=16)
plt.yticks(fontsize=16)

plt.figure(7)
plt.title('Spectral transmission: Grounddust Rwanda I', fontsize=30)
plt.plot(wavlen,avg_tms_ground_asyv)
plt.xlabel('Wavelength [nm]',size=18)
plt.ylabel('Transmission [%]', size=18)
plt.xticks([350,400,450,500,550,600,650,700,750,800,850,900,950,1000],
               fontsize=16)
plt.yticks(fontsize=16)

plt.figure(8)
plt.title('Spectral transmission: Cement', fontsize=30)
plt.plot(wavlen,avg_tms_cement)
plt.xlabel('Wavelength [nm]',size=18)
plt.ylabel('Transmission [%]', size=18)
plt.xticks([350,400,450,500,550,600,650,700,750,800,850,900,950,1000],
               fontsize=16)
plt.yticks(fontsize=16)
```

```
plt.show()
'''


'''
#Plot Transmission vs density



#Scatterplot showing all samples with logarithmic scale on y-axis, no
trendlines
plt.figure(1)
label=("Panel Jordan I","Panel Jordan II","Panel Egypt I","Ground Jordan
I",
                "Ground Jordan II","Ground Egypt I","Ground Rwanda I", "Ce-
ment")
plt.scatter(den_ejre,tot_avg_tms_ejre,c='chartreuse',marker='o',  s=150)
plt.errorbar(den_ejre,tot_avg_tms_ejre, yerr=tot_std_tms_ejre,
                xerr=den_uncertainty, ecolor='black', linestyle="None")
plt.scatter(den_oryx,tot_avg_tms_oryx,c='salmon',marker='o',  s=150)
plt.errorbar(den_oryx,tot_avg_tms_oryx, yerr=tot_std_tms_oryx,
                xerr=den_uncertainty, ecolor='black', linestyle="None")
plt.scatter(den_aswan,tot_avg_tms_aswan, c='lightskyblue',
                marker='o', s=150)
plt.errorbar(den_aswan,tot_avg_tms_aswan, yerr=tot_std_tms_aswan,
                xerr=den_uncertainty, ecolor='black',linestyle="None")
plt.scatter(den_ground_ejre, tot_avg_tms_ground_ejre, c='seagreen',
                marker='v', s=150)
plt.errorbar(den_ground_ejre, tot_avg_tms_ground_ejre,
                yerr=tot_std_tms_ground_ejre, xerr=den_uncertainty,
                ecolor='black',linestyle="None")
plt.scatter(den_ground_oryx, tot_avg_tms_ground_oryx, c='crimson',
                marker='v', s=150)
plt.errorbar(den_ground_oryx, tot_avg_tms_ground_oryx,
                yerr=tot_std_tms_ground_oryx, xerr=den_uncertainty,
                ecolor='black',linestyle="None")
plt.scatter(den_ground_aswan, tot_avg_tms_ground_aswan, c='darkblue',
                marker='v',  s=150)
plt.errorbar(den_ground_aswan, tot_avg_tms_ground_aswan,
                yerr=tot_std_tms_ground_aswan, xerr=den_uncertainty,
                ecolor='black',linestyle="None")
plt.scatter(den_ground_asyv, tot_avg_tms_ground_asyv, c='darkgrey',
                marker='v', s=150)
plt.errorbar(den_ground_asyv, tot_avg_tms_ground_asyv,
                yerr=tot_std_tms_ground_asyv, xerr=den_uncertainty,
                ecolor='black',linestyle="None")
plt.scatter(den_cement,tot_avg_tms_cement,c='fuchsia',marker='*',  s=150)
plt.errorbar(den_cement,tot_avg_tms_cement, yerr=tot_std_tms_cement,
                xerr=den_uncertainty, ecolor='black', linestyle="None")
plt.legend(label, fontsize=30)
plt.title('Mean spectral transmission vs density of dust', fontsize=40)
plt.xlabel('Density [$g/m^2$]',size=30)
plt.ylabel('Transmission [%]', size=30)
plt.xticks([0,25,50,75,100,125,150,175,200,225,250,275],fontsize=25)
plt.yscale('log')
plt.axes().yaxis.set_major_formatter(plt.ScalarFormatter())
plt.yticks([1,5,10,50,100],fontsize=25)
plt.ylim(0.45,110)
'''
'''
```

```
#Scatterplot all samples, no log-scale of y-axis, no trendlines
plt.figure(2)

label=("Panel Jordan I","Panel Jordan II","Panel Egypt I","Ground
       Jordan I",”Ground Jordan II","Ground Egypt I","Ground Rwanda I",
       "Cement")

plt.scatter(den_ejre,tot_avg_tms_ejre,c='chartreuse',marker='o',  s=150,
               label="Panel Jordan I")
plt.errorbar(den_ejre,tot_avg_tms_ejre, yerr=tot_std_tms_ejre,
               xerr=den_uncertainty, ecolor='black', linestyle="None")
plt.scatter(den_oryx,tot_avg_tms_oryx,c='salmon',marker='o', s=150,
               label="Panel Jordan II")
plt.errorbar(den_oryx,tot_avg_tms_oryx, yerr=tot_std_tms_oryx,
               xerr=den_uncertainty, ecolor='black', linestyle="None")
plt.scatter(den_aswan, tot_avg_tms_aswan, c='lightskyblue', marker='o',
               s=150, label="Panel Egypt I")
plt.errorbar(den_aswan, tot_avg_tms_aswan, yerr=tot_std_tms_aswan,
               xerr=den_uncertainty, ecolor='black',linestyle="None")
plt.scatter(den_ground_ejre, tot_avg_tms_ground_ejre, c='seagreen',
               marker='v', s=150, label="Ground Jordan I")
plt.errorbar(den_ground_ejre, tot_avg_tms_ground_ejre,
               yerr=tot_std_tms_ground_ejre, xerr=den_uncertainty,
               ecolor='black',linestyle="None")
plt.scatter(den_ground_oryx, tot_avg_tms_ground_oryx, c='crimson',
               marker='v', s=150, label="Ground Jordan II")
plt.errorbar(den_ground_oryx, tot_avg_tms_ground_oryx,
               yerr=tot_std_tms_ground_oryx, xerr=den_uncertainty,
               ecolor='black',linestyle="None")
plt.scatter(den_ground_aswan, tot_avg_tms_ground_aswan, c='darkblue',
               marker='v',  s=150, label="Ground Egypt I")
plt.errorbar(den_ground_aswan, tot_avg_tms_ground_aswan,
               yerr=tot_std_tms_ground_aswan, xerr=den_uncertainty,
               ecolor='black',linestyle="None")
plt.scatter(den_ground_asyv, tot_avg_tms_ground_asyv, c='darkgrey',
               marker='v', s=150, label="Ground Rwanda I")
plt.errorbar(den_ground_asyv, tot_avg_tms_ground_asyv,
               yerr=tot_std_tms_ground_asyv, xerr=den_uncertainty,
               ecolor='black',linestyle="None")
plt.scatter(den_cement, tot_avg_tms_cement, c='fuchsia', marker='*', s=150,
               label="Cement")
plt.errorbar(den_cement, tot_avg_tms_cement, yerr=tot_std_tms_cement,
               xerr=den_uncertainty, ecolor='black',linestyle="None")
plt.legend(label, fontsize=30)
plt.title('Mean spectral transmission vs density of dust', fontsize=40)
plt.xlabel('Density [$g/m^2$]',size=30)
plt.ylabel('Transmission [%]', size=30)
plt.xticks([0,25,50,75,100,125,150,175,200,225,250,275],fontsize=25)
plt.yticks(fontsize=25)
plt.ylim(0,110)

'''
'''
plt.figure(2)
#Scatterplot showing all samples with exponential trendlines

# define trendline function
def trendline_func(density, A, alfa):
    return A * np.exp(-alfa*density)
# curve fit
```

```
p0 = (1.,1.e-5) # starting search koefs

#Panel Jordan I
popt, pcov = curve_fit(trendline_func, den_ejre, tot_avg_tms_ejre, p0)
A, alfa = popt
# draw trendline
x2 = np.linspace(0, 200,50)
y2 = trendline_func(x2, A, alfa)
x3=np.array(den_ejre)
y3 = trendline_func(x3, A, alfa)
r2=r2_score(tot_avg_tms_ejre,y3)
plt.plot(x2, y2, color='lime', label='Fit. func Panel Jordan I: $T(\u03C1)
                =e^{-%.4f \u03C1}  ; R^2=%.3f$' % (alfa,r2))
plt.scatter(den_ejre, tot_avg_tms_ejre, c='chartreuse', marker='o', s=150,
                label="Panel Jordan I")
plt.errorbar(den_ejre, tot_avg_tms_ejre, yerr=tot_std_tms_ejre,
                xerr=den_uncertainty, ecolor='black', linestyle="None")

#Panel Jordan II
popt, pcov = curve_fit(trendline_func, den_oryx, tot_avg_tms_oryx, p0)
A, alfa = popt
# draw trendline
x2 = np.linspace(0, 275,30)
y2 = trendline_func(x2, A, alfa)
x3=np.array(den_oryx)
y3 = trendline_func(x3, A, alfa)
r2=r2_score(tot_avg_tms_oryx,y3)
plt.plot(x2, y2, color='r', label='Fit. func Panel Jordan II: $T(\u03C1) =
                e^{-%.4f \u03C1}; R^2=%.3f$' % (alfa,r2))
plt.scatter(den_oryx,tot_avg_tms_oryx,c='salmon',marker='o', s=150,
                label="Panel Jordan II")
plt.errorbar(den_oryx,tot_avg_tms_oryx, yerr=tot_std_tms_oryx,
                xerr=den_uncertainty, ecolor='black', linestyle="None")

#Panel Egypt I
popt, pcov = curve_fit(trendline_func, den_aswan, tot_avg_tms_aswan, p0)
A, alfa = popt
# draw trendline
x2 = np.linspace(0, 200,30)
y2 = trendline_func(x2, A, alfa)
x3=np.array(den_aswan)
y3 = trendline_func(x3, A, alfa)
r2=r2_score(tot_avg_tms_aswan,y3)
plt.plot(x2, y2, color='b', label='Fit. func Panel Egypt I: $T(\u03C1) =
                e^{-%.4f \u03C1} ; R^2=%.3f$' % (alfa,r2))
plt.scatter(den_aswan, tot_avg_tms_aswan, c='lightskyblue', marker='o',
                s=150, label="Panel Egypt I")
plt.errorbar(den_aswan, tot_avg_tms_aswan, yerr=tot_std_tms_aswan,
                xerr=den_uncertainty, ecolor='black',linestyle="None")

#Ground Jordan I
popt, pcov = curve_fit(trendline_func, den_ground_ejre,
tot_avg_tms_ground_ejre, p0)
A, alfa = popt
# draw trendline
x2 = np.linspace(0, 250,30)
y2 = trendline_func(x2, A, alfa)
x3=np.array(den_ground_ejre)
y3 = trendline_func(x3, A, alfa)
r2=r2_score(tot_avg_tms_ground_ejre,y3)
plt.plot(x2, y2, 'lime',linestyle='dashed', label='Fit. func Ground Jordan
```

```
                I:$T(\u03C1) = e^{-%.4f \u03C1} ; R^2=%.3f$' % (alfa,r2))
plt.scatter(den_ground_ejre, tot_avg_tms_ground_ejre, c='seagreen',
                marker='v', s=150, label="Ground Jordan I")
plt.errorbar(den_ground_ejre, tot_avg_tms_ground_ejre,
                yerr=tot_std_tms_ground_ejre, xerr=den_uncertainty,
                ecolor='black',linestyle="None")

#Ground Jordan II
popt, pcov = curve_fit(trendline_func, den_ground_oryx,
tot_avg_tms_ground_oryx, p0)
A, alfa = popt
# draw trendline
x2 = np.linspace(0, 290,30)
y2 = trendline_func(x2, A, alfa)
x3=np.array(den_ground_oryx)
y3 = trendline_func(x3, A, alfa)
r2=r2_score(tot_avg_tms_ground_oryx,y3)
plt.plot(x2, y2, 'r--', label='Fit. func Ground Jordan II: $T(\u03C1) =
                e^{-%.4f \u03C1} ; R^2=%.3f$' % (alfa,r2))
plt.scatter(den_ground_oryx, tot_avg_tms_ground_oryx, c='crimson',
                marker='v', s=150, label="Ground Jordan II")
plt.errorbar(den_ground_oryx, tot_avg_tms_ground_oryx,
                yerr=tot_std_tms_ground_oryx, xerr=den_uncertainty,
                ecolor='black',linestyle="None")

#Ground Egypt I
popt, pcov = curve_fit(trendline_func, den_ground_aswan,
tot_avg_tms_ground_aswan, p0)
A, alfa = popt
# draw trendline
x2 = np.linspace(0, 300,30)
y2 = trendline_func(x2, A, alfa)
x3=np.array(den_ground_aswan)
y3 = trendline_func(x3, A, alfa)
r2=r2_score(tot_avg_tms_ground_aswan,y3)
plt.plot(x2, y2, 'b--', label='Fit. func Ground Egypt I: $T(\u03C1) =
                e^{-%.4f \u03C1} ; R^2=%.3f$' % (alfa,r2))
plt.scatter(den_ground_aswan, tot_avg_tms_ground_aswan, c='darkblue',
                marker='v',  s=150, label="Ground Egypt I")
plt.errorbar(den_ground_aswan, tot_avg_tms_ground_aswan,
                yerr=tot_std_tms_ground_aswan, xerr=den_uncertainty,
                ecolor='black',linestyle="None")

#Ground Rwanda I
popt, pcov = curve_fit(trendline_func, den_ground_asyv,
tot_avg_tms_ground_asyv, p0)
A, alfa = popt
# draw trendline
x2 = np.linspace(0, 225,30)
y2 = trendline_func(x2, A, alfa)
x3=np.array(den_ground_asyv)
y3 = trendline_func(x3, A, alfa)
r2=r2_score(tot_avg_tms_ground_asyv,y3)
plt.plot(x2, y2, 'k--', label='Fit. func Ground Rwanda I: $T(\u03C1) =
                e^{-%.4f \u03C1} ; R^2=%.3f$' % (alfa,r2))
plt.scatter(den_ground_asyv, tot_avg_tms_ground_asyv, c='darkgrey',
                marker='v', s=150, label="Ground Rwanda I")
plt.errorbar(den_ground_asyv, tot_avg_tms_ground_asyv,
                yerr=tot_std_tms_ground_asyv, xerr=den_uncertainty,
                ecolor='black',linestyle="None")
```

```
#Cement
popt, pcov = curve_fit(trendline_func, den_cement, tot_avg_tms_cement, p0)
A, alfa = popt
# draw trendline
x2 = np.linspace(0, 50,30)
y2 = trendline_func(x2, A, alfa)
x3=np.array(den_cement)
y3 = trendline_func(x3, A, alfa)
r2=r2_score(tot_avg_tms_cement,y3)
plt.plot(x2, y2, 'm--', label='Fit. func Cement: $T(\u03C1) =
                e^{-%.4f \u03C1} ; R^2=%.3f$' % (alfa,r2))
plt.scatter(den_cement, tot_avg_tms_cement, c='fuchsia', marker='*', s=150,
                label="Cement")
plt.errorbar(den_cement, tot_avg_tms_cement, yerr=tot_std_tms_cement,
                xerr=den_uncertainty, ecolor='black',linestyle="None")

plt.legend(fontsize=16)
plt.title('Mean spectral transmission vs density of dust', fontsize=30)
plt.xlabel('Density \u03C1 [$g/m^2$]',size=18)
plt.ylabel('Transmission T(\u03C1) [%]', size=18)
plt.xticks([0,25,50,75,100,125,150,175,200,225,250,275],fontsize=16)
plt.yticks(fontsize=16)
plt.ylim(0,110)
'''

'''
#plt.figure(3)
#Scatterplot showing all exponential trendlines only

# define trendline function
def trendline_func(density, A, alfa):
    return A * np.exp(-alfa*density)
# curve fit
p0 = (1.,1.e-5) # starting search koefs

#Panel Jordan I
popt, pcov = curve_fit(trendline_func, den_ejre, tot_avg_tms_ejre, p0)
A, alfa = popt
# draw trendline
x2 = np.linspace(0, 200,50)
y2 = trendline_func(x2, A, alfa)
x3=np.array(den_ejre)
y3 = trendline_func(x3, A, alfa)
r2=r2_score(tot_avg_tms_ejre,y3)
plt.plot(x2, y2, color='lime', label='Fit. func Panel Jordan I: $T(\u03C1)
                =e^{-%.4f \u03C1}  ; R^2=%.3f$' % (alfa,r2))


#Panel Jordan II
popt, pcov = curve_fit(trendline_func, den_oryx, tot_avg_tms_oryx, p0)
A, alfa = popt
# draw trendline
x2 = np.linspace(0, 275,30)
y2 = trendline_func(x2, A, alfa)
x3=np.array(den_oryx)
y3 = trendline_func(x3, A, alfa)
r2=r2_score(tot_avg_tms_oryx,y3)
plt.plot(x2, y2, color='r', label='Fit. func Panel Jordan II: $T(\u03C1) =
                e^{-%.4f \u03C1}; R^2=%.3f$' % (alfa,r2))
```

```
#Panel Egypt I
popt, pcov = curve_fit(trendline_func, den_aswan, tot_avg_tms_aswan, p0)
A, alfa = popt
# draw trendline
x2 = np.linspace(0, 200,30)
y2 = trendline_func(x2, A, alfa)
x3=np.array(den_aswan)
y3 = trendline_func(x3, A, alfa)
r2=r2_score(tot_avg_tms_aswan,y3)
plt.plot(x2, y2, color='b', label='Fit. func Panel Egypt I: $T(\u03C1) =
                e^{-%.4f \u03C1} ; R^2=%.3f$' % (alfa,r2))


#Ground Jordan I
popt, pcov = curve_fit(trendline_func, den_ground_ejre,
tot_avg_tms_ground_ejre, p0)
A, alfa = popt
# draw trendline
x2 = np.linspace(0, 250,30)
y2 = trendline_func(x2, A, alfa)
x3=np.array(den_ground_ejre)
y3 = trendline_func(x3, A, alfa)
r2=r2_score(tot_avg_tms_ground_ejre,y3)
plt.plot(x2, y2, 'lime',linestyle='dashed', label='Fit. func Ground Jordan
                I:$T(\u03C1) = e^{-%.4f \u03C1} ; R^2=%.3f$' % (alfa,r2))


#Ground Jordan II
popt, pcov = curve_fit(trendline_func, den_ground_oryx,
tot_avg_tms_ground_oryx, p0)
A, alfa = popt
# draw trendline
x2 = np.linspace(0, 290,30)
y2 = trendline_func(x2, A, alfa)
x3=np.array(den_ground_oryx)
y3 = trendline_func(x3, A, alfa)
r2=r2_score(tot_avg_tms_ground_oryx,y3)
plt.plot(x2, y2, 'r--', label='Fit. func Ground Jordan II: $T(\u03C1) =
                e^{-%.4f \u03C1} ; R^2=%.3f$' % (alfa,r2))


#Ground Egypt I
popt, pcov = curve_fit(trendline_func, den_ground_aswan,
tot_avg_tms_ground_aswan, p0)
A, alfa = popt
# draw trendline
x2 = np.linspace(0, 300,30)
y2 = trendline_func(x2, A, alfa)
x3=np.array(den_ground_aswan)
y3 = trendline_func(x3, A, alfa)
r2=r2_score(tot_avg_tms_ground_aswan,y3)
plt.plot(x2, y2, 'b--', label='Fit. func Ground Egypt I: $T(\u03C1) =
                e^{-%.4f \u03C1} ; R^2=%.3f$' % (alfa,r2))

#Ground Rwanda I
popt, pcov = curve_fit(trendline_func, den_ground_asyv,
tot_avg_tms_ground_asyv, p0)
A, alfa = popt
# draw trendline
x2 = np.linspace(0, 225,30)
y2 = trendline_func(x2, A, alfa)
```

```
x3=np.array(den_ground_asyv)
y3 = trendline_func(x3, A, alfa)
r2=r2_score(tot_avg_tms_ground_asyv,y3)
plt.plot(x2, y2, 'k--', label='Fit. func Ground Rwanda I: $T(\u03C1) =
                e^{-%.4f \u03C1} ; R^2=%.3f$' % (alfa,r2))


#Cement
popt, pcov = curve_fit(trendline_func, den_cement, tot_avg_tms_cement, p0)
A, alfa = popt
# draw trendline
x2 = np.linspace(0, 50,30)
y2 = trendline_func(x2, A, alfa)
x3=np.array(den_cement)
y3 = trendline_func(x3, A, alfa)
r2=r2_score(tot_avg_tms_cement,y3)
plt.plot(x2, y2, 'm--', label='Fit. func Cement: $T(\u03C1) =
                e^{-%.4f \u03C1} ; R^2=%.3f$' % (alfa,r2))


plt.legend(fontsize=16)
plt.title('Mean spectral transmission vs density of dust', fontsize=30)
plt.xlabel('Density \u03C1 [$g/m^2$]',size=18)
plt.ylabel('Transmission T(\u03C1) [%]', size=18)
plt.xticks([0,25,50,75,100,125,150,175,200,225,250,275],fontsize=16)
plt.yticks(fontsize=16)
plt.ylim(0,110)

'''
'''
#Plot transmission vs density from 350-500nm
plt.figure(5)
#Scatterplot showing all samples with exponential trendlines

# define trendline function
def trendline_func(density, A, alfa):
    return A * np.exp(-alfa*density)
# curve fit
p0 = (1.,1.e-5) # starting search koefs

#Panel Jordan I
popt, pcov = curve_fit(trendline_func, den_ejre, UV_VIS_avg_tms_ejre, p0)
A, alfa_UV_VIS = popt
# draw trendline
x2 = np.linspace(0, 200,50)
y2 = trendline_func(x2, A, alfa_UV_VIS)
x3=np.array(den_ejre)
y3 = trendline_func(x3, A, alfa_UV_VIS)
r2=r2_score(UV_VIS_avg_tms_ejre,y3)
plt.plot(x2, y2, color='lime', label='Fit. func Panel Jordan I: $T(\u03C1)
                =e^{-%.4f \u03C1}  ; R^2=%.3f$' % (alfa_UV_VIS,r2))
plt.scatter(den_ejre, UV_VIS_avg_tms_ejre, c='chartreuse', marker='o',
                s=150, label="Panel Jordan I")
plt.errorbar(den_ejre, UV_VIS_avg_tms_ejre, yerr=UV_VIS_std_tms_ejre,
                xerr=den_uncertainty, ecolor='black', linestyle="None")

#Panel Jordan II
popt, pcov = curve_fit(trendline_func, den_oryx, UV_VIS_avg_tms_oryx, p0)
A, alfa_UV_VIS = popt
# draw trendline
x2 = np.linspace(0, 275,50)
```

```
y2 = trendline_func(x2, A, alfa_UV_VIS)
x3=np.array(den_oryx)
y3 = trendline_func(x3, A, alfa_UV_VIS)
r2=r2_score(UV_VIS_avg_tms_oryx,y3)
plt.plot(x2, y2, color='r', label='Fit. func Panel Jordan II: $T(\u03C1) =
                e^{-%.4f \u03C1}  ; R^2=%.3f$' % (alfa_UV_VIS,r2))
plt.scatter(den_oryx,UV_VIS_avg_tms_oryx,c='salmon',marker='o',  s=150,
                label="Panel Jordan II")
plt.errorbar(den_oryx,UV_VIS_avg_tms_oryx, yerr=UV_VIS_std_tms_oryx,
                xerr=den_uncertainty, ecolor='black', linestyle="None")

#Panel Egypt I
popt, pcov = curve_fit(trendline_func, den_aswan, UV_VIS_avg_tms_aswan, p0)
A, alfa_UV_VIS = popt
# draw trendline
x2 = np.linspace(0, 200,50)
y2 = trendline_func(x2, A, alfa_UV_VIS)
x3=np.array(den_aswan)
y3 = trendline_func(x3, A, alfa_UV_VIS)
r2=r2_score(UV_VIS_avg_tms_aswan,y3)
plt.plot(x2, y2, color='b', label='Fit. func Panel Egypt I: $T(\u03C1) =
                e^{-%.4f \u03C1} ; R^2=%.3f$' % (alfa_UV_VIS,r2))
plt.scatter(den_aswan, UV_VIS_avg_tms_aswan, c='lightskyblue', marker='o',
                s=150, label="Panel Egypt I")
plt.errorbar(den_aswan, UV_VIS_avg_tms_aswan, yerr=UV_VIS_std_tms_aswan,
                xerr=den_uncertainty, ecolor='black',linestyle="None")

#Ground Jordan I
popt, pcov = curve_fit(trendline_func, den_ground_ejre,
UV_VIS_avg_tms_ground_ejre, p0)
A, alfa_UV_VIS = popt
# draw trendline
x2 = np.linspace(0, 250,30)
y2 = trendline_func(x2, A, alfa_UV_VIS)
x3=np.array(den_ground_ejre)
y3 = trendline_func(x3, A, alfa_UV_VIS)
r2=r2_score(UV_VIS_avg_tms_ground_ejre,y3)
plt.plot(x2, y2, 'lime',linestyle='dashed', label='Fit. func Ground Jordan
                I:$T(\u03C1) = e^{-%.4f \u03C1} ; R^2=%.3f$'
                % (alfa_UV_VIS,r2))
plt.scatter(den_ground_ejre, UV_VIS_avg_tms_ground_ejre, c='seagreen',
                marker='v', s=150, label="Ground Jordan I")
plt.errorbar(den_ground_ejre, UV_VIS_avg_tms_ground_ejre,
                yerr=UV_VIS_std_tms_ground_ejre, xerr=den_uncertainty,
                ecolor='black',linestyle="None")

#Ground Jordan II
popt, pcov = curve_fit(trendline_func, den_ground_oryx,
UV_VIS_avg_tms_ground_oryx, p0)
A, alfa_UV_VIS = popt
# draw trendline
x2 = np.linspace(0, 290,30)
y2 = trendline_func(x2, A, alfa_UV_VIS)
x3=np.array(den_ground_oryx)
y3 = trendline_func(x3, A, alfa_UV_VIS)
r2=r2_score(UV_VIS_avg_tms_ground_oryx,y3)
plt.plot(x2, y2, 'r--', label='Fit. func Ground Jordan II: $T(\u03C1) =
                e^{-%.4f \u03C1} ; R^2=%.3f$' % (alfa_UV_VIS,r2))
plt.scatter(den_ground_oryx, UV_VIS_avg_tms_ground_oryx, c='crimson',
                marker='v', s=150, label="Ground Jordan II")
plt.errorbar(den_ground_oryx, UV_VIS_avg_tms_ground_oryx,
```

```
                yerr=UV_VIS_std_tms_ground_oryx, xerr=den_uncertainty,
                ecolor='black',linestyle="None")

#Ground Egypt I
popt, pcov = curve_fit(trendline_func, den_ground_aswan,
UV_VIS_avg_tms_ground_aswan, p0)
A, alfa_UV_VIS = popt
# draw trendline
x2 = np.linspace(0, 300,30)
y2 = trendline_func(x2, A, alfa_UV_VIS)
x3=np.array(den_ground_aswan)
y3 = trendline_func(x3, A, alfa_UV_VIS)
r2=r2_score(UV_VIS_avg_tms_ground_aswan,y3)
plt.plot(x2, y2, 'b--', label='Fit. func Ground Egypt I: $T(\u03C1) =
                e^{-%.4f \u03C1} ; R^2=%.3f$' % (alfa_UV_VIS,r2))
plt.scatter(den_ground_aswan, UV_VIS_avg_tms_ground_aswan, c='darkblue',
                marker='v',  s=150, label="Ground Egypt I")
plt.errorbar(den_ground_aswan, UV_VIS_avg_tms_ground_aswan,
                yerr=UV_VIS_std_tms_ground_aswan, xerr=den_uncertainty,
                ecolor='black',linestyle="None")

#Ground Rwanda I
popt, pcov = curve_fit(trendline_func, den_ground_asyv,
UV_VIS_avg_tms_ground_asyv, p0)
A, alfa_UV_VIS = popt
# draw trendline
x2 = np.linspace(0, 225,30)
y2 = trendline_func(x2, A, alfa_UV_VIS)
x3=np.array(den_ground_asyv)
y3 = trendline_func(x3, A, alfa_UV_VIS)
r2=r2_score(UV_VIS_avg_tms_ground_asyv,y3)
plt.plot(x2, y2, 'k--', label='Fit. func Ground Rwanda I: $T(\u03C1) =
                e^{-%.4f \u03C1} ; R^2=%.3f$' % (alfa_UV_VIS,r2))
plt.scatter(den_ground_asyv, UV_VIS_avg_tms_ground_asyv, c='darkgrey',
                marker='v', s=150, label="Ground Rwanda I")
plt.errorbar(den_ground_asyv, UV_VIS_avg_tms_ground_asyv,
                yerr=UV_VIS_std_tms_ground_asyv, xerr=den_uncertainty,
                ecolor='black',linestyle="None")

#Cement
popt, pcov = curve_fit(trendline_func, den_cement, UV_VIS_avg_tms_cement,
p0)
A, alfa_UV_VIS = popt
# draw trendline
x2 = np.linspace(0, 50,30)
y2 = trendline_func(x2, A, alfa_UV_VIS)
x3=np.array(den_cement)
y3 = trendline_func(x3, A, alfa_UV_VIS)
r2=r2_score(UV_VIS_avg_tms_cement,y3)
plt.plot(x2, y2, 'm--', label='Fit. func Cement: $T(\u03C1) =
                e^{-%.4f \u03C1} ; R^2=%.3f$' % (alfa_UV_VIS,r2))
plt.scatter(den_cement, UV_VIS_avg_tms_cement, c='fuchsia', marker='*',
                s=150, label="Cement")
plt.errorbar(den_cement, UV_VIS_avg_tms_cement, yerr=UV_VIS_std_tms_cement,
                xerr=den_uncertainty, ecolor='black',linestyle="None")


plt.legend(fontsize=16)
plt.title('Mean spectral transmission in UV/VIS (350-500nm) vs density of
                dust', fontsize=30)
plt.xlabel('Density \u03C1 [$g/m^2$]',size=18)
```

```
plt.ylabel('Transmission T(\u03C1) [%]', size=18)
plt.xticks([0,25,50,75,100,125,150,175,200,225,250,275],fontsize=16)
plt.yticks(fontsize=16)
plt.ylim(0,110)


#Plot transmission vs density from 500-800nm
plt.figure(6)
#Scatterplot showing all samples with exponential trendlines

# define trendline function
def trendline_func(density, A, alfa):
    return A * np.exp(-alfa*density)
# curve fit
p0 = (1.,1.e-5) # starting search koefs

#Panel Jordan I
popt, pcov = curve_fit(trendline_func, den_ejre, VIS_avg_tms_ejre, p0)
A, alfa_VIS = popt
# draw trendline
x2 = np.linspace(0, 200,50)
y2 = trendline_func(x2, A, alfa_VIS)
x3=np.array(den_ejre)
y3 = trendline_func(x3, A, alfa_VIS)
r2=r2_score(VIS_avg_tms_ejre,y3)
plt.plot(x2, y2, color='lime', label='Fit. func Panel Jordan I: $T(\u03C1)
                =e^{-%.4f \u03C1}  ; R^2=%.3f$' % (alfa_VIS,r2))
plt.scatter(den_ejre, VIS_avg_tms_ejre, c='chartreuse', marker='o', s=150,
                label="Panel Jordan I")
plt.errorbar(den_ejre, VIS_avg_tms_ejre, yerr=VIS_std_tms_ejre,
                xerr=den_uncertainty, ecolor='black', linestyle="None")

#Panel Jordan II
popt, pcov = curve_fit(trendline_func, den_oryx, VIS_avg_tms_oryx, p0)
A, alfa_VIS = popt
# draw trendline
x2 = np.linspace(0, 275,50)
y2 = trendline_func(x2, A, alfa_VIS)
x3=np.array(den_oryx)
y3 = trendline_func(x3, A, alfa_VIS)
r2=r2_score(VIS_avg_tms_oryx,y3)
plt.plot(x2, y2, color='r', label='Fit. func Panel Jordan II: $T(\u03C1) =
                e^{-%.4f \u03C1}  ; R^2=%.3f$' % (alfa_VIS,r2))
plt.scatter(den_oryx,VIS_avg_tms_oryx,c='salmon',marker='o',  s=150,
                label="Panel Jordan II")
plt.errorbar(den_oryx,VIS_avg_tms_oryx, yerr=VIS_std_tms_oryx,
                xerr=den_uncertainty, ecolor='black', linestyle="None")

#Panel Egypt I
popt, pcov = curve_fit(trendline_func, den_aswan, VIS_avg_tms_aswan, p0)
A, alfa_VIS = popt
# draw trendline
x2 = np.linspace(0, 200,50)
y2 = trendline_func(x2, A, alfa_VIS)
x3=np.array(den_aswan)
y3 = trendline_func(x3, A, alfa_VIS)
r2=r2_score(VIS_avg_tms_aswan,y3)
plt.plot(x2, y2, color='b', label='Fit. func Panel Egypt I: $T(\u03C1) =
                e^{-%.4f \u03C1} ; R^2=%.3f$' % (alfa_VIS,r2))
plt.scatter(den_aswan, VIS_avg_tms_aswan, c='lightskyblue', marker='o',
```

```
                s=150, label="Panel Egypt I")
plt.errorbar(den_aswan, VIS_avg_tms_aswan, yerr=VIS_std_tms_aswan,
                xerr=den_uncertainty, ecolor='black',linestyle="None")

#Ground Jordan I
popt, pcov = curve_fit(trendline_func, den_ground_ejre,
VIS_avg_tms_ground_ejre, p0)
A, alfa_VIS = popt
# draw trendline
x2 = np.linspace(0, 250,30)
y2 = trendline_func(x2, A, alfa_VIS)
x3=np.array(den_ground_ejre)
y3 = trendline_func(x3, A, alfa_VIS)
r2=r2_score(VIS_avg_tms_ground_ejre,y3)
plt.plot(x2, y2, 'lime',linestyle='dashed', label='Fit. func Ground Jordan
                I:$T(\u03C1) = e^{-%.4f \u03C1} ; R^2=%.3f$'
                %(alfa_VIS,r2))
plt.scatter(den_ground_ejre, VIS_avg_tms_ground_ejre, c='seagreen',
                marker='v', s=150, label="Ground Jordan I")
plt.errorbar(den_ground_ejre, VIS_avg_tms_ground_ejre,
                yerr=VIS_std_tms_ground_ejre, xerr=den_uncertainty,
                ecolor='black',linestyle="None")

#Ground Jordan II
popt, pcov = curve_fit(trendline_func, den_ground_oryx,
VIS_avg_tms_ground_oryx, p0)
A, alfa_VIS = popt
# draw trendline
x2 = np.linspace(0, 290,30)
y2 = trendline_func(x2, A, alfa_VIS)
x3=np.array(den_ground_oryx)
y3 = trendline_func(x3, A, alfa_VIS)
r2=r2_score(VIS_avg_tms_ground_oryx,y3)
plt.plot(x2, y2, 'r--', label='Fit. func Ground Jordan II: $T(\u03C1) =
                e^{-%.4f \u03C1} ; R^2=%.3f$' % (alfa_VIS,r2))
plt.scatter(den_ground_oryx, VIS_avg_tms_ground_oryx, c='crimson',
                marker='v', s=150, label="Ground Jordan II")
plt.errorbar(den_ground_oryx, VIS_avg_tms_ground_oryx,
                yerr=VIS_std_tms_ground_oryx, xerr=den_uncertainty,
                ecolor='black',linestyle="None")

#Ground Egypt I
popt, pcov = curve_fit(trendline_func, den_ground_aswan,
VIS_avg_tms_ground_aswan, p0)
A, alfa_VIS = popt
# draw trendline
x2 = np.linspace(0, 300,30)
y2 = trendline_func(x2, A, alfa_VIS)
x3=np.array(den_ground_aswan)
y3 = trendline_func(x3, A, alfa_VIS)
r2=r2_score(VIS_avg_tms_ground_aswan,y3)
plt.plot(x2, y2, 'b--', label='Fit. func Ground Egypt I: $T(\u03C1) =
                e^{-%.4f \u03C1} ; R^2=%.3f$' % (alfa_VIS,r2))
plt.scatter(den_ground_aswan, VIS_avg_tms_ground_aswan, c='darkblue',
                marker='v',  s=150, label="Ground Egypt I")
plt.errorbar(den_ground_aswan, VIS_avg_tms_ground_aswan,
                yerr=VIS_std_tms_ground_aswan, xerr=den_uncertainty,
                ecolor='black',linestyle="None")

#Ground Rwanda I
popt, pcov = curve_fit(trendline_func, den_ground_asyv,
```

```
VIS_avg_tms_ground_asyv, p0)
A, alfa_VIS = popt
# draw trendline
x2 = np.linspace(0, 225,30)
y2 = trendline_func(x2, A, alfa_VIS)
x3=np.array(den_ground_asyv)
y3 = trendline_func(x3, A, alfa_VIS)
r2=r2_score(VIS_avg_tms_ground_asyv,y3)
plt.plot(x2, y2, 'k--', label='Fit. func Ground Rwanda I: $T(\u03C1) =
                e^{-%.4f \u03C1} ; R^2=%.3f$' % (alfa_VIS,r2))
plt.scatter(den_ground_asyv, VIS_avg_tms_ground_asyv, c='darkgrey',
                marker='v', s=150, label="Ground Rwanda I")
plt.errorbar(den_ground_asyv, VIS_avg_tms_ground_asyv,
                yerr=VIS_std_tms_ground_asyv, xerr=den_uncertainty,
                ecolor='black',linestyle="None")

#Cement
popt, pcov = curve_fit(trendline_func, den_cement, VIS_avg_tms_cement, p0)
A, alfa_VIS = popt
# draw trendline
x2 = np.linspace(0, 50,30)
y2 = trendline_func(x2, A, alfa_VIS)
x3=np.array(den_cement)
y3 = trendline_func(x3, A, alfa_VIS)
r2=r2_score(VIS_avg_tms_cement,y3)
plt.plot(x2, y2, 'm--', label='Fit. func Cement: $T(\u03C1) =
                e^{-%.4f \u03C1} ; R^2=%.3f$' % (alfa_VIS,r2))
plt.scatter(den_cement, VIS_avg_tms_cement, c='fuchsia', marker='*', s=150,
                label="Cement")
plt.errorbar(den_cement, VIS_avg_tms_cement, yerr=VIS_std_tms_cement,
                xerr=den_uncertainty, ecolor='black',linestyle="None")


plt.legend(fontsize=16)
plt.title('Mean spectral transmission in VIS (500-800nm) vs density of
                dust', fontsize=30)
plt.xlabel('Density \u03C1 [$g/m^2$]',size=18)
plt.ylabel('Transmission T(\u03C1) [%]', size=18)
plt.xticks([0,25,50,75,100,125,150,175,200,225,250,275],fontsize=16)
plt.yticks(fontsize=16)
plt.ylim(0,110)

#Plot transmission vs density from 500-800nm
plt.figure(7)
#Scatterplot showing all samples with exponential trendlines

# define trendline function
def trendline_func(density, A, alfa):
    return A * np.exp(-alfa*density)
# curve fit
p0 = (1.,1.e-5) # starting search koefs

#Panel Jordan I
popt, pcov = curve_fit(trendline_func, den_ejre, VIS_NIR_avg_tms_ejre, p0)
A, alfa_VIS_NIR = popt
# draw trendline
x2 = np.linspace(0, 200,50)
y2 = trendline_func(x2, A, alfa_VIS_NIR)
x3=np.array(den_ejre)
y3 = trendline_func(x3, A, alfa_VIS_NIR)
```

```
r2=r2_score(VIS_NIR_avg_tms_ejre,y3)
plt.plot(x2, y2, color='lime', label='Fit. func Panel Jordan I: $T(\u03C1)
                =e^{-%.4f \u03C1}  ; R^2=%.3f$' % (alfa_VIS_NIR,r2))
plt.scatter(den_ejre, VIS_NIR_avg_tms_ejre, c='chartreuse', marker='o',
                s=150, label="Panel Jordan I")
plt.errorbar(den_ejre, VIS_NIR_avg_tms_ejre, yerr=VIS_NIR_std_tms_ejre,
                xerr=den_uncertainty, ecolor='black', linestyle="None")

#Panel Jordan II
popt, pcov = curve_fit(trendline_func, den_oryx, VIS_NIR_avg_tms_oryx, p0)
A, alfa_VIS_NIR = popt
# draw trendline
x2 = np.linspace(0, 275,50)
y2 = trendline_func(x2, A, alfa_VIS_NIR)
x3=np.array(den_oryx)
y3 = trendline_func(x3, A, alfa_VIS_NIR)
r2=r2_score(VIS_NIR_avg_tms_oryx,y3)
plt.plot(x2, y2, color='r', label='Fit. func Panel Jordan II: $T(\u03C1) =
                e^{-%.4f \u03C1}  ; R^2=%.3f$' % (alfa_VIS_NIR,r2))
plt.scatter(den_oryx,VIS_NIR_avg_tms_oryx,c='salmon',marker='o',  s=150,
                label="Panel Jordan II")
plt.errorbar(den_oryx,VIS_NIR_avg_tms_oryx, yerr=VIS_NIR_std_tms_oryx,
                xerr=den_uncertainty, ecolor='black', linestyle="None")

#Panel Egypt I
popt, pcov = curve_fit(trendline_func, den_aswan, VIS_NIR_avg_tms_aswan,
p0)
A, alfa_VIS_NIR = popt
# draw trendline
x2 = np.linspace(0, 200,50)
y2 = trendline_func(x2, A, alfa_VIS_NIR)
x3=np.array(den_aswan)
y3 = trendline_func(x3, A, alfa_VIS_NIR)
r2=r2_score(VIS_NIR_avg_tms_aswan,y3)
plt.plot(x2, y2, color='b', label='Fit. func Panel Egypt I: $T(\u03C1) =
                e^{-%.4f \u03C1} ; R^2=%.3f$' % (alfa_VIS_NIR,r2))
plt.scatter(den_aswan, VIS_NIR_avg_tms_aswan, c='lightskyblue', marker='o',
                s=150, label="Panel Egypt I")
plt.errorbar(den_aswan, VIS_NIR_avg_tms_aswan, yerr=VIS_NIR_std_tms_aswan,
                xerr=den_uncertainty, ecolor='black',linestyle="None")

#Ground Jordan I
popt, pcov = curve_fit(trendline_func, den_ground_ejre,
VIS_NIR_avg_tms_ground_ejre, p0)
A, alfa_VIS_NIR = popt
# draw trendline
x2 = np.linspace(0, 250,30)
y2 = trendline_func(x2, A, alfa_VIS_NIR)
x3=np.array(den_ground_ejre)
y3 = trendline_func(x3, A, alfa_VIS_NIR)
r2=r2_score(VIS_NIR_avg_tms_ground_ejre,y3)
plt.plot(x2, y2, 'lime',linestyle='dashed', label='Fit. func Ground Jordan
                I:$T(\u03C1) = e^{-%.4f \u03C1} ; R^2=%.3f$'
                %(alfa_VIS_NIR,r2))
plt.scatter(den_ground_ejre, VIS_NIR_avg_tms_ground_ejre, c='seagreen',
                marker='v', s=150, label="Ground Jordan I")
plt.errorbar(den_ground_ejre, VIS_NIR_avg_tms_ground_ejre,
                yerr=VIS_NIR_std_tms_ground_ejre, xerr=den_uncertainty,
                ecolor='black',linestyle="None")

#Ground Jordan II
```

```
popt, pcov = curve_fit(trendline_func, den_ground_oryx,
VIS_NIR_avg_tms_ground_oryx, p0)
A, alfa_VIS_NIR = popt
# draw trendline
x2 = np.linspace(0, 290,30)
y2 = trendline_func(x2, A, alfa_VIS_NIR)
x3=np.array(den_ground_oryx)
y3 = trendline_func(x3, A, alfa_VIS_NIR)
r2=r2_score(VIS_NIR_avg_tms_ground_oryx,y3)
plt.plot(x2, y2, 'r--', label='Fit. func Ground Jordan II: $T(\u03C1) =
                e^{-%.4f \u03C1} ; R^2=%.3f$' % (alfa_VIS_NIR,r2))
plt.scatter(den_ground_oryx, VIS_NIR_avg_tms_ground_oryx, c='crimson',
                marker='v', s=150, label="Ground Jordan II")
plt.errorbar(den_ground_oryx, VIS_NIR_avg_tms_ground_oryx,
                yerr=VIS_NIR_std_tms_ground_oryx, xerr=den_uncertainty,
                ecolor='black',linestyle="None")

#Ground Egypt I
popt, pcov = curve_fit(trendline_func, den_ground_aswan,
VIS_NIR_avg_tms_ground_aswan, p0)
A, alfa_VIS_NIR = popt
# draw trendline
x2 = np.linspace(0, 300,30)
y2 = trendline_func(x2, A, alfa_VIS_NIR)
x3=np.array(den_ground_aswan)
y3 = trendline_func(x3, A, alfa_VIS_NIR)
r2=r2_score(VIS_NIR_avg_tms_ground_aswan,y3)
plt.plot(x2, y2, 'b--', label='Fit. func Ground Egypt I: $T(\u03C1) =
                e^{-%.4f \u03C1} ; R^2=%.3f$' % (alfa_VIS_NIR,r2))
plt.scatter(den_ground_aswan, VIS_NIR_avg_tms_ground_aswan, c='darkblue',
                marker='v',  s=150, label="Ground Egypt I")
plt.errorbar(den_ground_aswan, VIS_NIR_avg_tms_ground_aswan,
                yerr=VIS_NIR_std_tms_ground_aswan, xerr=den_uncertainty,
                ecolor='black',linestyle="None")

#Ground Rwanda I
popt, pcov = curve_fit(trendline_func, den_ground_asyv,
VIS_NIR_avg_tms_ground_asyv, p0)
A, alfa_VIS_NIR = popt
# draw trendline
x2 = np.linspace(0, 225,30)
y2 = trendline_func(x2, A, alfa_VIS_NIR)
x3=np.array(den_ground_asyv)
y3 = trendline_func(x3, A, alfa_VIS_NIR)
r2=r2_score(VIS_NIR_avg_tms_ground_asyv,y3)
plt.plot(x2, y2, 'k--', label='Fit. func Ground Rwanda I: $T(\u03C1) =
                e^{-%.4f \u03C1} ; R^2=%.3f$' % (alfa_VIS_NIR,r2))
plt.scatter(den_ground_asyv, VIS_NIR_avg_tms_ground_asyv, c='darkgrey',
                marker='v', s=150, label="Ground Rwanda I")
plt.errorbar(den_ground_asyv, VIS_NIR_avg_tms_ground_asyv,
                yerr=VIS_NIR_std_tms_ground_asyv, xerr=den_uncertainty,
                ecolor='black',linestyle="None")

#Cement
popt, pcov = curve_fit(trendline_func, den_cement, VIS_NIR_avg_tms_cement,
p0)
A, alfa_VIS_NIR = popt
# draw trendline
x2 = np.linspace(0, 50,30)
y2 = trendline_func(x2, A, alfa_VIS_NIR)
x3=np.array(den_cement)
```

```
y3 = trendline_func(x3, A, alfa_VIS_NIR)
r2=r2_score(VIS_NIR_avg_tms_cement,y3)
plt.plot(x2, y2, 'm--', label='Fit. func Cement: $T(\u03C1) =
                e^{-%.4f \u03C1} ; R^2=%.3f$' % (alfa_VIS_NIR,r2))
plt.scatter(den_cement, VIS_NIR_avg_tms_cement, c='fuchsia', marker='*',
                s=150, label="Cement")
plt.errorbar(den_cement, VIS_NIR_avg_tms_cement,
                yerr=VIS_NIR_std_tms_cement, xerr=den_uncertainty,
                ecolor='black',linestyle="None")


plt.legend(fontsize=16)
plt.title('Mean spectral transmission in VIS/NIR (800-1000nm) vs density of
                dust', fontsize=30)
plt.xlabel('Density \u03C1 [$g/m^2$]',size=18)
plt.ylabel('Transmission T(\u03C1) [%]', size=18)
plt.xticks([0,25,50,75,100,125,150,175,200,225,250,275],fontsize=16)
plt.yticks(fontsize=16)
plt.ylim(0,110)
'''
'''
plt.figure(3)
label=("Panel Jordan I","Panel Jordan II","Panel Egypt I")
plt.scatter(den_ejre,tot_avg_tms_ejre,c='chartreuse',marker='o', s=150)
plt.errorbar(den_ejre,tot_avg_tms_ejre, yerr=tot_std_tms_ejre,
                xerr=den_uncertainty, ecolor='black', linestyle="None")
plt.scatter(den_oryx,tot_avg_tms_oryx,c='salmon',marker='o', s=150)
plt.errorbar(den_oryx,tot_avg_tms_oryx, yerr=tot_std_tms_oryx,
                xerr=den_uncertainty, ecolor='black', linestyle="None")
plt.scatter(den_aswan, tot_avg_tms_aswan, c='lightskyblue', marker='o',
                s=150)
plt.errorbar(den_aswan, tot_avg_tms_aswan, yerr=tot_std_tms_aswan,
                xerr=den_uncertainty, ecolor='black',linestyle="None")
plt.legend(label, fontsize=30)
plt.title('Mean spectral transmission vs density of paneldust',
                fontsize=40)
plt.xlabel('Density [$g/m^2$]',size=30)
plt.ylabel('Transmission [%]', size=30)
plt.xticks([0,25,50,75,100,125,150,175,200,225,250,275],fontsize=25)
plt.yticks(fontsize=25)
#plt.yscale('log')
plt.ylim(0,110)
'''
'''
plt.figure(4)
label=("Ground Jordan I","Ground Jordan II","Ground Egypt I","Ground Rwanda
I")
plt.scatter(den_ground_ejre, tot_avg_tms_ground_ejre, c='seagreen',
                marker='v', s=150)
plt.errorbar(den_ground_ejre, tot_avg_tms_ground_ejre,
                yerr=tot_std_tms_ground_ejre, xerr=den_uncertainty,
                ecolor='black',linestyle="None")
plt.scatter(den_ground_oryx, tot_avg_tms_ground_oryx, c='crimson',
                marker='v', s=150)
plt.errorbar(den_ground_oryx, tot_avg_tms_ground_oryx,
                yerr=tot_std_tms_ground_oryx, xerr=den_uncertainty,
                ecolor='black',linestyle="None")
plt.scatter(den_ground_aswan, tot_avg_tms_ground_aswan, c='darkblue',
                marker='v',  s=150)
plt.errorbar(den_ground_aswan, tot_avg_tms_ground_aswan,
                yerr=tot_std_tms_ground_aswan, xerr=den_uncertainty,
```

```
                ecolor='black',linestyle="None")
plt.scatter(den_ground_asyv, tot_avg_tms_ground_asyv, c='darkgrey',
                marker='v', s=150)
plt.errorbar(den_ground_asyv, tot_avg_tms_ground_asyv,
                yerr=tot_std_tms_ground_asyv, xerr=den_uncertainty,
                ecolor='black',linestyle="None")
plt.legend(label, fontsize=30)
plt.title('Mean spectral transmission vs density of grounddust',
                fontsize=40)
plt.xlabel('Density [$g/m^2$]',size=30)
plt.ylabel('Transmission [%]', size=30)
plt.xticks([0,25,50,75,100,125,150,175,200,225,250,275],fontsize=25)
plt.yticks(fontsize=25)
#plt.yscale('log')
plt.ylim(0,110)
'''

'''
plt.show()
```

F Additional results

The following additional results are meant to serve as supporting material for the reader to better understand the discussion on several topics in chapter 5.

Figure F.2: Visual comparison of raw ground dust (left) and sieved ground dust (right) from Jordan I. Collected 16th March 2019. The ground dust was sieved with 80 µm mesh size.

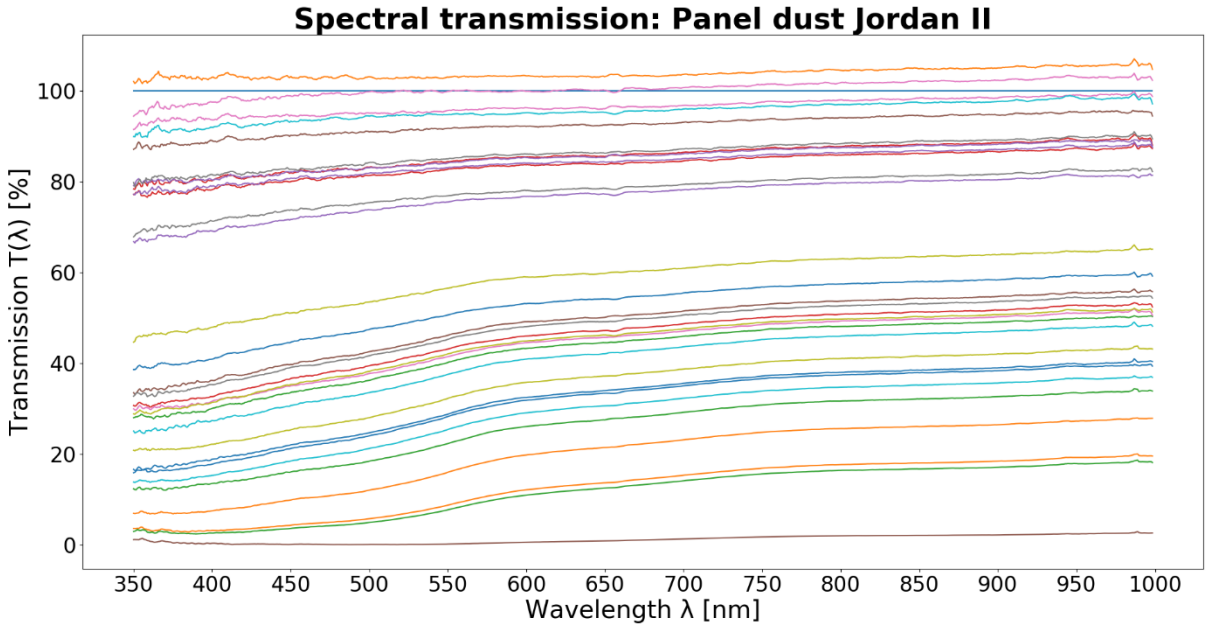

Figure F.3: Spectral transmission of 31 different densities of panel dust from Jordan II, on the PV cover plate. Every colored curve represents a certain dust density given in appendix D, table D.1. The spectrometer measures from UV light at 350 nm to NIR light at 1000 nm.

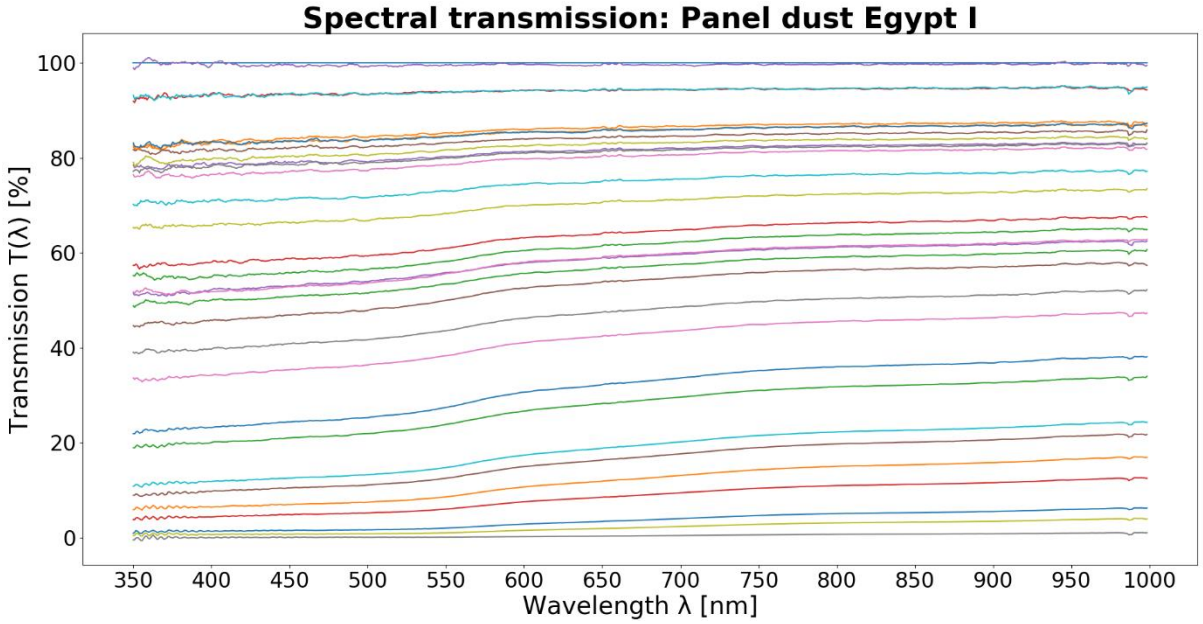

Figure F.4: Spectral transmission of 31 different densities of panel dust from Egypt I, on the PV cover plate. Every colored curve represents a certain dust density given in appendix D, table D.1. The spectrometer measures from UV light at 350 nm to NIR light at 1000 nm.

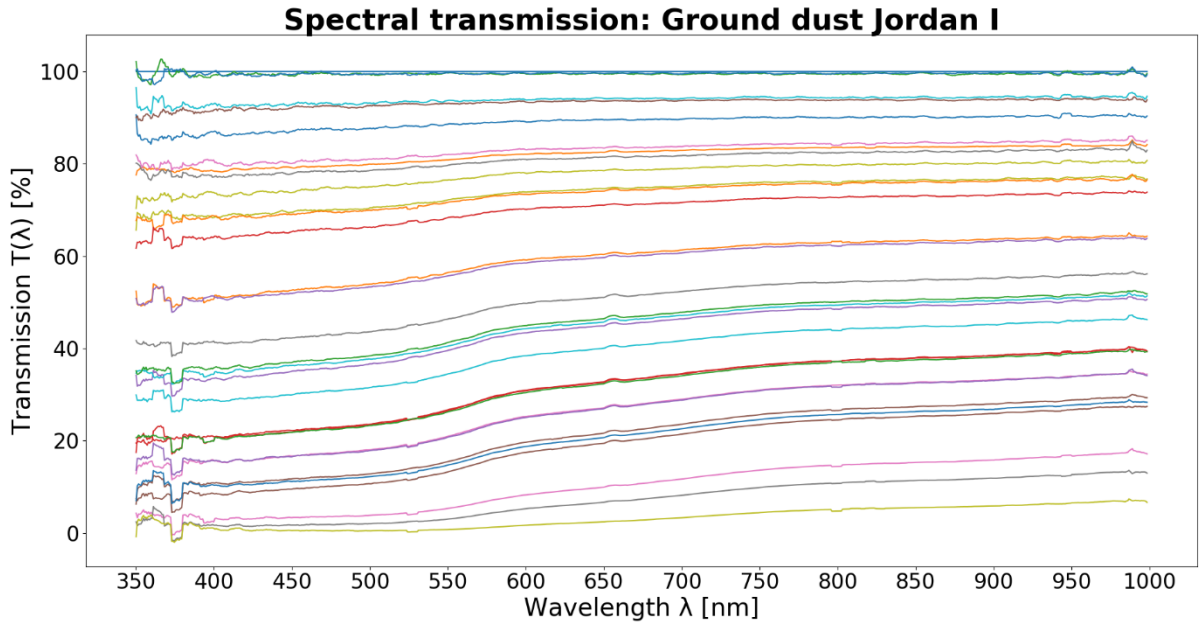

Figure F.5: Spectral transmission of 31 different densities of ground dust from Jordan I, on the PV cover plate. Every colored curve represents a certain dust density given in appendix D, table D.1. The spectrometer measures from UV light at 350 nm to NIR light at 1000 nm.

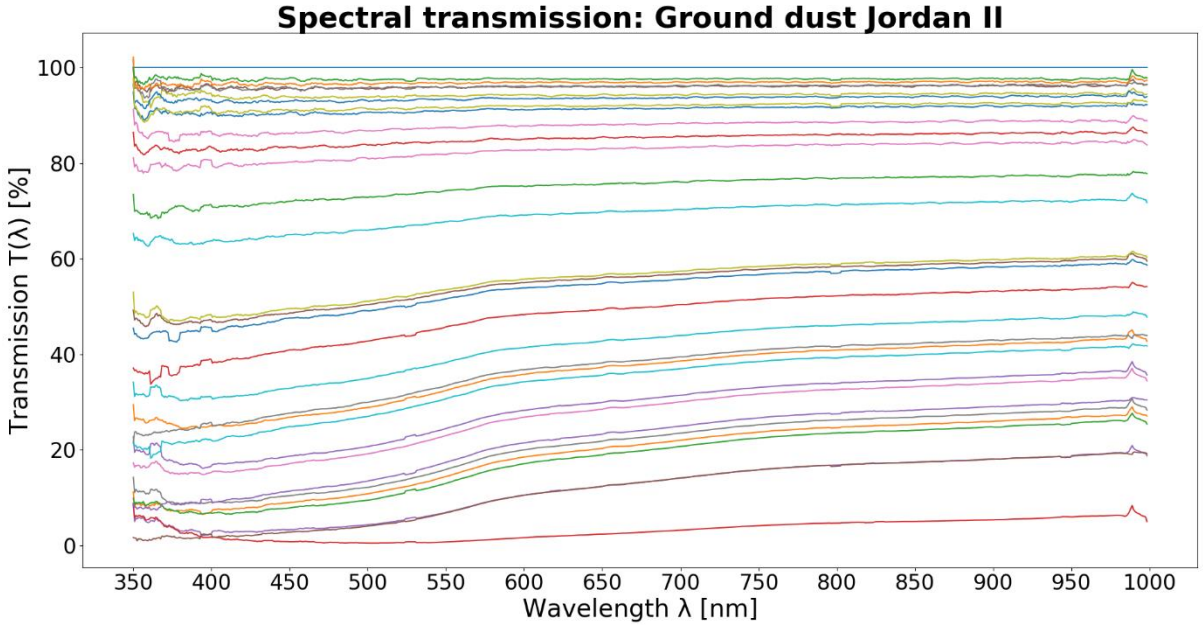

Figure F.6: Spectral transmission of 31 different densities of ground dust from Jordan II, on the PV cover plate. Every colored curve represents a certain dust density given in appendix D, table D.1. The spectrometer measures from UV light at 350 nm to NIR light at 1000 nm.

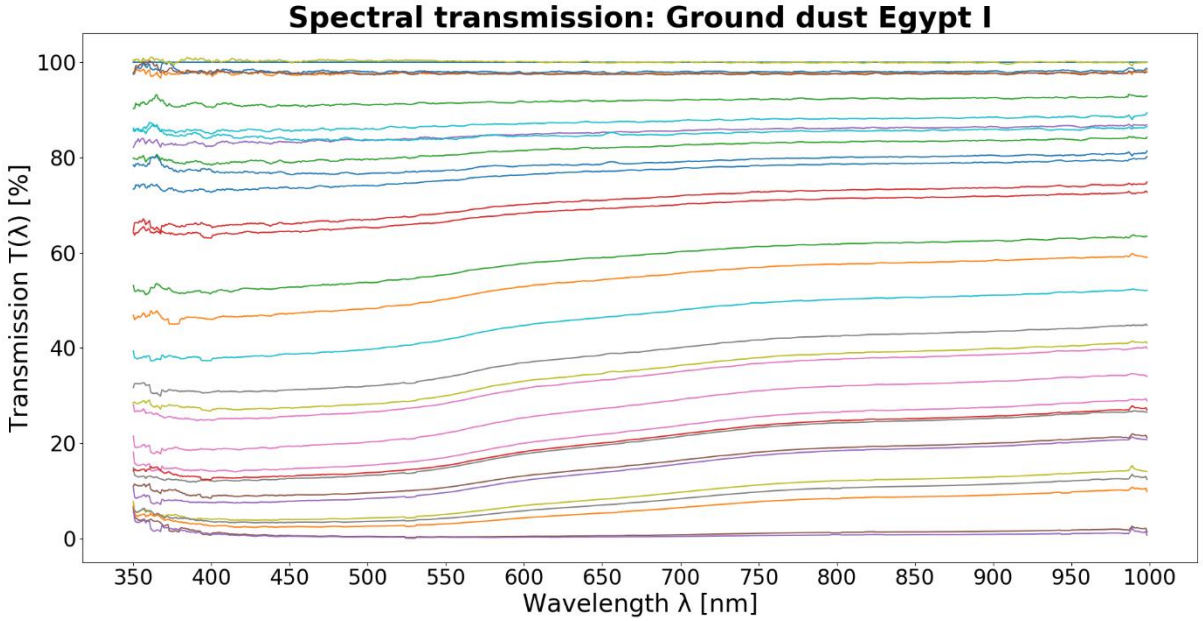

Figure F.7: Spectral transmission of 31 different densities of ground dust from Egypt I, on the PV cover plate. Every colored curve represents a certain dust density given in appendix D, table D.1. The spectrometer measures from UV light at 350 nm to NIR light at 1000 nm.

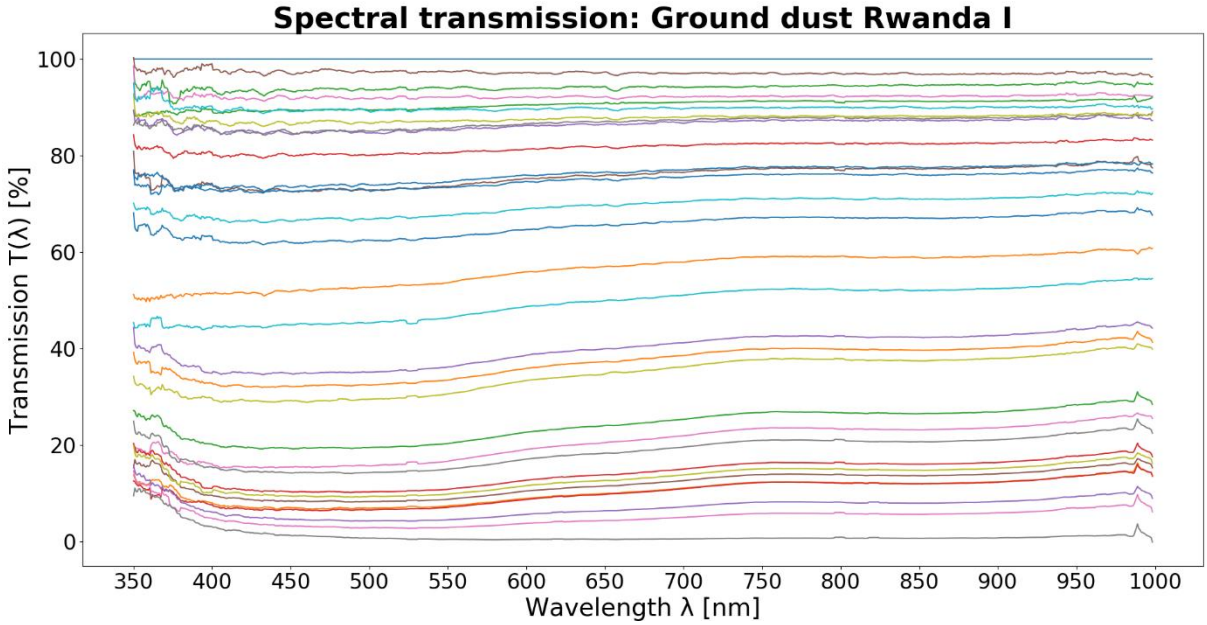

Figure F.8: Spectral transmission of 31 different densities of ground dust from Rwanda I, on the PV cover plate. Every colored curve represents a certain dust density given in appendix D, table D.1. The spectrometer measures from UV light at 350 nm to NIR light at 1000 nm.

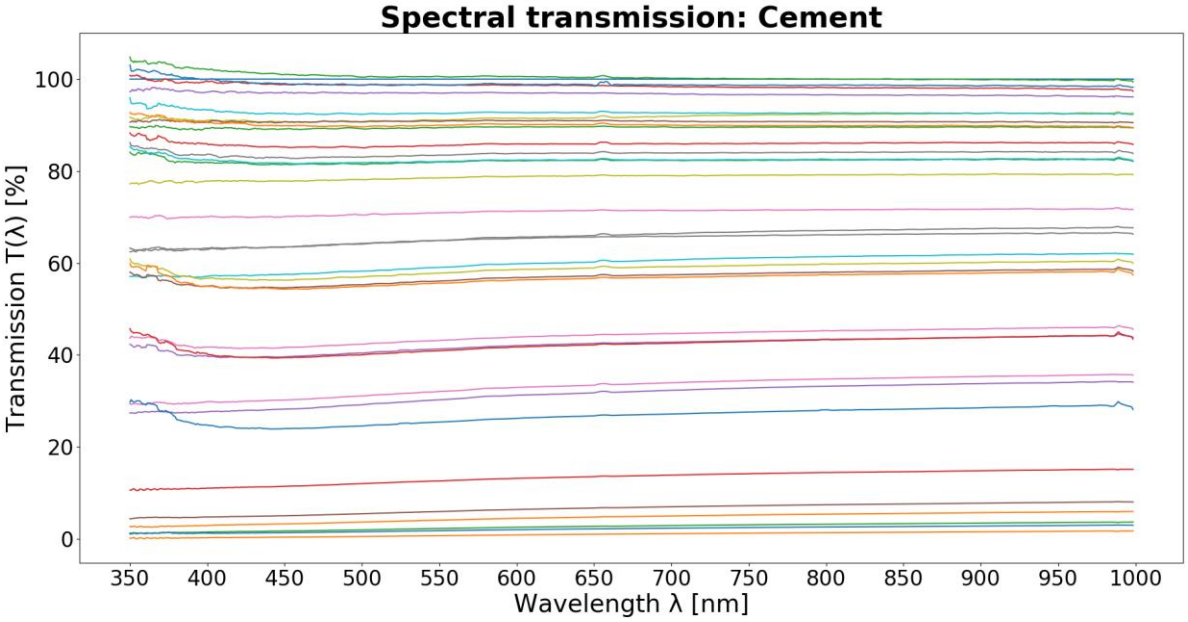

Figure F.9: Spectral transmission of 34 different densities of cement dust on the PV cover plate. Every colored curve represents a certain dust density given in appendix D, table D.1. The spectrometer measures from UV light at 350 nm to NIR light at 1000 nm.

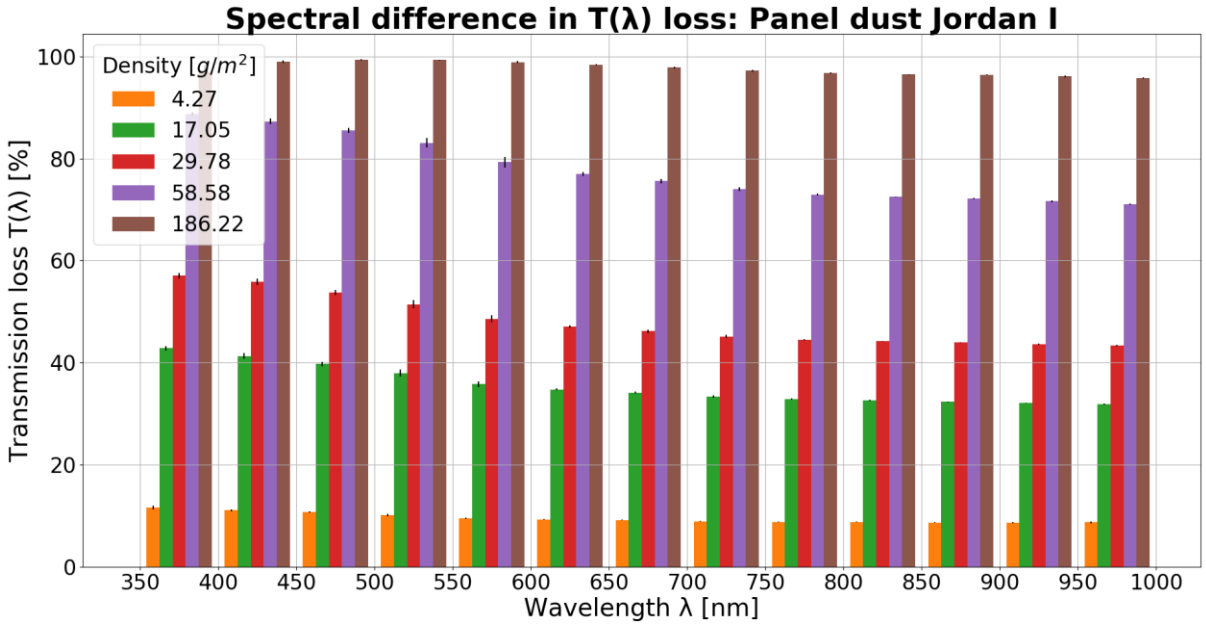

Figure F.10: Spectral differences in attenuation of sunlight. The graph shows the average transmission loss for five selected densities of panel dust from Jordan I in wavelength intervals of 50 nm from 350 – 1000 nm.

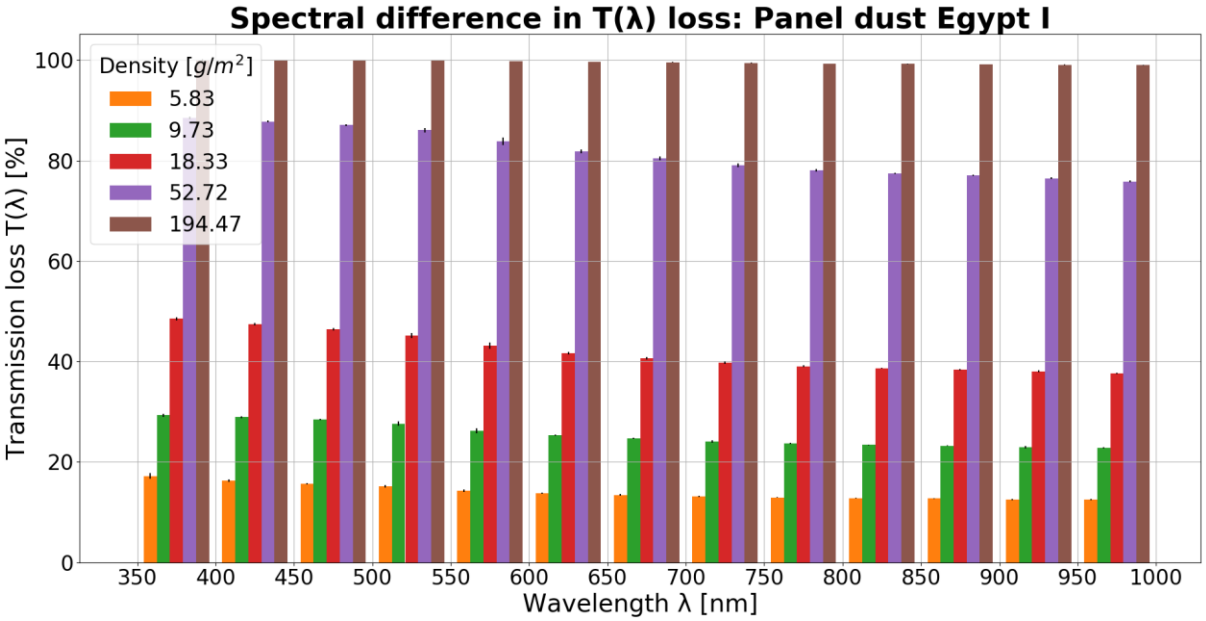

Figure F.11: Spectral differences in attenuation of sunlight. The graph shows the average transmission loss for five selected densities of panel dust from Egypt I in wavelength intervals of 50 nm from 350 – 1000 nm.

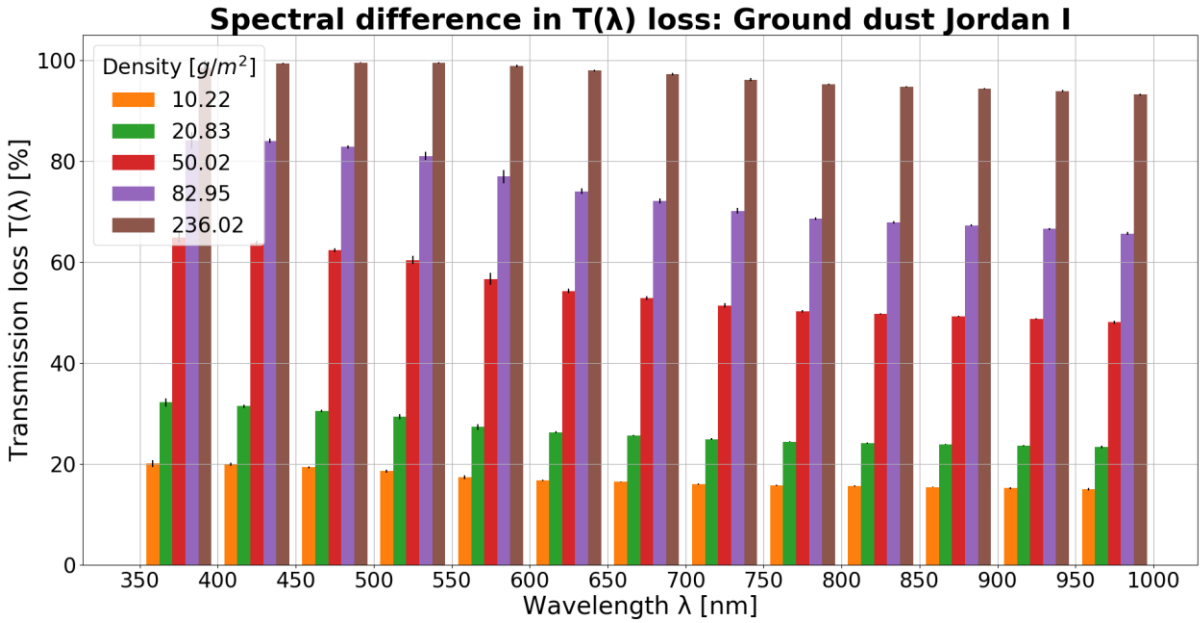

Figure F.12: Spectral differences in attenuation of sunlight. The graph shows the average transmission loss for five selected densities of ground dust from Jordan I in wavelength intervals of 50 nm from 350 – 1000 nm.

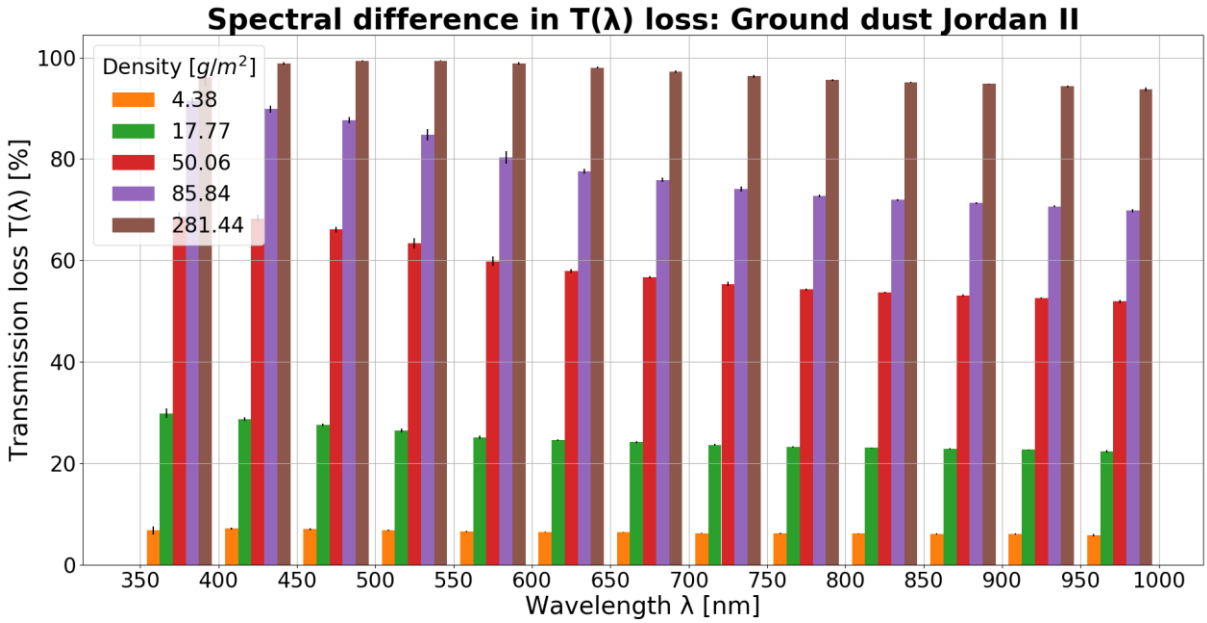

Figure F.13: Spectral differences in attenuation of sunlight. The graph shows the average transmission loss for five selected densities of ground dust from Jordan II in wavelength intervals of 50 nm from 350 – 1000 nm.

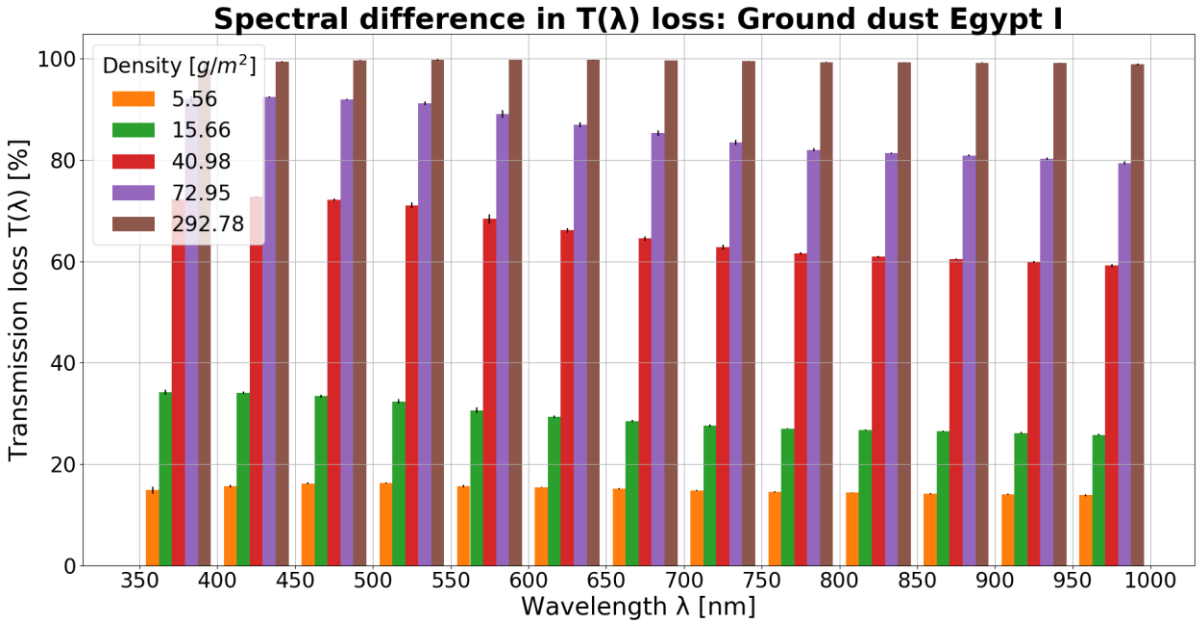

Figure F.14: Spectral differences in attenuation of sunlight. The graph shows the average transmission loss for five selected densities of ground dust from Egypt I in wavelength intervals of 50 nm from 350 – 1000 nm.

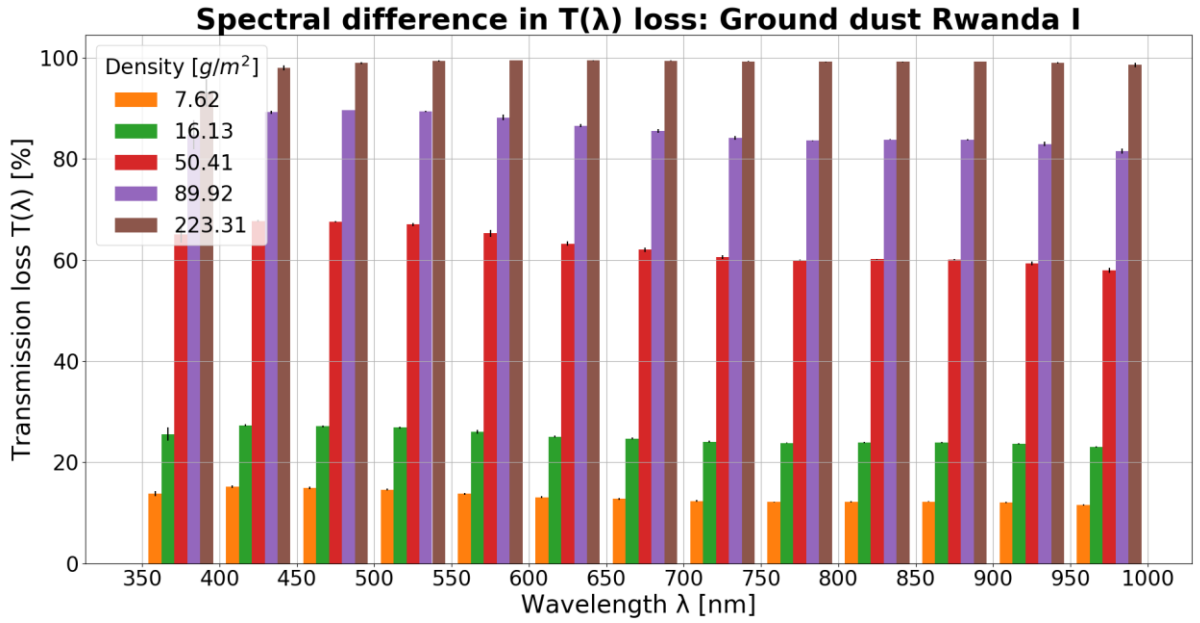

Figure F.15: Spectral differences in attenuation of sunlight. The graph shows the average transmission loss for five selected densities of ground dust from Rwanda I in wavelength intervals of 50 nm from 350 – 1000 nm.

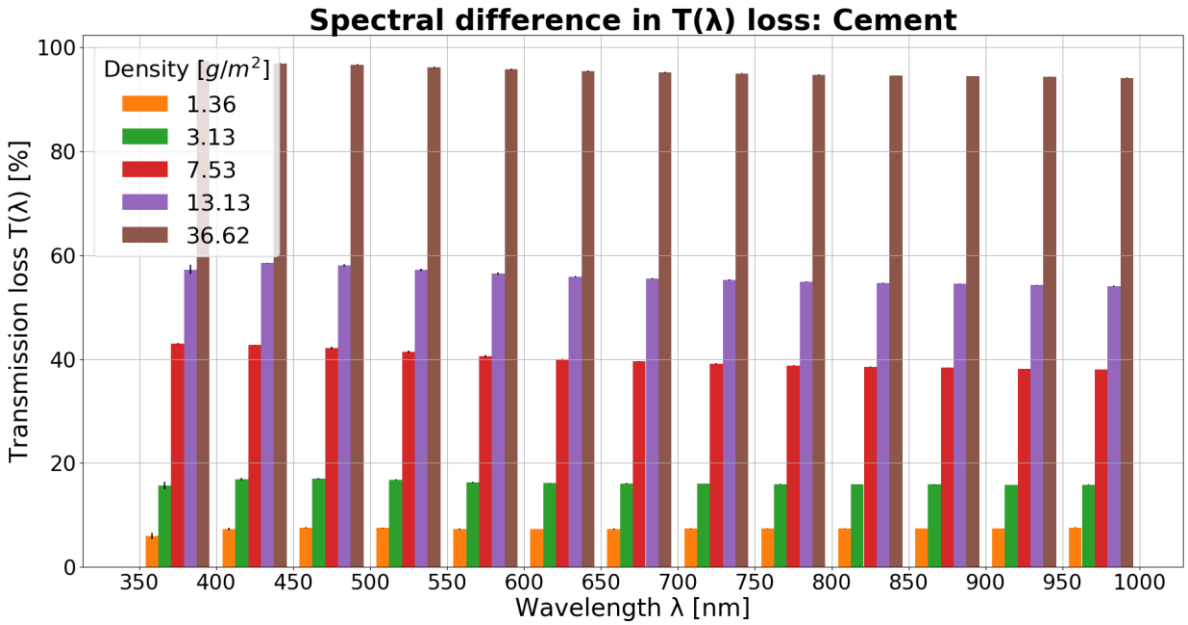

Figure F.16: Spectral differences in attenuation of sunlight. The graph shows the average transmission loss for five selected densities of cement in wavelength intervals of 50 nm from 350 – 1000 nm.

Table F.2: Regression analysis on the influence of particle size distribution, albedo and iron oxide content on the α-coefficient of the exponential fit function from figure 5.27.

	Coefficients	Std Error	t -Stat	p-value	Confidence interval
Intercept	0,0484	0,0181	2,673	0,0755	[0.0058 – 0.0911]
Particle size	-0,0034	0,0009	-3,579	0,0373	[-0.0056 – -0.0012]
Albedo	-0,0335	0,0303	-1,107	0,3491	[-0.1047 – 0.0377]
Iron oxide	-0,0879	0,2143	-0,410	0,7093	[-0.5922 – 0.4165]